

Dynamics of colloidal systems of magnetic nanoparticles under influence of magnetic fields investigated by XPCS

Dissertation
zur Erlangung des Doktorgrades
an der Fakultät der Mathematik, Informatik und
Naturwissenschaften
Fachrichtung Physik
der Universität Hamburg

vorgelegt von

Alexander Schavkan

geboren am 22.08.1985

in Krasnodar

Hamburg
2017

Gutachter der Dissertation:	Prof. Dr. Gerhard Grübel Prof. Dr. Christian Schroer
Gutachter der Disputation:	Prof. Dr. Gerhard Grübel Prof. Dr. Wilfried Wurth Prof. Dr. Daniela Pfannkuche Prof. Dr. Melanie Schnell
Datum der Disputation:	20.04.2017
Vorsitzender des Prüfungsausschusses:	Prof. Dr. Wolfgang Hansen
Vorsitzender des Promotionsausschusses:	Prof. Dr. Wolfgang Hansen
Leiter des Fachbereichs Physik:	Prof. Dr. Michael Potthoff
Dekan der Fakultät Mathematik, Informatik und Naturwissenschaften :	Prof. Dr. Heinrich Graener

Abstract

This thesis investigates structural properties and the underlying microscopic dynamics of suspensions of α -FeOOH goethite platelets in water under the influence of magnetic fields. Goethite particles show unusual physical properties and a rich phase diagram, which makes their suspensions an object of high interest for research in the area of "smart nanoparticles". Five nanoparticle concentrations were chosen such that different liquid crystal phases could be studied. The suspensions of platelets of these chosen concentrations were exposed to magnetic fields of varying strength. Small angle X-ray scattering and X-ray photon correlation spectroscopy data were taken and evaluated. The appearing phases and phase transitions were studied as a function of concentration and applied magnetic field. For this purpose, order parameters, ellipticity, radial and azimuthal peak positions and widths of scattering features were investigated to clarify the structural properties in detail. For the analysis of the underlying dynamics, the relaxation rates and the shape of measured time correlation functions were evaluated. The results show that with increasing magnetic field a partial realignment of the platelets occurs. This realignment is connected to the magnetic properties of the particles. The dynamics of the corresponding phases revealed a dependence on the concentration of nanoparticles in the suspension. At a concentration of $c = 20$ vol% the transition from the nematic to the anti-nematic phase traverses a mixed state. The nematic and anti-nematic phases show ballistic motion and very similar properties, even though a realignment of the particles from an orientation with the long axis parallel to the applied magnetic field in the nematic phase to an orientation with the long axis perpendicular to the magnetic field in the anti-nematic phase occurs. The mixed state of 20 vol%-suspension exhibits a diffusive motion of the particles and different characteristics. A significant difference was observed for $c = 16$ vol%, where the original nematic state has a transition into the anti-nematic phase via an intermediate state of the mixed phase, too. In contrast to the behaviour at $c = 20$ vol% the underlying motion at $c = 16$ vol% shows ballistic dynamics only for the nematic state. At this concentration the mixed state and the anti-nematic phase show both diffusive motions. The formation of different phases and underlying microscopic dynamics are explained through the establishment of qualitative model based on dipole-dipole interactions. The results obtained in this thesis describe the structural properties of goethite suspensions and try to our knowledge for first time to

link the microscopic dynamics of the platelets in the suspensions to their structural and unusual physical properties.

Kurzfassung

In dieser Arbeit wurden die strukturellen Eigenschaften und die dazugehörige Dynamik von Goethitesuspensionen, α -FeOOH Plättchen in Wasser unter Einfluss magnetischer Felder untersucht. Im Bereich "smarter" Nanopartikel erwecken Goethitepartikel ein hohes wissenschaftliches Interesse, da ihre Suspensionen ungewöhnliche physikalische Eigenschaften und ein vielfältiges Phasendiagramm zeigen. Im Rahmen dieser Dissertation wurden fünf ausgewählte Konzentrationen von Goethitesuspensionen untersucht, die unterschiedliche Flüssigkristallphasen ausbilden sollten. In Magnetfeldern unterschiedlicher Feldstärke wurden die mikroskopische Struktur und Dynamik der Suspensionen mithilfe der Röntgenkleinwinkelstreuung (Small Angle X-ray Scattering oder SAXS) und Röntgenphotonenkorrelationsspektroskopie (X-ray Photon Correlation Spectroscopy oder XPCS) analysiert. Induzierte Flüssigkristallphasen und Phasenübergänge wurden dabei auf Abhängigkeit von der Konzentration und der magnetischer Feldstärke hin untersucht. Um die strukturellen Eigenschaften aufzuklären, wurden Ordnungsparameter, Elliptizität sowie radiale und azimuthale Peakpositionen und -breiten ausgewertet. Im Zuge der Untersuchung der zugrundeliegenden Dynamik der Plättchen wurden die Relaxationsraten und die Form der Zeitkorrelationsfunktionen analysiert. Die Ergebnisse haben gezeigt, dass eine partielle Reorientierung der Teilchen mit wachsender Magnetfeldstärke stattfindet. Diese Reorientierung, von einer Ausrichtung mit der langen Teilchenachse parallel zum angelegten magnetischen Feld zu einer Ausrichtung dieser langen Achse senkrecht zum magnetischen Feld, ist mit den magnetischen Eigenschaften der Plättchen verbunden. Die Analyse der Dynamik hat gezeigt, dass die dazugehörigen Phasenübergänge konzentrationsabhängig sind. Beim Übergang von der nematischen zur anti-nematischen Phase bei einer Konzentration von $c = 20 \text{ vol\%}$ wird eine gemischte Phase beobachtet. In der nematischen und der anti-nematischen Phasen ist die Bewegung ballistisch und nur in der Mischphase diffusiv. Trotz der Reorientierung der Teilchen ist die zugrundeliegende Dynamik in der nematischen Phase und der anti-nematischen Phase bei $c = 20 \text{ vol\%}$ sehr ähnlich. Ein signifikanter Unterschied wird bei einer Konzentration von $c = 16 \text{ vol\%}$ beobachtet. Die Suspension wechselt zwar auch von einer ursprünglich nematischen Phase über einen gemischten Zustand in die anti-nematische Phase, aber, im Gegensatz zu dem Verhalten bei der Konzentration $c = 20 \text{ vol\%}$ zeigte die Suspension mit der Konzen-

tration $c = 16 \text{ vol\%}$ nur in der nematischen Phase eine ballistische Dynamik. Sowohl die Mischphase als auch die anti-nematische Phase zeigten bei dieser Konzentration Bewegungen mit diffusiven Charakter. Unterschiedliche Arten der Phasenübergänge und der zugrundeliegenden Dynamiken wurden mithilfe von qualitativen Wechselwirkungsmodellen erklärt, bei denen Dipol-Dipol Wechselwirkung als Basis angenommen wurde. Die Ergebnisse dieser Arbeit haben die vorliegenden Kenntnisse über die Struktur von Goethitesuspensionen präzisiert und, soweit uns bekannt, zum ersten Mal die mikroskopische Dynamik der Plättchen in Suspension mit ihren strukturellen und ungewöhnlichen physikalischen Eigenschaften in Verbindung gebracht.

Contents

Abstract	iii
Kurzfassung	v
1. Introduction	1
2. Instrumentation	3
2.1. The synchrotron source Positron-Electron Tandem Ring Anlage III . . .	3
2.2. The Coherence Beamline P10 at PETRA III	5
2.3. The sample environment and experimental setup at P10	8
2.4. Experimental parameters	10
3. Design of a magnet system for Coherence Beamline P10	13
3.1. Theoretical estimation of the achievable magnetic field at the sample .	13
3.2. The implemented magnetic sample system	14
3.3. Performance of the sample system	17
4. Synthesis and characterization of goethite α-FeOOH samples	19
4.1. Different approaches to synthesize goethite platelets	19
4.1.1. Synthesis of Goethite platelets by Olowe et al. and Gilbert et al.	19
4.1.2. Synthesis of Goethite platelets by Krehula et al.	21
4.1.3. Synthesis of Goethite platelets after Thies-Weesie et al.	21
4.2. Evaluation of the synthesis products	22
4.2.1. Results and discussion of the synthesis of goethite platelets after Gilbert et al.	22
4.2.2. Results of the synthesis of the goethite platelets after Krehula et al.	23
4.2.3. Results of the XRD- and TEM-analysis of the synthesis by Thies- Weesie et al.	24
4.2.4. Goethite synthesis summary	24
4.3. Characterization of the goethite particles	25
5. Theoretical background	29
5.1. Small Angle X-ray Scattering	29

5.2. Orientation distribution function and ordering parameters	33
5.3. X-ray Photon Correlation Spectroscopy	39
5.4. Goethite and its magnetic properties	44
6. Small Angle X-ray Scattering analysis	51
6.1. Introduction	51
6.2. Preliminary discussion	52
6.3. Low concentration suspensions	56
6.3.1. Summary of structural analysis of low concentration suspensions	64
6.4. High concentration suspensions	66
6.4.1. Summary of structural analysis of high concentration suspensions	71
6.5. Magnetic energy of the suspension	72
6.6. Conclusions of the structural analysis	77
7. XPCS analysis	81
7.1. XPCS analysis procedure	81
7.2. XPCS data	86
7.2.1. XPCS analysis of 20 vol%-suspensions	86
7.2.2. XPCS analysis of 16 vol%-suspensions	100
7.2.3. Comparison of the dynamics in the nematic and anti-nematic phases of 20 vol%- and 16 vol%-suspensions	113
7.2.4. The microscopic dynamics of the mixed phases	115
7.2.5. Comparison of the dynamics in the nematic and the anti-nematic phases with the dynamics in the mixed phases	127
7.3. Discussion and interpretation of the XPCS data	129
7.3.1. Preliminary discussion	129
7.3.2. Discussion and interpretation of the dynamics in the 20 vol%- suspensions	133
7.3.3. Discussion and interpretation of the dynamics in the 16 vol%- suspensions	135
7.4. Model of the behaviour of the goethite nanoplatelets in suspensions under influence of a magnetic field	139
7.4.1. Model for the behaviour of goethite particles in the nematic and anti-nematic phases in 20 vol%-suspension	139
7.4.2. Model for the behaviour of goethite particles in the nematic and anti-nematic phases in a 16 vol%-suspension	142
7.4.3. Model for the dynamic behaviour of goethite particles in the mixed phases	144

7.4.4. Summarized model behaviour of the goethite particles under influence of an increasing magnetic field	146
8. Summary	147
9. Outlook	151
A. Appendix A: order parameter	153
B. Appendix B: structure peaks	155
B.1. Low concentration samples	155
B.2. High concentration samples	157
C. Appendix C: missing contrast evaluation	159
List of Figures	163
List of Tables	175
Bibliography	177
Publications	183
Acknowledgements	185
Eidesstattliche Erklärung	187

1. Introduction

Suspensions of colloidal particles have been a topic of great interest in research for more than a century. Many systems consisting of inorganic, polymer, core-shell or anisotropic shaped particles are described [12, 53, 73]. Nevertheless, most often the investigated systems are model systems, because they can be characterized more accurately. Therefore, suspensions of spherical particles received more attention [46, 65]. In comparison, only a small number of anisotropic systems were investigated even though suspensions of anisotropic particles often have a rich phase diagram [37, 46, 70, 71].

Because of possible uses in catalytic schemes, biotechnology and bio-medicine, controlled colloid or "smart nanoparticle" suspensions under the influence of a driving force, e.g. an electric or magnetic field, received much attention in research lately [43, 58, 60]. For these purposes, anisotropic colloidal systems with a rich phase diagram are extremely interesting. A long-known system is based on goethite particles (α -FeOOH). It was used for centuries mostly for colouring purposes, but its suspensions are also used in the research of liquid crystalline phases. Goethite suspensions form a variety of liquid crystalline phases (isotropic, nematic, smectic A, columnar and others) [37, 40, 41, 42, 71]. Two particular properties of goethite suspensions are the particle alignment parallel to an applied weak magnetic field and the realignment perpendicular to the field after a critical field B_{crit} is exceeded. These properties are not completely understood yet [41, 42, 69]. One reason is that suspensions of goethite platelets are not perfect model systems, due to the high polydispersity of the particles and the complex synthesis, which does not allow to control the axis ratio precisely.

Structural investigations of the goethite suspensions properties are numerous [35, 36, 37, 38, 40, 41, 42, 49, 69, 70, 71, 72]. The aim of this thesis was to choose a stable synthesizing method for α -FeOOH platelets under accessible conditions and to investigate the structural and dynamical behaviour of suspensions of the produced particles. To our knowledge it has not been tried to link the unique properties of goethite suspensions to the microscopic dynamics of the platelets. Therefore our aim was that the structural analysis would form a foundation for the analysis of the underlying microdynamics of the platelets investigated by means of X-ray photon correlation spectroscopy. This approach promises to deliver new hints towards the understanding

of goethite liquid phase formation and ultimately lead to new developments in the promising fields of catalysis or biomedicine.

This thesis has been written as part of the research program at Deutsches Elektronen-Synchrotron (DESY) - specifically at the synchrotron PETRA III as part of the Inhouse program of the Coherence Beamline P10 and has the following structure. **Chapter 2** explains the experimental facilities, the beamline, the setup and the experimental procedure. Beamline P10 required a new magnetic sample chamber, where the magnetic field could be changed in amplitude and direction, as well as set to zero. The development of such a system was included in the definition of this thesis and is presented in **Chapter 3**, where the design and tests of the performance of the magnetic sample system for Coherence Beamline P10 are depicted. After some discussion, a fascinating physical system with not completely understood properties - goethite suspensions - was chosen. The reaction of the system to the applied magnetic field allowed to perform first scientific experiments on the newly designed magnetic sample system. It was decided to study the properties of the sample system by means of small angle X-ray scattering (SAXS) and X-ray photon correlation spectroscopy (XPCS) - standard methods at P10. In order to find stable synthesis conditions for goethite platelets under the available laboratory conditions several reaction methods were tried. The methods used and the respective outcomes are summarized in **Chapter 4**. The theoretical overview of the methods used - small angle X-ray scattering (SAXS) and X-ray photon correlation spectroscopy (XPCS), as well as the already known structural behaviour of the goethite suspensions are presented in **Chapter 5**. The structural data taken in the experiments with small angle X-ray scattering, its analysis, interpretation and results are described in **Chapter 6**. The microscopic dynamics of the platelets in suspensions was investigated using X-ray photon correlation spectroscopy. The analysis is shown together with the respective interpretation and the according quantitative model in **Chapter 7**. The results are summarized in **Chapter 8** and prospective developments and possible future experiments are presented in **Chapter 9**.

2. Instrumentation

X-ray radiation is widely utilized to study different properties of matter. Various methods employing X-ray fluorescence, absorption, scattering and diffraction have been developed to study structural, electronic and dynamical properties of materials. Structural investigations of soft matter systems are often accomplished using the small angle X-ray scattering (SAXS) method [25]. The recent development of synchrotron sources and X-ray free-electron lasers have enabled the production of coherent X-rays. These can be used to study dynamics in colloidal systems by X-ray photon correlation spectroscopy (XPCS). This chapter describes the instrumentation needed for SAXS and XPCS experiments at a synchrotron source. The experiments were conducted at the Positron-Electron Tandem Ring Anlage III (PETRA III) synchrotron facility at DESY Hamburg, which is briefly described in Section 2.1. The next section - Section 2.2, describes the Coherence Beamline P10. The SAXS and XPCS experimental setup are depicted in Section 2.3. The SAXS and XPCS experimental procedure used in the experiments, as implemented at P10 beamline for this thesis, is presented in Section 2.4.

2.1. The synchrotron source Positron-Electron Tandem Ring Anlage III

The development of X-ray sources is visualized in fig. 2.1. In order to describe the properties of an X-ray beam a new quantity *Brilliance* was defined as:

$$Brilliance = F/(A \cdot \Omega \cdot 0.1 \%BW), \quad (2.1)$$

where F is the flux in photons/s, A is the area of the source in mm^2 , Ω is the opening angle of the source, which describes the divergence of the beam, and BW is the fixed bandwidth, usually given in 0.1 %BW.

An electron moving in an infinite constant magnetic field B experiences a Lorentz force. As a result of the acting Lorentz force an electron accelerates and moves in a plane perpendicular to the applied magnetic field B . The path of the electron is then circular. An electron in a synchrotron arc experiences constant acceleration and thus radiates continuously through the entire orbit. The radiation emitted by a relativistic

electron is concentrated in a collimated cone. Even though an electron radiates along its full circular path, the observer, positioned at a tangential point of the arc, can see the radiation only when the electron passes the arc at this tangential point.

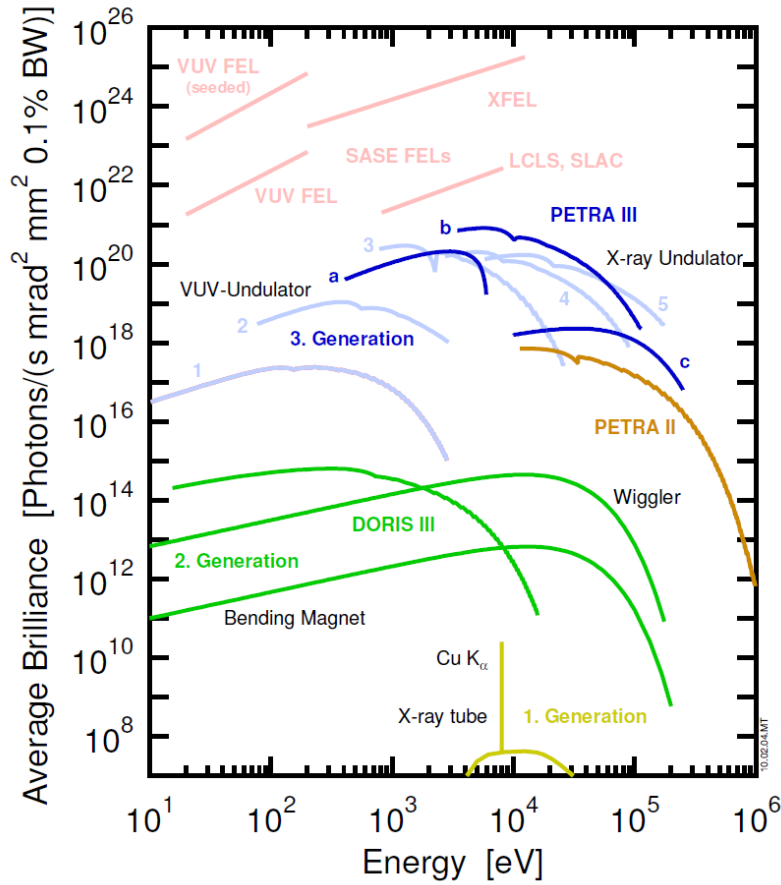


Figure 2.1.: Comparison chart for brilliance of several X-ray sources [14]

The emitting direction of the electron is the direction of the instantaneous velocity of the electron and the opening angle of the cone is $\gamma^{-1} = m_e c^2 / E_e$, where m_e is the mass of an electron, c is speed of light in vacuum and E_e is the energy of an electron. An outstanding feature of synchrotron radiation is the ability to cover the frequency range between infrared light and hard X-rays, which provides multiple experimental possibilities.

The most efficient way to produce X-rays is to insert magnetic devices in straight sections of a synchrotron, which force the electrons to execute oscillations in the horizontal plane. This behaviour is enforced by an array of permanent magnets, which produces an alternating magnetic field along the path. The field changes the sign along the path of the electrons. These devices are known as wigglers and undulators.

Wigglers and undulators share a similar design, but the oscillations in an undulator have a lower amplitude. An undulator, as implemented in the PETRA III facility, is characterized by γ^{-1} and the spatial undulator period λ_u . In order to characterize the amplitude of the oscillations the K parameter is used, defined as $K = e \cdot B_0 / (m_e \cdot c \cdot k_u)$, where e is the elementary charge. B_0 is the peak magnetic field in the undulator and

$k_u = 2\pi/\lambda_u$. K is describing the maximum angular deviation from the undulator axis and measures the interaction of the electron beam with the peak magnetic field B_0 .

The fundamental wavelength of an undulator is proportional to its spatial period. The wavelength of an undulator is defined by:

$$\lambda_n = \frac{\lambda_u}{2n\gamma^2} (1 + K^2/2 + \theta^2\gamma^2). \quad (2.2)$$

The resulting spectral width is then

$$\frac{\Delta\lambda}{\lambda} = \frac{\Delta E}{E} \approx \frac{1}{nN}. \quad (2.3)$$

Here n is number of the undulator harmonics, θ is the observation angle and N is number of the undulator periods. These values are directly influencing the brilliance, which again is used as a measure for the quality of the beam produced by a synchrotron.

PETRA III is a new 3rd generation synchrotron source at DESY, which operates since 2009 (fig. 2.2, left shows a aerial view). PETRA III is currently the most brilliant third generation synchrotron radiation source of the world with a brilliance of 10^{21} ph/(s * mm * mrad * 0.1%BW) [14]. The PETRA III experimental hall has a length of nearly 300m and an area of 7000m². It currently houses 14 beamlines and 30 experimental stations, which are schematically shown in fig. 2.2 on the right.

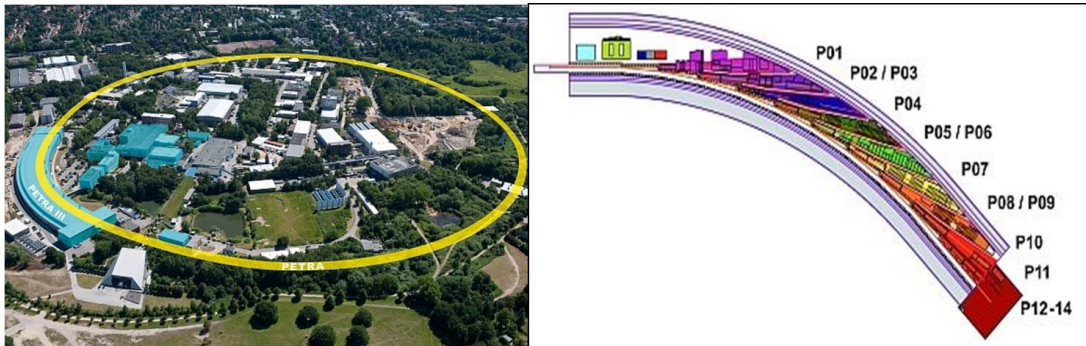


Figure 2.2.: Aerial view of the PETRA III ring on the left and schematic position of the beamlines in the PETRA III hall on the right [15].

2.2. The Coherence Beamline P10 at PETRA III

The Coherence Beamline P10 is located in sector 7 of PETRA III. The coherent flux at the beamline is displayed in table 2.1 [74].

The source of the beamline is a 5 m-long U29 undulator with 168 periods. The spacing between individual magnets is 29 mm. The source size was $\sigma_v \times \sigma_h \equiv 6 \times 36 \mu\text{m}^2$ and after the PETRA III extension in 2014 increased to $\sigma_v \times \sigma_h \equiv 8 \times 41 \mu\text{m}^2$. P10 can

Table 2.1.: Photon flux at P10 at $E = 8$ keV and according longitudinal coherence length [74].

$\Delta\lambda/\lambda$	$\sigma_l[\mu\text{m}]$	$Flux_{coh}$	Energy [keV]
$1 \cdot 10^{-4}$ (Si(111))	1.5	$2.3 \cdot 10^{11}$	8
$3 \cdot 10^{-5}$ (Si(311))	5.0	$6 \cdot 10^{10}$	8

provide an energy range between 3.8 keV (limited by a minimum opening gap of the undulator of 9.8 mm) and 30 keV.

The Coherence Beamline P10 is dedicated to coherent scattering and diffraction applications using inter alia XPCS and coherent diffraction imaging (CDI) techniques. The combination of the low emittance of the PETRA III source and the versatility of the available instruments gives an outstanding opportunity to perform experiments with coherent scattering techniques in the medium-hard X-ray range. XPCS is the extension of Dynamic Light Scattering (DLS) from the visible light to the X-ray regime. The method allows to study dynamics of matter on length scales not accessible by visible light and frequencies not accessible by inelastic neutron scattering or inelastic x-ray scattering techniques [26]. CDI is an imaging technique which uses coherent diffraction intensities for ab initio reconstruction of the electron density of nanomaterials using phase retrieval algorithms [45].

The beamline and supporting infrastructure are depicted in fig. 2.3 and consists of the front-end, the optics hutch and two experimental hutches. It includes supporting units such as mechanical workshop, preparation and electronics laboratories. The core of the beamline consists of a front-end, where two power slits systems PS1 and PS2 are installed, an optics hutch (OH) and two experimental hutches: experimental hutch 1 (EH1) - at a distance of ≈ 67 m from the source and experimental hutch 2 (EH2) at a distance of ≈ 83 m from the source.

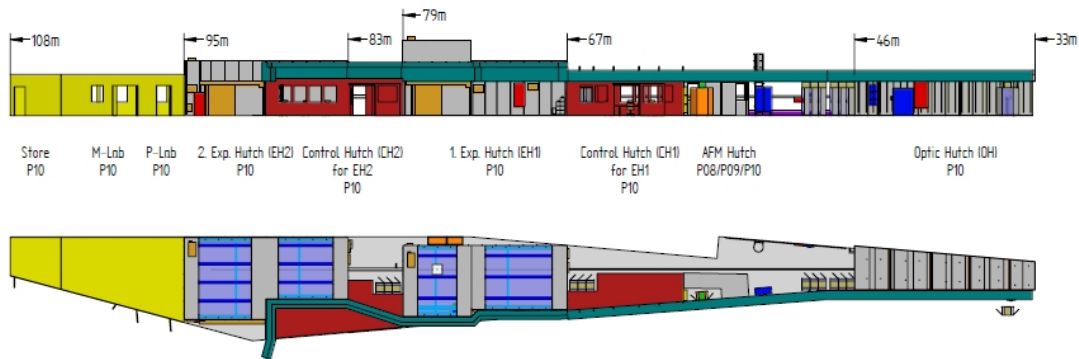


Figure 2.3.: Layout drawing of P10 beamline [74].

At ≈ 38 m from the source in the optics hutch a high heat load monochromator is installed. At the moment there are two options for the monochromator - a Si(111)

double crystal monochromator and a single crystal Si(111) channel-cut monochromator. For the experiments presented in this thesis the Si(111) double crystal monochromator was used.

After the monochromator a pair of horizontal reflecting mirrors is installed. They have a radius $r > 100\text{ km}$ and are partially coated with stripes of Pt and Rd to provide adjusted cut off energies for higher X-ray energies.

The experiments described in this thesis were performed in the experimental hutch 2 (EH2). It begins at $\approx 83\text{ m}$ distance from the source and is 12m long. Some optical elements are positioned on an optical table called OT2. These elements are: pink-beam compatible slits (Galil 2), an intensity monitor, a beam-deflecting unit (BDU) and Beryllium compound refraction lenses (CRL) transfocator optics. The beryllium lens changer consists of a vacuum chamber with 12 slots containing individual lens stacks consisting of CRLs made out of beryllium. It is positioned at 1.57 m upstream of the sample and can be adjusted by $\pm 140\text{ mm}$. A $2 - 5\ \mu\text{m}$ focal spot size can be achieved at the sample position for energies between 5 and 18 keV with help of these beryllium lenses. The BDU unit can be used optionally and allows the adjustment of the incident beam angle (e.g. for studying liquid surfaces) by using a pair of Ge crystals.

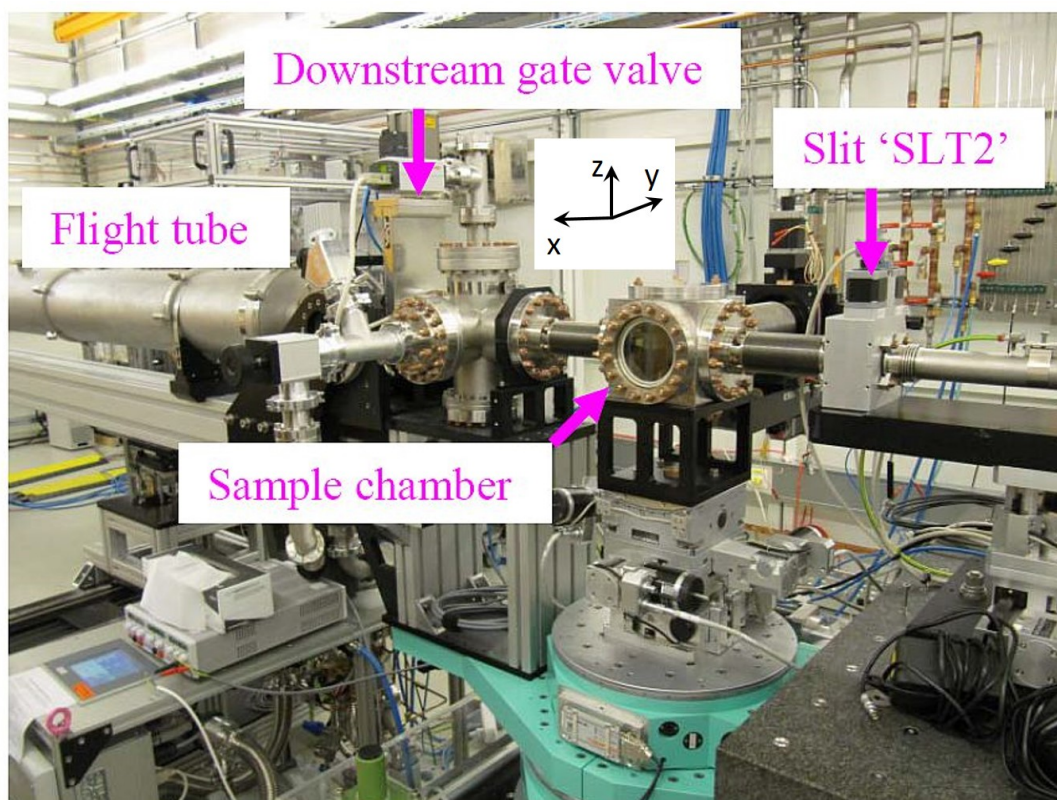


Figure 2.4.: Image of the sample chamber at EH2. The sample chamber is mounted on the diffractometer stage. Some additional elements have been marked. The operative coordinate system at the beamline is indicated [74].

After OT2 a sample diffractometer stage is installed, which allows precise positioning of the sample in the beam. The sample chamber is mounted onto a X-Y-Z translation stage located on top of a 4-circle diffractometer in horizontal geometry as shown in fig. 2.4. The coordinate system used at the beamline is shown in fig. 2.4. X-direction is parallel to the beam with positive direction facing away from the source. The z-direction is perpendicular to x-direction in the vertical plane. The y-direction is perpendicular to x-direction in the horizontal plane.

The sample chamber is directly connected to the 5 m long flight tube, which is installed after the sample chamber. The sample area is separated by gate valves from the upstream and downstream to allow a windowless operation in vacuum (see fig. 2.4). Upstream of the sample chamber a pair of JJ X-ray slits ("SLT1" and "SLT2") are mounted on a separate Y-Z table. JJ slits are used as the final beam defining slits in the case of the unfocused beam. The exit opening of the tube has a diameter of 240 mm and is covered by a 125 μm thick Kapton foil. A beamstop and a silicon diode are placed inside the flight tube. The beamstop can be adjusted horizontally and vertically. At 5 m distance behind the sample a detector positioning table is installed on a long translational stage in EH2. The detectors are mounted on this table. For the experiments in this thesis a PILATUS 300k and a LAMBDA detector were used [74].

2.3. The sample environment and experimental setup at P10

The described setup in EH2 of P10 beamline allows to perform high resolution SAXS and WAXS experiments in transmission and reflection modes. In this thesis experiments using standard SAXS and XPCS in SAXS geometry were performed. These setups implemented the sample environments shown in fig. 2.6. The standard SAXS sample environment is positioned in EH2 at a distance of 87.8 m from the source.

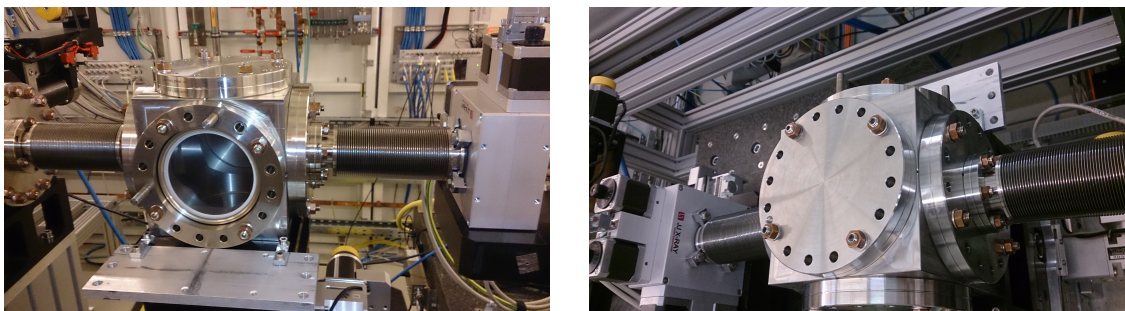


Figure 2.5.: The vacuum chamber of the 4-circle setup. Left - side view of DN100 cube and right - top view of DN100 cube

The main part of the sample environment is a DN100 cube with an edge length of 6 in and openings with diameter of 4 in, which is shown in the fig. 2.5. This cube is sealed with flanges during the experiment and is connected to the beamline vacuum via a 6-way cross and two DN40 bellows, which allow to move the cube separately from other parts of the beamline. It is mounted on a combination of Huber 440 and 430 goniometers and can be translated in x, y and z direction and rotated around x- and y-axis. The cube is connected to the 170 mm \times 170 mm goniometer stage with a spacer, which is designed to place the centre of the cube in the centre of the rotation of the goniometer stage. The centre of the DN100 cube is mounted at a typical distance of 5050 mm from the detector stage.

Upstream of the cube three slit systems are installed. The guard (G) and beam defining (BD) slits are positioned at a distance of 250 mm and 800 mm from the centre of the cube respectively. Upstream before the slits a DN40 gate valve is installed. All the slits are integrated into a shared vacuum. Downstream after the 6-way cross a DN100

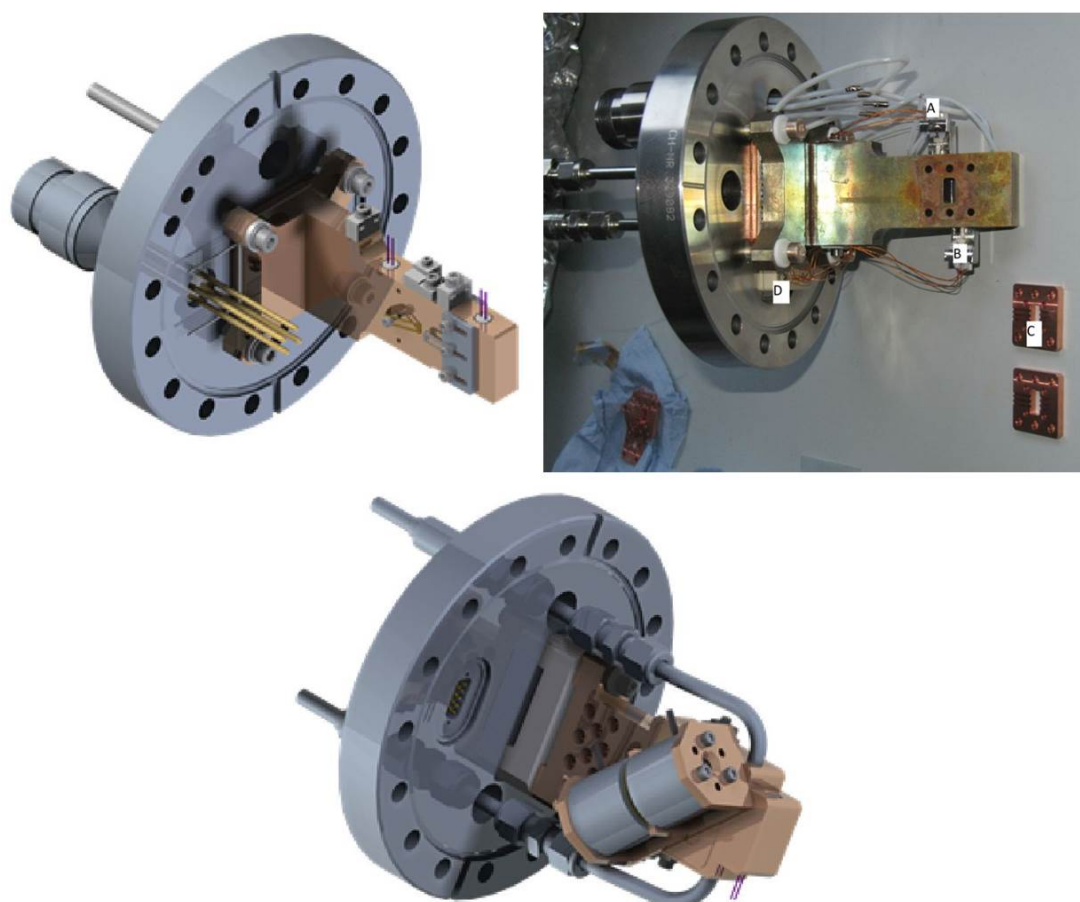


Figure 2.6.: Images of the standard sample insert. Top left: the drawing of the standard sample insert; top right: photo of the standard sample insert before operation and at the bottom: drawing of the standard sample insert with mounted holder for permanent magnets.

gate valve is installed. The gate valves allow to separate the cube from the vacuum in the beamline and the flight tube and to change samples or sample inserts within minutes. The standard samples allow to keep the beamline aligned, while offering a flexibility in setting of the external parameters at the sample.

Two kinds of magnetic sample inserts were mounted on the cube in the experiments performed for this thesis. A standard sample holder with and without permanent magnets and a specially designed magnetic insert with electromagnets. The standard sample holder, shown in fig. 2.6 in the top row, mounts from top to hold sample capillaries as and consists of a solid copper block connected to a CN100 flange. The flange is thermally isolated from the copper block by a Peltier element, which can be used for heating or cooling. Two impedance heaters (IH) are mounted to the copper block and are used to control the temperature. Additional cooling, as needed for stable temperature control, is provided by tubes (SC), which can be connected to a water chiller and remove heat from the sample chamber.

The temperature is measured via two Pt100 elements mounted inside the copper block and processed by a Lakeshore 340, which controls the temperature. All electric elements are connected to a Lakeshore 340 via a 9-pin vacuum compatible connector (VC). The holder for permanent magnets with spacers can be attached to the copper block, allowing to use a magnetic field between 180 mT and 900 mT perpendicular to the beam in the x-y plane.

The sample insert for a magnetic system with variable field, which was designed as part of this thesis, will be explained in detail in the next Chapter.

2.4. Experimental parameters

The SAXS/XPCS experimental setup of beamline P10 as described above was used to perform the experiments of this thesis. The samples used in the experiments were goethite nanoparticle suspensions, therefore the X-ray energy used in all of the experiments was set to 7.05 keV - below the iron edge at 7.112 keV. The XPCS measurements were carried out with a beam size ranging from $15 \times 15 \mu\text{m}^2$ to $25 \times 25 \mu\text{m}^2$. For the SAXS measurements the slits could be opened up to a size of $150 \times 150 \mu\text{m}^2$. The sample-detector distance was 5050 mm.

All the samples used in the measurements were filled into 0.7 mm thick capillaries with wall thickness of 0.007 mm. The capillaries were sealed vacuum tight with glue. The measurements were performed at temperatures in the range of 275 K to 355 K. For SAXS measurement a PILATUS 300k detector with pixel size of $172 \mu\text{m} \times 172 \mu\text{m}$ was used. Typically SAXS measurements were used in order to collect information on the form and structure factor of the suspensions. For every experimental dataset scattering

patterns of the solvent only - water - were taken, which were later used for background correction. The exposure time in the SAXS experiments varied from 0.002s to 10s. For the experiments performed to evaluate the dynamic response of the suspensions to applied magnetic fields and temperature changes, shorter exposure times were chosen. The Q-range was limited by the detector and the beamstop. For the SAXS measurements using a PILATUS 300k the typical Q-range was $0.002 \text{ \AA}^{-1} < Q < 0.03 \text{ \AA}^{-1}$.

For the XPCS experiment a Medipix based LAMBDA 700k detector was used. It has a pixel size of $55 \mu\text{m} \times 55 \mu\text{m}$ and respective dimensions of 516×1556 pixels. The exposure times with this unit were usually 0.002s in order to capture the fast dynamics.

In order to repeat an experimental protocol with identical parameters, macros were used to switch the field and to control the temperature. If the samples showed very slow dynamics, series of images with delay time between them were used. In order to prevent beam damage the beam position on the sample was changed after every data series acquisition. Additionally absorbers were used to prevent beam damage at the sample and to prevent overexposure of the detector.

3. Design of a magnet system for Coherence Beamline P10

The Coherence Beamline P10 provides a variety of sample inserts for the sample chamber, which allows to change a high number of experimental conditions. In order to accomplish the goal of this thesis and to extend the beamline capabilities an ad hoc magnetic system with varying magnetic field was designed. It consists of a combination of electromagnets and a specially designed sample insert.

The design goal was to allow to control the temperature in the range of 0 – 200°C and the magnetic flux B at the sample. Specifically, it should be possible to set the magnetic flux B to zero and to tune its amplitude and the direction from –100 mT to 100 mT both perpendicular and parallel to the beam. The magnetic flux should have the specified value at the position of the sample and cover the volume of the sample in the beam as uniformly as possible.

This chapter is organized as follows: Section 3.1 depicts the theoretical framework for the construction of the magnetic system, Section 3.2 describes the magnetic system implemented at the beamline and in the Section 3.3 the measurements, which tested the performance of the chamber, are described.

3.1. Theoretical estimation of the achievable magnetic field at the sample

A schematic view of developed electromagnet is shown in fig. 3.1. The magnetization force of a solenoid H_s can be calculated using [4]:

$$H_s = \sum_i \frac{0.5 \cdot N_i \cdot I}{l_s} \cdot \left(\frac{a}{\sqrt{r_i^2 + a^2}} + \frac{l_s - a}{\sqrt{r_i^2 + (l_s - a)^2}} \right), \quad (3.1)$$

where I is the electric current, N_i the number of loops per layer of the solenoid and i is the number of layers. l_s is length of the solenoid, while r_i denotes the radius of the respective layer of the solenoid. The minimum radius of the solenoid layers is equal to the radius of the core of the yoke plus half of the thickness of the wire used:

$r_{min} = r_{core} + r_{wire}$. It was assumed that $a = l_s/2$, which means that the field is induced in the centre of the solenoid. The equation 3.1 is valid for a solenoid without core.

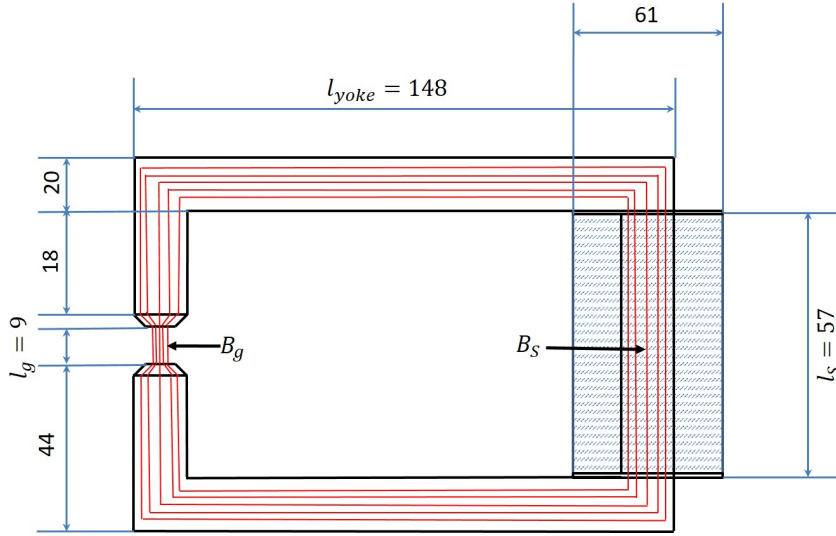


Figure 3.1.: Schematic view of the solenoid wound around a core with attached yoke pieces. The dimensions (in mm) of the components are displayed.

To calculate the magnetic flux density in the center of a solenoid without a core $B_s = \mu_0 H_s$ can be used. The magnetizing force of an solenoid with $r_{min} = 10.5$ mm, $r_{max} = 30.5$ mm, $i = 20$ and $N = 57$ was calculated to $H_s \approx 200$ Oe, which should provide a saturation flux density of $B_s = 1.3$ T in the yoke.

In the design at hand a core was used and therefore the equation $B_s = \mu_r \mu_0 H_s$ has to be used. Then the flux density in the air gap is given as [4]:

$$B_g = B_s \cdot \frac{l_s}{(l_{yoke} + \mu_r \cdot l_g)} = \frac{\mu_0 H_s l_s}{(l_{yoke}/\mu_r + l_g)}. \quad (3.2)$$

l_{yoke} is the length of the yoke and l_g is the width of the gap. According to this equation a magnetic field strength of $B_g \approx 170$ mT is expected for $\mu_r = 7000$.

The relative permeability μ_r of the core and the size of the gap l_g have high influence on the value of the magnetic flux in the gap B_g . The higher the value of the relative permeability and the smaller the length of the gap, the higher is the flux in the gap.

3.2. The implemented magnetic sample system

The layout of the beamline P10 and the standard sample environment define limitations for the design of the switchable magnetic sample insert. The standard sample chamber at the beamline is mounted on an X-Y-Z translation platform of a 4-circle diffractometer. The central piece of the sample chamber at P10 is a vacuum DN100

cube with a side length $a = 6$ in (152.4 mm) and openings on the faces of the cube with $d = 4$ in (101.6 mm), as shown in fig. 2.5 in Chapter 2. These dimensions define the main geometrical limits for the design of a new insert with the possibility to vary a magnetic field. The design is based on electromagnets and consists of two parts: a solenoid with a metal core and attached yoke, which provides magnetic field, and the sample insert with cooling. Yokes were used to redirect the induced magnetic flux towards the sample position. Several possible variations of the design were discussed before the final design was chosen, which is shown in the fig. 3.2.

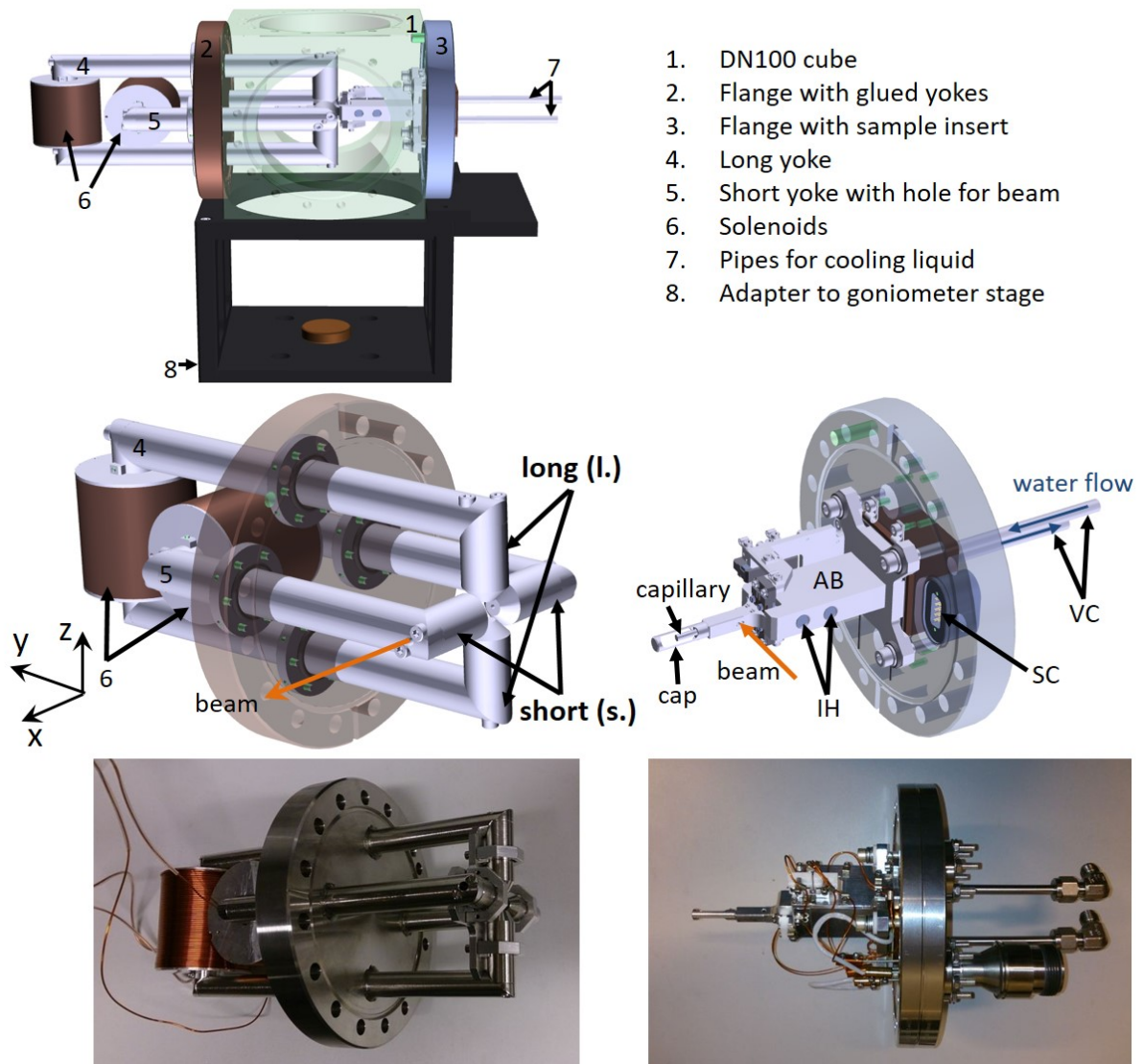


Figure 3.2.: Magnetic sample system for variable magnetic field at P10. Top: complete sample environment with part numbers on the left and description on the right side. Central row: the two key elements of the setup: left - the flange with attached yokes; right - the sample insert (AB - aluminum block, IH - impedance heater, SC - sensor cable connector, VC - vacuum isolated couplings for cooling liquid). Bottom: left - photograph of the flange with yokes; right - photograph of the sample insert.

The whole construction is placed on an adapter (number 8 in fig. 3.2, on top), which is attached and centred on the X-Y-Z platform on the 4-circle diffractometer. As shown in fig. 3.2 on the bottom left the main part of the setup consists of two solenoids positioned outside of the sample chamber one above the other with the long axes perpendicular to each other. The solenoids were wound directly at the core, and fixed with aluminium discs on the edges. Two long parts of the yoke are attached perpendicular to each core. These four long parts run through the flange, which seals the vacuum inside the DN100 cube and are glued into it. To each of the four ends of the yokes a short piece with a pole is attached parallel to the core of the respective solenoid. The yokes and small pieces redirect the magnetic flux induced by the solenoids to the gap. The cylindrical shaped poles guide the magnetic field into the gap and therefore to the sample position. One of the yokes (the shorter one) has a hole, making it possible, to direct the X-ray beam parallel to the magnetic field induced by the solenoid. Therefore the final design allows to induce magnetic flux B parallel and perpendicular to the X-ray beam.

The distance between the point of interaction and the start of the hole is $l_g/2 = 4.5$ mm. There are two holes inside each short piece with a pole cap, positioned directly behind each other and forming a "cone", which leads the field to the gap. The first one has a radius $r_1 = 1$ mm and length $l_1 = 17$ mm and the second one, positioned behind the first, has a radius $r_2 = 2$ mm and length $l_2 = 30$ mm. The maximal angle accessible for Small Angle X-ray Scattering (SAXS) through these holes is:

$$\theta_{max} = \arctan(r_2/(l_g/2 + l_1 + l_2)) \approx 2.23^\circ. \quad (3.3)$$

ARMCO pure iron with iron content of 99.85% was used as the material for the solenoid cores and the yokes. It has relative magnetic permeability $\mu_r^{theo} \leq 7000$ and saturation magnetization of $B_{sat} = 1.6$ T. The diameter of the solenoid cores was $d_{core} = 20$ mm. Copper wire with a diameter $d_{wire} = 1$ mm insulated with capton was used to manufacture the coils. The number of windings N is $N_s = 525$ on the short yoke and $N_l = 803$ on the long yoke. Both solenoids have a length of $l = 57$ mm.

The design presented above guides the induced magnetic flux to the gap where the sample is placed. The placement of the solenoids outside of the vacuum allows much easier cooling, which was implemented through air cooling provided by fans. It left enough space for the magnetic system and the temperature control inside vacuum. The direct mounting of the yokes into the flanges made the construction very stable without the need for additional supporting elements.

In order to complete the magnetic system a sample insert was designed as shown in figure 3.2 on the right in the centre and in the bottom row. It consists of a flange with attached connections for heaters, Peltier elements, bipolar Kepco power supply

and Lakeshore 340 for temperature control. The in- and outlet for the water cooling are positioned on the outer side of the flange, too. On the vacuum side the sample holder consists of a Peltier elements, a block of aluminium with inserted temperature sensors and heater elements, as well as the capillary holder and a hole for the X-ray beam. The heat system allows to reach temperature in the range from $\vartheta = -10^\circ$ to $\vartheta = 200^\circ$.

3.3. Performance of the sample system

The performance of the magnetic system was tested by measuring the flux density at the sample position between the yokes. The field was measured with a Teslometer mounted on a stage, which could be moved in all three directions. The measurements were performed in air and at room temperature, varying the current in the range $I = -4.8 - 4.8$ A. The results of the measurements are shown in fig. 3.3.

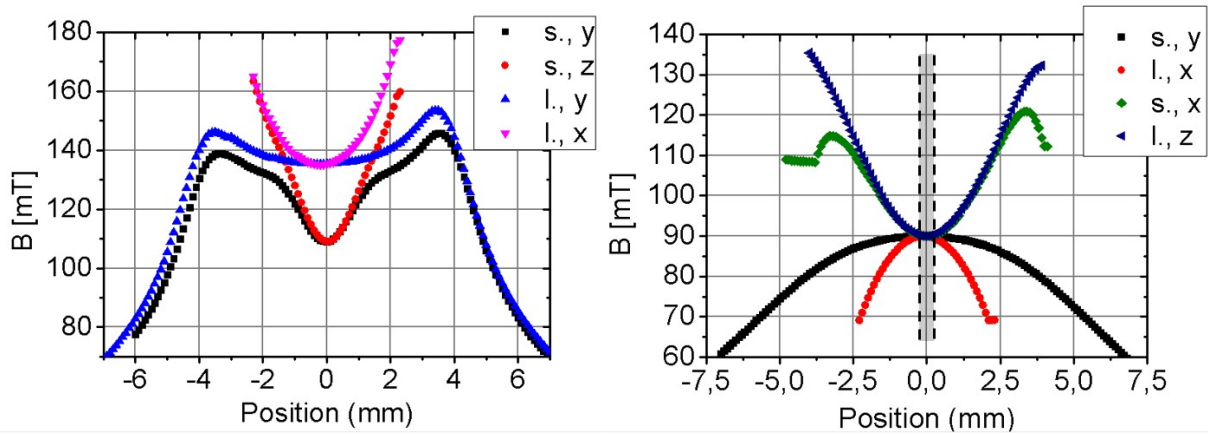


Figure 3.3.: Scans of the magnetic field. s. - for short yoke, l. - for long yoke. The axes are defined in fig. 3.2. Left: Scans at the edge of the yoke: black squares and blue triangles pointing up - along y-direction for respective short and long yoke; red circles and magenta triangles pointing down - along z- and x-directions respective for short and long yoke. Right: Scans in center of the gap. Black squares - short yoke along y-direction; green diamonds - short yoke along x-direction; red circles - long yoke along x-direction; blue triangles - long yoke along z-direction. The scans of long yoke along y and x give the same values as respective scans of short yoke along y and z. The area between dashed lines represents a size of a standard capillary.

On the left the magnetic field generated at the pole pieces is shown. The scans were performed along y- and x-directions (in blue and magenta respective) for the longer yoke without hole and along y- and z-axis (in black and red respective) for the shorter yoke with hole, as shown in fig. 3.2. The scans are divided in two groups. In the first group the scan was limited by the caps of another yoke (x-direction for longer yoke and z-direction for shorter one) and in the second group the scan was not limited (y- direction for both yokes). The scans show the similar shape for high deviation from centre $position = 0$ mm for both groups. The scans across the cap of the shorter yoke

show the drop of the values at the central position, which clearly arises from the hole. The value during the scanning towards the edge of the cap grows continuously.

To measure the field distribution in the centre of the gap, the field was set to $B = 90 \text{ mT}$ (see fig. 3.3 on the right). Afterwards the field distribution was scanned. The black scan shows the measurement in y-direction and red scan in x-direction. The scans for both yokes in the center of the gap showed the same values. Therefore only one scan along a respective direction is shown. Y - direction is equal for both yokes, while z-direction for short yoke corresponds with x-direction for the long one and vice versa. If the field parallel to the beam is set to $B = 90 \text{ mT}$ in the centre of the gap it drops while moving the sensor out of the centre. Even though the curves behave differently the most important property is that the value of the magnetic field stays the same in the centre, where a sample capillary would be positioned.

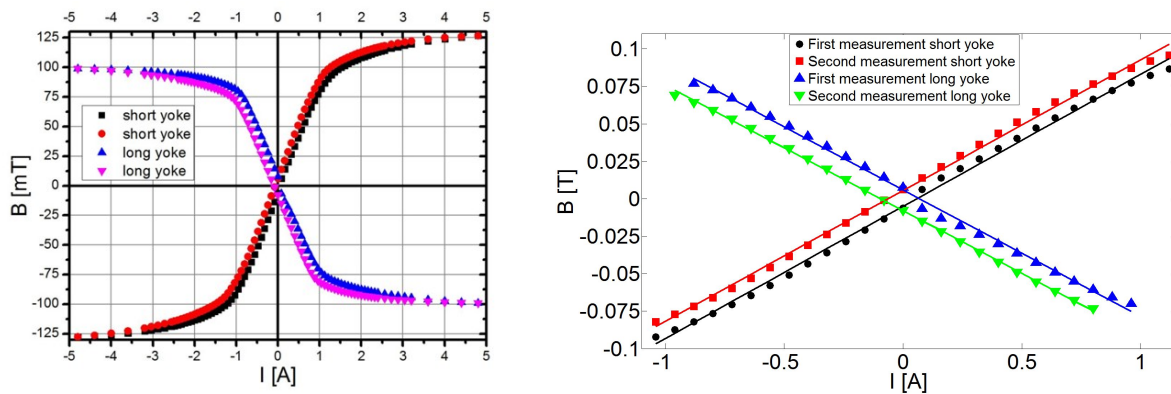


Figure 3.4.: On the left: hysteresis of the magnetic sample system; on the right: same data in the linear area with linear fits

If the scan is performed along the field (in-plane), it measures the deviation of the field along the applied field. The field has a higher value at the cap and drops during movements of the sensor towards the centre of the gap. This is shown respectively for short yoke with hole with the blue triangles and the long one without hole with green diamonds. Because of the hole in the cap of the short yoke the maximum value of the magnetic field is not directly on the cap, but at distance $a = 3 \text{ mm}$ before. After that the field drops to a constant value.

The graph in fig. 3.4 on the left shows the hysteresis of the yokes in both directions. The results of the hysteresis measurements are perfectly reproducible, so the chamber can be used to perform the experiments.

With the new sample environment the flux densities of $B_{\parallel} = 125 \text{ mT}$ parallel to the beam and $B_{\perp} = 110 \text{ mT}$ perpendicular to the beam are achievable. These values are deviating from the theoretical values by a factor 0.74 and 0.65 respectively. The differences could arise, because the yokes are built of several parts or because the solenoids do not provide the expected magnetizing force. The material of the yoke showed the typical hysteresis behaviour.

4. Synthesis and characterization of goethite $\alpha - FeOOH$ samples

The sample systems used for the experiments described in this thesis were colloidal suspensions of goethite (α -FeOOH) in water. Goethite is a mineral, which was already used in prehistoric times as a pigment. Nowadays it is still mainly used for this purpose in industrial processes [59]. Modern research of solution phase chemistry induced new interest in lyotropic liquid crystal systems, which are formed by suspensions of mineral nanoparticles.

α -FeOOH platelets are not commercially available and were thus synthesized single-handedly. Goethite is a well studied system. Several synthesizes approaches are available, but nevertheless it is not possible to precisely control the shape, size and size ratio of the platelets. This results in a high polydispersity of the synthesized particles. Therefore goethite colloidal suspensions form different phases and have a rich structural phase diagram as a function of concentration c and temperature ϑ and show additionally a high sensitivity to an applied magnetic field B [41, 42].

4.1. Different approaches to synthesize goethite platelets

In literature several approaches to synthesize goethite nanoparticles are described. One task of this thesis was to find a method, which would deliver goethite platelets as end product reproducibly under accessible laboratory conditions. Several known approaches were tried and their outcomes were compared.

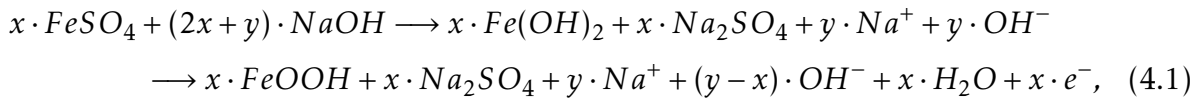
4.1.1. Synthesis of Goethite platelets by Olowe et al. and Gilbert et al.

A study focusing on the synthesis of goethite was performed by Olowe et al. [48]. This synthesis only involves the educts melanterite ($FeSO_4 \cdot H_2O$) and sodium hydroxide (NaOH). It has several tunable parameters: concentration of melanterite solution, concentration of sodium hydroxide solution, stirring speed and time of the reaction.

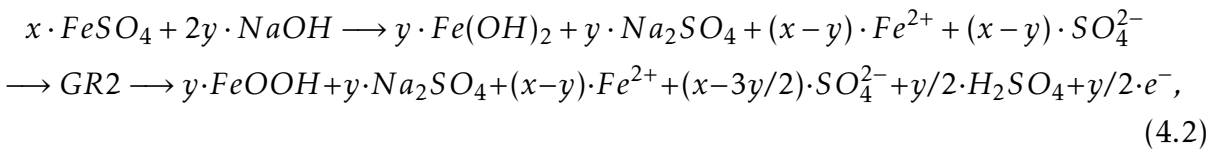
This process also has several end products like magnetite, goethite and lepidocrocite, depending on the chosen reaction conditions.

In order to start a synthesis Olowe et al. prepared 100ml of melanterite and mixed it gradually with 100ml of sodium hydroxide while stirring. In this investigation the main focus was laid on the outcomes of the reaction depending on its conditions - the ratio $R = \frac{c(FeSO_4 \cdot 7H_2O)}{c(NaOH)} = \frac{c(Fe^{2+})}{c(OH^-)} = \frac{c(SO_4^{2-})}{c(OH^-)} = \frac{x}{y}$ and the time of the oxidation.

A basic reaction described by Olowe et al. was chosen also later by Gilbert et al. to synthesize goethite particles [23]. Here both procedures have been followed. Goethite is favorably synthesized in presence of large excess of either OH^- - or Fe^{2+} -ions. These conditions correspond respectively to the ratio values $R = 0.2$ and $R = 2.5$. Therefore, the two following reactions promised the highest goethite production under respective conditions of $\vartheta = 25^\circ C$, $c(FeSO_4 \cdot 7H_2O) = 0.15 \text{ mol} \cdot l^{-1}$, $c(NaOH) = 0.75 \text{ mol} \cdot l^{-1}$ and thus $R = 0.2$ and $\vartheta = 45^\circ C$, $c(FeSO_4 \cdot 7H_2O) = 0.5 \text{ mol} \cdot l^{-1}$, $c(NaOH) = 0.2 \text{ mol} \cdot l^{-1}$ and thus $R = 2.5$ [23, 48]:



for $R < 0.5$ and excess of OH^- -ions and



for $R > 0.5$ and excess of Fe^{2+} -ions. Here GR2 is green rust.

For both reactions 100ml of $FeSO_4 \cdot 7H_2O$ in H_2O and 100ml of $NaOH$ in H_2O had to be mixed. The stirring speed was set to 760 rpm.

Gilbert et al. point out that the exact nature of the final products depends on several conditions, such as the concentration of the reactants, the concentration ratio $R = c(Fe^{2+})/c(OH^-)$, the temperature, the stirring speed and the nature of the $Fe(II)$ salt. Goethite is only one of the possible products. In order to be able to study the magnetic properties of goethite it has to be assured, that during the synthesis no other magnetic phases as magnetite, maghemite or hematite are synthesized.

4.1.2. Synthesis of Goethite platelets by Krehula et al.

Another approach to synthesize goethite was proposed by Krehula et al. [32]. This synthesis procedure has the big advantage of flexibility, because Krehula et al. proposed 7 different approaches at varying conditions. The basic reaction involves $\text{FeCl}_3 \cdot \text{H}_2\text{O}$ and Tetramethylammoniumhydroxide (TMAH). The preparation of the reaction is straight-forward. A prepared solution of TMAH is added to a solution of $\text{FeCl}_3 \cdot \text{H}_2\text{O}$ and is then stirred for the needed time at the according temperature. The possible conditions, which are leading to goethite as end product, are described in table 4.1.

Method	2M FeCl_3	25 % w/w TMAH	H_2O	ϑ [$^\circ\text{C}$]	aging time
1	5 ml	25 ml	70 ml	room temperature	1 d
2	5 ml	25 ml	70 ml	room temperature	21 d
3	5 ml	25 ml	70 ml	60	1 d
4	5 ml	25 ml	70 ml	60	21 d
5	15 ml	75 ml	10 ml	60	7 d
6	2 ml	10 ml	28 ml	160	2 h
7	2 ml	10 ml	28 ml	160	3 d

Table 4.1.: Reaction conditions for the synthesis of goethite as proposed by Krehula et al.

Methods #6 and #7 from table 4.1 were ruled out, due to the high synthesis temperature. Methods #2, #4 and #5 were also excluded, because Thies-Weesie et al. proposed similar method based on the method proposed by Krehula et al., which did not involve highly higroscopic and thus much more difficult to handle iron chloride. The method proposed by Thies-Weesie et al. is explained in following, nevertheless its running time was 9 to 12 days. Therefore methods #1 and #3 would allow to decrease the preparation time significantly and were tried.

4.1.3. Synthesis of Goethite platelets after Thies-Weesie et al.

Thies-Weesie et al. proposed a different synthesis based on the methods proposed by Olowe et al./Gilbert et al. and Krehula et al. [23, 32, 48, 65].

Room temperature synthesis

For the synthesis of goethite platelets at room temperature 1 M of NaOH was added to 0.1 M aqueous solution of iron nitrate $\text{Fe}(\text{NO}_3)_3$. The whole process was carried out under vigorous stirring till the pH of the resulting suspension reached 11-12. Immediately after addition of the base a dark red brown precipitate formed. The suspension was aged for 9 days. During this time the colour of the suspension turned from dark red-brown to the ochre of goethite. After 9 days the

supernatant was removed and fresh water was added. The suspension was homogenized and centrifuged at 5500 rpm for 35 minutes. Again the supernatant was replaced by water and the suspension was homogenized for a second and third time. Finally the precipitate was dispersed in 3 M HNO₃ in plastic tubes to positively charge the particles. The suspension was homogenized and centrifuged at 10000 rpm for 25 min. After that the acidic supernatant was replaced by water and the steps were repeated two more times in order to obtain a stable goethite solution in water at $pH = 3$ [65].

High temperature synthesis Here an adjusted method was followed, which is based on forced hydrolysis method described by Krehula et al. For this synthesis iron nitrate was used. To a solution of (0.106 – 0.190)M Fe(NO₃)₃ · 9H₂O in 70 ml of water 25 ml of 25 vol% TMAH was added under vigorous stirring. This resulted in a very dark mixture. After stirring for 30 min the solution was heated to $\vartheta = 100^\circ\text{C}$. The higher the chosen temperature the faster the formation of goethite occurred. The mixture was left under these conditions for 12 days. Finally the particles were precipitated by centrifugation and the supernatant replaced by water after stabilizing with nitric acid as described in the section before [65].

4.2. Evaluation of the synthesis products

Particles obtained from different methods were evaluated with X-ray diffraction (XRD) and transmission electron microscopy (TEM) at the University of Hamburg, department physical chemistry. XRD measurements were performed with a powder diffractometer Panalytical MPD X'Pert Pro. TEM measurements were performed with HTTEM Phillips CM 300.

4.2.1. Results and discussion of the synthesis of goethite platelets after Gilbert et al.

Because Gilbert et al. and Olowe et al. used very similar methods and the method used by Gilbert et al. was based on the synthesis proposed by Olowe et al., only the method proposed by Gilbert et al. was carried out [23, 48]. The results of the XRD analysis of the end products produced by the synthesis proposed by Gilbert et al. are shown in fig. 4.1. The result of a synthesis at $\vartheta = 45^\circ\text{C}$ are shown on the left and the results of two different attempts at $\vartheta = 25^\circ\text{C}$ are shown on the right.

The synthesis at $\vartheta = 45^\circ\text{C}$ resulted in magnetite. A possible explanation for the outcome of the reaction at $\vartheta = 45^\circ\text{C}$ would be a instability of the temperature in the

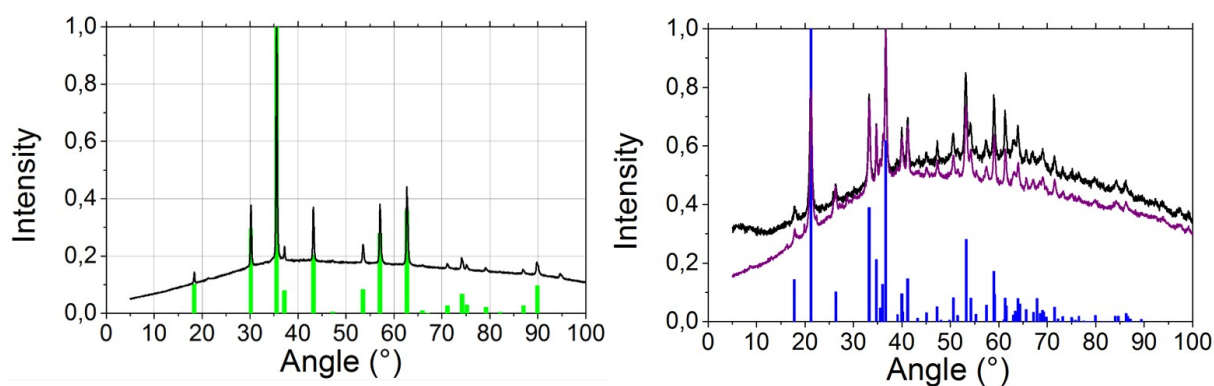


Figure 4.1.: Results of the XRD analysis of the end products of the synthesis protocols proposed by Gilbert et al. [23] Left: In black the XRD data obtained from the batch produced on 02.07.2013 at $\vartheta = 45^\circ\text{C}$ and in green the magnetite reference from ICSD. Right: in black and violet the XRD data obtained from batches produced on 02.03.2013 and 03.07.2013 at $\vartheta = 25^\circ\text{C}$ respectively and in blue the goethite reference from ICSD.

laboratory setup. Also deviations of the ratio of reactants R , impurities or age of the used chemicals, could have caused the result.

Two attempts were performed at room temperature. Both resulted in goethite, which is shown in fig. 4.1 on the right. The reactions proposed by Olowe et al. and Gilbert et al. depend on many parameters and could result in the different compositions of the end products. Even slight deviations of the starting conditions could change the outcome of the reactions. Therefore it was decided to look for a more reproducible synthesis procedure.

4.2.2. Results of the synthesis of the goethite platelets after Krehula et al.

The end products of the methods #1 and #3 by Krehula et al. were analysed by XRD [32]. An example of the outcome is shown in fig. 4.2.

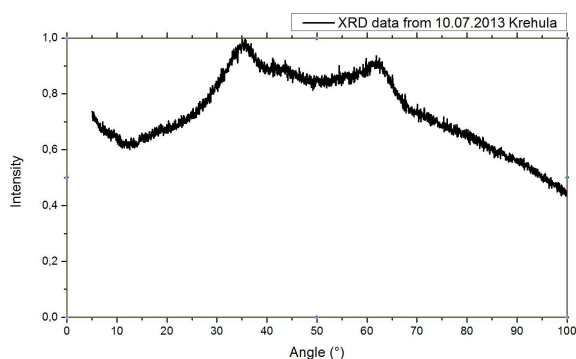


Figure 4.2.: XRD data of the synthesis product of method #3 by Krehula et al. [32]

The analysis of the XRD data of method #3 shows that methods #1 and #3 after Krehula et al., which delivered similar data, were not successful. The shape of the curve allows the conclusion that no crystals of significant size have grown in the solution. A

reason might be that the time of the reaction was not long enough, as for example in methods #2 and #4 of table 4.1.

4.2.3. Results of the XRD- and TEM-analysis of the synthesis by Thies-Weesie et al.

The products of the reactions by Thies-Weesie et al. were analysed by XRD- and TEM [65]. The results of the XRD-analysis are shown in fig. 4.3.

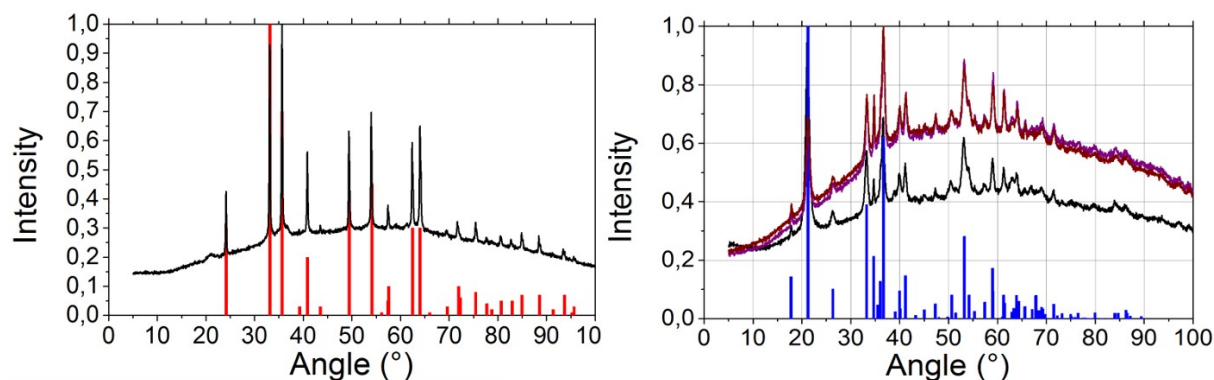


Figure 4.3.: Results of XRD analysis of the end products of the approaches proposed by Thies-Weesie et al. [65] Left: in black the XRD data obtained from the batch produced at high temperature of $\vartheta = 100^\circ\text{C}$ and in red the hematite reference from ICSD. Right: in violet, black and brown the XRD data obtained from batches produced in the first attempt, second attempt and third attempt at room temperature respectively and in blue the goethite reference from ICSD.

The approach at high temperature promised the fastest reaction, therefore the reaction at $\vartheta = 100^\circ$ was chosen, but failed. The end product of this synthesis was hematite, as proven by XRD (see fig. 4.3, left). An explanation could be a change in the synthesis process we had to make. Thies-Weesie et al. proposed to put a hermetically closed bottle in a preheated oven. The safety of such approach could not be guaranteed, so we used reflux and an electrical heater. Therefore it was difficult to establish the stability of the temperature for several days in a row as needed.

There were three attempts to produce goethite using the room temperature method as proposed by Thies-Weesie et al. The results are shown in fig. 4.3 on the right. The syntheses at room temperature delivered reproducible results and the end product was goethite in all cases.

4.2.4. Goethite synthesis summary

To produce goethite platelets in a reproducible manner several synthesis routes were evaluated. The basic approach proposed by Olowe et al. and Gilbert et al. was tried [23, 48]. Only the reaction at $\vartheta = 25^\circ\text{C}$ delivered goethite as end product reliably. The

approaches #1 and #3 (see table 4.1) proposed by Krehula et al. were also tried, especially due to the promising short duration of the syntheses [32]. However, no crystalline structure was detected. A probable cause might be the short reaction time. The reactions proposed by Thies-Weesie et al. were tried last [65]. At high temperature Thies-Weesie et al. proposed an adaptation of the reactions proposed by Krehula et al. with much shorter synthesis time. The high temperature reactions didn't deliver the desired results. The reaction at room temperature showed reproducible and stable results. Also it needed no highly toxic TMAH as reagent and took only 9 days. Additionally it run at room temperature, which made temperature control unnecessary.

As a result the reaction at room temperature as proposed by Thies-Weesie et al. was chosen for further experiments. Despite its long synthesis time it delivered stable and reproducible results. The synthesized particles were investigated by TEM to ensure the right shape. Two of the resulting batches are shown in fig. 4.4 - batch 10102013rT on the left and batch 22052015rT on the right. Both show goethite particles of typical platelet shape and dimensions in the nanometer range.

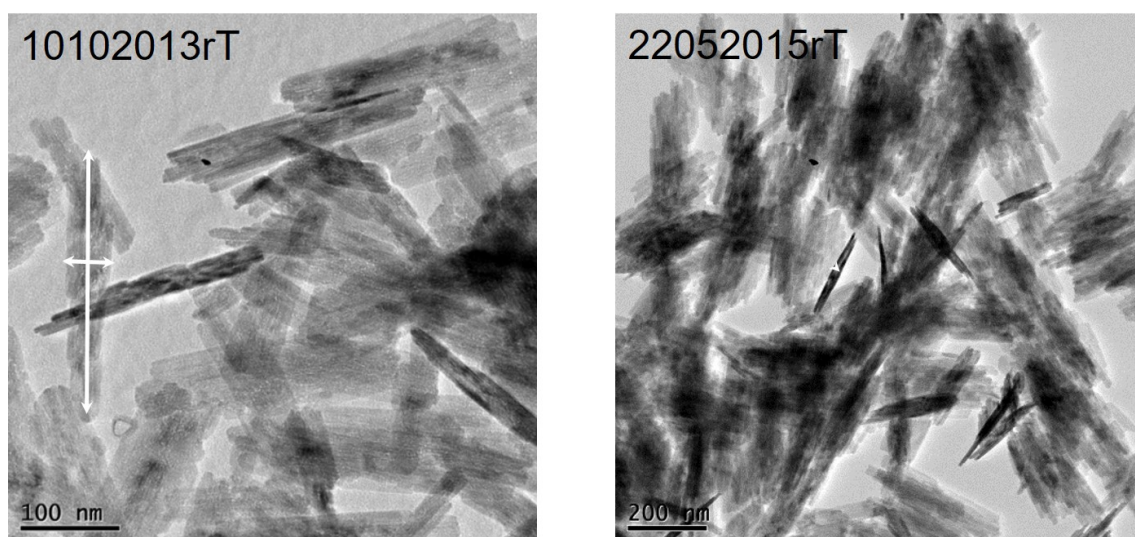


Figure 4.4.: TEM images of goethite particles from two different batches. Left: TEM image of the particles synthesized in batch 10102013rT on 10.10.2013 at room temperature. Right: TEM image of the particles synthesized in batch 22052015rT on 22.05.2015 at room temperature.

4.3. Characterization of the goethite particles

The dimensions of particles from all available TEM images were determined by evaluating the images. In fig. 4.5 the resulting distributions of the length l , width w and thickness t with corresponding fits of a gaussian distribution are shown on the right hand side, respectively on the top, in the centre and on the bottom. The produced goethite particles show a high polydispersity, as already predicted by Thies-Weesie et al.

[65] and reported by Lemaire et al. [38, 41, 42]. From the measured size distributions the dimensions of a average goethite nanoplatelet of $l = 215 \pm 36$ nm, $w = 51 \pm 10$ nm and $t = 18 \pm 7$ nm were derived. The length distribution showed two peaks - fitted separately they result in two average lengths: $l_1 = 219 \pm 26$ nm and $l_2 = 146 \pm 30$ nm.

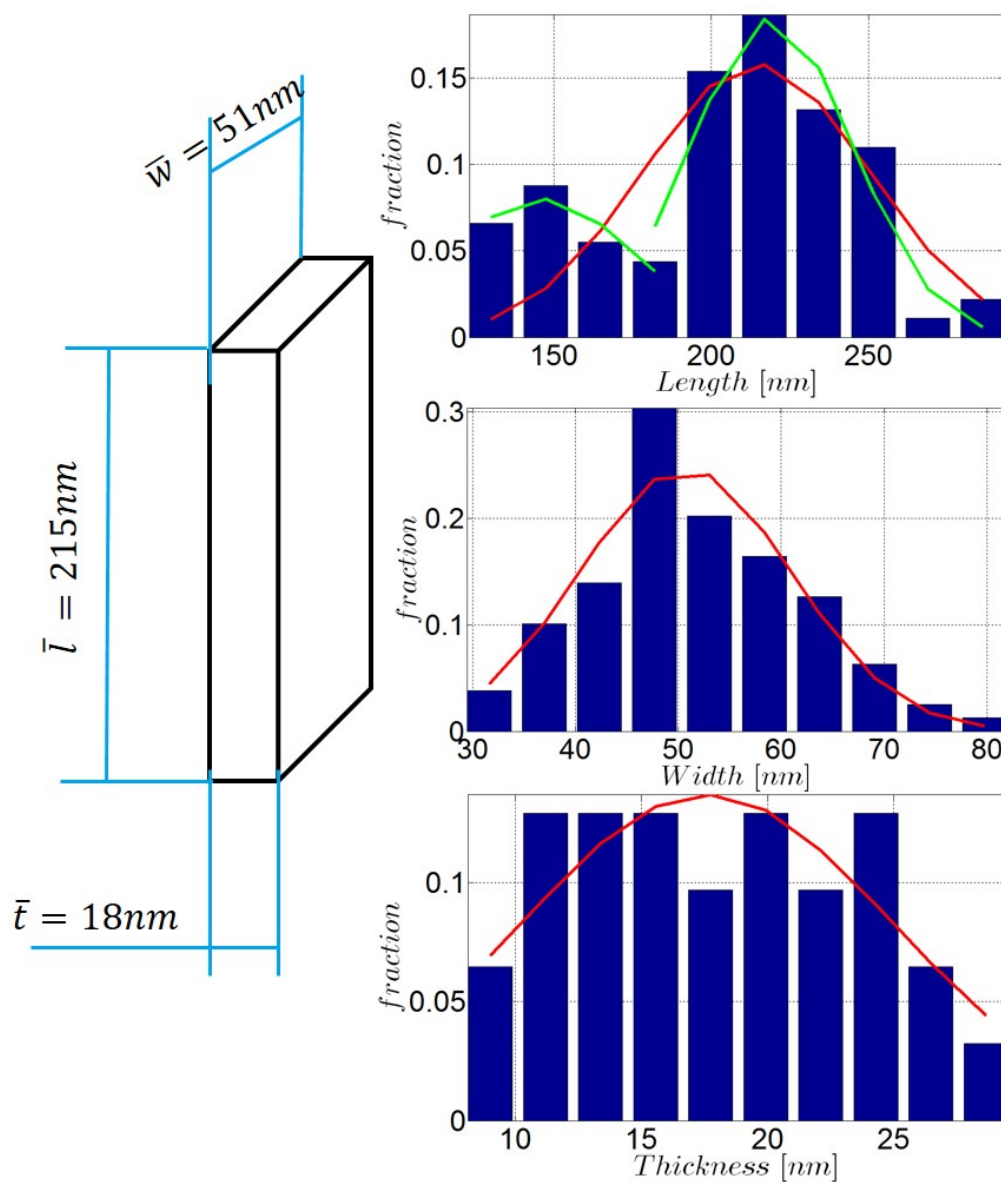


Figure 4.5.: Left: A model of an average goethite nanoplatelet based on the size distributions shown on the right. Right: Size distributions of the particles received by simple counting and measuring of the particles on the TEM images. The distributions are the mean from all analysed batches, because otherwise the counting statistics would be too low for reliable results. From top to bottom the distributions of length, width and thickness of the goethite particles are shown.

A sketch of a goethite nanoplatelet is shown in fig. 4.5 on the left with respective dimensions. For calculation of average polydispersity the equation: $P = \sigma/\mu$ was used. It is the ratio of square root of variance σ and mean value μ as obtained from the Gaussian fits to the size distributions [69]. The polydispersities were calculated as $P_t = 0.39$, $P_w = 0.2$ and $P_l = 0.17$, where respective indices t , w and l indicate the polydispersities

of the thickness t , width w and length l . If two length distributions are fitted separately the respective polydispersities are $P_{l1} = 0.12$ and $P_{l2} = 0.21$ for $l1 < l2$.

The high polydispersity of the goethite nanoplatelets is one of the reasons why suspensions of these particles can form several liquid crystal phases [37, 41, 46]. Some of the phases and typical scattering patterns, which can be formed by the particle suspensions, are shown in the fig. 4.6 and 4.7.

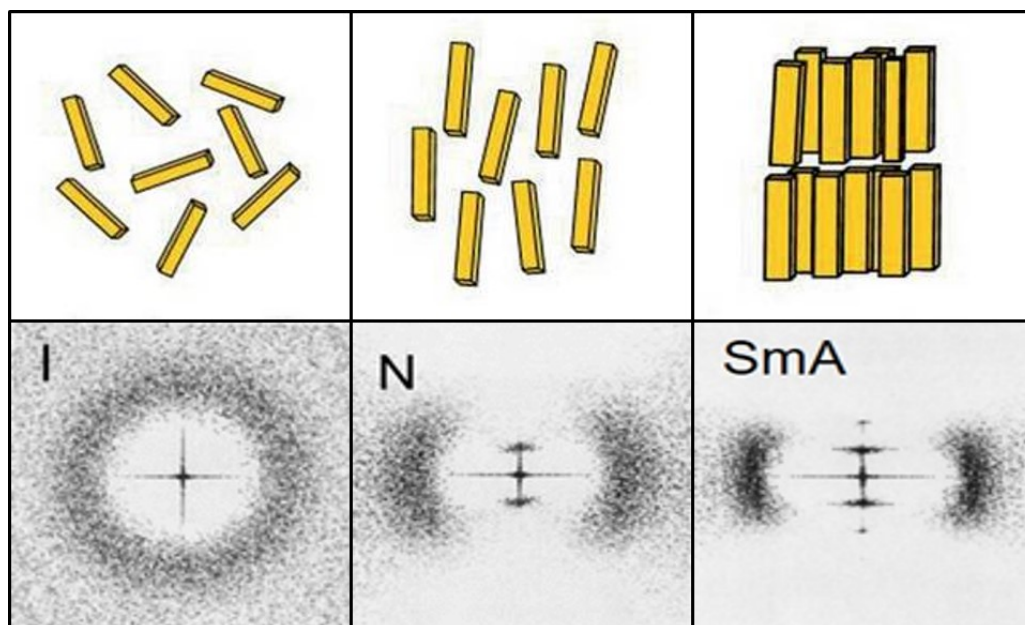


Figure 4.6.: Models of different phases of goethite suspensions and simulations of the respective scattering pattern: 1) Top row: models of the orientation of the particles in the respective phases - from left to right: isotropic (I), nematic (N) and smectic A (SmA), the images were taken from reference [37]; 2) Bottom row: simulated scattering pattern for these respective orientations are shown, the images were taken from reference [3].

The most common phases, which can be found in goethite suspensions, are the isotropic and the nematic phases. Both were observed in experiments covered by this thesis. In the isotropic phase the orientation of particles in the suspension is without preferred direction and the SAXS scattering pattern is thus also isotropic. This is shown in the top left and bottom left images of fig. 4.6. The top left image is a model of possible orientation of platelets in the suspension [37]. The image below shows a simulation of the isotropic scattering observed [3]. In the nematic phase the particles are aligned along a preferred direction, but a long range order is not present. Such an alignment is shown as model in the top centre image of fig. 4.6. It results in the scattering pattern, which is shown in the central image at the bottom. Goethite suspensions form other liquid crystalline phases - e.g. smectic A and C or columnar phase, too. As example, the smectic A phase is shown in fig. 4.6 on the right and columnar phase is illustrated in fig. 4.7. On the top right the model of the particle ordering in a smectic A phase is depicted. The simulation of the resulting scattering pattern is presented at the bottom on right. In

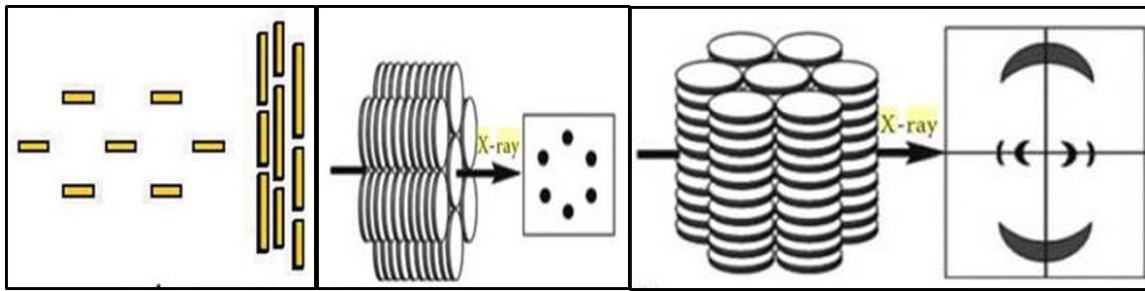


Figure 4.7.: Two possible orientations of the particles in columnar phases are shown: Left - the two possible stacking directions of the platelets in the columnar phase are shown (taken from reference [37]); centre - possible orientation with stacking parallel to the beam and resulting scattering pattern (taken from the reference [34]); right - a possible orientation with stacking perpendicular to the direction of the beam and resulting scattering pattern (taken from the reference [34]).

fig. 4.7 two possible orientations of platelets in the columnar phase relative to the beam and the resulting scattering patterns are shown.

For the experiments in this thesis five concentrations were chosen: $c = 4 \text{ vol\%}$, $c = 7.8 \text{ vol\%}$, $c = 10 \text{ vol\%}$, $c = 16 \text{ vol\%}$ and $c = 20 \text{ vol\%}$. Lemaire et al. investigated the dependence of the induced phases on the concentration of the goethite suspensions. There exist four important points: if $c < 5.5 \text{ vol\%}$, the phase will be isotropic. For $5.5 \text{ vol\%} < c < 8.5 \text{ vol\%}$ a transition from isotropic to the nematic phase and a coexistence region of both were observed. If $8.5 \text{ vol\%} < c < 20 \text{ vol\%}$ the nematic phase is present. If concentration exceeds $c = 20 \text{ vol\%}$ than almost only the columnar phase is present. In the region $8.5 \text{ vol\%} < c < 20 \text{ vol\%}$ the transition from nematic to columnar phase was observed [40, 41, 42].

The following concentrations were therefore chosen for further investigations. The concentration $c = 4 \text{ vol\%}$ would deliver a suspension in the isotropic phase. A suspension with $c = 7.8 \text{ vol\%}$ would give a transition state between isotropic and nematic phase and $c = 10 \text{ vol\%}$ would result in a suspension in the nematic phase. Because water was used, the suspensions with low concentrations could be too fast for dynamics investigation. Therefore two high concentration samples at $c = 16 \text{ vol\%}$ and $c = 20 \text{ vol\%}$, which would result in the nematic phase of the suspension, were additionally prepared for the experiments.

5. Theoretical background

Two of the standard experimental methods employed at Coherence Beamline P10 are SAXS and XPCS as already described in Chapter 2. These two techniques were used in this thesis. SAXS was used to investigate the structure of the liquid crystalline phases of goethite suspensions and XPCS was used to examine the underlying microscopic dynamics. The theoretical fundamentals of these methods are described in this chapter in Sections 5.1 and 5.3 respectively. The Section 5.2 describes a specific order parameter evaluation method, used to extract the degree of alignment in the liquid crystalline phases from SAXS data. In the Section 5.4 the already known magnetic and structural properties of goethite suspensions are summarized.

5.1. Small Angle X-ray Scattering

Small angle X-ray scattering is a high resolution technique to probe the structural details of amorphous materials on the mesoscale. The standard Q -range of roughly $0.001 - 0.65 \text{ \AA}^{-1}$ in SAXS experiments enables the investigation of structural details approximately ranging from 1 to 600 nm. The range of length scales can be extended by using either Ultra Small Angle X-ray Scattering (USAXS) for larger length scales or Wide Angle X-ray Scattering (WAXS) for smaller features. SAXS can be used to investigate biological materials, polymers, colloids, chemicals, nanocomposites, metals, minerals, food and pharmaceuticals. Because of its non-destructive approach and large variety of applications, it can be used in research as well as in quality control [1, 7, 25, 28].

At small angles only elastic scattering gives a significant contribution to the total scattering signal. This allows to use a quasi-elastic scattering approximation throughout this thesis. A typical scattering geometry of a SAXS-experiment is shown in fig. 5.1.

X-rays from a source are collimated by slits to a parallel beam. The X-ray beam illuminates a sample positioned behind the slits. A small fraction of the incident beam will be scattered due to interactions with electrons of atoms of the sample. The incident and scattered wave vectors \mathbf{k}_i and \mathbf{k}_s enclose the angle 2θ , as sketched in fig. 5.1. The scattering process is described via the momentum transfer \mathbf{Q} , which is defined as

$$\mathbf{Q} = \mathbf{k}_i - \mathbf{k}_s \quad \text{and} \quad |\mathbf{Q}| = \frac{4\pi}{\lambda} \cdot \sin(2\theta/2), \quad (5.1)$$

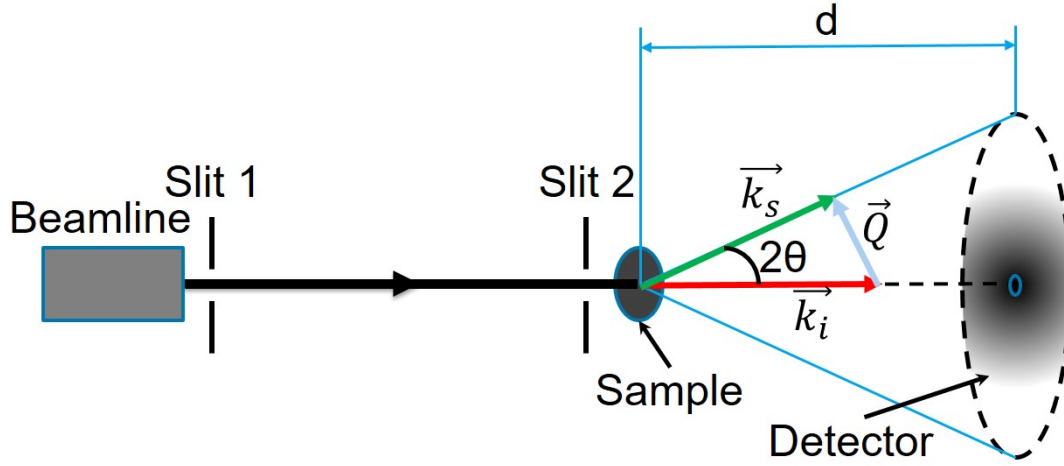


Figure 5.1.: A schematic sketch of a typical experimental SAXS setup.

where λ is the wavelength of the X-rays. If the approximation of quasi-elastic scattering is valid, then it can be assumed that $\lambda := \lambda_i = \lambda_s$, where λ_i and λ_s are the wavelengths of incident and scattered X-rays respectively. As a consequence it follows that $|\mathbf{k}_i| = |\mathbf{k}_s| = k = \frac{2\pi}{\lambda}$.

The most basic scattering event is the scattering of an X-ray photon by a free electron. In this case the scattered intensity $I^S(\theta)$ at scattering angle 2θ is given in photons per unit of time by the Thomson formula [2, 28]:

$$I^S(\theta) = \Phi_0 \cdot \frac{d\sigma(\theta)}{d\Omega} \Delta\Omega. \quad (5.2)$$

Here $\Delta\Omega$ is the solid angle and Φ_0 is the initial flux of the incident beam in photons per unit of area per unit of time. $\frac{d\sigma(\theta)}{d\Omega}$ is the scattering differential cross-section. The classical radius of an electron r_e gives a definition of the differential cross section:

$$\frac{d\sigma(\theta)}{d\Omega} = r_e^2 \cdot \begin{cases} 1 & \text{vertical scattering plane at a synchrotron} \\ \cos^2(2\theta) & \text{horizontal scattering plane at a synchrotron} \\ \frac{1}{2} \cdot (1 + \cos^2(2\theta)) & \text{unpolarized source} \end{cases} \quad (5.3)$$

The differential cross-section describes an angular distribution of photons scattered into a specific volume element and can be written as

$$\frac{d\sigma}{d\Omega}(\mathbf{Q}) = A(\mathbf{Q}) \cdot A^*(\mathbf{Q}), \quad (5.4)$$

where $A(\mathbf{Q})$ is the scattering amplitude and $A^*(\mathbf{Q})$ its complex conjugate. It implies that the scattering amplitude $A(\mathbf{Q})$ for a single electron is equal to r_e at small scattering angles.

The scattering of an atom can be seen as scattering from its Z electrons, which are surrounding the atom as a cloud with density distribution $\rho(\mathbf{r})$. The scattering amplitude of an atom can be written as $A_a = -r_e \cdot f_a$, where f_a is the atomic scattering factor [2]:

$$f_a(\mathbf{Q}, \frac{hc}{\lambda}) = f_0(\mathbf{Q}) + f'_a(\frac{hc}{\lambda}) + i \cdot f''_a(\frac{hc}{\lambda}), \quad (5.5)$$

where h is the Planck constant and c is the speed of light. The second and third term in equation 5.5 are the so-called dispersion corrections. $f'_a(\frac{hc}{\lambda})$ arises from the fact that electrons are bound to an atom and $f''_a(\frac{hc}{\lambda})$ describes the absorption of photons. These terms are energy dependent. At energies much higher than the absorption energy of the considered element their contribution can be neglected [2]. The first term $f_0(\mathbf{Q})$ depends only on the momentum transfer. This term corresponds to the Fourier transform of the electron density $\rho(\mathbf{r})$. The scattered intensity from an atom within given solid angle $\Delta\Omega$ is then a superposition of the single contributions from each part of the electron density distribution:

$$\begin{aligned} I_a^S &= \Phi_0 \cdot r_e^2 \cdot f_0(\mathbf{Q}) f_0^*(\mathbf{Q}) = \Phi_0 \cdot r_e^2 \cdot \int \rho(\mathbf{r}) \cdot \exp(i\mathbf{Q}\mathbf{r}) d\mathbf{r} \int \rho(\mathbf{r}') \cdot \exp(-i\mathbf{Q}\mathbf{r}') d\mathbf{r}' = \\ &= \Phi_0 \cdot r_e^2 \cdot \begin{cases} Z^2 & \text{for } \mathbf{Q} \rightarrow 0 \\ 0 & \text{for } \mathbf{Q} \rightarrow \infty \end{cases} \end{aligned} \quad (5.6)$$

The atomic form factor can easily be expanded to a molecular form factor f_{mol} by a summation of the single contributions of the electrons of every atom with index k :

$$f_{mol}(\mathbf{Q}) = \sum_k f_k(\mathbf{Q}) \cdot \exp(i\mathbf{Q} \cdot \mathbf{r}_k) \quad (5.7)$$

In SAXS experiment, where X-ray are scattered from non-interacting particles suspended in an isotropic medium, the effective scattering electron density of the particles is $\Delta\rho = \rho_P - \rho_M$, where ρ_P and ρ_M are the uniform electron density of a particle and the average density of the suspending medium respectively. The scattering intensity can then be written as:

$$I_{SAXS}(\mathbf{Q}) = \Phi_0 \cdot r_e^2 \cdot \left| \int_V \Delta\rho \cdot \exp(i\mathbf{Q} \cdot \mathbf{r}_k) dV \right|^2 = \Phi_0 \cdot r_e^2 \cdot \Delta\rho^2 V_p^2 |F(\mathbf{Q})|^2. \quad (5.8)$$

Here $P(\mathbf{Q}) = |F(\mathbf{Q})|^2$ is the particle form factor, which depends on the shape and size of the particles in a suspension, as demonstrated by the integral over the volume of the particle. Equation 5.8 is valid for dilute suspensions. In the case that a suspension can not be considered as dilute eq. 5.8 has to be extended to include an additional term:

$$I_{SAXS}(\mathbf{Q}) = \Phi_0 \cdot r_e^2 \cdot \Delta\rho^2 V_p^2 P(\mathbf{Q}) \cdot S(\mathbf{Q}). \quad (5.9)$$

$S(\mathbf{Q})$ is the static structure factor and accounts for correlations between the particles. It depends on the nature of the interparticle interactions and can be derived from the scattered intensity, if the particle form factor is known [2].

Equations 5.8 and 5.9 are only valid for the case of spherical particles. In this thesis particles with the shape of parallelepipedons were used. For anisotropic identical particles the scattering intensity within a solid angle $d\Omega$ is given by [52]:

$$I_{SAXS}(\mathbf{Q}) = \Phi_0 \cdot r_e^2 \cdot \Delta\rho^2 V_p^2 \left[\sum_i F_i(\mathbf{Q}, \mathbf{e}_i)^2 + \sum_{i,j} F_i(\mathbf{Q}, \mathbf{e}_i) F_j(\mathbf{Q}, \mathbf{e}_j) S_{ij}(\mathbf{Q}, \mathbf{e}_i, \mathbf{e}_j) \right]. \quad (5.10)$$

Here the summation is over all particles in the suspension and $F_i(\mathbf{Q}, \mathbf{e}_i)$ is the amplitude of the form factor for the i -th particle with orientation given by the unit vector \mathbf{e}_i . $S_{ij}(\mathbf{Q}, \mathbf{e}_i, \mathbf{e}_j)$ are partial structure factors, which depend on the orientation of two particles with respect to each other. The first sum in equation 5.10 is the orientational averaged form factor $P(\mathbf{Q}) = |F_0(\mathbf{Q})|^2$, which is defined for particles with the shape of platelets and dimensions $a > b > c$ by [52]:

$$P(\mathbf{Q}) = \frac{1}{V_p^2} \int_0^R \int_0^{2\pi} \int_0^\pi (\exp(i\mathbf{Q}r \cos\theta) r^2)^2 \sin\theta d\theta d\phi dr = \frac{1}{V_p^2} \int_0^{2\pi} \int_0^\pi \left(\frac{\sin((qa \sin\theta \cos\phi)/2)}{(qa \sin\theta \cos\phi)/2} \cdot \frac{\sin((qb \sin\theta \sin\phi)/2)}{(qb \sin\theta \sin\phi)/2} \cdot \frac{\sin((qc \cos\theta)/2)}{(qc \cos\theta)/2} \right)^2 \sin\theta d\theta d\phi. \quad (5.11)$$

Equation 5.10 is valid for the case of monodisperse particles. If the particles vary in size as in the experiments presented in this thesis, it has to be expanded. To account for polydispersity, the scattering intensity from a suspension can be written as:

$$I_{SAXS}(\mathbf{Q}) = \Phi_0 \cdot r_e^2 \cdot \Delta\rho^2 \left[\int_0^\infty D(a)D(b)D(c) \cdot V(a,b,c)^2 \cdot F(\mathbf{Q}, a, b, c)^2 d^3r + \int_0^\infty \int_0^\infty D(a)D(b)D(c) \cdot V(a,b,c) \cdot D(a')D(b')D(c') \cdot V(a',b',c') \cdot \right]$$

$$\cdot F(Q, a, b, c) \cdot F(Q, a', b', c') \cdot S(a, b, c, a', b', c', Q) d^3 r d^3 r']. \quad (5.12)$$

Here a, b, c are the basis of a parallelepipedon, $S(a, b, c, a', b', c', Q)$ is the structure factor, $V(a, b, c)$ is the volume of a parallelepipedon and D is the respective size distribution. As example, $D(a)$ represents the distribution of the particle axis size a and is normalized to $\int_0^a D(a) da = 1$. A commonly used distribution is a Schulz-Flory function, which is given by:

$$D(a) = \left(\frac{z+1}{\bar{a}} \right)^{z+1} \frac{a^z}{\Gamma(z+1)} \exp\left(- (z+1) \frac{a}{\bar{a}}\right), \quad (5.13)$$

where \bar{a} is the average axis size and z is a parameter, which controls the spread of the size. In the limit of $z \rightarrow \infty$ $D(a)$ converges to a delta function. The Schulz-Flory distribution produces expressions, which are easy to calculate analytically or numerically for a range of particle shapes. The inclusion of the particle size distribution introduces additional smearing of the scattering curve.

5.2. Orientation distribution function and ordering parameters

Oriented particles in suspensions can be compared to liquid-crystalline phases. A long range orientational order is characteristic for such phases. The orientational order can be described by the orientation distribution function $f(\beta)$ (ODF), where β is the angle between the long particle axis and the director \mathbf{m} . Throughout this thesis the direction of the applied magnetic field \mathbf{B} will be used as director \mathbf{m} . The preferred direction of the orientation of the long axis of the platelets will be \mathbf{n} and the direction of the long axis of the scattering feature is defined as \mathbf{p} , whereas $\mathbf{n} \perp \mathbf{p}$ (see fig. 5.2).

The ODF can be expanded into a series:

$$f(\beta) = \sum_{n=0}^{\infty} (n+1/2) \overline{P_n(\cos \beta)} P_n(\cos \beta), \quad (5.14)$$

where $(n+1/2)$ is a weighting factor [17]. The orientation order parameters (OP) are defined as:

$$S_n = \overline{P_n} = \int_0^{\pi/2} P_n(\cos \beta) f(\beta) d(\cos \beta). \quad (5.15)$$

Here $P_n(x)$ is the n -th Legendre polynomial. Using Raman and/or resonance spectroscopy techniques it is only possible to access the OP's S_2 and S_4 . The more important property $f(\beta)$ can not be measured directly [16]. In liquid crystal science the order parameter S_2

is almost universally used. Sometimes additionally S_4 is presented. In this thesis also S_1 was calculated, since it can be connected to the remanent magnetization M of the suspension [41].

For X-ray scattering Leadbetter and Norris developed a method to determine the ODF, which is sketched in fig. 5.2 on the left. Here particles in the nematic phase are shown on top together with respective the direction of the director $\mathbf{m} \parallel \mathbf{B}$ and the nematic orientation direction \mathbf{n} . The according schematic scattering pattern is displayed at the bottom with respective high intensity peaks in red. The peaks along Q_z result from the length of the platelets and, as the case may be, from the short range order in this direction. If the order increases, the peaks will lose their diffuseness and increase in number, as shown in examples in fig. 5.2 on the right for smectic phases. The arcs crossing Q_x arise because of diffraction perpendicular to the long axis of the platelets. With perfect alignment these arcs would condense into sharp peaks. The direction of the long axis of the scattering feature is defined than as \mathbf{p} .

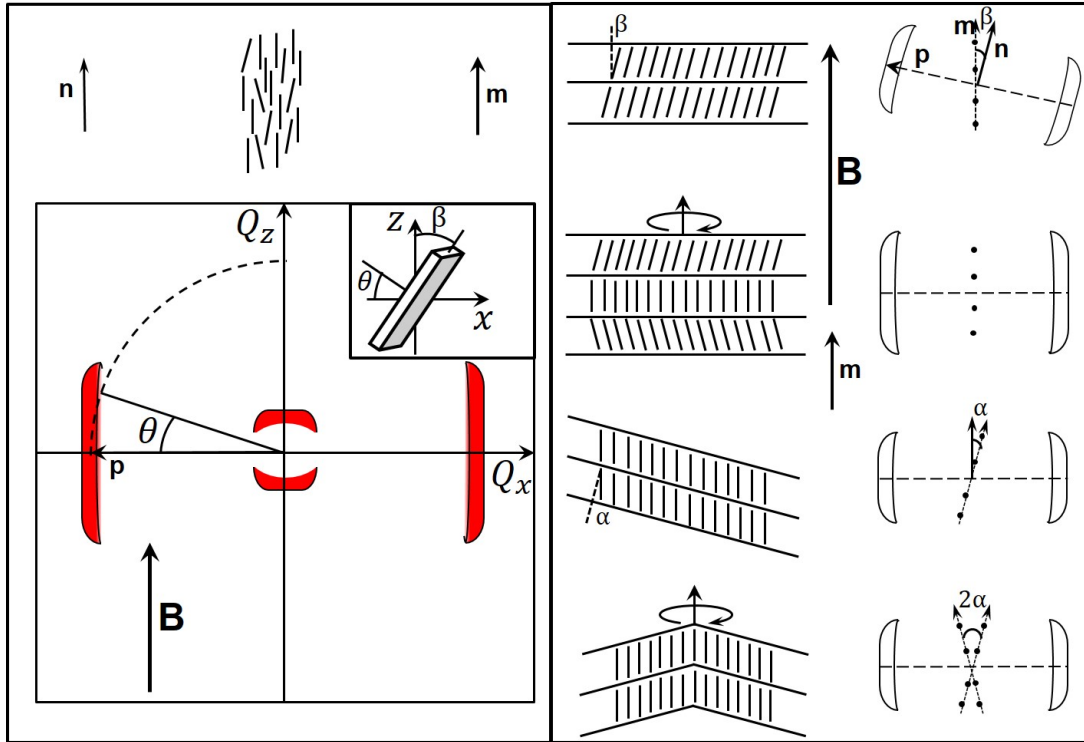


Figure 5.2.: Figure for definition of the angles β and θ for the ODF analysis, drawn after figure 1 Leadbetter et al. [35]. On the left: top - sketch of partially aligned particles in the nematic phase with the direction of the director $\mathbf{m} \parallel \mathbf{B}$ and of the average nematic orientation direction \mathbf{n} . Bottom: schematic drawing of the resulting scattering pattern with insert showing a position of one particle from the sketch above with according angles β and θ . On the right: sketches of the particles in four different smectic phases and respective schematic scattering pattern. Additionally the directions of the magnetic field \mathbf{B} and the director $\mathbf{m} \parallel \mathbf{B}$ are shown.

In fig. 5.2 on the right for examples of smectic phases are shown. The short range order of well defined layers in the z -direction results in sharp peaks in Q_z -direction,

which depend on the orientation of the layers. The orientation of the particles in the layers influence the orientation and extent of the arcs, which cross Q_x . The direction of the B -field and of the director $\mathbf{m}||B$ are indicated in the centre. The nematic orientation direction \mathbf{n} and the orientation of the scattering arc, which shows the orientation of the particles, \mathbf{p} are shown as example for one smectic phase on top. The angle β is the angle between the long axis of a particle and the director \mathbf{m} . It is visible that the image on top has a well defined distances between particle layers, which result in set of sharp peaks in the scattering pattern of the right. If the layers are perpendicular to \mathbf{m} then these sharp peaks in Q_z direction are parallel to \mathbf{m} . This is visible in the first and second images from the top. In other images the layers have an angle α respective to \mathbf{m} , which yields same inclination of the sharp peaks in the scattering pattern. The scattering from the long axis of the particles results in the arcs crossing Q_x . Because the particle in the layers in the image on top are inclined in one direction, the axis connecting the scattering features is inclined respective \mathbf{m} , too. In the images below the axis connecting the arcs crossing Q_x is not inclined, because the particles have an average orientation, which is parallel to \mathbf{m} . The more particles deviate from the orientation parallel to \mathbf{m} the wider are the arcs, as shown in second image from the top.

The azimuthal scattering intensity distribution $I(\theta)$ from particles in an experiment at the Q of the highest intensity in the azimuthal arcs (dashed line) is usually connected to the real space orientation distribution function for particles as:

$$I(\theta) = C \int_{\theta}^{\pi/2} f_d(\beta) \left(\frac{(\tan^2 \beta - \tan^2 \theta)^{-1/2}}{\cos^2 \theta} \right) \sin \beta d\beta. \quad (5.16)$$

Here θ is the azimuthal angle along scattering pattern at the Q of the structural arc. It is obvious that $\beta = 0^\circ$ if the particle is aligned with long axis parallel to the director \mathbf{m} . Because β and θ are connected, $\theta = 0^\circ$ would be at the position of the high intensity arc crossing Q_x and perpendicular to the director \mathbf{m} . This comes from the fact that these arcs arise from scattering perpendicular to the long axis of the platelet and carry the information about the degree of alignment of the particles in a suspension, as shown in fig. 5.2.

Leadbetter and Norris computed equation 5.16 numerically and calculated the ODF and OP's [35]. In suspensions clusters of different orientation can be induced sometimes. The ODF of molecular clusters (several areas with different orientation of the nematic orientation direction \mathbf{n}) is in general not equal to singlet ODF (where particles do not build clusters and therefore only one \mathbf{n} is present). However, different studies showed that thermotropic liquid crystals fulfil the ordering conditions, under which equation 5.16 is valid. Under these conditions $f_d(\beta)$ approaches the singlet function $f(\beta)$ and therefore, for the case considered by Deutsch [16] and in this thesis, the approximation $f_d(\beta) \approx f(\beta)$ was used.

Starting from equation 5.16 Deutsch calculated an analytical solution for the ODF. Originally two solutions were calculated. However, only the second one, which promises significant error reduction was used in this work:

$$f(\beta) = -(N \sin \beta)^{-1} \frac{d}{d\beta} \times \left(\int_{\beta}^{\pi/2} I(\theta) \tan \theta (\tan^2 \theta - \tan^2 \beta)^{-1/2} d\theta \right), \quad (5.17)$$

where $N = \int_0^{\pi/2} I(\theta) d\theta$ is a normalizing constant. From equation 5.17 it is possible to calculate the OP S_1 , S_2 and S_4 using equation 5.15.

Also a direct formula for calculating OP from the intensity distribution $I(\theta)$ was derived by Deutsch et al.:

$$S_n = N^{-1} \left(\int_0^{\pi/2} I(\theta) d\theta - \int_0^{\pi/2} \sin \beta \frac{dP_n(\cos \beta)}{d(\cos \beta)} \int_{\beta}^{\pi/2} I(\theta) \tan \theta (\tan^2 \theta - \tan^2 \beta)^{-1/2} d\theta \right), \quad (5.18)$$

which allows to calculate OP without calculating $f(\beta)$ first and reduces the errors [16].

The order parameters OP are known in the literature as nematic ordering parameters and used to describe the degree of order in the nematic phase [9]. S_1 can be connected to the magnetization M of the particles in suspension and S_2 to their magnetic energy E_m , as described in Chapter 5.4 [41]. The order parameter have values:

- $0 \leq S_1 \leq 1$,
- $-0.5 \leq S_2 \leq 1$ and
- $-0.5 \leq S_4 \leq 1$.

In fig. 5.3 three ideal cases are shown. In case of the completely random orientation of the particles the intensity distribution shows a ring and a constant intensity $I(\theta)$ occurs (fig. 5.3 top row). This will cause constant values of the ODF $f(\beta)$ and result in order parameters $S_1 = S_2 = S_4 = 0$. If the particles show a perfect alignment parallel to the director \mathbf{m} , a very narrow peak in the intensity $I(\theta)$ occurs perpendicular to the long axis of the particles \mathbf{n} and therefore $\mathbf{p} \perp \mathbf{m}$ (fig. 5.3 centre row). This result in delta function shape of $I(\theta)$ versus θ at $\theta = 0^\circ$ and therefore a delta function in $f(\beta)$ versus β at $\beta = 0^\circ$. This intensity distribution has OP values $S_1 = S_2 = S_4 = 1$ as outcome.

Also a perfect alignment of the particles perpendicular to the direction of the magnetic field ($\mathbf{n} \perp \mathbf{m}$) may occur (fig. 5.3 bottom row). In this case the narrow peak of intensity appears $\mathbf{p} \parallel \mathbf{m}$ and results in delta function of $f(\beta)$ versus β at $\beta = 90^\circ$ and OP values $S_1 = 0$, $S_2 = -0.5$ and $S_4 = 0.5$ [17].

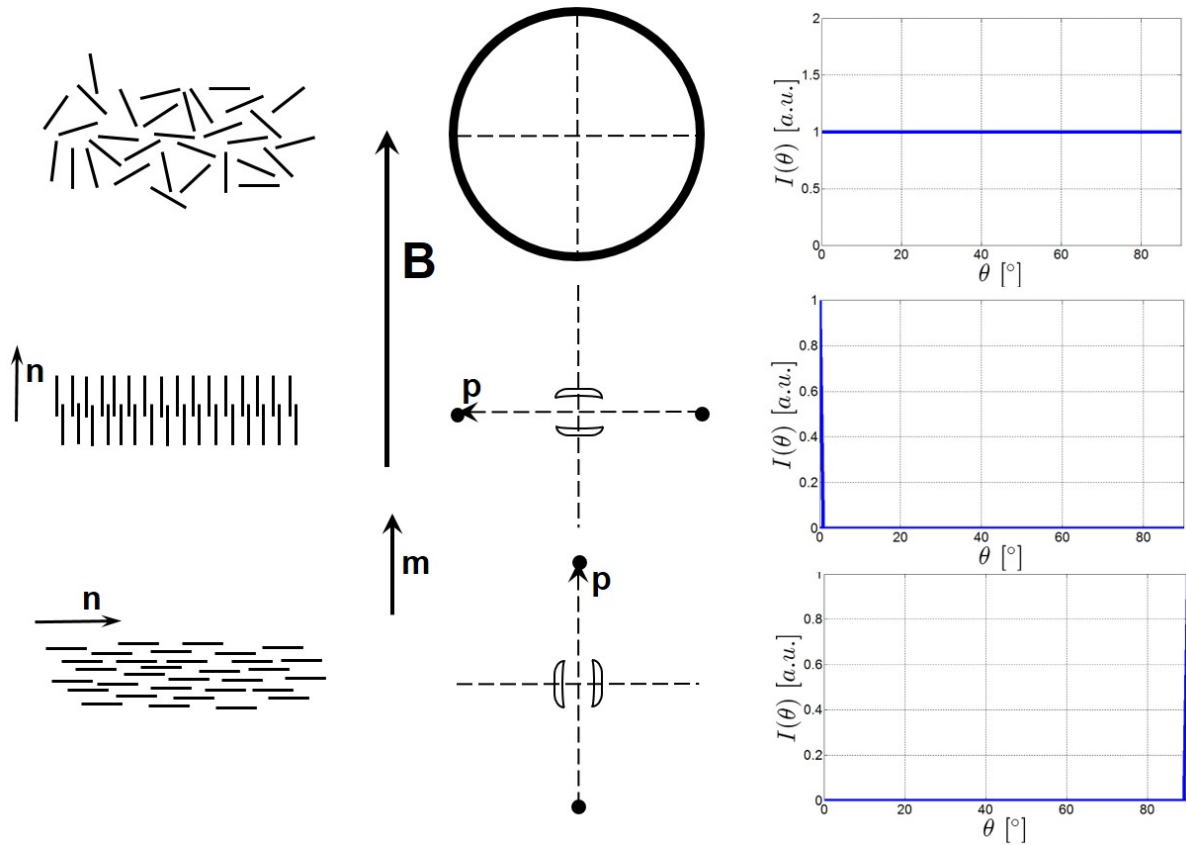


Figure 5.3.: Three ideal particle orientations in a suspension. Top row: for ideally isotropic distribution of the particles; centre: for particles ideally aligned with long axis parallel to the field ($\mathbf{n} \parallel \mathbf{m}$); bottom: for particles ideally aligned with long axis perpendicular to the field ($\mathbf{n} \perp \mathbf{m}$). Left is a schematic view of the particles in suspension, in the centre the resulting scattering pattern and on the right in blue the resulting intensity distribution $I(\theta)$ from the scan at the peak Q.

In fig. 5.4 the simulated Gaussian azimuthal intensity distributions $I(\theta)$ are plotted versus θ on the left and the respective theoretical orientation distribution functions $f(\beta)$ versus β on the right. The colour represents the azimuthal width w of the intensity distribution and of the according orientation distribution function: $w = 5^\circ, 10^\circ, 20^\circ, 40^\circ$, which are respectively indicated by black, red, blue and green colours. Here only the functions, which depict different centre position at $\theta = 0.5^\circ$, which was chosen for numerical reasons, are shown. In the image below the respective OP's are plotted versus $FWHM$ [$^\circ$] of the respective ODF $f(\beta)$. It is apparent that all three curves have similar shape and values close to 1 at $\theta = 0.5^\circ$ and $FWHM = 5^\circ$. As $FWHM$ increases, which means wider distribution of the angles of the long axis of the particles respective to a director, the orientation parameters decrease and reach minimum at $FWHM = 40^\circ$, whereby S_4 has the lowest value and S_1 stays close to 1.

In order to illustrate the dependence of the OP parameter on width and centre position of the azimuthal distribution function $I(\theta)$ the equations derived by Deutsch

were used on the simulated intensity distribution functions $I(\theta)$ with same widths: $w = 5^\circ, 10^\circ, 20^\circ, 40^\circ$, but at different centre positions: $\theta = 20.5^\circ, \theta = 40.5^\circ, \theta = 60.5^\circ, \theta = 80.5^\circ$ were used. The according ODF and the orientation parameters S_1 (top), S_2 (center) and S_4 (bottom) are shown in fig. 5.5.

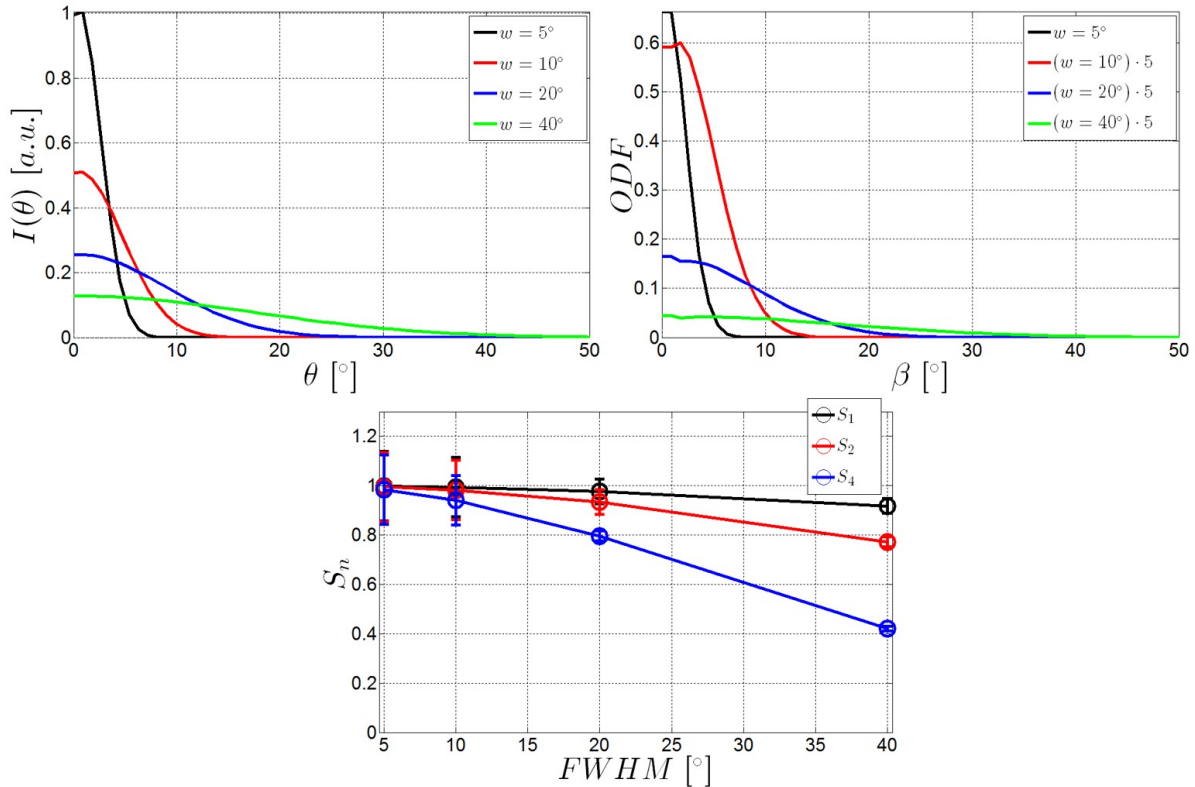


Figure 5.4.: On top - Left: Simulated intensity distributions $I(\theta)$ with equal areas versus θ with different width of the arc. Right: according orientation distribution functions $f(\beta)$ (ODF) versus β resulting from original $I(\theta)$ distributions on the left, with widths indicated by colours: $w = 5^\circ, 10^\circ, 20^\circ, 40^\circ$ with black, red, blue and green. The red, blue and green curves are multiplied by 5 for better visibility. At the bottom: the according order parameter S_n with S_1 in black, S_2 in red and S_4 in blue.

From the plots in figure 5.5 it is visible that the values of the order parameter do not strongly depend on the width of the ODF (and $I(\theta)$) curve), but on the centre position of the curve. Wider FWHM of the intensity distribution result in lower absolute value of OP, but the curves of OP versus centre position (fig. 5.5 on the left) show respectively very similar trends.

The method presented here connects the intensity distribution of the X-ray diffraction pattern $I(\theta)$, which can easily be obtained experimentally, with real space orientation distribution function (ODF) $f(\beta)$ of the platelets and allows to express the order of the alignment in a suspension with one number - the order parameter S_2 . Order parameter of different order allow to access a more detailed information, e.g. about magnetization M or the additional information on the alignment in the sample.

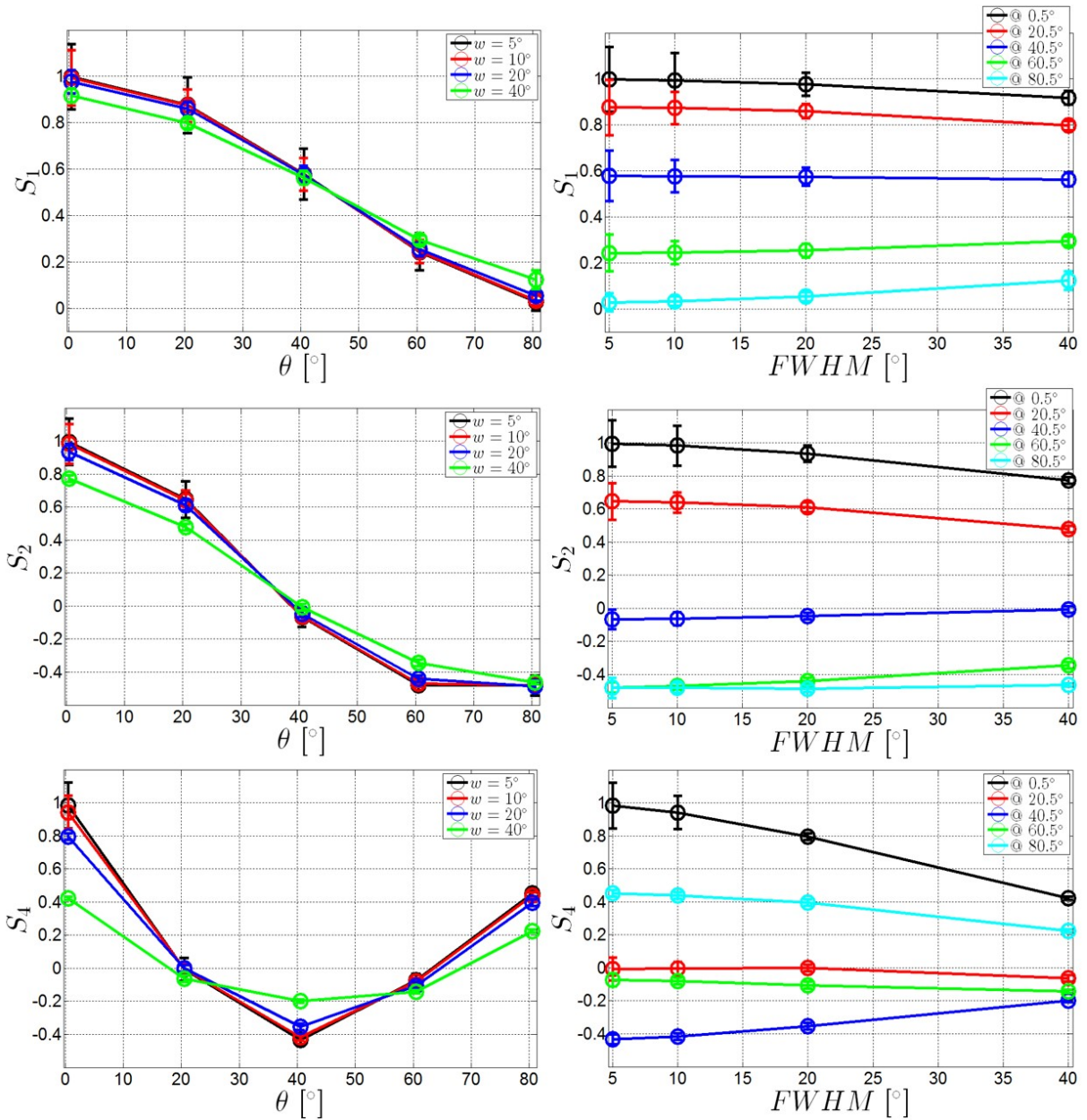


Figure 5.5.: The dependence of the OP on the width (FWHM) and position of the ODF: Left - dependence of S_1 (top), S_2 (center) and S_4 (bottom) on the position of the ODF; right - dependence of S_1 (top), S_2 (center) and S_4 (bottom) on the width of the ODF

5.3. X-ray Photon Correlation Spectroscopy

X-ray Photon Correlation Spectroscopy (XPCS) exploits the ability of third generation synchrotron sources to produce coherent X-rays. Scattered coherent light from a disordered sample produces an interference or so-called "speckle" pattern. Speckles are well-known for visible laser light, but are as well created using coherent X-rays. An example of a speckle pattern is shown in fig. 5.6 on the left [26]. These patterns are directly related to the exact spatial arrangement of scatterers in the disordered sample [1, 64, 67, 68]. If the arrangement of the scatterers in the sample changes, the speckle

pattern changes accordingly. This is the essential difference to diffraction experiments with incoherent light, where only an ensemble average of these fluctuations provides information about average correlations in the sample. The changes in the speckle patterns supply information on the underlying dynamics of the disordered sample.

XPCS provides information about the dynamics of samples at low frequencies ($10^7 - 10^{-3}$ Hz) and at large momentum transfer Q ($10^{-4} - 10^{0.5} \text{ \AA}^{-1}$). These ranges are not easily accessible by other techniques, which makes XPCS an advanced investigation method to study equilibrium critical fluctuations, low frequency dynamics in disordered hard and soft condensed matter materials, complex fluids, polymer systems, colloidal systems and dynamics close to the glass transition. The right image in fig. 5.6 places XPCS in a frequency and wavevector range diagram together with various other techniques [26].

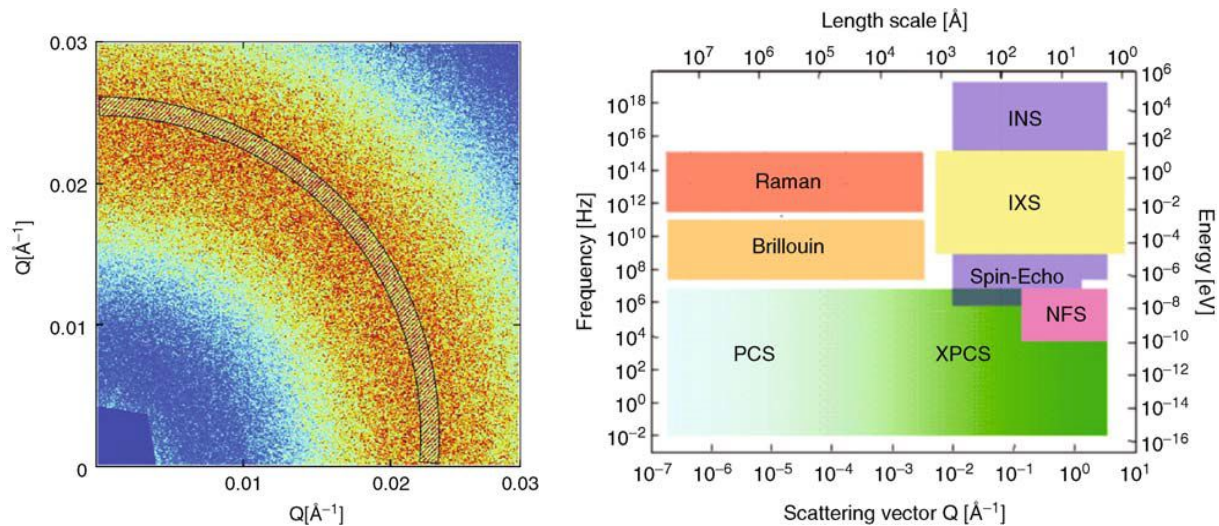


Figure 5.6.: Left: an example for an X-ray speckle pattern; right: frequency-scattering vector space covered by XPCS and complementary techniques such as photon correlation spectroscopy (PCS), Nuclear Forward Scattering (NFS), Spin-Echo Spectroscopy, Inelastic X-ray Scattering (IXS), Inelastic Neutron Scattering (INS), Raman- and Brillouin-Scattering [26].

To provide coherent radiation for XPCS the X-ray source has to be coherent or partially coherent. This is the case if the electric fields of two points in space and/or time are correlated to each other. To describe the coherence of the synchrotron source usually the terms of transversal and longitudinal coherence are used. The transversal coherence describes, if the wave is able to produce interference pattern in a Young-double-slit experiment (if the distance between the slits is larger than several coherence lengths no interference pattern will be seen). The longitudinal coherence specifies the ability of the wave to interfere with a temporal copy of itself (like in the Michelson-Interferometer experiment) [21, 57]. The transversal and longitudinal coherence lengths are given respectively by:

$$\xi_t = \frac{\lambda R_s}{2d_s}; \quad \xi_l = \frac{\lambda^2}{2\Delta\lambda}. \quad (5.19)$$

Here λ is the wavelength of the X-rays, d_s is the source size, R_s is the distance from the source to the sample point and $\Delta\lambda$ is the wavelength spread of the source, so $\Delta\lambda/\lambda$ is the relative bandwidth of the source.

If a coherent beam impinges on a sample, then the scattered light contains information about the exact spatial arrangement of the sample, if the coherence volume is larger than the illuminated sample volume. The scattered intensity provides information about the dynamical structure factor of the sample ($I_{coh}(\mathbf{Q}, t) \propto S(\mathbf{Q}, t)$). This is in contrast to incoherent light, which probes only averages of the structure factor ($I_{incoh} \propto \langle S(\mathbf{Q}, t) \rangle$) and provides the information about the ensemble average over all possible spatial arrangements. The monitored intensity is naturally a time average of the measured intensity over the acquisition time $\langle I(\mathbf{Q}, t) \rangle_T$. For ergodic systems the time average for infinitely long exposure time $\langle I(\mathbf{Q}, t) \rangle_T$ is equivalent to the ensemble average $\langle I(\mathbf{Q}, t) \rangle$.

A static speckle pattern contains not only information on the system, but also information on the radiation that produced it. Especially the information on the degree of coherence and the illuminated volume size are included. The ratio $\beta = \sigma^2/\langle I \rangle^2$ is the definition of the contrast of the speckle pattern, where $\langle I \rangle$ is the mean intensity and $\sigma = (\langle I^2 \rangle - \langle I \rangle^2)^{1/2}$. Under fully coherent conditions the contrast is $\beta = 1$. Usual experimental conditions only allow for a partial coherent illumination of the sample. In these cases the sample volume is bigger than the coherence volume. This can be described by dividing the scattering volume in N small volume elements. It changes the probability distribution of the intensity, which results to $\sigma = \langle I \rangle/N^{1/2}$ and $\beta = (1/N)$. The contrast β is reduced and reaches zero in the incoherent limit ($N \rightarrow \infty$). Only the coherent part of the incident beam gives rise to interference, which results in a speckle pattern. The constant part - the incoherent fraction $(1 - \alpha)$ - reduces the contrast by a factor α^2 , so $\beta = (\alpha^2/N)$. N is Q -dependent for a partially coherent beam. Accordingly the contrast β decreases with increasing Q . This effect is weak for monochromatic beam and low Q -values as usually probed in SAXS geometry.

In contrast to a static speckle pattern, fluctuations of the spatial arrangement of the scattering points will cause changes in the speckle pattern. The resulting fluctuations of the scattered intensity reveal information on the dynamics of the system. The normalized (second order) intensity correlation function $g_2(\mathbf{Q}, t)$ is used to measure temporal correlations.

The time autocorrelation function correlates the scattered intensity at a given point in reciprocal space at two different times and is defined by:

$$g_2(\mathbf{Q}, t) = \frac{\langle I(\mathbf{Q}, \tau)I(\mathbf{Q}, \tau + t) \rangle}{\langle I(\mathbf{Q}) \rangle^2}. \quad (5.20)$$

Here $I(\mathbf{Q}, \tau)$ is the intensity at wave vector \mathbf{Q} and time τ . Approximations for small and large delay times result in the following limits for the nominator of $g_2(\mathbf{Q}, t)$:

$$\lim_{t \rightarrow \infty} \langle I(\mathbf{Q}, \tau)I(\mathbf{Q}, \tau + t) \rangle = \langle I(\mathbf{Q}) \rangle^2, \quad (5.21)$$

and

$$\lim_{t \rightarrow 0} \langle I(\mathbf{Q}, \tau)I(\mathbf{Q}, \tau + t) \rangle = \langle I^2(\mathbf{Q}) \rangle. \quad (5.22)$$

For times $t \rightarrow \infty$ and $t = 0$ $g_2(\mathbf{Q}, t)$ obviously achieves the respective minimum and maximum values of 1 and $1 + \beta$. The contrast β is a beamline and experimental setup specific parameter, which can be determined experimentally [18].

The experimentally observable intensity autocorrelation function $g_2(\mathbf{Q}, t)$ can be related to the normalized intermediate scattering function $f(\mathbf{Q}, t)$ due to the Siegert relation [26, 44] with

$$g_2(\mathbf{Q}, t) - 1 = \beta(\mathbf{Q}) |f(\mathbf{Q}, t)|^2, \quad (5.23)$$

where $f(\mathbf{Q}, t) = S(\mathbf{Q}, t)/S(\mathbf{Q}, 0)$. $S(\mathbf{Q}, 0)$ is the static structure factor and $S(\mathbf{Q}, t)$ is the dynamic structure factor. It is described by

$$S(\mathbf{Q}, t) = \sum_{n=1}^N \sum_{m=1}^N \langle b_n(\mathbf{Q}) b_m(\mathbf{Q}) \exp(i\mathbf{Q} \cdot [\mathbf{r}_n(t) - \mathbf{r}_m(0)]) \rangle, \quad (5.24)$$

where $b_n(\mathbf{Q})$ is the scattering amplitude of the n -th scatterer in the sample at position $\mathbf{r}_n(t)$. The dynamic structure factor gives access to the dynamic behaviour of the system. It represents one of the main possibilities to compare experimental results to theory.

The case of monodisperse spherical particles with radius R undergoing Brownian motion is the standard example in XPCS. If these particles do not interact, their positions are not correlated and the mean square value of displacement is given by

$$\langle (\mathbf{r}(0) - \mathbf{r}(t))^2 \rangle = 6D_0t, \quad (5.25)$$

where D_0 is the Stokes-Einstein coefficient of diffusion. If the surrounding medium has a viscosity η , with k_B being the Boltzmann constant and T being the temperature, then $D_0 = k_B T / 6\pi\eta R$. Using this relation eq. 5.23 can be written as:

$$g_2(\mathbf{Q}, t) - 1 = \beta(\mathbf{Q}) |\exp(-D_0 Q^2 t)|^2. \quad (5.26)$$

A useful property can be introduced by setting $\Gamma(\mathbf{Q}) = \lim_{t \rightarrow 0} d/dt[\ln f(\mathbf{Q}, t)] = D_0 \cdot Q^2$. $\Gamma(\mathbf{Q})$ is called the decay rate of the exponential function g_2 and is the initial slope ($t \rightarrow 0$) of the measured intermediate scattering function $f^M(\mathbf{Q}, t)$. Equation 5.26 is not valid if particle interactions are present, and has to be adjusted using the effective diffusion coefficient $D(\mathbf{Q})$, which is dependent on the wave vector. Using this new property eq. 5.26 can be rewritten as:

$$g_2(\mathbf{Q}, t) - 1 = \beta(\mathbf{Q}) \left| \exp(-D(\mathbf{Q}) \cdot Q^2 t) \right|^2 = \beta(\mathbf{Q}) \exp(-2\Gamma(\mathbf{Q})t). \quad (5.27)$$

Equation 5.27 is a special form of the Kohlrausch-Williams-Watts (KWW) expression:

$$g_2(\mathbf{Q}, t) - 1 = \beta(\mathbf{Q}) \exp(-2[\Gamma(\mathbf{Q})t]^\gamma), \quad (5.28)$$

where $\Gamma(\mathbf{Q}) = 1/\tau_c(\mathbf{Q})$ is the relaxation rate, $\tau_c(\mathbf{Q})$ is the relaxation time and the shaping exponent $\gamma = 1$.

This single exponential form of the g_2 -function is characteristic for free diffusion or Brownian motion [5, 26]. The factor 2 results due to the use of a homodyne detection scheme [26, 44]. The Brownian theory assumes random motion caused by forces consisting of systematic frictional and random fluctuating components.

In general, the diffusion coefficient has the form

$$D(Q) = \frac{D_0 H(Q)}{S(Q)}, \quad (5.29)$$

where $H(Q)$ is a function of the hydrodynamic interactions due to the velocity field of the surrounding particles and $S(Q)$ is the dynamic structure factor, describing direct interparticle interaction of the sample particles [67].

If the underlying dynamics is more complicated, the shape of the time correlation function can be different. E.g. glass-forming liquids (solutions of colloidal nanoparticles in polymer solvents) show deviations of the diffusion during the transition to the glass state.

If the shaping exponent is $\gamma > 1$, the decay of $g_2(\mathbf{Q}, t) - 1$ is faster, and if $\gamma < 1$, than the decay is slower than single exponential behavior [19, 50]. If the dynamics is diffusive ($\Gamma \propto Q^2$), then the according motion are called hyper- and subdiffusive, respectively.

The diffusive motion is not the only type of motion, which was observed. If $\Gamma \propto Q$ the underlying dynamics is not diffusive anymore. The combination of $\Gamma \propto Q$ and $\gamma = 2$ is a property of a *ballistic* motion with a characteristic velocity v . In this model the particles move a long distance without any interactions (large mean free path). The velocities are assumed to have a Boltzmann-distribution. The g_2 -function has then the form:

$$g_2(\mathbf{Q}, t) - 1 = \beta \exp(-2[\Gamma(\mathbf{Q})t]^2). \quad (5.30)$$

The most important theories, explaining the origin of the ballistic motion, are continuous time random walk and stress field relaxation models [50]. According to the value of the exponent γ different models for the motions of the particles are applicable. The proportionality of relaxation rate to Q can vary, depending on the underlying microscopic dynamics, too.

5.4. Goethite and its magnetic properties

Goethite is a common and stable iron-oxide. Bulk goethite has a density of $\rho_{FeOOH} \approx 4.3 \text{ g/cm}^3$ and is a typical antiferromagnetic material. The crystallographic structure of goethite is represented by the orthorhombic $Pnma$ space group with unit cell parameters $a = 0.995 \text{ nm}$, $b = 0.302 \text{ nm}$ and $c = 0.460 \text{ nm}$, which is shown in fig. 5.7. The structure can be described as a stacking of the double chains of oxygen octahedral with Fe^{3+} cation in the centre in the b direction. The interlink between neighboring double chains works through shared corners and hydrogen bonds [41].

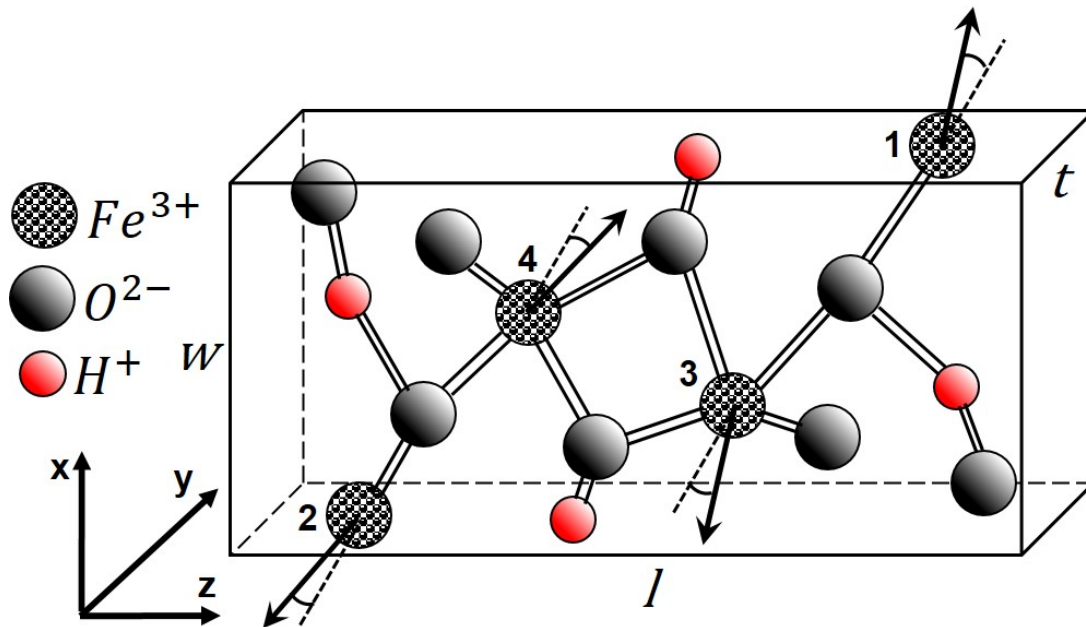


Figure 5.7.: A schema of the crystal and magnetic structure of goethite, drawn after figure 1 in [11]. The big black and white, checked circles represent iron Fe^{3+} -ions, the big circles coloured with gradient of grey stand for oxygen O^{2-} -ions and small red gradient circles depict hydrogen H^+ -ions. The dimensions of particles are noted with letters and directions of the spins of iron ions are shown by the black arrows. According antiferromagnetic sublattices are inclined by $\pm 13^\circ$ to spin directions of the iron ions.

These structural details lead to rectangular goethite nanoplatelets. The particles have a width w , thickness t and length l respectively oriented along the x , y and z directions. Depending on the size of the particles and the synthesis process the nanoplatelets might be a single crystalline structure [41] or consist of multidomains [23, 65]. The particles are stacked together by the addition of smaller platelets.

The magnetic properties of goethite depend on the size and polydispersity of the particles and the temperature of the environment. The antiferromagnetic axis is the z -axis (the long axis), because of the antiferromagnetic coupling between the neighboring oxygen chains. Here \parallel refers to the direction parallel to the antiferromagnetic (long) axis of a nanoplatelet and \perp perpendicular to it along x -direction (width of the platelet). The Neel temperature T_N , at which the goethite becomes paramagnetic varies between $T_N = 325\text{ K}$ and $T_N = 400\text{ K}$. In natural goethite the parallel χ_{\parallel} and perpendicular χ_{\perp} susceptibilities show the classical behaviour of an antiferromagnetic material. The magnetic-susceptibility anisotropy $\Delta\chi = \chi_{\parallel} - \chi_{\perp}$ is negative. It decreases with increasing temperature until it vanishes at T_N .

Nevertheless goethite nanoplatelets show a weak ferromagnetic moment M oriented mainly along the z -axis. This moment arises due to non-compensated surface spins. There is also a smaller ferromagnetic moment along the x -axis. These moments are the result of the inclination of the magnetic moment in the particle. At temperature $T = 274\text{ K}$ an iron atom is expected to have a magnetic moment of $\mu_{Fe} = 3.9\mu_B$. Due to the inclination of this moment the moment along the z -axis was measured to be $\mu_z = 2.87\mu_B$ and along the x -axis to be $\mu_x = 0.82\mu_B$ [6]. The "spin-flop" transition occurs at $B = 20\text{ T}$ at $T = 4.2\text{ K}$ and is still (depending on the size and polydispersity of the nanoparticles) as high as several Tesla at room temperature [11, 41].

Goethite suspensions show a variety of phases, which depend on concentration c , temperature T and applied magnetic field B . The reported phases are isotropic, nematic, smectic and columnar, as summarized in section 4 in fig. 4.6 and 4.7. Lemaire et al. report that without applied magnetic field at room temperature suspensions below $c = 5.5\text{ vol\%}$ are in the isotropic phase. Above $c = 8.5\text{ vol\%}$ the suspensions are in the nematic phase. If the concentration increases above $c = 20\text{ vol\%}$, the whole suspension is in the columnar phase. The isotropic-nematic and nematic-columnar phase transition were reported in the respective ranges: $5.5\text{ vol\%} < c < 8.5\text{ vol\%}$ and $15\text{ vol\%} < c < 20\text{ vol\%}$ [39, 42], respectively.

Lemaire et al. used the Lee model and the Onsager model to describe the transitions [36, 49]. The Lee model gave a transition concentration $c_i = c_n = 17\text{ vol\%}$. The Onsager model for rods with length L and diameter D predicts the concentration for isotropic-nematic phase transition at $c_i = c_n = 15\text{ vol\%}$. The model is only precise for rods with a length to diameter ratio $L/D \geq 100$, which is not the case for goethite parti-

cles. In addition, due to particle interactions at these high concentrations an effective diameter D_{eff} and effective concentration c_{eff} have to be introduced. Nevertheless of these improvements of the original theory, experimental values still show deviation from theory, which can be accounted for by variation of the size, shape and aspect ratio of the particles [42].

The Onsager model is the main model, which is commonly used to explain the behaviour of goethite suspensions. Lemaire et al. applied this theory and tried to calculate the according orientation distribution function (ODF). The phase behaviour and reaction to the applied magnetic field is explained with the help of the free energy F , which depends on positional entropy, orientational entropy, excluded volume interactions and interactions between the cylinders themselves and particles and magnetic field:

$$\frac{F}{Nk_B T} = \frac{F_0}{Nk_B T} + \ln \Lambda^3 \rho - 1 + \int f(\theta) \ln(4\pi f(\theta)) d\Omega + \\ + 1/2\rho \int v_{exc}(\Omega, \Omega') f(\theta) f(\theta') d\Omega d\Omega' + \frac{1}{k_B T} \int f(\theta) E_m(\theta) d\Omega. \quad (5.31)$$

Here V is the volume of a cylindrical goethite particle, N is the number of particles in the suspension, V_{susp} the considered volume of the suspension, $\rho = N \cdot V/V_{susp}$ the numerical density of the suspension, Λ the De Broglie wavelength, F_0 the orientation- and concentration independent part of the free energy and $v_{exc}(\Omega, \Omega')$ the excluded volume of two cylinders with orientation $\Omega = (\theta, \psi)$, $\Omega' = (\theta', \psi')$ and $E_m(\theta)$ is the magnetic energy of the nanoplatelets.

The Onsager model for nematic ordering can be interpreted as a change in entropy. The orientational entropy decreases, while excluded volume entropy by packing increases. From this theory predictions for the nematic order parameter S_2 and therefore for the orientation of particles can be made. At high concentrations these interactions are responsible for the spontaneous alignment of the particles in the suspension. Nevertheless it has to be pointed out that goethite suspensions are rather poor nematic model systems, since goethite particles are platelets with small aspect ratio and high polydispersity and carry a strong electrostatic surface charge [42].

Suspensions of goethite are very sensitive to a magnetic field. Goethite particles align in small magnetic fields of $B \geq 40$ mT. An especially interesting fact is that the rods realign, if the applied field is increased beyond a critical field strength B_{crit} , which depends on the shape and size of the particles. B_{crit} has usually a value of several hundreds of millitesla. In fields $B < B_{crit}$ the particles tend to align parallel to the field. If the field $B > B_{crit}$ the particles realign perpendicular to the applied field.

In order to achieve a qualitative understanding of the behaviour of goethite nanoplatelets in static or changing magnetic fields the calculation of the magnetic

energy of the nanoplatelets is necessary. Assuming, that particles have the same size and volume, it follows that they carry the same longitudinal magnetic moment μ . The magnetic susceptibility is anisotropic and uniaxial and the magnetic susceptibility-anisotropy $\Delta\chi$ is negative.

If a particle is oriented at an angle β respective to the magnetic field B , the magnetic energy of the particle consists of two terms. The first term accounts for the interaction between the particle dipole and the field - the so called Zeeman energy. The second term results from the induced magnetization. The field inside the particle itself has to be considered in order to include a demagnetizing effect. $H_i = H_e - NM$, where H_i is the internal field, H_e is the external field, N the tensor of the demagnetising field coefficients and M the induced magnetization. The full expression for magnetic energy becomes then

$$E_m(\beta) = -\mu B \cos \beta \cdot \frac{1 + \chi_{\parallel}}{1 + N_{\parallel}\chi_{\parallel}} - \frac{VB^2}{2\mu_0} \cdot \cos^2 \beta \cdot \left[\frac{\chi_{\parallel}}{(1 + N_{\parallel}\chi_{\parallel})^2} - \frac{\chi_{\perp}}{(1 + N_{\perp}\chi_{\perp})^2} \right]. \quad (5.32)$$

N_{\parallel} and N_{\perp} are demagnetizing coefficients and have values between 0 and 1. Because of the multiplication with susceptibilities χ_{\parallel} and χ_{\perp} with values of the order of 10^{-3} their influence can be neglected, which in total leads to

$$E_m(\beta) = -\mu B \cos \beta - \frac{\Delta\chi \cdot VB^2}{2\mu_0} \cdot \cos^2 \beta. \quad (5.33)$$

From this equation it is obvious that in a static field the magnetic energy is a function of the angle β . The factors μ and $\frac{\Delta\chi V}{2\mu_0}$ are of the same order of magnitude, if the respective values are considered ($\mu \approx 1000\mu_B$, $V \approx 3.7 \times 10^{-23} \text{ m}^3$, $\Delta\chi \approx -3 \times 10^{-4}$). So the influence of both terms on the magnetic energy of an particle directly depends on the magnitude of the field B .

In low fields the first term with B , which depends on $\cos \beta$ dominates. The minimum is then at $\beta = 0$, so the particles tend to align parallel to the low field. In large fields the term with B^2 dominates. The minimum of the magnetic energy is then at $\beta = \pi/2$. The particles tend to align perpendicular to the field. The crossover between the two regimes is achieved at $B_{crit} = \frac{\mu\mu_0}{|\Delta\chi|V}$, which is on the order of several 100mT. This is a remarkable behaviour, which gives suspension of goethite platelets unique properties under influence of increasing magnetic field B .

The magnetic energy depends on $\cos \beta$ and $\cos^2 \beta$, which allows to make a connection to the orientation order parameters as defined in Section 5.2 and connect the orientation of the particles to their magnetic properties and reaction to an applied magnetic field. The magnetic energy of a particle can be written as:

$$E_m(\beta) = -\mu B P_1(\cos \beta) - \frac{\Delta\chi \cdot V B^2}{3\mu_0} \cdot P_2(\cos \beta). \quad (5.34)$$

Here $P_1(\cos \beta)$ and $P_2(\cos \beta)$ are Legendre polynomials of respective first and second degree. The magnetization of a particle can be written as

$$M = \rho\mu \int d\Omega f(\theta) \cos\theta = \rho\mu S_1, \quad (5.35)$$

where $f(\theta)$ is the ODF as described in Section 5.2.

The free energy and orientational distribution of the particles in the suspension can be described by the orientation distribution function $f(\beta)$ from the calculation of the first and second moments S_1 and S_2 , which can be computed from measured M and E_m or from the azimuthal scattering intensity [41].

Lemaire et al. assumed that particles are spherocylinders [41]. They exclude Van-der-Waals forces and introduce electrostatic interaction using hard-core repulsion of the Onsager model. For this purpose they introduce an effective diameter D_{eff} and follow Vroege et al. [71] to define the free-energy, where they simply add a magnetic term to the free energy of the Onsager model. Following these steps the expressions for the ODF is

$$f(\theta) = \frac{1}{Z} \exp\left(-\frac{E_{exc}(f, \Omega) + E_m(\theta)}{k_B T}\right), \quad (5.36)$$

and hard core repulsion for particles oriented at $\Omega = (\theta, \psi)$ to the applied field

$$E_{hcr}(f, \Omega) = \frac{32}{\pi} k_B T \frac{c}{c^*} \int d\Omega' f(\theta') |\sin(\gamma(\Omega, \Omega'))|. \quad (5.37)$$

Here γ is the angle between the long axes of two particles, c is the concentration of the particles in suspension and $c^* = 16V_{eff}/(\pi L^2 D_{eff})$ is the maximum volume fraction for a stable isotropic state of the suspension. The equation 5.36 can only be solved numerically and Lemaire et al. provide the solution for two cases:

- dilute suspensions
- concentrated suspensions at low fields.

In case of dilute suspensions the hard core interactions between particles can be disregarded and the ODF has the form:

$$f^d(\theta) = \frac{1}{Z^d} \exp(KB \cos \theta + JB^2 P_2(\cos \theta)), \quad (5.38)$$

where $K = \frac{\mu}{k_B T} > 0$, $J = \frac{\Delta\chi V}{3\mu_0 k_B T} < 0$, $P_2(\cos \theta) = 3/2 \cdot \cos^2 \theta - 1$ and superscript d stands for diluted. The orientational partition function Z^d can be calculated by integration of the

ODF over the angular distribution and the first and second moments of the ODF can be derived as:

$$S_1^d = \frac{1}{B} \frac{\partial \ln Z^d}{\partial K} = \frac{\mu B}{3k_B T} \quad (5.39)$$

and

$$S_2^d = \frac{1}{B^2} \frac{\partial \ln Z^d}{\partial J} = \frac{B^2}{15} \cdot \left(\frac{\Delta \chi V}{\mu_0 k_B T} + \left(\frac{\mu}{k_B T} \right)^2 \right). \quad (5.40)$$

In the case of concentrated suspensions the electrostatic repulsion can not be neglected anymore. However, the free energy can be expanded into a series to derive

$$S_1 = \frac{\mu B}{3k_B T} \quad (5.41)$$

and

$$S_2 = \frac{B^2}{15(1 - c/c^*)} \cdot \left(\frac{\Delta \chi V}{\mu_0 k_B T} + \left(\frac{\mu}{k_B T} \right)^2 \right). \quad (5.42)$$

The increasing nematic order can be described by nematic order parameters: the dipolar order parameter S_1 and the quadrupolar order parameter S_2 . Two basic effects are contributing to the increase:

- gradual freezing of macroscopic nematic fluctuations ($\Delta S \propto B$)
- Couton-Mutton effect ($\Delta S \propto B^2$) [41, 42].

The theoretical elaborations on the magnetic energy E_m of the suspension in this chapter are essential for understanding of the behaviour of goethite platelets in suspensions. The explanation based on the magnetic energy E_m can be therefore extended for understanding of the formation of the liquid crystalline phases formed by the goethite suspensions, which are connected with the unusual properties of the goethite platelets in increasing magnetic field B , such as alignment of the particles with the long axis parallel to the field B at $B < B_{crit}$ and the realignment with the long axis perpendicular to the field, if $B > B_{crit}$. With formulas shown above it is also possible to connect the magnetic energy E_m with order parameters and magnetization M , which are later essential for the structural analysis of the goethite suspensions and the establishment of the qualitative behaviour models of the microscopic dynamics of the goethite platelets in water suspensions.

6. Small Angle X-ray Scattering analysis

6.1. Introduction

The behaviour and properties of goethite suspensions in magnetic fields were studied by investigation of the microscopic structure and dynamics with Small Angle X-ray Scattering (SAXS) and X-ray Photon Correlation Spectroscopy (XPCS). The SAXS evaluation of the experiments provides an understanding of the structural characteristics of the investigated suspensions, which is later important to understand the underlying dynamics.

In SAXS experiments with lyotropic nematic liquid crystals of rod-like particles the main contribution to the scattered intensity (p) is found in the direction perpendicular to the preferred orientation of the long axis of the particles (n). A diffuse peak results in this case from the liquid-like positional order of the particles in the plane perpendicular to the particle director (n). Its position corresponds to the average distance between particles and is proportional to the concentration of the suspension. The same properties are valid for an isotropic phase of goethite suspensions, only the positional order has a higher range. In this part of the thesis, the orientation of the particles with respect to the magnetic field (with direction m) and nematic order parameter (OP) are the main investigated properties. They are responsible for an identification of liquid crystal phases, formed by the samples [41].

Five water based goethite suspensions with different concentrations were prepared. The concentrations $c = 4 \text{ vol\%}$, 7.8 vol\% , 10 vol\% , 16 vol\% and 20 vol\% were chosen, based on the phase diagrams of goethite suspensions from the previous experimental studies [40, 41, 42]. For $c < 5.5 \text{ vol\%}$ an isotropic phase is expected. In the range $5.5 \text{ vol\%} < c < 8.5 \text{ vol\%}$ an coexistence region of isotropic and nematic phase was observed. If $8.5 \text{ vol\%} < c \leq 16 \text{ vol\%}$ only a nematic phase is expected to form. The region $16 \text{ vol\%} < c \leq 20 \text{ vol\%}$ is the region of a coexistence of the nematic and the columnar phase. Finally, if concentration exceeds $c = 20 \text{ vol\%}$ a columnar phase is expected.

The goal was to investigate the structure and dynamics of the suspensions in the isotropic and nematic phases. Therefore concentrations $c = 4 \text{ vol\%} (< 5.5 \text{ vol\%})$

and $c = 10 \text{ vol\%}$ ($> 8.5 \text{ vol\%}$) were chosen to induce these phases. The concentration $c = 7.8 \text{ vol\%}$ falls into the isotropic/nematic coexistence region, $c = 16 \text{ vol\%}$ delivers a pure nematic state with highest possible concentration and $c = 20 \text{ vol\%}$ represents a sample in the nematic/columnar coexistence region.

The analysis of the samples in the state directly after filling the capillaries is not a part of this thesis, because they were not in an undisturbed state. Immediately after the filling procedure the suspensions showed a prealignment, which was random in orientation. This primary state is clearly different from the forced state at $B = 0 \text{ mT}$, which was achieved after $B \neq 0 \text{ mT}$ was applied.

In Section 6.2 the details necessary for the understanding of the following SAXS investigation are given. The SAXS data of the suspensions at different magnetic fields and low concentrations $c \leq 10 \text{ vol\%}$ are analysed in Section 6.3. These data give more precise structural information on isotropic goethite suspensions, but was not used in the investigation of the dynamics, because of their fast microscopic motion. The suspensions at high concentration $c \geq 16 \text{ vol\%}$ will be discussed in Section 6.4. They were later used for the dynamical investigation in Chapter 7. The dependence of the orientations and phases on magnetic energy E_m will be explained in Section 6.5 and the results of the SAXS analysis will be summarized in Section 6.6.

6.2. Preliminary discussion

For all SAXS measurements a PILATUS 300k detector was used, therefore all the SAXS images throughout this chapter share the same dimensions. This particular model of detector has 619×487 pixels with a pixel dimensions of $172 \mu\text{m} \times 172 \mu\text{m}$. The complete detector consists of three modules with about one hundred thousand pixels each. There are two gaps between the chips. Each gap is 17 pixel wide, which corresponds to $\approx 3 \text{ mm}$. The maximum Q in the presented experiments was $Q_{max} \approx 0.03 \text{ \AA}^{-1}$. For the purposes of simpler explanation 18 Q -values and 3 Q -regions had to be defined. The 18 Q -values, used in this thesis, are shown in table 6.1. The three additional Q -regions were defined as: $Q_{r1} < 0.005 \text{ \AA}^{-1}$, $0.005 \text{ \AA}^{-1} < Q_{r2} < 0.011 \text{ \AA}^{-1}$ and $0.011 \text{ \AA}^{-1} < Q_{r1} < 0.016 \text{ \AA}^{-1}$, and will be used later.

Fig. 6.1 shows the SAXS pattern from the liquid crystal phases, which were induced with magnetic field during this experiment. For the experiments a set of permanent magnets with spacers was used. With this experimental setup field strength values of $B_1 = 180 \text{ mT}$, $B_2 = 240 \text{ mT}$, $B_3 = 310 \text{ mT}$, $B_4 = 370 \text{ mT}$, $B_5 = 410 \text{ mT}$ and $B_6 = 900 \text{ mT}$ were achieved. In the centre of each image a beamstop is visible, which blocks the direct beam. In this experiment $E = 7050 \text{ eV}$ was chosen. The beam is usually not fully centred on the detector, but slightly shifted vertically, so that different areas of the

Table 6.1.: The colour of the different lines for the Q values chosen from Q - ϕ^B -partitions as shown in fig. 7.2 for illustration of the g_2 -examples. In the images the colour bar shows the according Q values, which stay constant through whole thesis.

Color	black	red	blue	green	cyan	magenta
Q Number	Q_1	Q_2	Q_3	Q_4	Q_5	Q_6
$Q[\text{\AA}^{-1}]$	0.0024	0.0034	0.0046	0.0064	0.0081	0.0108
Color	orange	yellow	gray	brown	purple	violet
Q Number	Q_7	Q_9	Q_{12}	Q_{15}	Q_{17}	$Q_{18} = Q_{max}$
$Q[\text{\AA}^{-1}]$	0.013	0.015	0.02	0.025	0.028	0.03

scattering pattern are covered by the gaps of the detector sensitive area. Four circles in the image on the top left visualize the investigated Q -range: blue marks $Q_3 \approx 0.005 \text{\AA}^{-1}$, magenta - $Q_6 \approx 0.011 \text{\AA}^{-1}$, yellow - $Q_9 \approx 0.015 \text{\AA}^{-1}$ and brown - $Q_{15} \approx 0.025 \text{\AA}^{-1}$, as defined in table 6.1. In all figures, which show SAXS pattern this visualization will stay the same. The definition of the Q -values stays the same throughout the manuscript.

The top left pattern in fig. 6.1 is from a 4vol%-suspension at $B = 370 \text{ mT}$. The pattern can not be distinguished from an isotropic (I) pattern without detailed analysis. Nevertheless it was possible to distinguish contributions from the oriented isotropic (OI), where the align preferably with they long axis parallel to the magnetic field ($\mathbf{n} \parallel \mathbf{m}$), and anti-oriented isotropic (AOI) phases, where $\mathbf{n} \perp \mathbf{m}$. SAXS pattern from these single phases are shown in fig. 6.1 on top right and in the centre on the left, respectively. The isotropic phases and accordingly the isotropic scattering pattern are characteristic for low concentration suspension at $c \leq 10 \text{ vol\%}$. The pattern decays smoothly in all directions, but might be extorted (ellipsoid in OI or AOI phases).

The images in the centre on the right and in the bottom row show phases characteristic for high concentration suspensions at $c \geq 16 \text{ vol\%}$. The scattering pattern on the in the centre on the right arises from a nematic phase (N), where $\mathbf{n} \parallel \mathbf{m}$ and which shows characteristic peaks near Q_6 ($\parallel \mathbf{p}$) and near Q_3 ($\perp \mathbf{p}$). With increasing magnetic field it traverses into a mixed phase (e.g. combination of positive nematic (pN) and positive anti-nematic (pAN) phases), which is shown in the image in the bottom row on the left. The anti-nematic phase (AN), where $\mathbf{n} \perp \mathbf{m}$, is induced at highest field and is shown in the bottom row on the right.

The phases described above can be classified using the order parameters OP, which were explained in detail in section 5.2. They are widely used in order to classify the order of alignment in liquid crystal phases. The values for the respective phases are shown in the table 6.2. The values for isotropic and nematic phases are defined in literature [9, 34]. Other phases are not that common and therefore the according values were defined based on the results of this thesis.

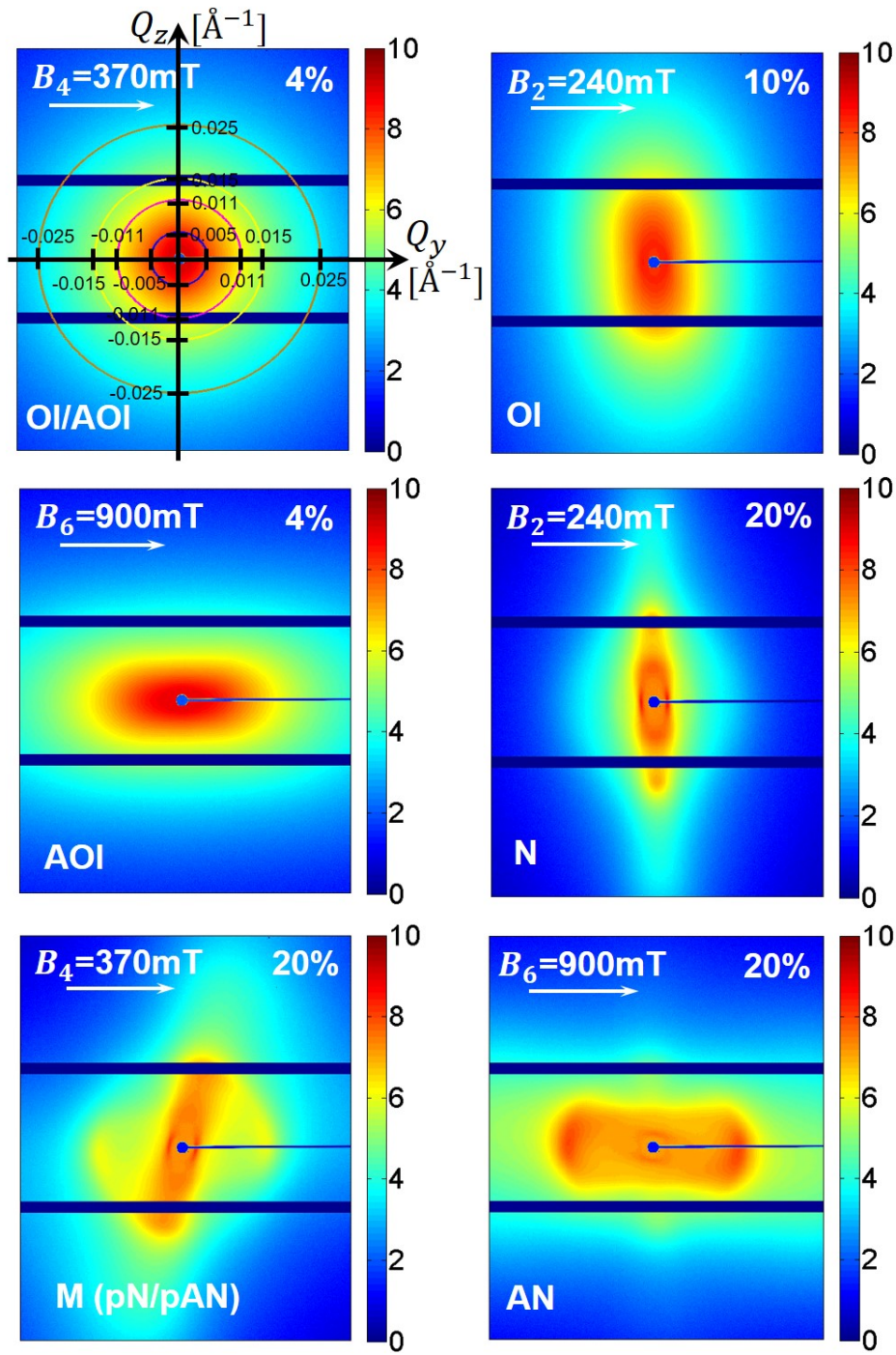


Figure 6.1.: Examples of the scattering patterns from different phases observed during the measurements. Top left: exemplary SAXS pattern from combination of oriented isotropic phase and anti-oriented isotropic phase observed from a 4 vol%-suspension at $B = 370$ mT. The colour circles in the image on top left visualize the Q -range: blue - $Q_3 = 0.005 \text{ \AA}^{-1}$, magenta - $Q_6 = 0.011 \text{ \AA}^{-1}$, yellow - $Q_9 = 0.015 \text{ \AA}^{-1}$ and brown - $Q_{15} = 0.025 \text{ \AA}^{-1}$. In addition, the Q -axes are inserted, to visualize the Q -values once, as they stay constant through whole thesis. Top right: pattern from oriented isotropic phase from a 10 vol%-suspension at $B = 240$ mT. Centre left: pattern from anti-oriented isotropic phase from a 4 vol%-suspension at $B = 900$ mT. Centre right: exemplary SAXS pattern from nematic phase from a 20 vol%-suspension at $B = 240$ mT. Bottom left: pattern from mixed phase, which is a combination of positive nematic and positive anti-nematic phases observed from a 20 vol%-suspension at $B = 370$ mT. Bottom right: pattern from anti-nematic phase from a 20 vol%-suspension at $B = 900$ mT.

Table 6.2.: Basic phases identified from the SAXS scattering patterns

Phase Name	Short Name	vectors	S_1	S_2	S_4
Isotropic	I	disordered	≈ 0.5	≈ 0	≈ 0
Oriented Isotropic	OI	$\mathbf{n} \parallel \mathbf{m}$	> 0.5	> 0	> 0
Anti-Oriented Isotropic	AOI	$\mathbf{n} \perp \mathbf{m}$	< 0.5	< 0	> 0
Nematic	N	$\mathbf{n} \parallel \mathbf{m}$	> 0.5	> 0.5	> 0
Antinematic	AN	$\mathbf{n} \perp \mathbf{m}$	< 0.5	$\ll 0$	> 0

Additionally to the order parameter analysis analyses of the ellipticity and structural peak positions were performed. These analyses are explained in Sections 6.3 and 6.4 respectively for suspensions with low and high concentrations. The creation of the isotropic, oriented isotropic and nematic phases as well as uncommon anti-oriented isotropic and anti-nematic phases is explained in Section 6.5 based on the magnetic energy of the goethite platelets in a suspension. The results of the structural analysis, as well as the deduced phase diagram are presented in Section 6.6.

6.3. Low concentration suspensions

The scattering patterns for the suspension with concentration of $c = 4 \text{ vol}\%$ are shown in fig. 6.2 for different magnetic field strengths.

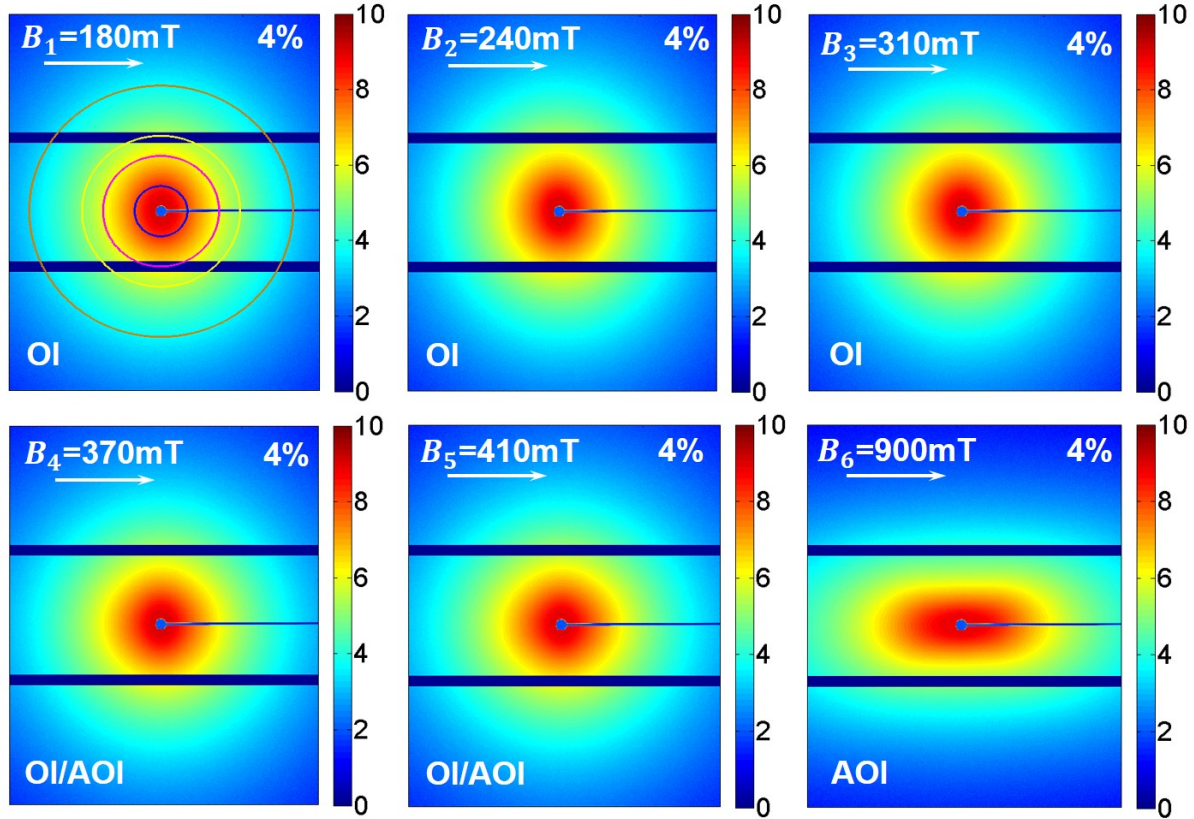


Figure 6.2.: The SAXS patterns from the 4 vol%-suspension are shown for different magnetic field strengths. The direction of the field \mathbf{m} is shown by white arrows. An elongated pattern along vertical direction ($\mathbf{p} \perp \mathbf{m}$) indicates a preferred horizontal alignment direction of the particles ($\mathbf{n} \parallel \mathbf{m}$) and vice versa.

The direction of the magnetic field is horizontal in the images. In all the images the highest intensity is close to the beamstop. Then it decreases with increasing Q without other features. At the first two field strengths (top row, left and centre of fig. 6.2) the scattering patterns are slightly elongated in the direction perpendicular to the magnetic field ($\mathbf{p} \perp \mathbf{m}$). At $B_3 = 310 \text{ mT}$ (top row on the right in fig. 6.2) the elongation decreases and seems to vanish at $B_4 = 370 \text{ mT}$ (bottom row on the left in fig. 6.2). The pattern at $B_5 = 410 \text{ mT}$ (bottom row in the centre in fig. 6.2) starts to elongate in the horizontal direction - parallel to the field ($\mathbf{p} \parallel \mathbf{m}$). At $B_6 = 900 \text{ mT}$ (bottom row on the right in fig. 6.2) the pattern is strongly elongated in the direction parallel to the field. The shape is ellipsoid.

The circular shape of the scattering patterns shows that the particles are randomly oriented. Only at $B_6 = 900 \text{ mT}$ the shape is an ellipsoid with its long axis parallel to the magnetic field, which means that the preferred orientation direction of the particles is

$n \perp m$. An asymmetric scattering feature has a long axis with a direction p (see fig. 6.2, where $p \parallel m$). This axis is linked with the preferred direction of alignment of particles in the suspension as $p \perp n$.

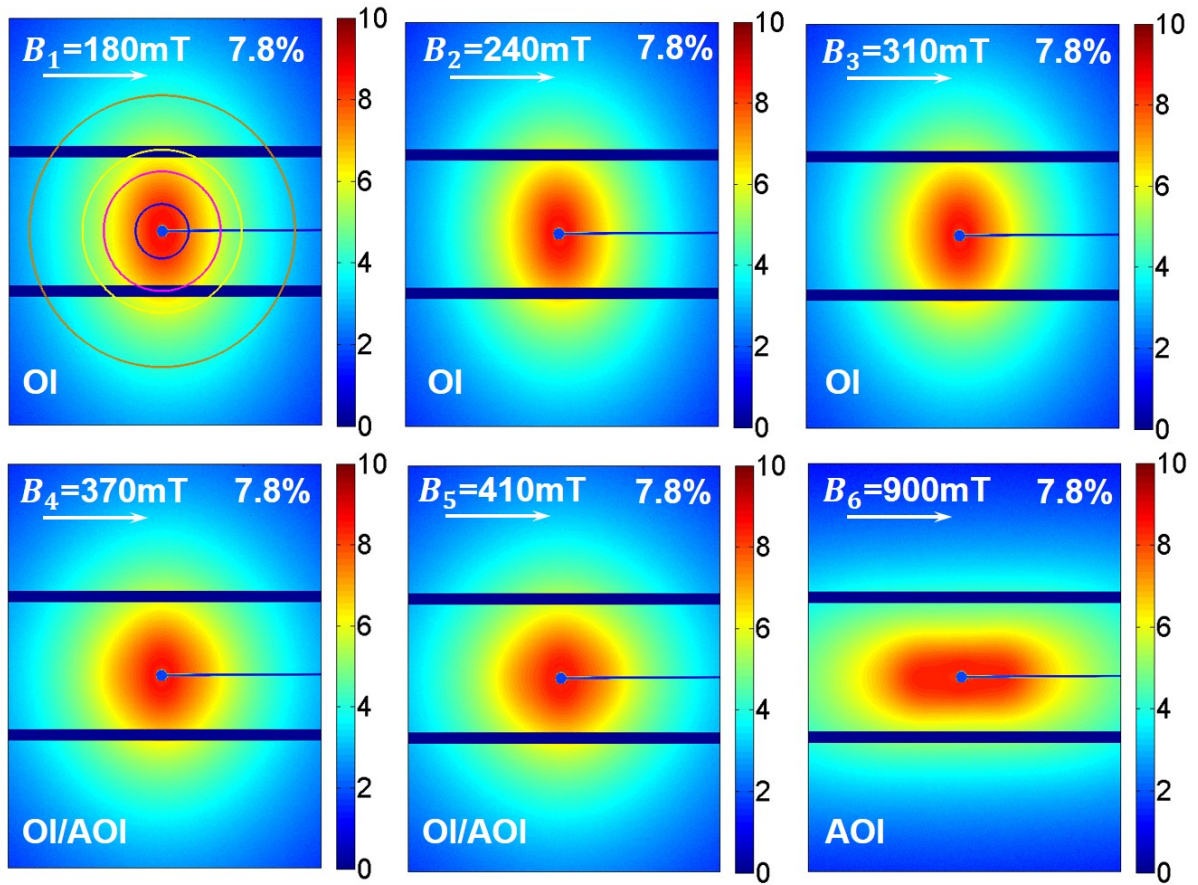


Figure 6.3.: The SAXS patterns from 7.8 vol%-suspension at different magnetic field strengths, as already explained in 6.2.

In fig. 6.3 the scattering patterns from goethite suspension with $c = 7.8$ vol% are shown. In the top row from left to right the scattering patterns for $B_1 = 180$ mT, $B_2 = 240$ mT, $B_3 = 310$ mT are shown and in the bottom row the patterns for $B_4 = 370$ mT, $B_5 = 410$ mT, $B_6 = 900$ mT are represented respective. In all patterns the maximal intensity is close to the beamstop and decreases with increasing Q . The patterns for $B \leq 240$ mT have ellipsoid shape with long axis perpendicular to the magnetic field ($p \perp m$). The long axis of the scattering feature grows shorter and the small axis larger at $B_3 = 310$ mT, which means that the preferred orientation of the feature perpendicular to the applied magnetic field is decreasing. It becomes almost circular at $B_4 = 370$ mT (fig. 6.3 bottom left). Therefore the partial order is completely lost and the particles in the suspension are randomly oriented. The pattern becomes rhomboidal at $B_5 = 410$ mT (fig. 6.3 bottom centre), which indicates an overlapping of two preferred orientation directions - $p_1 \perp m$ and $p_2 \parallel m$. The axis parallel to the magnetic field has grown longer. At $B_6 = 900$ mT (fig. 6.3 bottom right) the pattern becomes strongly elongated. The long

axis is parallel to the magnetic field ($\mathbf{p} \parallel \mathbf{m}$) as for the 4 vol%-suspension, which implies that particles reoriented with long axis perpendicular to the field ($\mathbf{n} \perp \mathbf{m}$).

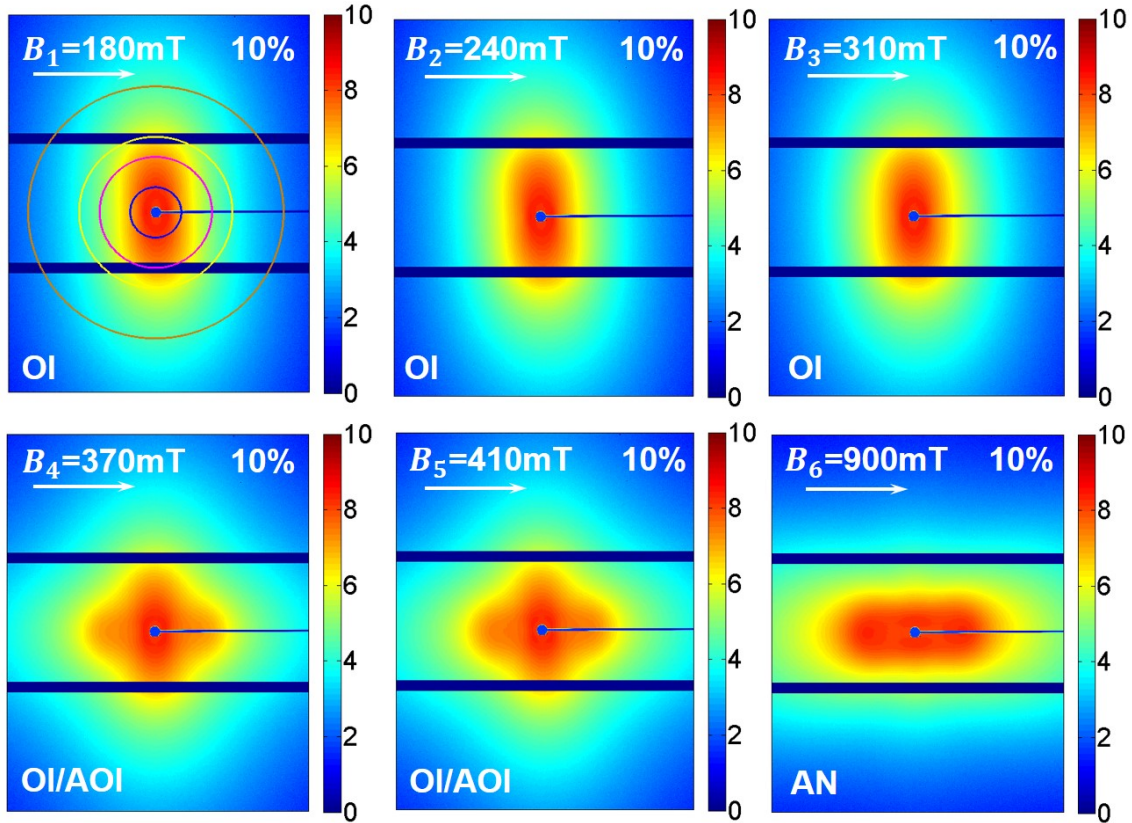


Figure 6.4.: The SAXS patterns from 10 vol%-suspension at different magnetic field strengths, as already explained in 6.2 and 6.3.

The scattering patterns from goethite suspension with $c = 10$ vol% are shown in the same order as before in fig. 6.4. In all patterns the maximal intensity is close to the beamstop and decreases with increasing Q . The three patterns for $B \leq 310$ mT have ellipsoid shape with long axis perpendicular to the magnetic field ($\mathbf{p} \perp \mathbf{m}$), as shown in the top row in fig. 6.4. The long axis of the scattering feature grows shorter and the small axis larger at $B_3 = 310$ mT. The platelets are therefore oriented with long axis parallel to the magnetic field ($\mathbf{n} \parallel \mathbf{m}$). The images at 370 mT $\leq B \leq 410$ mT show a cross shaped pattern (fig. 6.4 bottom left and centre). The cross consists of two overlapping ellipsoids - one with long axis perpendicular and another with long axis parallel to the magnetic field. This implies that at these field strengths two preferred orientation directions of the platelets are present at the same time - with long axis perpendicular ($\mathbf{p}_1 \perp \mathbf{m}$) and parallel ($\mathbf{p}_2 \parallel \mathbf{m}$) to the applied magnetic field. At $B_5 = 410$ mT the feature with $\mathbf{p}_2 \parallel \mathbf{m}$ is more pronounced than the feature with $\mathbf{p}_1 \perp \mathbf{m}$. At $B_6 = 900$ mT (fig. 6.4 bottom right) the pattern is strongly elongated, but with long axis parallel to the magnetic field ($\mathbf{p} \parallel \mathbf{m}$). Therefore the particles in the suspension are oriented with long axis perpendicular to the magnetic field ($\mathbf{n} \perp \mathbf{m}$).

This qualitative evaluation does not allow to make precise statement about the underlying phases. Therefore the exact phase will be determined with orientation parameter (OP) analysis and the analysis of linecuts along specific directions.

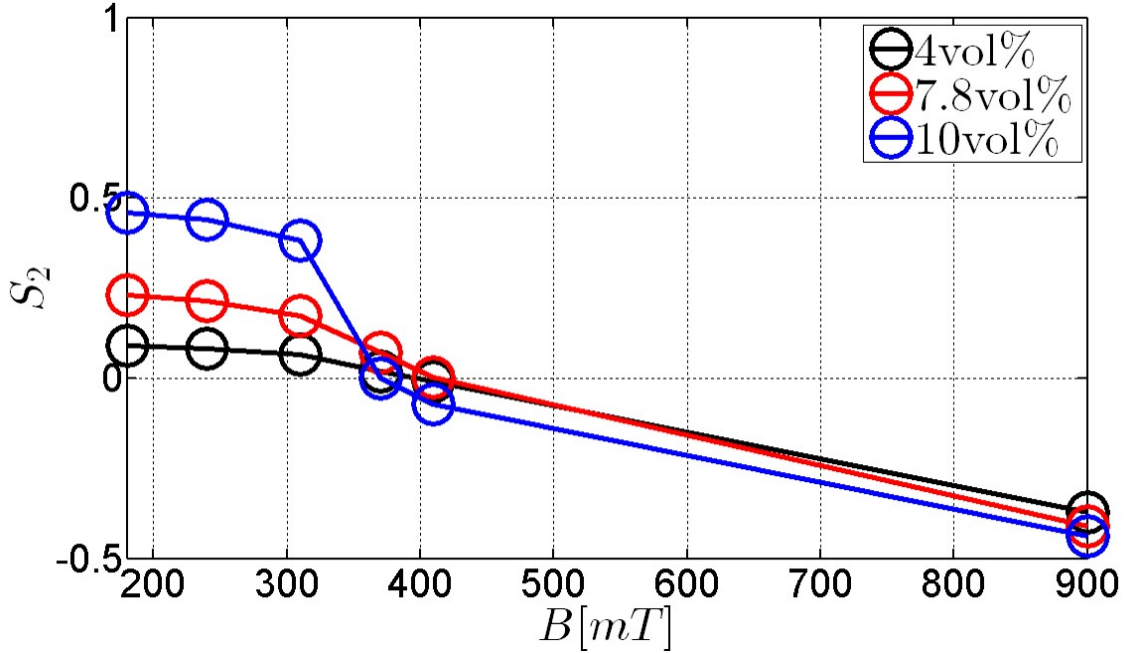


Figure 6.5.: S_2 order parameter versus magnetic field strength B at low concentrations: $c \leq 10$ vol%. Black: $c = 4$ vol%; red: $c = 7.8$ vol% and blue: $c = 10$ vol%

The orientation parameter (OP) are used for determination of the degree of alignment of the particles, as explained in section 5.2. Using the parameter S_1 , S_2 and S_4 it is possible to determine exactly the alignment of a single phase, as shown in fig. 5.5 in Chapter 5. Additionally these values are connected to the magnetization M of the particles and their magnetic energy E_m . Typically, for calculation of OP arcs of intensity $I(\phi^B)$ at the Q position of a structural peak along \mathbf{p} are used. At low concentrations there is no clear structural peak and $Q_5 = 0.008 \text{ \AA}^{-1}$ was chosen.

The plots of nematic order parameter S_2 versus magnetic field are shown in fig. 6.5, where lines are guidelines for the eyes. Although all three order parameter were calculated, only S_2 values are shown. These values describe the trend well enough. In general S_1 and S_4 can be used to make a more precise distinction of the liquid crystalline phases. However, in this case S_1 basically followed S_2 and S_4 only showed small changes in its values. Therefore a discussion of these values was discarded.

The second order parameter S_2 shows similar behaviour for all low concentration suspensions. It starts with plateau with small inclination for $B \leq 310$ mT and decreases to $S_2 \approx 0$ at $370 \text{ mT} \leq B \leq 410$ mT. The decrease continues until it reaches a minimum at $B_6 = 900$ mT. With increasing concentration the absolute values of S_2 at $B = 180$ mT

and at $B_6 = 900$ mT grow. Also the inclination of the drop for $B > 310$ mT increases with raising concentration.

The trend described above implies that the sample at $B_1 = 180$ mT has a preferred orientation direction with $\mathbf{n} \parallel \mathbf{m}$ (see section 5.2). The primary alignment increases with the concentration of the suspension. The degree of alignment decreases somewhat, but stays almost constant with increasing B up to $B \leq 310$ mT. At $B > 310$ mT the alignment decreases more strongly until it reaches completely isotropic state. This trend of the second order parameter indicates a loss of preferred orientation in the suspension with increasing magnetic field. At $B_6 = 900$ mT the value of S_2 is highly negative and indicates a high order of orientation of the platelets with long axis perpendicular to the field. This was also observed in the scattering pattern itself.

However, e.g. the scattering pattern at $B_5 = 410$ mT for 10 vol% shows clearly two preferred directions of orientation with $\mathbf{p}_1 \perp \mathbf{m}$ and $\mathbf{p}_2 \parallel \mathbf{m}$. This is also true for the pattern at $B_4 = 370$ mT. This suggests that the simple OP analysis is not sufficient to identify the phases for these cases exactly. The OP analysis shows only the main preferred orientation direction. However, it can not distinguish the cases, where two or more preferred orientations, are present.

To clarify this, new parameters - the ellipticities E_{perp} and E_{dia} are introduced and evaluated. They are defined as:

$$E_{perp} = I_{para}/I_{perp} - 1, \quad (6.1) \quad E_{dia} = I_{para}/I_{dia} - 1. \quad (6.2)$$

Here I_{perp} , I_{para} and I_{dia} are the intensity values taken respective perpendicular, parallel or diagonal to the magnetic field at specified Q , as indicated in fig. 6.6. For E_{perp} and E_{dia} the subscripts are assigned according to the value in the denominator of the respective definition. In order to measure the according values of the intensities, three linecuts were made through SAXS patterns for each concentration and field strength - in the direction perpendicular to the applied magnetic field, parallel to it and at the angle of 45° (diagonal) to it. This is illustrated in fig. 6.6 on the top left, where the white arrow on top is showing the direction of the applied magnetic field. The white arrows starting in centre of the image are showing the direction of the linecuts.

In the next step the intensities of the linecuts at two Q -positions were taken. $Q_{12} = 0.02 \text{ \AA}^{-1}$ and $Q_{17} = 0.028 \text{ \AA}^{-1}$ were chosen. In general the scattering intensity decreases with increasing Q depending on the formfactor of the particles in the suspension. It is only possible to compare the intensity in the images at different Q -values, if the proportionality of this decrease is known. If particles are asymmetric the resulting scattering pattern is asymmetric, too. In case of the ellipsoid shape of the scattering pattern the visible ellipsoid is misleading, because the intensity values at different Q values have to be scaled depending on Q . The proportionality of the intensity decrease

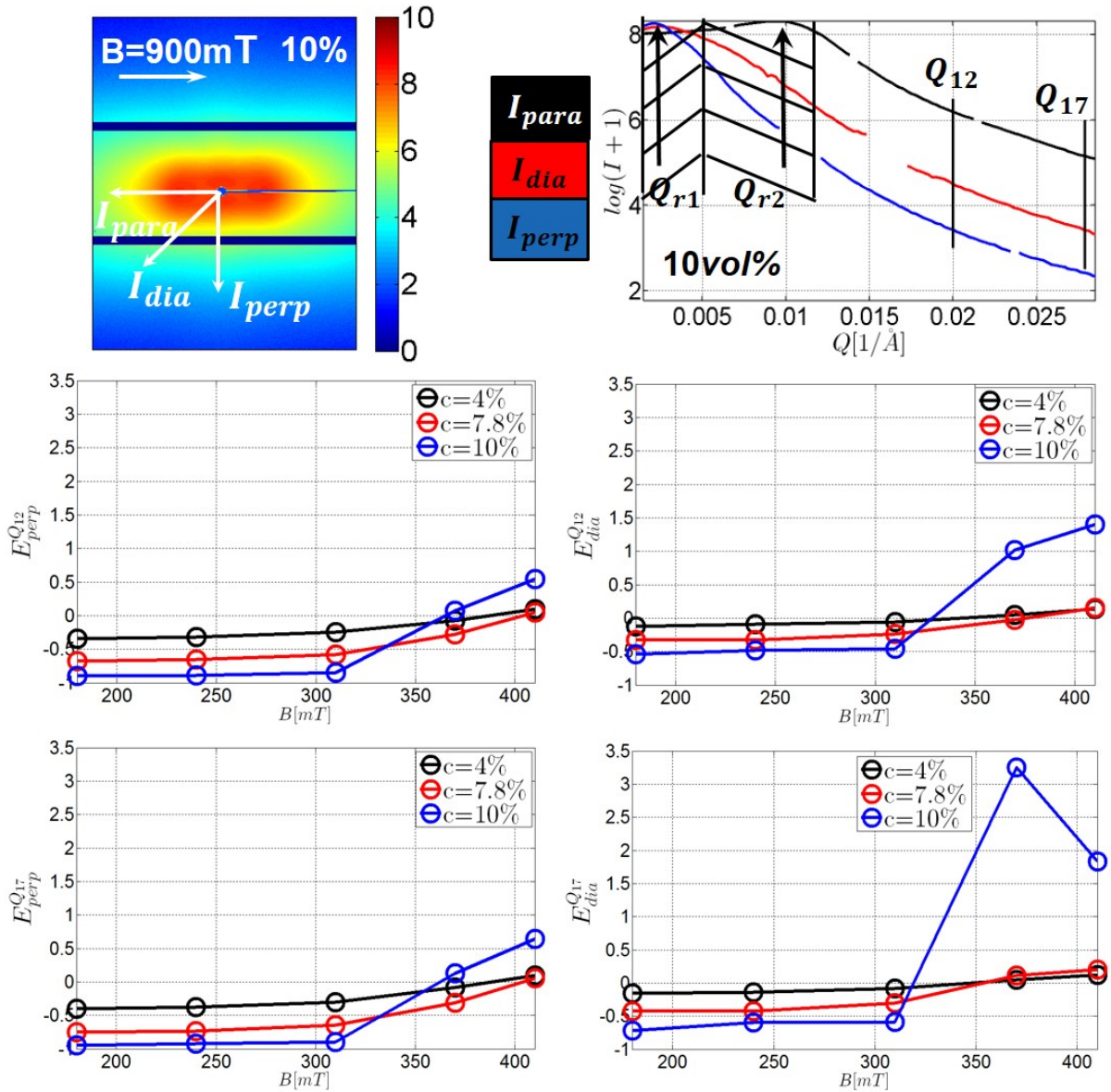


Figure 6.6.: Ellipticity for low concentrations: top row: left - an example of the SAXS pattern indicating the directions of the linecuts; right - the resulting linecuts for $c = 10\text{vol}\%$ and $B_0 = 900\text{mT}$. The structural peaks have a different position in Q depending on direction of the linecut - the peaks are falling either in Q_{r1} or in Q_{r2} region, as defined in Section 6.2. The black lines indicate Q 's chosen for calculation of the ellipticity, calculated with equations 6.1 and 6.2. Center row: left - $E_{perp}^{Q_{12}}$ versus B ; right - $E_{dia}^{Q_{12}}$ versus B . Bottom row: left - $E_{perp}^{Q_{17}}$ versus B ; right - $E_{dia}^{Q_{17}}$ versus B .

with increasing Q is difficult to determine for platelet-shaped particles, because it varies depending on axis sizes and allowed degrees of rotation. Therefore only the intensities at the same Q 's can be compared directly.

The ellipticity compares the decrease of intensity along varying directions. There are two possibilities for this particular system, which shows scattering from long and short axes:

- one phase present: $I_{para} < I_{dia} < I_{perp}$ or $I_{para} > I_{dia} > I_{perp}$
- two phases present: $I_{para} > I_{dia} < I_{perp}$ or $I_{para} < I_{dia} > I_{perp}$.

Strictly speaking in the last case one phase with preferred orientation along the diagonal direction could be present, but this option is excluded by visual examination.

The results of the ellipticity evaluation for suspensions with low concentration and at different magnetic field strengths are shown in fig. 6.6 in the centre and bottom rows. It is visible that in general the trends are very similar. In all four images at all concentrations the ellipticity starts negative at low field and turns positive at B_6 . The higher the concentration the higher the amplitude of the ellipticity. In fact the only very strong deviations are visible in the images on the right for E_{dia} at $c = 10\%$. That results from the strongly expressed cross shape. Here it is also possible to distinguish several cases:

1. if $E_{perp} < 0$ and $E_{dia} < 0$ and $E_{perp} < E_{dia}$, then $\mathbf{n} \parallel \mathbf{m}$;
2. if $E_{perp} > 0$ and $E_{dia} > 0$ and $E_{perp} > E_{dia}$, then $\mathbf{n} \perp \mathbf{m}$;
3. if $E_{perp} = E_{dia} \approx 0$, then the platelets in the suspension are randomly oriented;
4. if the obtained values deviate from these three conditions, then a mix of preferred orientation directions is present.

The shape of scattering pattern suggests that at 10 vol% and $B_4 = 370$ mT as well as at $B_5 = 410$ mT a mix of the preferred orientations parallel and perpendicular to the field is present. At $B < 370$ mT the particles in the suspension are oriented with long axis parallel to the field ($\mathbf{n} \parallel \mathbf{m}$) and the first set of conditions is true at both evaluated Q 's. For $B_4 = 370$ mT and $B_5 = 410$ mT both values are positive, but $E_{perp} < E_{dia}$, which fulfils the fourth condition and indicates the mixture of the orientations.

The case that two preferred alignment directions for the 10 vol%-suspension are present, leads to the suspicion that the 4 vol%- and 7.8 vol%-suspensions at $B_4 = 370$ mT and $B_5 = 410$ mT could also be in a mixed state of two preferred orientations. The similar behaviour of the S_2 confirms this assumption. At $c \leq 7.8$ vol% and $B < 370$ mT the first condition is valid. At $B_4 = 370$ mT for $c = 4$ vol% $E_{perp} < 0 < E_{dia}$ at both chosen Q 's, whereas for $c = 7.8$ vol% we find $E_{perp}^{Q_{12}} = E_{dia}^{Q_{12}} < 0$, but $E_{perp}^{Q_{17}} < 0$ and $E_{dia}^{Q_{17}} > 0$. This indicates that two orientations are present - parallel ($\mathbf{n} \parallel \mathbf{m}$) and perpendicular ($\mathbf{n} \perp \mathbf{m}$) to the field with the first one slightly dominant. At $B = 410$ mT at both concentrations $E_{dia}^{Q_{12}} > E_{perp}^{Q_{12}} > 0$ and $E_{dia}^{Q_{17}} > E_{perp}^{Q_{17}} > 0$, which indicates a mix of the orientations parallel and perpendicular to the field with small dominance of the perpendicular orientation ($\mathbf{n} \perp \mathbf{m}$).

For determination of a liquid crystalline phase the degree of alignment and the corresponding positions of structure peaks are distinguishing features of different phases, as shown in simulated scattering patterns in fig. 4.6 and 4.7 in Chapter 4. The

preferred partial orientation in the low concentration suspensions was estimated by the orientation parameter analysis. The ellipticity showed that at $370\text{ mT} \leq B \leq 410\text{ mT}$ a mix of preferred partial orientations is present. To identify the phases in these cases, an analysis of presence and position of structure peaks was conducted by investigation of selected linecuts through the scattering images.

In fig. 6.6 on top right, linecuts of the SAXS patterns at $c = 10\text{ vol\%}$ and $B = 900\text{ mT}$ are shown, which are representative for all curves at low concentrations. The positions of structural peaks in the linecuts are documented in Appendix B.

The detailed analysis of the structural peak positions and widths, as listed in Appendix B, showed that in all directions for the suspension with $c = 4\text{ vol\%}$ at $B \leq 410\text{ mT}$ there is only one structural peak, which is located in Q_{r1} -region ($Q_{r1} \leq 0.005\text{ \AA}^{-1}$), as defined in Section 6.2). This is illustrated by the blue curve in the fig. 6.6 on top right. The peak position close to beamstop creates difficulties, since it is not clear, if the intensity drop is real or because of the beamstop. Additionally it is more complicated to define the width of the peak. The evaluation of the structural peaks close to beamstop was done bearing these facts in mind. For $c = 7.8\text{ vol\%}$ and $c = 10\text{ vol\%}$ at $B \leq 410\text{ mT}$ the behaviour of the first peak is similar, only the Q values and widths change slightly.

For the suspension with $c = 7.8\text{ vol\%}$ at $B < 900\text{ mT}$ the detailed inspection of the data showed that the positions of the structural peaks are found at higher Q -values and the peaks grew wider compared to $c = 4\text{ vol\%}$ (see Appendix B). At $B_6 = 900\text{ mT}$ the single ring of structural peak split up in two: an arc in Q_{r1} -region for $\mathbf{p} \perp \mathbf{m}$ and a peak in Q_{r2} -region ($0.005\text{ \AA}^{-1} \leq Q_{r2} \leq 0.011\text{ \AA}^{-1}$) for $\mathbf{p} \parallel \mathbf{m}$. Therefore the trend stays the same, but with increasing concentration the average interparticle distances grow smaller.

The 10 vol\% -suspension shows similar behaviour to $c \leq 7.8\text{ vol\%}$ at $B < 370\text{ mT}$. The detailed investigation of data shows that at $B \geq 370\text{ mT}$ additionally to the ring of intensity in Q_{r1} -region a second peak in Q_{r2} -region for $\mathbf{p} \parallel \mathbf{m}$ appears. It is located close to $Q_6 = 0.011\text{ \AA}^{-1}$. At $B_6 = 900\text{ mT}$ the ring in Q_{r1} -region turns to an arc, which is only present for $\mathbf{p} \perp \mathbf{m}$. The presence of two peak sets - one for $\mathbf{p} \perp \mathbf{m}$ in Q_{r1} -region and another for $\mathbf{p} \parallel \mathbf{m}$ in Q_{r2} -region indicates the anti-nematic phase (AN), where the particles are oriented with long axis perpendicular to the magnetic field ($\mathbf{n} \perp \mathbf{m}$).

The combination of order parameter values and analysis of the ellipticity, as listed in Appendix A and shown in fig. 6.6, allows to conclude that the 4 vol\% -suspension is in isotropic phase independent of the strength of the applied field. Nevertheless there is a change in the preferred direction of the weak partial alignment: at $B \leq 310\text{ mT}$ the preferred orientation direction is $\mathbf{n} \parallel \mathbf{m}$. That defines a oriented isotropic phase (OI). At the highest field strength $B_6 = 900\text{ mT}$ the preferred orientation changes to $\mathbf{n} \perp \mathbf{m}$, which indicates anti-oriented isotropic phase (AOI).

Lemaire et al. called the nematic phase reoriented perpendicular to the applied magnetic field the anti-nematic phase (AN). Accordingly to this connection the realigned oriented isotropic phase is named anti-oriented isotropic phase (AOI) [41]. At $370\text{ mT} \leq B \leq 410\text{ mT}$ the positions of the structure peaks suggest oriented isotropic phase and the orientation parameter an isotropic phase (I). However, the ellipticity analysis showed that actually a mix of phases is present. There are two preferred partial orientations - parallel and perpendicular to the field present at the same time. Therefore at these field strengths a mix of the oriented isotropic and the anti-oriented isotropic phases is present in the 4 vol% - suspension.

The same conclusions are valid for 7.8 vol%-suspension. The only difference is that the final state at $B_6 = 900\text{ mT}$ is in the anti-nematic phase. Therefore it was possible for us to force a 7.8 vol%-suspension into an anti-nematic phase solely by increasing of the magnetic field strength. The 10 vol%-suspension also shows reorientation with increasing field strength. Already at $B_4 = 370\text{ mT}$ and $B_5 = 410\text{ mT}$ in the 10 vol%-suspension a mix of the phases is present. Opposite to suspensions at $c \leq 7.8\text{ vol}\%$ the presence and position of the structure peaks indicate, that it is already a mix of the OI and AN phases - which is for our knowledge the first reported mix of these phases of goethite suspension, forced in this state with applied magnetic field. The final state for 10 vol%-suspension at $B_6 = 900\text{ mT}$ is also in the AN phase.

In all low concentration suspension the average interparticle distances are large - $\bar{d} \approx 300\text{ nm}$. Because of the low concentration and long interparticle distances particles are free to move fast and probably even rotate, where two rotational movements would be allowed. Only in the anti-nematic phase (AN) the average distances parallel to the field are shorter.

6.3.1. Summary of structural analysis of low concentration suspensions

The suspensions of goethite at low concentrations $c \leq 10\text{ vol}\%$ were investigated with order parameter, ellipticity and structural peak analysis. It was found that most of the phases formed by low concentrations suspensions are isotropic. However, there are differences dependent on the magnetic field strength and concentration of the goethite in a suspension. At $B \leq 310\text{ mT}$ the platelets weakly aligned with the long axis parallel to the field and formed an oriented isotropic phase (OI). The degree of alignment was increasing with increasing magnetic field and concentration.

At $B_6 = 900\text{ mT}$ the particles partially realigned mainly with the long axis perpendicular to the magnetic field and formed anti-oriented isotropic phase (AOI). The scattering pattern of the anti-oriented isotropic phase (AOI) is shown in fig. 6.1 in

central row on the left. It is caused by partial reorientation of particles with long axis perpendicular to the field and named so in parallel with anti-nematic phase by Lemaire et al. [42]. The pattern is similar to the OI - only the long axis of the scattering patterns is turned by 90° . However, at $B_6 = 900\text{ mT}$ and $7.8\text{ vol}\% \leq c \leq 10\text{ vol}\%$ the phase was anti-nematic (AN). This is for our knowledge the first time a formation of anti-nematic phase from the isotropic phase, enforced through magnetic field, was documented. In addition an appearance of mixed phases is reported for first time to our knowledge. The mixed phases were observed at $370\text{ mT} \leq B \leq 410\text{ mT}$ and turned out as coexistence of oriented isotropic (OI) and anti-oriented isotropic (AOI) phases for $c \leq 7.8\text{ vol}\%$ and of oriented isotropic (OI) and anti-nematic (AN) phases for $c = 10\text{ vol}\%$. This insights lead to an update of the goethite liquid crystalline phase diagram.

6.4. High concentration suspensions

In fig. 6.7 the scattering patterns for the 16 vol%-suspension are shown. All the pattern are clearly anisotropic. At $B \leq 310$ mT the scattering feature has a long axis perpendicular to the direction of the applied magnetic field ($\mathbf{p} \perp \mathbf{m}$). It indicates that the platelets have a preferred orientation direction with the long axis parallel to the magnetic field ($\mathbf{n} \parallel \mathbf{m}$). In all three images the detailed examination of data reveals three sets of peaks - two for $\mathbf{p} \perp \mathbf{m}$ in the Q_{r3} -region ($0.011 \text{ \AA}^{-1} \leq Q_{r3} \leq 0.016 \text{ \AA}^{-1}$) and in the Q_{r2} -region, respectively, and an arc for $\mathbf{p} \parallel \mathbf{m}$ in the Q_{r1} -region.

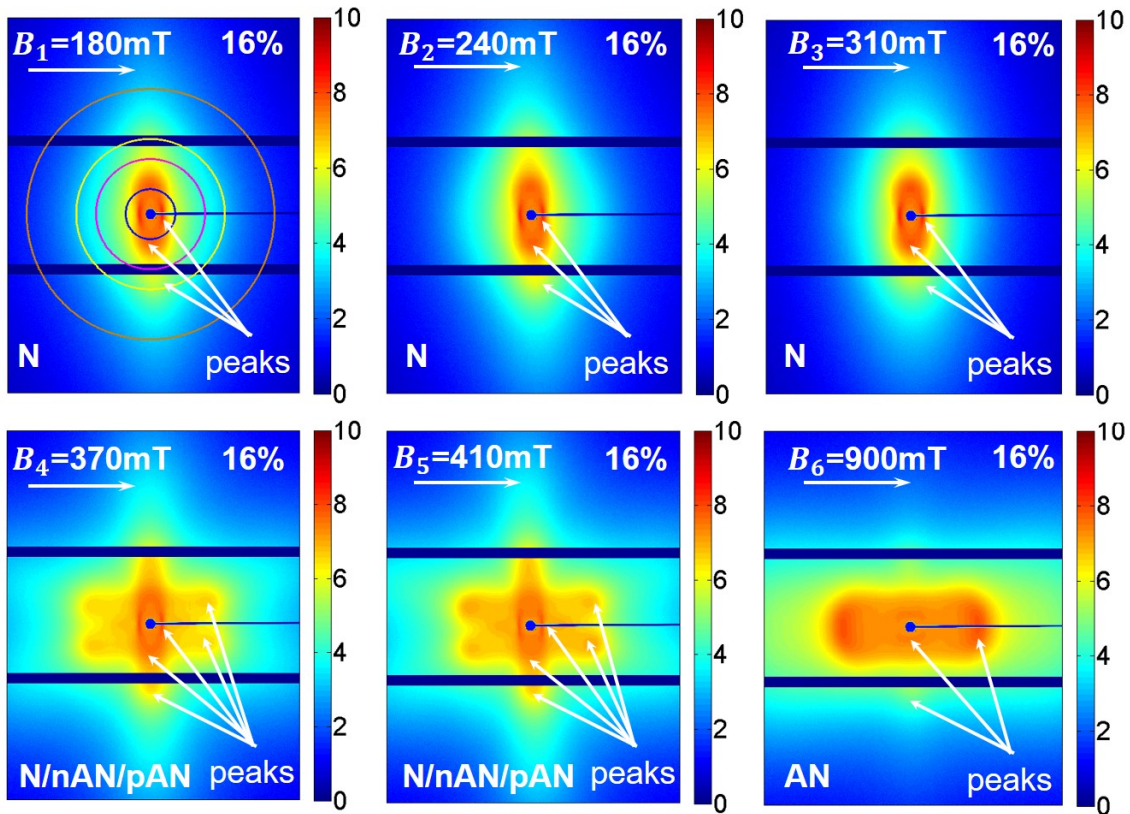


Figure 6.7.: The scattering patterns from 16 vol%-suspension at different magnetic field strength

The arcs in Q_{r1} -region parallel to the field and two structural peaks in Q_{r2} - and Q_{r3} -regions imply a nematic phase (N) with presmectic order, but this has to be confirmed. The detailed analysis shows only two sets of structural peaks at $B_6 = 900$ mT - a weaker arc in Q_{r1} -region for $\mathbf{p} \perp \mathbf{m}$ and a stronger one in Q_{r3} -region for $\mathbf{p} \parallel \mathbf{m}$. These two structural peaks imply a anti-nematic phase (AN), which means, that the particles turned with long axis perpendicular to the applied magnetic field ($\mathbf{n} \perp \mathbf{m}$). The structural peaks grew wider in ϕ^B , compared to the peaks in the nematic phase.

The two images, left and centre of the bottom row, are similar, but show a more complex pattern. After a detailed investigation three features can be recognized. The first one, perpendicular to the field ($\mathbf{p} \perp \mathbf{m}$), seems to be similar to the feature at $B \leq 310$ mT.

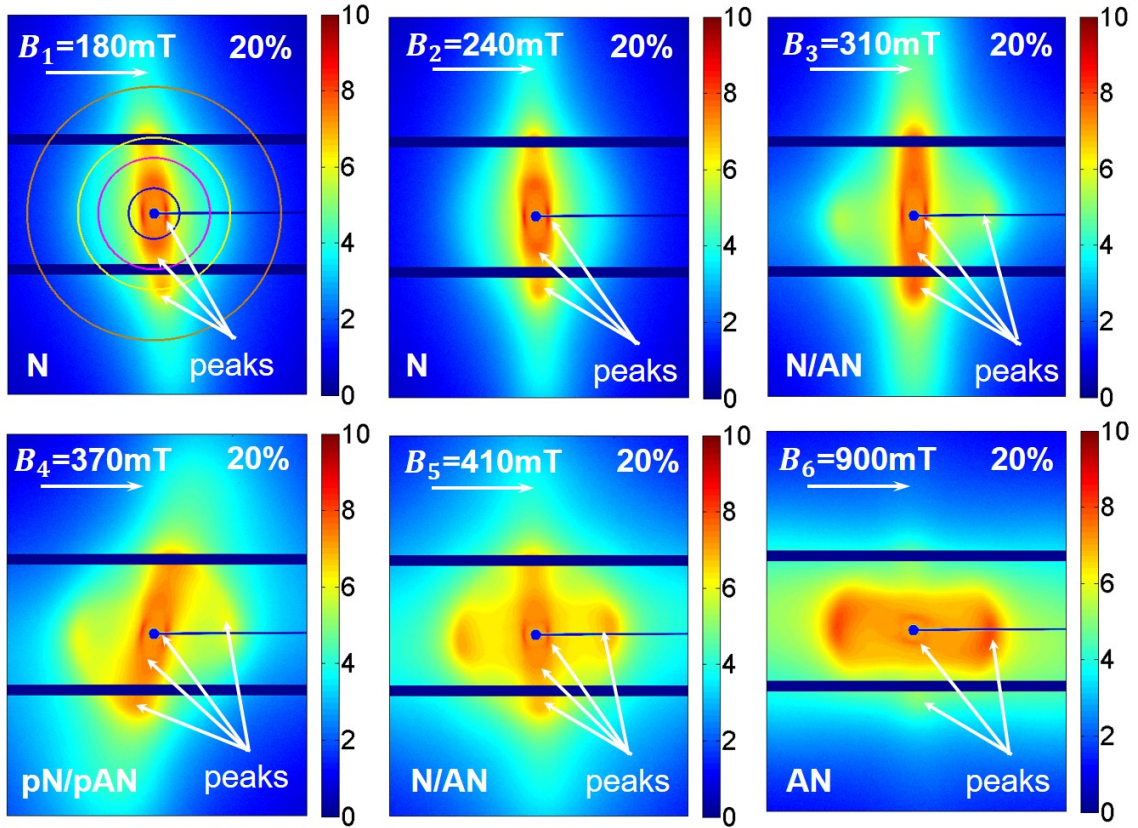


Figure 6.8.: The scattering patterns from 20 vol%-suspension at different magnetic field strength

Another two features are positioned at finite angles at $\phi^B \approx \pm 19^\circ$ respective the direction of the applied magnetic field. The feature perpendicular to the field shows also three sets of structural peaks - as the features at $B \leq 310$ mT, which also would imply a nematic phase with presmectic order. Both scattering features at finite angle seem to have two sets of structural peaks - one in Q_{r1} -region perpendicular to the long axis of the scattering pattern and one in Q_{r3} -region parallel to long axis of scattering feature. The position of the structural peaks and orientation of the scattering features suggest two not complete anti-nematic phases AN at finite angle.

In fig. 6.8 the scattering patterns for the 20 vol%-suspension are shown. Again at $B < 310$ mT the scattering feature has an long axis $\mathbf{p} \perp \mathbf{m}$ and indicates that the platelets are aligned parallel to the magnetic field ($\mathbf{n} \parallel \mathbf{m}$).

At $B_3 = 310$ mT two phases can be observed. A detailed examination showed that a weaker feature in Q_{r3} -region for $\mathbf{p} \parallel \mathbf{m}$ appeared. It indicates that some platelets already turned with long axis perpendicular to the applied magnetic field ($\mathbf{n} \parallel \mathbf{m}$). Together with the position of the scattering feature they suggest the anti-nematic phase (AN). The main feature remained in Q_{r3} -region with $\mathbf{p} \perp \mathbf{m}$. Three sets of structural peaks are visible - two in Q_{r3} - and Q_{r2} -regions for $\mathbf{p} \perp \mathbf{m}$ and one in Q_{r1} -region for $\mathbf{p} \parallel \mathbf{m}$. They imply, that the particles are still mainly aligned parallel to the field ($\mathbf{n} \parallel \mathbf{m}$), and indicate a

nematic phase N with presmectic order. A similar feature distribution was discovered at $B_5 = 410\text{mT}$ upon detailed analysis of the scattering patterns. However, the supposedly anti-nematic feature is stronger and nematic one is weaker.

At $B_6 = 900\text{mT}$ the detailed analysis found the main feature in Q_{r3} -region with $p\parallel m$, which suggests, that the particles are turned with long axis perpendicular to the applied magnetic field ($n\perp m$). Two sets of structural peaks are clearly visible - in Q_{r1} -region with $p\perp m$ and in Q_{r3} -region with $p\parallel m$. These structural peaks are much wider in ϕ^B and Q than the structural peaks in the patterns at $B \leq 310\text{mT}$. Together with the position of the scattering feature they imply the anti-nematic phase (AN). There is a possible small leftover part of the feature in the direction $p\perp m$ in Q_{r3} -region.

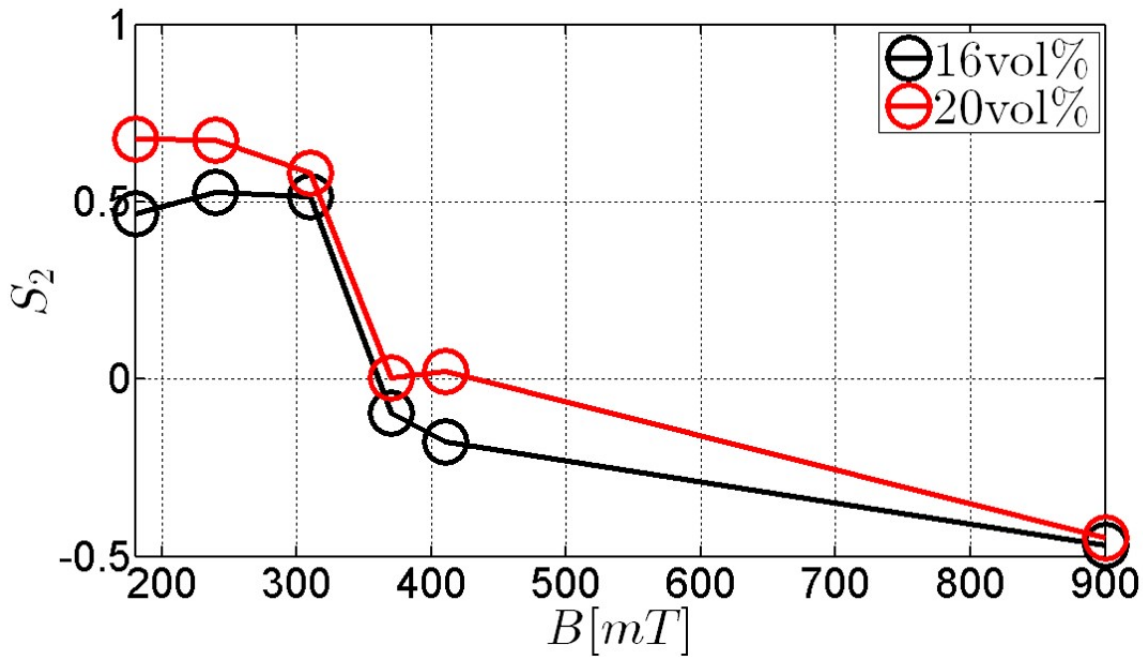


Figure 6.9.: Nematic order parameter S_2 versus magnetic field strength B . Black: for $c = 16\text{vol}\%$; red: for $c = 20\text{vol}\%$. Lines are guidelines for eyes

The image at $B_4 = 370\text{mT}$ shows a patterns similar to the image for $B_3 = 310\text{mT}$. Only both features are turned at some finite angle. Similar to the analysis of the low concentration suspensions, the orientation parameter (OP) analysis was performed. It allows to define the degree of alignment of the particles in the suspension. The nematic order parameter S_2 for the suspensions with $c = 16\text{vol}\%$ (black) and $c = 20\text{vol}\%$ (red) are shown in fig. 6.9. For calculation of the orientation distribution function (ODF) and the order parameter (OP) the intensity arcs $I(\phi^B)$ at the Q of the structure peaks were used. For 16 vol%-suspension it was $Q = 0.013\text{\AA}^{-1}$ and for 20 vol% it was $Q = 0.014\text{\AA}^{-1}$.

The first conclusions derived from the scattering patterns can be partly confirmed with OP. Again there are high S_2 values at $B_1 = 180\text{mT}$ with a plateau for $B \leq 310\text{mT}$ and a sudden drop at $B > 310\text{mT}$. S_2 is close to zero at $B_4 = 370\text{mT}$ for both high

concentrations and additionally at $B_5 = 410$ mT for $c = 20$ vol%. This implies an original alignment of particles with long axis parallel to the field, which vanishes with increasing field strength. In the end a high degree of alignment with long axis perpendicular to the field is achieved, which correspond with negative values of S_2 with high magnitude at $B_6 = 900$ mT for both high concentrations.

To exactly clarify the appearance and position of the phases, intensity linecuts were taken in all SAXS pattern, as already explained for low concentrations. In fig. 6.10 linecuts from the SAXS patterns of the suspensions with $c = 16$ vol% and $c = 20$ vol% are shown. The cuts were made at $\phi^B = 0^\circ$ and $\phi^B = 90^\circ$. The top row shows the linecuts for suspension with $c = 16$ vol%, the bottom row the cuts for $c = 20$ vol%, where on the left the cuts at $\phi^B = 0^\circ$ and at the right the cuts at $\phi^B = 90^\circ$ are shown. As already mentioned in the introduction the magnetic field strengths are indicated in all plots with symbols B_1, B_2, B_3, B_4, B_5 and B_6 . In lineplots throughout this Chapter the magnetic field strengths are indicated with colours and indications as shown in table 6.3. A higher value of the index indicates a larger magnetic field.

Table 6.3.: The line and symbol colours used for different magnetic field strengths. In the images the colourbar shows the according B values, which will be always the same in the whole thesis.

Color	green	cyan	magenta	orange	brown	pink
B Number	B_1	B_2	B_3	B_4	B_5	B_6
B	180 mT	240 mT	310 mT	370 mT	410 mT	900 mT

For both concentrations and at all field strengths there is a structure peak for $p \parallel m$ in Q_{r1} -region, as shown images on the left of fig. 6.10. Here the values Q_{r1}, Q_{r2} and Q_{r3} define the region of the position of the structural peaks with $Q_{r1} < 0.005 \text{ \AA}^{-1}$, $0.005 \text{ \AA}^{-1} \leq Q_{r2} \leq 0.011 \text{ \AA}^{-1}$ and $0.011 \text{ \AA}^{-1} \leq Q_{r3} \leq 0.016 \text{ \AA}^{-1}$, as stated before. The peak in Q_{r1} -region gets weaker with increasing magnetic field until it almost vanishes at $B_6 = 900$ mT. At $B \geq 310$ mT for both high concentrations a peak in Q_{r3} -region for $p \parallel m$ appears.

In the linecuts in the direction $p \perp m$ (fig. 6.10 right) there are two strong pronounced structural peaks visible at $B \leq 240$ mT. These structural peaks are positioned in Q_{r2} - and Q_{r3} -regions. The peak in Q_{r2} -region decreases with increasing magnetic field. The peak in Q_{r3} -region increases for $B = 310$ mT and decreases for $B > 310$ mT. With increasing field a third peak in Q_{r1} -region for $p \perp m$ appears.

The linecuts confirm the assignment of phases. The particles are strongly aligned at high concentrations and $B \leq 240$ mT. In addition the linecuts verify that there is a peak parallel to the applied magnetic field and two structural peaks perpendicular to it at these strengths of magnetic field, which points to a nematic phase with presmectic

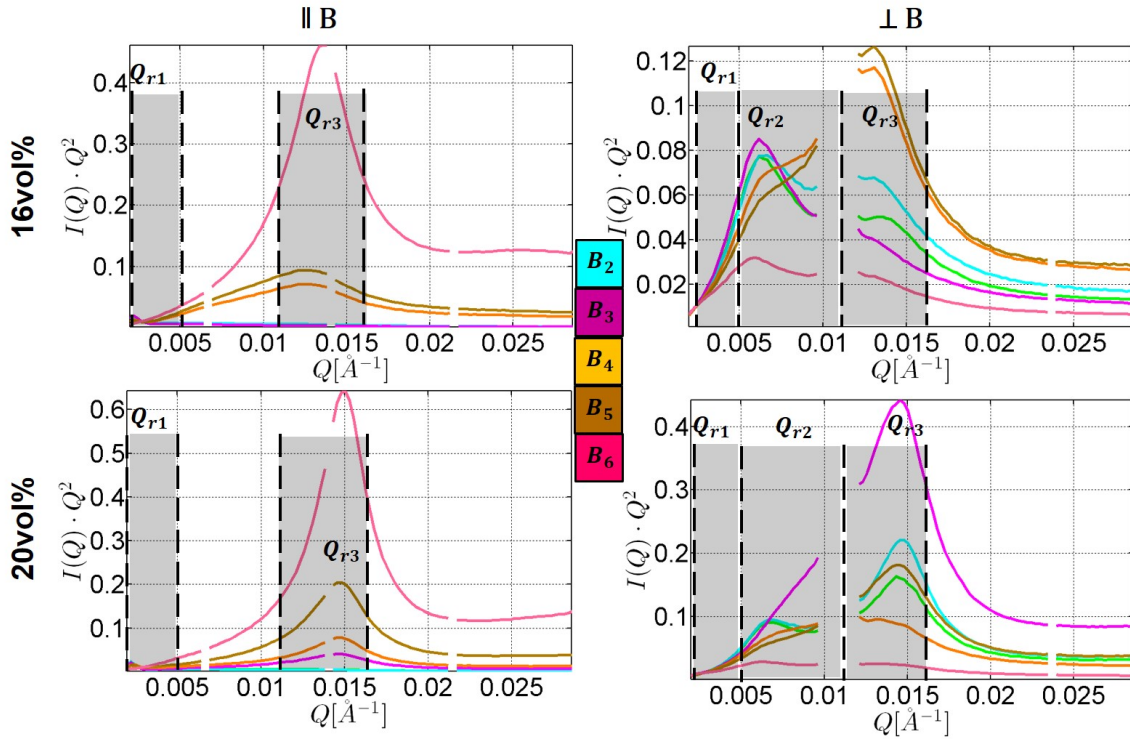


Figure 6.10.: Plots of $I \cdot Q^2$ versus Q at varying B . Top row: for $c = 16$ vol%; left - parallel to the field, right - perpendicular to the field. Bottom row: for $c = 20$ vol%; left - parallel to the field, right - perpendicular to the field.

order [33]. The structural peaks in Q_{r1} -region arise from the interparticle distances along the length of the particles, the structural peaks in Q_{r2} - and Q_{r3} -regions from the interparticle lengths along their width. The peak in Q_{r2} -region vanishes first, which means that the presmectic order is destroyed.

The peak in Q_{r3} -region decreases, because of partial reorientation of the particles with long axis perpendicular to the field ($\mathbf{n} \perp \mathbf{m}$), too. The change of the peak position in ϕ^B confirms the change from the nematic phase to the anti-nematic phase at $B_6 = 900$ mT. However, there are structural peaks in Q_{r1} for $\mathbf{p} \perp \mathbf{m}$ and in Q_{r3} for $\mathbf{p} \parallel \mathbf{m}$. The presence of the weak structural peaks, which were connected to the nematic phase, implies that nematic phase did not vanish completely.

For $310 \text{ mT} \leq B \leq 410 \text{ mT}$ it is apparent that a mix of both phases is present for $c = 20$ vol%. At $B_4 = 370$ mT the phases are at finite angle to the B-field. Therefore at this field strength the phases are called positive nematic (pN) and positive anti-nematic (pAN) phases, where positive direction is the direction of the nematic orientation direction \mathbf{n} , if it turned clockwise respective to the direction of the magnetic field. For $c = 16$ vol% at $B_3 = 310$ mT still a pure nematic phase is present, which realigns then at $370 \text{ mT} \leq B \leq 410 \text{ mT}$ in two directions in positive anti-nematic (pAN) and negative anti-nematic (nAN) phases.

6.4.1. Summary of structural analysis of high concentration suspensions

The order parameter and structure peak analysis distinguished nematic phases at high concentrations $c \geq 16$ vol%. Two phases were observed: the nematic phase (N) and the anti-nematic phase (AN). These phases can be identified by a long range order, which result in two sets of peaks: one set in Q_{r1} -region and perpendicular to it a second set in Q_{r3} -region. The nematic phase was observed at low field $B \leq 310$ mT and the anti-nematic at $B_6 = 900$ mT. At $370 \text{ mT} \leq B \leq 410 \text{ mT}$ mixed phases were observed.

The right image in the central row and both images in the bottom row in fig. 6.1 show examples of scattering patterns from the the nematic phases observed in the experiments. On the left the scattering pattern of the nematic phase (N) aligned in a weak magnetic field is shown. It can be distinguished by a very sharp scattering pattern with long scattering axis perpendicular to the applied field, structure factor peak in long scattering direction and structure factor arcs in short scattering direction (see centre 6.1), obtained by the structural peak analysis and high values of order parameters (see Appendix B). This phase is caused by partial orientation of the particles with long axis parallel to the field.

At high magnetic fields the goethite platelets in the nematic phase reorient perpendicular to the field and form the anti-nematic phase (AN) [42]. It has the long scattering axis parallel to the applied magnetic field and in general the same structural peaks as the nematic phase only turned by $\phi^B = 90^\circ$. The structural peaks in the long scattering direction are much wider in ϕ^B , as documented in table 6.4. Its pattern is shown in the 6.1 on the bottom on the right. At intermediate field strengths $370 \text{ mT} \leq B \leq 410 \text{ mT}$ the mixed phases, arising from the overlapp of the nematic and anti-nematic phases, were observed.

6.5. Magnetic energy of the suspension

The magnetic energy E_m as defined in eq. 5.34 depends on the orientation parameters and explains the behaviour of goethite particles for increasing magnetic field strength. If the applied magnetic field is $B < 200$ mT then the dipolar term of E_m is dominant and the particles tend to align with the long axis parallel to the field ($\mathbf{n} \parallel \mathbf{m}$). S_2 grows constantly until it reaches high values around $S_2 \approx 0.95$. For high field $B > 350$ mT the quadrupolar (induced magnetization) term of E_m is dominant and the particles realign with the long axis perpendicular to the field ($\mathbf{n} \perp \mathbf{m}$). S_2 is decreasing and switching at some point to negative values. If the field is sufficiently high then it will reach values of $S_2 \approx -0.5$.

Theoretical calculations showed that for monodisperse particles no nematic-nematic phase separation can occur [72]. However, experimentally van den Pol et al. showed that a larger polydispersity of the system strengthens a N-N phase separation [69]. Platelets of different sizes have different magnetic energy.

In fig. 6.11 the magnetic energy E_m for the suspensions of particles with length $l_1 = 219$ nm with $c = 16$ vol% (left) and $c = 20$ vol% (right) for different magnetic fields versus different angles ϕ^B respective to the applied field is shown [41, 42]. E_m was calculated using eq. 5.34 from Chapter 5 using the order parameter P_1 and P_2 .

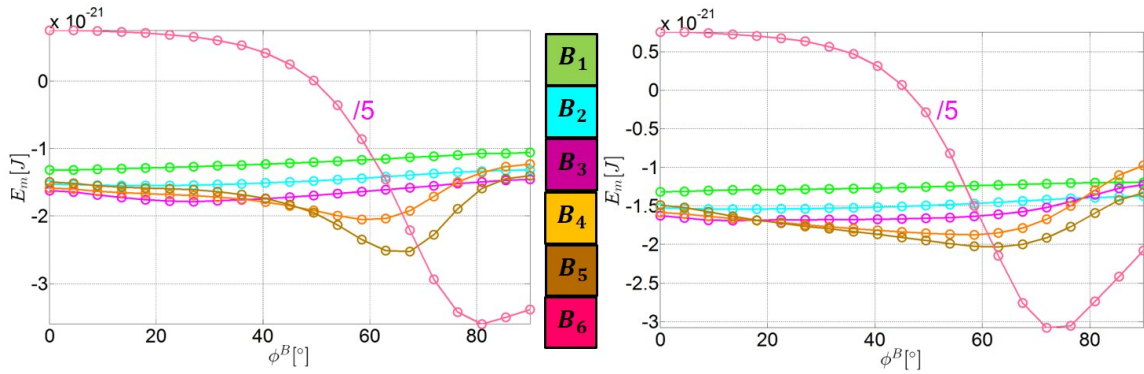


Figure 6.11.: Magnetic energy E_m of long particles with $l_1 = 219$ nm versus ϕ^B . Left: for $c = 16$ vol%; right: for $c = 20$ vol%. The magnetic energy for $B_6 = 900$ mT is divided by 5 to ensure better comparability of the curves. The colours represent the magnetic fields as previously explained.

Fig. 6.11 illustrates a shift of the minimum of the magnetic energy E_m with increasing amplitude of magnetic field B . For both concentrations the energy minimum shows a similar behaviour. It is roughly at $\phi^B = 0^\circ$ for $B \leq 240$ mT. At $B_3 = 310$ mT it shifts to $\phi^B \approx 20^\circ$. With increasing magnetic field strength the minimum shifts to higher ϕ^B values and reaches $\phi^B \approx 80^\circ$ at $B_6 = 900$ mT. It is apparent that with growing strength of magnetic field the minimum in the magnetic energy shifts from $\phi^B \approx 0^\circ$ to

$\phi^B \approx 80^\circ$. If only one length of the particles could be considered, then the particles would be mostly oriented with long axis parallel to the field ($\mathbf{n} \parallel \mathbf{m}$) at $B \leq 310$ mT, than turn with a very broad angle distribution approximately to $\phi^B \approx 40^\circ$ at $370 \text{ mT} \leq B \leq 410 \text{ mT}$ and at last realign mostly perpendicular to the applied magnetic field ($\mathbf{n} \perp \mathbf{m}$), due to average between realignment at $\phi^B \approx \pm 80^\circ$, which are equally allowed.

However, goethite particles are very polydisperse and therefore different sizes of the particles have to be considered. To illustrate the influence of the size on the magnetic energy E_m the later was recalculated using $l_2 = 146$ nm, which is the smaller average size from the counted size distribution, calculated in Chapter 4. The magnetic energy E_m plotted versus angle ϕ^B for different magnetic field strengths is shown in fig. 6.12.

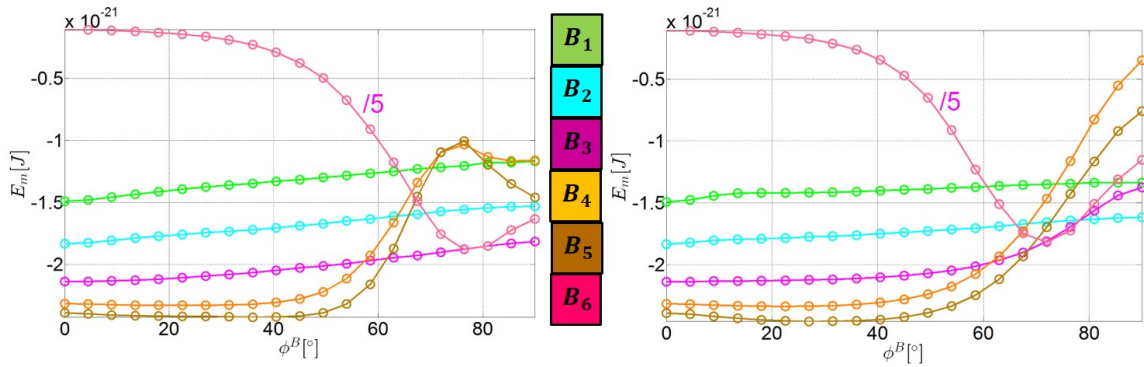


Figure 6.12.: Magnetic energy E_m of short particles with $l_2 = 146$ nm versus ϕ^B . Left: for $c = 16$ vol%; right: for $c = 20$ vol%. The magnetic energy for $B_6 = 900$ mT is divided by 5 to ensure better comparability of the curves. The colours represent the magnetic fields as previously explained.

For the short particles at $B \leq 240$ mT the minimum of the magnetic energy E_m is at $\phi^B \approx 0^\circ$, too. At $B_3 = 310$ mT the minimum is still at $\phi^B \approx 0^\circ$, but the steepness of the curve is lower. The minima of the energy shift at $370 \text{ mT} \leq B \leq 410 \text{ mT}$ to $\phi^B \approx 40^\circ$. For both concentrations at $B_6 = 900$ mT the magnetic energy E_m reaches the minimum at $\phi^B \approx 75^\circ$.

From the comparison of images 6.11 and 6.12 it is apparent that the minima of the magnetic energy are size dependent - for the small particles the second term of eq. 5.34 is lower, because the induced magnetization in smaller particles is lower. Therefore they tend to realign at higher magnetic fields.

The comparison between the curves shows strong correspondence between the minimum position of E_m at ϕ^B and the position and width of the structural peaks of the SAXS patterns. Before analysing the values it is important to recall that a minimum in E_m corresponds with a favourable orientation angle θ of the platelet's long axis in real space respective to the direction of the applied magnetic field.

The structural peaks for the high concentration suspensions are found in Q_{r1} -, Q_{r2} - and Q_{r3} -region. The increasing of the concentration in the suspension leads to

B[mT]	Phase 16 vol%	0.0131 Å ⁻¹		Phase 20 vol%	0.0141 Å ⁻¹	
		ϕ^B [°]	FWHM [°]		ϕ^B [°]	FWHM [°]
180	N	≈ 90	42	N	≈ 90	25
240	N	≈ 90	42	N	≈ 90	23
310	N	≈ 90	59	N	≈ 90	23
310	–	–	–	AN	≈ 0	44
370	N	≈ 90	32	pN	74	38
370	pAN	26	39	pAN	10	65
370	nAN	–29	39	–	–	–
410	N	≈ 90	28	N	≈ 90	34
410	pAN	18	37	AN	≈ 0	47
410	nAN	–20	36	–	–	–
900	AN	≈ 0	64	AN	≈ 0	53
900	N	≈ 90	22	N	100	45

Table 6.4.: Angle and azimuthal FWHM of the scattering structural peaks in ϕ^B depending on the strength of the applied magnetic field for high concentration suspensions

shorter interparticle distances and therefore higher Q values for structural peaks at $c = 20$ vol%. For both concentrations the peak in Q_{r2} -region is present only for pure nematic phase at $\phi_p^B \approx 90^\circ$ ($\mathbf{p} \perp \mathbf{m}$), where subscript p indicates angle of the long axis of the scattering pattern. For $c = 20$ vol% this peak is narrower and is also present for pN phase at $B_4 = 370$ mT, where it is shifted to $\phi_p^B \approx 80^\circ$.

The values of E_m indicate that short particles would prefer an orientation $\mathbf{n} \parallel \mathbf{m}$ for $B \leq 310$ mT. For the long particles the minimum shifts from $\phi_m^B = 0^\circ$ to $\phi_m^B = 27^\circ$, where subscript m indicates the angle between the preferred orientation direction of the long axis of the particles \mathbf{n} and the magnetic field. The shift of the minimum of the magnetic energy E_m for long particles corresponds with the observation that the structural peaks for both Q 's are located at $\phi_p^B = 90^\circ$ ($\mathbf{p} \perp \mathbf{m}$), but the width of the structural peaks grows.

The peak in Q_{r3} -region indicates nematic order and is still present at $B_4 = 370$ mT at $\mathbf{p} \perp \mathbf{m}$, but gets much narrower, because two more preferred orientation directions are present. These two directions at $\phi_p^B \approx \pm 30^\circ$ correspond very well with the minimum of E_m at $\phi_m^B \approx 60^\circ$ for long particles. The long axis of particle would try to achieve a position, which correlates with the angle of the minimum of E_m . Therefore a scattering feature in Q_{r3} would arise from short axis at the angle occupied by the long axis $\pm 90^\circ$ ($\phi_p^B = \phi_m^B \pm 90^\circ$). As there is only the peak in Q_{r3} -region present, only nematic order exists in these directions and a presmectic order vanished. The appearance of two directions can be explained through the nonexistence of the preferred direction for realignment of the particles. In the direction at $\mathbf{p} \perp \mathbf{m}$ two structural peaks are still present, but the one in the Q_{r2} -region is much wider compared to $B \leq 310$ mT. The

direction at $\mathbf{p} \perp \mathbf{m}$ ($\mathbf{n} \parallel \mathbf{m}$) does not correlate with energy minima, but could be preferred due it is a direction predefined through the original alignment direction of nematic phase.

At $B_5 = 410$ mT three preferred directions are still present likely due to the same reasons as at $B_4 = 370$ mT. Two features at $\phi_p^B \approx \pm 30^\circ$ for $B_4 = 370$ mT now shifted to $\phi_p^B \approx \pm 20^\circ$. They corresponds with the shift of the energy minimum for long particles at $\phi_m^B \approx 75^\circ$. Additionally, the original peak in Q_{r2} -region widened again.

At $B_6 = 900$ mT the two reorienting directions merge to one wide peak with centre at $\phi_p^B \approx 0^\circ$ ($\mathbf{p} \parallel \mathbf{m}$) and large FWHM. The position and the width of the peak correspond to the shift of the minimum of E_m to $\phi_m^B \approx 80^\circ$. The coexistence of the different preferred directions causes the broad width of the peak. Only one of the original structural peaks at $\phi_p^B \approx 90^\circ$ and in the Q_{r3} -region is still present. It is weak, which indicates that smectic preorder vanished and nematic phase almost disappeared.

The same analysis was done for the 20 vol%-suspension. Remarkably at $B_3 = 310$ mT a weak scattering feature at $\phi_p^B \approx 0^\circ$ ($\mathbf{p} \parallel \mathbf{m}$) arises, which corresponds with minimum at $\phi_m^B \approx 90^\circ$ ($\mathbf{n} \perp \mathbf{m}$) for E_m . That could be explained by the realignment of the longest particles, which are even longer as l_1 . At $B_4 = 370$ mT a large part of the particles starts to realign - forming a huge arc with maxima at $\phi_p^B \approx 80^\circ$ and $\phi_p^B \approx 10^\circ$ in the Q_{r3} -region and at $\phi_p^B \approx 75^\circ$ in the Q_{r1} -region with much higher width at both Q , which probably represents the whole width of the minima in E_m for the complete distribution of the particle lengths.

At $B_5 = 410$ mT a significant amount of the particles realigned at $\phi_p^B \approx 0^\circ$ ($\mathbf{n} \perp \mathbf{m}$), while another part remained roughly at $\phi_p^B \approx 90^\circ$ ($\mathbf{n} \parallel \mathbf{m}$) in presmectic order. The position of the peak at $\phi_p^B \approx 0^\circ$ does not fit to the minimum of E_m at $\phi_m^B \approx 60^\circ$. The platelets partially realigned back into the original nematic state, which could be forced by the excluded volume of two partially aligned phases in coexistence [69]. At $B_6 = 900$ mT a strong peak is present at $\phi_p^B \approx 0^\circ$ ($\mathbf{p} \parallel \mathbf{m}$) with maximum in the Q_{r3} -region, which corresponds to the minimum of E_m for both particle lengths at $\phi_m^B \approx 70^\circ$, if we take the width of the peak in account. Only a weak peak is left in the original direction of $\phi_p^B \approx 90^\circ$, which is also present only in the Q_{r3} -region and indicates therefore that the presmectic order is completely gone. Because of the higher concentration and therefore closer packing the particles show complexer behaviour in the 20 vol%-suspension. This is probably caused by the enforcement of the collective realignment, which is less present in the 16 vol%-suspension.

The magnetic energies for the particle sizes used above were also calculated for low concentration samples. The behaviour dependent on the chosen size of the particles and magnetic field strength is similar to the behaviour at high concentrations.

The short particles favour demixing, which causes a larger width of the curves in polydisperse suspensions [69]. The angles of the structural peaks of low concentration suspensions are $\phi_p^B \approx 0^\circ$ and $\phi_p^B \approx 90^\circ$. The angle $\phi_p^B \approx 0^\circ$ is valid for all low concentrations at $B \leq 310$ mT and for $c \leq 7.8$ vol% at $B \leq 370$ mT. The angle $\phi_p^B \approx 90^\circ$ can only be observed for $B_6 = 900$ mT. For $B \leq 410$ mT at low concentrations and for $c = 10$ vol% at $B_4 = 370$ mT both angles are present.

For low field strength the minimum of E_m is at $\phi_m^B \approx 0^\circ$. With increasing field strength the minimum gets lower. Therefore the partial alignment gets stronger and the OI phase is more defined. At highest field strength the minimum is close to $\phi_m^B \approx 90^\circ$, which causes all suspensions to realign to some extent at this angle and forces the suspensions into the AN phase for $c \geq 7.8$ vol% and in the AOI phase for $c = 4$ vol%. All directions are present, but higher amount of the particles align - forced through the partial alignment of the neighbours - in either of the direction, causing the two angles to be preferential directions.

At the intermediate field strengths $370 \text{ mT} \leq B \leq 410 \text{ mT}$ both phases are present. For $c \leq 7.8$ vol% the orientation of the particles is random, with slightly preferred directions at $\phi_m^B \approx 0^\circ$ and $\phi_m^B \approx 90^\circ$, which was determined by ellipticity analysis. At $c = 10$ vol% the preference grew, but all directions are still present. It grew because of the enforcement of the alignment directions through increased concentration.

6.6. Conclusions of the structural analysis

The variety of phases, which can be induced in suspensions of goethite particles have been discussed before [3, 34, 37, 39]. The structural analysis identified two main liquid crystalline phase groups - the isotropic and nematic groups, which are distinguished by the degree of order, measured with order parameters S_1 , S_2 and S_4 . The dominant phases in the groups were the oriented isotropic (OI) and the anti-oriented isotropic (AOI) phases as well as nematic (N) and the anti-nematic (AN) phases. The transitional states between the phases were also observed as mixed phases (M). In the oriented isotropic (OI) and nematic (N) phases the particles align mostly parallel to the magnetic field B as in anti-oriented isotropic (AOI) and anti-nematic (AN) phases the preferred alignment of platelets is with the long axis perpendicular to the magnetic field. The preferred orientations of the particles can be explained by the magnetic energy E_m of the system, if polydispersity of the platelets is taken in account, as explained in Section 6.5. In fig. 6.1 the scattering patterns of the observed phases are shown. After structural analysis it is possible to exactly classify and generalize these patterns, and to derive hints for the analysis of the more complex or mixed patterns.

Low concentrations The phases from the isotropic group at low concentrations $c \leq 10$ vol% were formed by the platelets without or only with low partial alignment in a preferred direction under the influence of a magnetic field. This was confirmed the order parameter analysis. All order parameter values are listed in Appendix A. The isotropic phases could be identified by a single uninterrupted ring (ellipsoid) of peak intensity by the structural peak analysis. At $B \leq 310$ mT the platelets weakly aligned with the long axis parallel to the field and formed an oriented isotropic phase (OI). The degree of alignment was increasing with increasing magnetic field and concentration.

At $B_6 = 900$ mT the particles partially realigned mainly with the long axis perpendicular to the magnetic field and formed oriented anti-isotropic phase (AOI). At $7.8 \text{ vol\%} \leq c \leq 10 \text{ vol\%}$ the phase was anti-nematic (AN), which is for our knowledge the first time a formation of this phase from the isotropic phase was observed. Additionally, at $370 \text{ mT} \leq B \leq 410 \text{ mT}$ an coexistence of oriented isotropic (OI) and anti-oriented isotropic (AOI) phases for $c \leq 7.8 \text{ vol\%}$ and of oriented isotropic (OI) and anti-nematic (AN) phases for $c = 10 \text{ vol\%}$ were observed. These mixed phases are also reported for first time to our knowledge. In order to distinguish the mixed phases in addition to the order parameter and structural peak analysis the ellipticity analysis was performed.

In the top left fig. 6.1 an seemingly isotropic SAXS pattern is shown. An completely isotropic pattern would be induced by a random orientation of the goethite platelets in the isotropic phase (I). Nevertheless the detailed analysis of the scattering pattern shown in fig. 6.1 on top left demonstrated that it actually consists of the mixed

contribution from oriented isotropic (OI) and anti-oriented isotropic (AOI) phases. However this scattering pattern, similarly to the isotropic pattern, has no preferred direction of the scattering and only one weak structure factor peak in Q_{r1} -region can be found, which was shown by the structure peak analysis, which is documented in Appendix B.

In the top row and in central row on the left of figure 6.1 the scattering patterns from isotropic phases are represented. Nevertheless it is obvious that there are significant differences of the scattering patterns shown in the top row on the right and in the central row on the left compared to the isotropic scattering pattern in top row on the left. The scattering patterns in top row on the right of the fig. 6.1 is caused by isotropic phase partially oriented parallel to a weak magnetic field (OI). Only one interrupted structure factor in ellipsoid form in Q_{r1} -region can be found. Especially in isotropic phases even under influence of strong magnetic field the alignment is weak, the particles are fast and have translational and rotational freedom degrees of movement.

The scattering pattern of the anti-oriented isotropic phase (AOI) is shown in fig. 6.1 in central row on the left. It is caused by partial reorientation of particles with long axis perpendicular to the field and named so in parallel with anti-nematic phase by Lemaire et al. [42]. The pattern is similar to the OI - only the long axis of the scattering patterns is turned by 90° .

High concentrations At high concentrations $c \geq 16$ vol% two phases were observed: the nematic phase (N) and the anti-nematic phase (AN). These phases can be identified by a long range order, which result in two sets of peaks: one set in Q_{r1} -region and perpendicular to it a second set in Q_{r3} -region. The nematic phase was observed at low field $B \leq 310$ mT and the anti-nematic at $B_6 = 900$ mT. At 370 mT $\leq B \leq 410$ mT mixed phases were observed.

The right image in the central row and both images in the bottom row in fig. 6.1 show examples of scattering patterns from the the nematic phases observed in the experiments. On the left the scattering pattern of the nematic phase (N) aligned in a weak magnetic field is shown. It can be distinguished by a very sharp scattering pattern with long scattering axis perpendicular to the applied field, structure factor peak in long scattering direction and structure factor arcs in short scattering direction (see centre 6.1), obtained by the structural peak analysis and high values of order parameters (see Appendix B). This phase is caused by partial orientation of the particles with long axis parallel to the field.

At high magnetic fields the goethite platelets in the nematic phase reorient perpendicular to the field and form the anti-nematic phase (AN) [42]. It has the long scattering axis parallel to the applied magnetic field and in general the same structural

peaks as the nematic phase only turned by $\phi^B = 90^\circ$. The structural peaks in the long scattering direction are much wider in ϕ^B , as documented in table 6.4. Its pattern is shown in the fig. 6.1 on the bottom on the right. At intermediate field strengths $370\text{mT} \leq B \leq 410\text{mT}$ the mixed phases, arising from the overlapp of the nematic and anti-nematic phases, were observed.

General results All the observed phases were combined in a phase diagram, shown in fig. 6.13. In this figure green colour indicates the isotropic subphases and blue colour the nematic ones. Dark colour shade corresponds to measured data, while lighter shade shows the estimated outreach of the respective phase. The oriented phases correlate with vertical lines, while the anti-oriented phases are shown with horizontal lines and the areas of coexistence with combination of vertical and horizontal lines, which results in a grid.

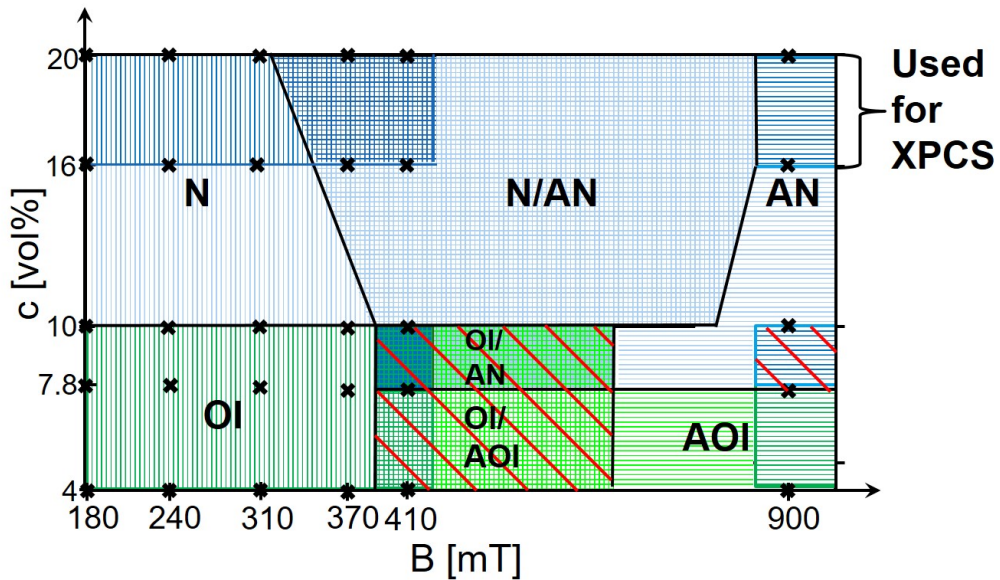


Figure 6.13.: Phase diagram of the liquid crystalline phases of goethite suspensions plotted versus magnetic field B on the bottom and concentration of the suspension c on the left. Dark colours indicate measured phases, lighter shadows of the same colour denote the estimation of the outreach of the phase. Green stands for isotropic subphases and blue for nematic ones. Black crosses show the measured points. The red diagonal lines indicate the subphases, which were reported for the first time.

7. XPCS analysis

Unusual and complex scenarios of phase transitions are observed in goethite suspensions [42]. Magnetic properties of the goethite platelets lead to several structural properties, such as forming a lyotropic nematic phase exposed to magnetic field $B < B_c$, where the particles are oriented with long axis parallel to magnetic field ($\mathbf{n} \parallel \mathbf{m}$) and a "paranematic" or anti-nematic phase, where the platelets are realigned with long axis reorienting perpendicular to the magnetic field ($\mathbf{n} \perp \mathbf{m}$), if the field exceeds a critical value B_c [38]. In this part of the thesis the behaviour of high concentration goethite suspensions ($c \geq 16 \text{ vol\%}$) is investigated by the means of XPCS. This method can reveal the microscopic particle dynamics in the nematic and anti-nematic phases. Combined with the previously known structural behaviour these data help to understand the physical properties of goethite suspensions in greater detail.

In Section 7.1 the procedure, which was used to analyse the XPCS data, is presented. Exemplary curves and extracted parameters are presented in Section 7.2. The conclusions on the microscopic dynamics for all the observed phases, based on the fitted parameters, are discussed in Section 7.3. In the last part (Section 7.4) the findings are summarized by establishing of respective qualitative models.

7.1. XPCS analysis procedure

The presented XPCS measurements aim to investigate the dynamic behaviour of goethite particles in different structural phases. The isotropic (I), oriented isotropic (OI) and anti-oriented isotropic (AOI) phases were only observed in low concentration suspensions of $c \leq 10 \text{ vol\%}$. These suspensions could not be included in the XPCS analysis since their dynamics were not accessible due to the corresponding fast time scales. Only high concentration suspensions of $c \geq 16 \text{ vol\%}$ were studied by XPCS. In fig. 6.7 and 6.8 in Chapter 6 the corresponding SAXS patterns of the nematic (N), anti-nematic (AN) and the mixed phases are shown.

Multi-tau XPCS analysis averages over many pixels inside a partition to improve the statistics of information about dynamical properties. It requires an uniform intensity distribution inside each partition to normalize the time autocorrelation function correctly. The SAXS patterns show strong radial and azimuthal intensity variations for all

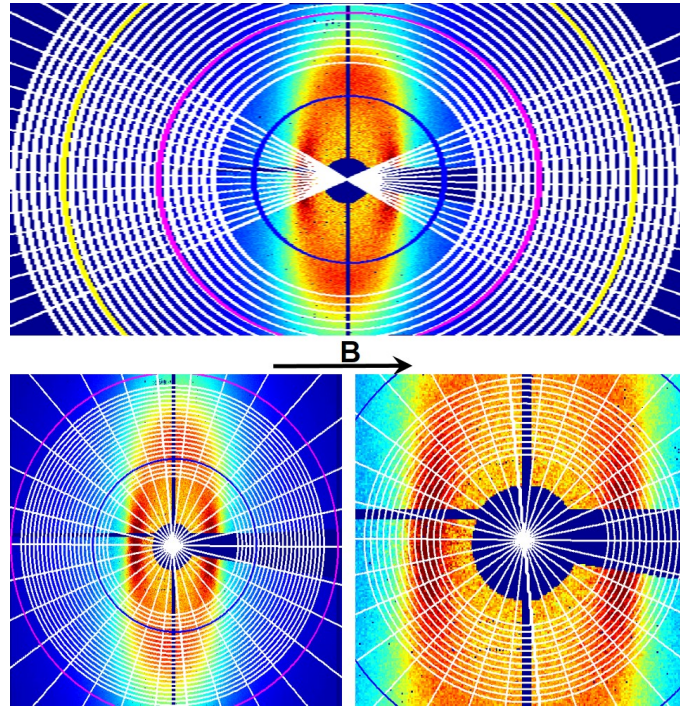


Figure 7.1.: The Q - ϕ -partitioning is shown with white grid for $Q \geq 0.007 \text{ \AA}^{-1}$ on top, $Q = 0.004 - 0.009 \text{ \AA}^{-1}$ on the bottom left and $Q = 0.002 - 0.004 \text{ \AA}^{-1}$ on the bottom right. The coloured rings mark respective Q -values: blue - $Q_3 = 0.005 \text{ \AA}^{-1}$, magenta - $Q_6 = 0.011 \text{ \AA}^{-1}$ and yellow - $Q_9 = 0.015 \text{ \AA}^{-1}$.

high concentration phases. Therefore the partitioning in Q (radial) and ϕ^B (angular) had to be chosen carefully depending on the particular scattering pattern. The azimuthal angle ϕ^B indicates the difference between the selected angle and the direction of the magnetic field (\mathbf{m}). Considering the shape of the SAXS patterns three Q -regions were chosen for separate partitioning to ensure an uniform intensity distribution as good as possible. This approach led to very small sizes of the partitions, which resulted in some cases in poorer statistics. To enhance the statistics, Friedel's law and the corresponding axial (180°) symmetry of the scattering patterns was used and thus the data of two partitions at identical Q and $\Delta\phi^B$ of 180° combined. The chosen regions and corresponding partitions are summarized in fig. 7.1.

The XPCS measurements were performed with a Lambda detector. It has a chip size ratio of 3 : 1 with 1556×556 pixels, where each pixel has a size of $55 \times 55 \mu\text{m}^2$. Three Q -regions were chosen for evaluation. The Q -regions were defined as the average value of a partition - $Q_s = 0.002 - 0.004 \text{ \AA}^{-1}$, $Q_m = 0.004 - 0.009 \text{ \AA}^{-1}$ and $Q_l \geq 0.007 \text{ \AA}^{-1}$. Q_s and Q_m covered the whole π -range (axial symmetry of the scattering pattern), whereas in Q_l only 0.31π were accessible. For the Q_s and Q_m the evaluated range of 180° was split into 15 ϕ -partitions with a $\Delta\phi^B = 12^\circ$. For the Q_l also 15 ϕ^B -partitions were used, but with a $\Delta\phi^B \approx 3.7^\circ$. Therefore only parts of ϕ^B -rings along magnetic field direction (\mathbf{m}) are accessible at $Q_l \geq 0.007 \text{ \AA}^{-1}$. The Q -partitions in every Q -range were divided into equal intervals - 12 for Q_s and 21 for Q_m and Q_l .

For each Q - ϕ^B -partition of each data batch a g_2 -function was calculated. As it is not possible to show all calculated functions, only examples of g_2 -functions at the cross-sections of the coloured lines and circles will be shown (see fig. 7.2). The depicted colour code will be used to indicate the respective Q 's and ϕ^B 's. These chosen values are illustrated in fig. 7.2 for scattering patterns of the nematic and anti-nematic phases of a 16 vol%-suspension at $B = 240$ mT (on top) and $B = 900$ mT (at the bottom), respectively. They will be indicated in the following figures with colour and according number in the colour bar, as shown in tables 7.1 and 7.2.

Table 7.1.: The colour code for the Q values chosen from Q - ϕ^B -partitions as shown in fig. 7.2 for illustration of examples of time autocorrelation function. In the images the colours in the bar show the according Q values, which stay constant through the whole thesis.

Color	black	red	blue	green	cyan	magenta	orange
Q Number	Q_1	Q_2	Q_3	Q_4	Q_5	Q_6	Q_7
$Q[\text{\AA}^{-1}]$	0.0024	0.0034	0.0046	0.0064	0.0081	0.0108	0.013

All $g_2(Q, t)$ -functions, which are shown e.g. in fig. 7.5, were fitted using the KWW expression (see Chapter 5, eq. refeq:KWW):

$$g_2(Q, t) = b + \beta \cdot \exp(-2(\Gamma t)^\gamma), \quad (7.1)$$

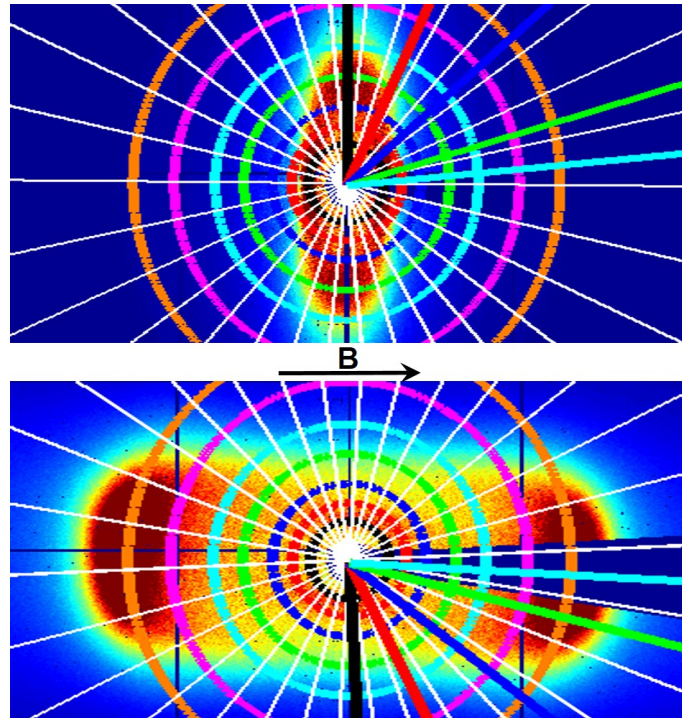


Figure 7.2.: Q - ϕ -partitioning illustrating, which examples of g_2 -functions will be shown later. On top for a nematic and on the bottom for an anti-nematic scattering pattern. The circles of different colours in fig. 7.2 represent chosen Q 's. In the images the colours in the bar assigns the colour to a Q value as listed in table 7.1. The straight lines of different colour indicate different angles ϕ^B , which are explained in table 7.2.

Table 7.2.: The colour code for the angles ϕ^B chosen from Q - ϕ^B -partitions as shown in fig. 7.2 for illustration of examples of time autocorrelation function. In the images the colours in the bar show the according number of the angle, which stays constant through whole thesis.

Colour	ϕ^B	N and M at 16 vol%	AN	M at 20 vol%
black	$\approx \perp$ to B ($\perp \mathbf{m}$)	$\phi_1^B = -89^\circ$	$\phi_1^B = 86^\circ$	$\phi_1^B = -96^\circ$
red	$\approx 60^\circ$ to B	$\phi_2^B = -66^\circ$	$\phi_2^B = 64^\circ$	$\phi_2^B = -60^\circ$
blue	$\approx 40^\circ$ to B	$\phi_3^B = -42^\circ$	$\phi_3^B = 40^\circ$	$\phi_3^B = -48^\circ$
green	$\approx 20^\circ$ to B	$\phi_4^B = -18^\circ$	$\phi_4^B = 16^\circ$	$\phi_4^B = -24^\circ$
cyan	$\approx \parallel$ to B ($\parallel \mathbf{m}$)	$\phi_5^B = -7^\circ$	$\phi_5^B = 3^\circ$	$\phi_5^B = 0^\circ$

where b is the baseline, β is the contrast, Γ is the relaxation rate and γ is the relaxation exponent.

In addition, the stability of the incoming beam intensity during the experiment was evaluated. In figure 7.3 an example of the intensity integrated on the Lambda throughout one measurement series is shown. It is very stable with deviation of ± 4 vol% from the mean value. For each experimental data batch the beam stability was checked before the data analysis was performed. The stability check is crucial, because it can indicate problems during the measurement (beam damage, beam loss, drop in the beam intensity etc.).

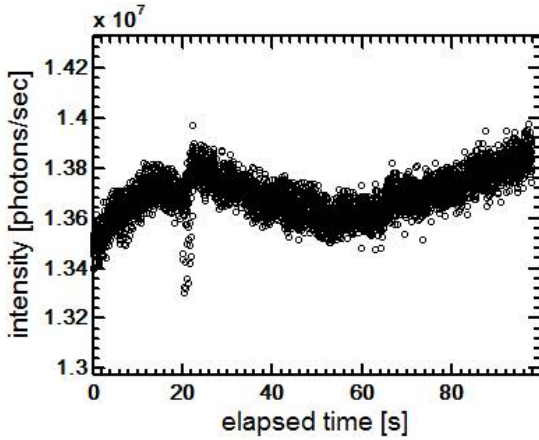


Figure 7.3.: Evaluation of the total integrated intensity, as a function of the elapsed experimental time in seconds.

The three images in figure 7.4 show two-time correlation functions for a 16 vol%-sample at $B = 240$ mT for different Q - ϕ^B 's. The two-time correlation function analysis is not a mayor part of the analysis of this thesis, but the general shape of the function allows to see, if the sample was in an equilibrium state when the data was taken. It is apparent that the width along the main diagonal is almost constant. This is a property of systems in equilibrium and allows to average g_2 -functions over the complete time interval of the measurement. Only data sets in equilibrium have been considered for the following analysis.

Two important parameters for XPCS evaluation are the contrast and the baseline. The contrast typically depends only on experimental settings. The according values for

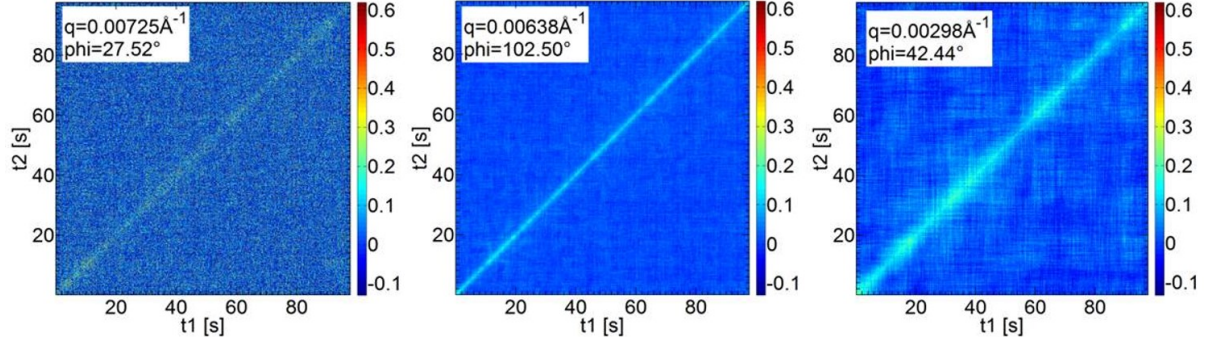


Figure 7.4.: Example of two-time correlation functions at different Q - ϕ^B 's for a sample at $c = 16\text{ vol}\%$ and $B = 240\text{ mT}$.

the beam size of $30 \times 30 \mu\text{m}^2$ were measured as $\beta_{\text{lambda}} = 0.175$ for the Lambda-detector using a calibration 90 vol%-aerogel sample of 1 mm thickness.

The baseline was estimated from a 4 vol% goethite sample, which shows fast dynamics. The XPCS analysis of such a sample results in a $g_2(Q, t)$ function, which is completely relaxed to the baseline as the sample dynamics is faster than the 2D-image repetition rate. The value obtained from this evaluation was $b = 1.002$.

7.2. XPCS data

The structural investigation of the suspensions with high particle concentration showed that two phases appeared in the experiments. At low magnetic fields the nematic phase N was common and at high fields the anti-nematic phase AN was dominant. At intermediate fields $310\text{ mT} \leq B \leq 410\text{ mT}$ more complicated states appeared, which resulted in more complicated SAXS pattern. These mixed states consist of mixtures of nematic and anti-nematic phases. These structural properties were elaborated in detail in Section 6.4. The XPCS analysis was performed with XPCSGui [63] calculating the time correlation functions $g_2(Q, t)$ as described in the Chapter 5.

In the following sections exemplary data is presented for all the phases. The angles ϕ^B , used throughout this chapter, are defined as the angle respective to the direction of the applied magnetic field (\mathbf{m}). In order to understand the microscopic dynamics of the suspensions the purest nematic and anti-nematic phases were analysed by XPCS primarily - first at $c = 20\text{ vol\%}$ and then at $c = 16\text{ vol\%}$. Afterwards the mixed states were analysed. All the sections begin with Paragraph "Preamble", which shows the exemplary g_2 -functions together with the respective scattering pattern and the indicated Q and ϕ^B values (see e.g. fig. 7.5). The g_2 -functions are discussed and the values, which were acquired from the fits with eq. 5.28 are summarized in Q - ϕ^B -maps. The discussion of the single values in maps is split into discussion of baseline b and contrast β in Paragraph "Baseline b and contrast β " and stretching exponent γ and relaxation rate Γ in Paragraph "Stretching exponent γ and relaxation rate Γ ". The values of the stretching exponent γ and relaxation rate Γ are important to describe the dynamical behaviour. The baseline b and contrast β are discussed to ensure the stability and quality of the evaluation. The results of each phase are then summarized in Paragraph "Short summary". The results for different phases are compared.

7.2.1. XPCS analysis of 20 vol%-suspensions

XPCS analysis of the nematic phase (N) at $B = 240\text{ mT}$

Preamble In the following, the microscopic dynamics for platelets at $c = 20\text{ vol\%}$ in the nematic phase N are analysed. In this phase the platelets are mostly aligned with the long axis l parallel to the applied magnetic field ($\mathbf{n} \parallel \mathbf{m}$), where \mathbf{n} is the preferred orientation direction of the long axis l of the platelets (nematic orientation direction) and \mathbf{m} is the direction of the magnetic field. In the directions perpendicular to the applied magnetic field ($\perp \mathbf{m}$) presmectic order can be observed (see Chapter 6).

In fig. 7.5 on top the scattering pattern on the Lambda-detector together with evaluated Q and ϕ^B values is depicted. Below the scattering pattern exemplary g_2 -functions as a functions of lag time τ are shown.

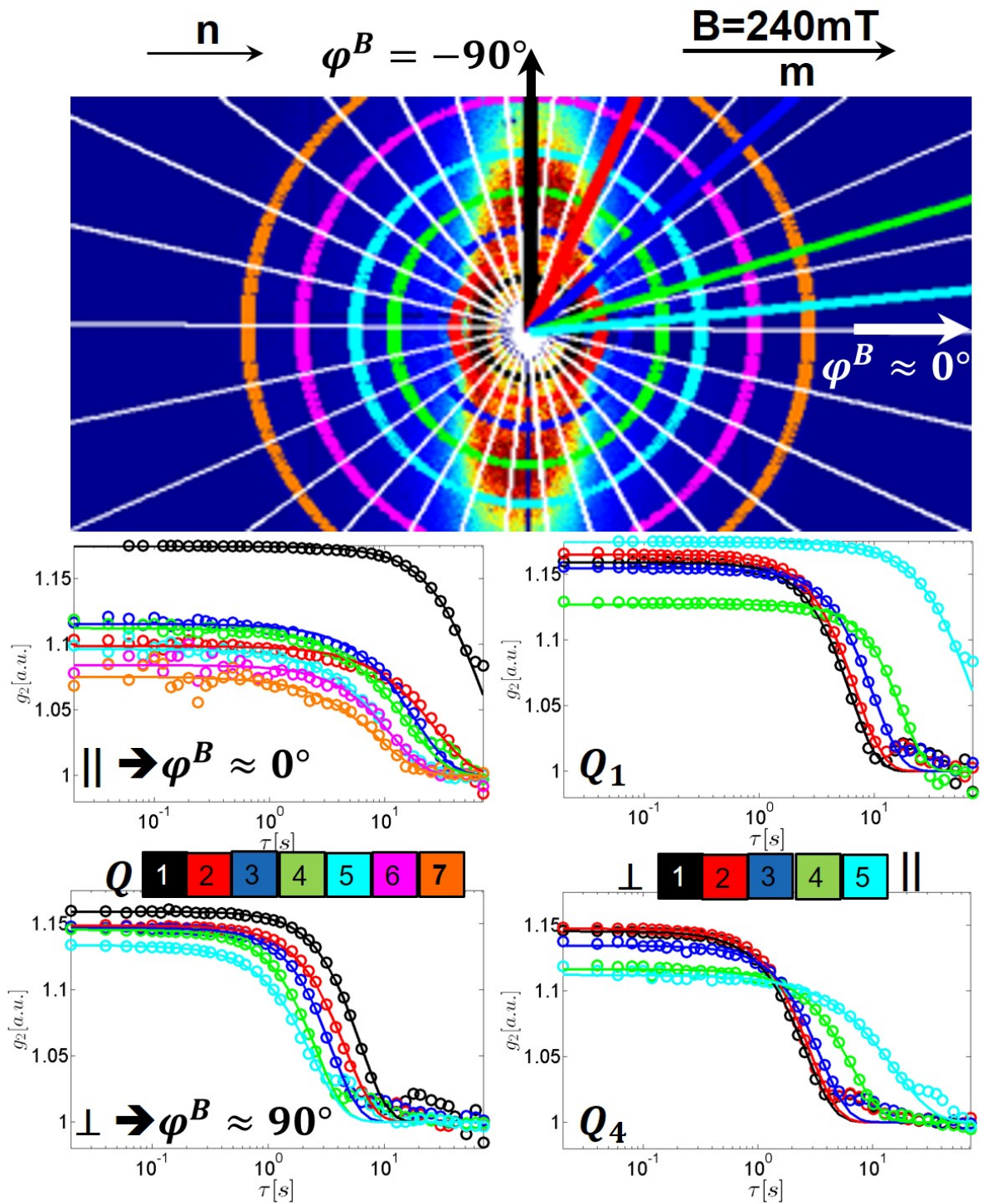


Figure 7.5.: Top: SAXS scattering pattern with Q rings and φ^B lines as explained in Section 7.1. Structural peaks are found near Q_1 ($\parallel \mathbf{m}$) and near Q_4 ($\perp \mathbf{m}$), which are respectively shown as black and green circles. Below: Examples of the calculated $g_2(Q, \varphi^B)$ -functions. Left: for different Q 's at $\varphi^B \approx 0^\circ$ in the central row and at $\varphi^B \approx -90^\circ$ at the bottom. Right: for different directions in φ^B at $Q_1 = 0.0024 \text{ \AA}^{-1}$ in the central row and $Q_4 = 0.0064 \text{ \AA}^{-1}$ at the bottom. Solid lines represent fits of the data with eq. 7.1.

The coloured squares indicate the respective values - Q values on the right and ϕ^B values on the left, as explained in the previous section. The plots on the left show $g_2(Q, \phi^B)$ -functions at $\phi^B \approx 0^\circ$ in the central row and at $\phi^B \approx -90^\circ$ at the bottom for different Q 's. The plots on the right display $g_2(Q, \phi^B)$ -functions at $Q_1 = 0.0024 \text{ \AA}^{-1}$ in the central row and $Q_4 = 0.0064 \text{ \AA}^{-1}$ at the bottom for different values of ϕ^B . This order as well as the respective colour code is identical in all following sections, if $g_2(Q, \phi^B)$ -functions are plotted.

At first glance at the constant ϕ^B data on the left, it is apparent that the relaxation times τ_c , as defined in Section 5.3 are larger parallel to the field than perpendicular to it. In addition, the contrast decreases and the dynamics gets faster with increasing Q for both directions. The shape of the curves can be described by a compressed single exponential decay, as indicated by the solid lines in the respective colour. In all plots, the solid lines show fits of the data with eq. 7.1, as in all plots of $g_2(Q, \phi^B)$ -functions in following sections. The shaping exponent γ is lower for $\phi^B \approx 0^\circ$ compared to $\phi^B = -90^\circ$ and decreases slightly with increasing Q . The plots at constant Q on the right show that the dynamics gets slower for ϕ^B values going from perpendicular to parallel to the direction of the applied magnetic field, as already observed when top left and bottom left in the same figure.

Important indicators of the microscopic dynamics is the behaviour of the parameters obtained from a fit of the g_2 -functions. By fitting with eq. 7.1 four parameters were obtained: baseline b , contrast β , relaxation rate Γ and relaxation exponent γ . These parameters will be discussed in the following for each phase and concentration in a similar way.

Fig. 7.6 shows maps of the baseline values b on the top left, the contrast values β on the top right, the relaxation exponent values γ on bottom left and the relaxation rate values Γ on the bottom right. The obtained values are plotted as 2D-maps with Q on the vertical axis and ϕ^B on the horizontal axis and the values are indicated by the colour scale. These plots will be plotted in same order for each phase in following sections. Here, the maps are not fully centred at $\phi^B = 0^\circ$. Even though the width of the partitions $\Delta\phi^B = 12^\circ$ was constant, the centre of the scattering feature could slightly vary, to ensure more homogeneous distribution of intensity inside the partitions.

Baseline b and contrast β With the exception of an arc of elevated numbers, all values of the baseline are close to the expected value of $b = 1.002$, which was obtained from a low concentration sample. The partitions of the Q - ϕ^B -map, from which these elevated values were calculated, are located exactly at the edge of the scattering feature, which results in an inhomogeneous intensity distribution inside these partitions, as illustrated in fig. 7.7. This inhomogeneity leads to the evaluated values of the baseline,

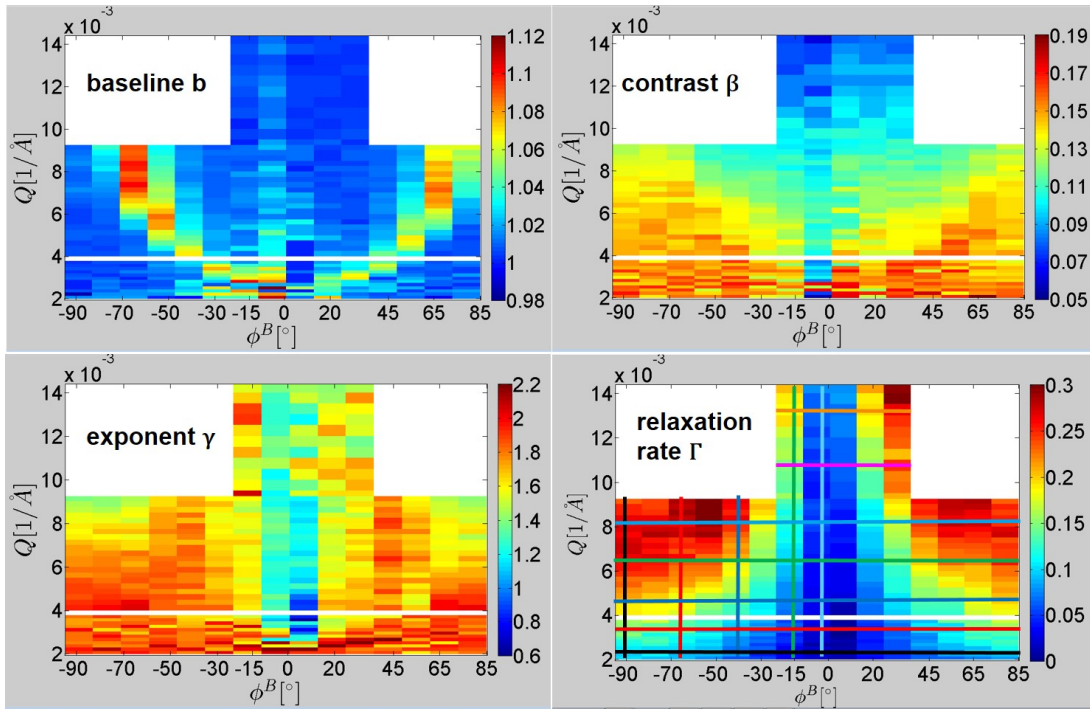


Figure 7.6.: Maps of the baseline values b on the top left, the contrast values β on the top right, the relaxation exponent values γ on the bottom left and the relaxation rate values Γ on the bottom right for nematic phase N. The obtained values are plotted as 2D-maps with Q on the vertical axis and ϕ^B on the horizontal axis. The coloured lines in the Γ map indicate Q values $Q_1 - Q_7$ and ϕ^B values $\phi_{\parallel}^B = 0^\circ$ to $\phi_{\perp}^B = 90^\circ$, as described before. These values are also valid for other maps and correspond to the shown g_2 -functions evaluated on the same Q and ϕ^B values. The white spaces show areas not accessible at high Q , due to the shape of the Lambda detector.

which is not connected to the dynamic processes in the sample and has therefore no physical meaning for the investigated system. All other g_2 -functions show dynamics, which fully decorrelates during the time series. The average standard deviation arising from the data and the fit is $\overline{\Delta b} = \pm 0.002$.

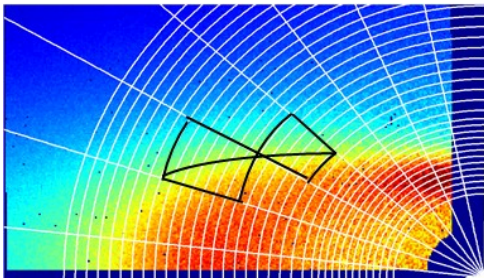


Figure 7.7.: Illustration of the inhomogeneous partitions at the border of the scattering feature at $B = 240 \text{ mT}$, which leads to elevated baseline values b

The contrast has high values at low Q 's and lower values at high Q 's. The maximum of $\beta_{max} = 0.188$ is close to the expected value of $\beta_{aerogel} = 0.175$. The average standard deviation calculated for the contrast is $\overline{\Delta \beta} = \pm 0.003$. The contrast decreases abruptly close to $\phi^B \approx 0^\circ$. The decrease of β as a function of Q is slower for higher $|\phi^B|$ values. The isolines of small contrast values form the shape of an inverse triangle centred at $\phi^B \approx 0^\circ$, which is caused by the ellipsoidal shape of the scattering feature. A

reason for the decrease of the contrast with increasing Q could be the existence of a faster non-ergodic process, which is not covered by the time window of the experiment. In the literature the assumption is made, that the autocorrelation function decays to the non-ergodicity level. The decrease of contrast based on this assumption is discussed in Section 7.3.1 based on fits shown in Appendix C.

Stretching exponent γ and relaxation rate Γ The Q - ϕ^B -map of the relaxation exponent γ is shown in fig. 7.6 on the bottom left. The values are higher for small Q 's and lower for high Q 's. Along ϕ^B the map shows similar values for all angles, except for the direction parallel to the magnetic field. In this direction the exponent is significantly lower compared to all other directions. Close to $\phi^B \approx 0^\circ$ the relaxation exponent is $\gamma \approx 1.2 \pm 0.2$. For all other angles it displays values $\gamma \geq 1.7 \pm 0.2$. The average standard deviation is $\overline{\Delta\gamma} = \pm 0.2$.

The relaxation rate Γ is shown in fig. 7.6 on the bottom right. At low Q the relaxation rate is low and increases with increasing Q . An area of low relaxation rate values is located at $\phi^B \approx 0^\circ$. With increasing deviation from $\phi^B \approx 0^\circ$ the relaxation rate increases, too. The maximal values of relaxation rate are found at highest accessible Q values in the range $\phi^B \approx \pm(50^\circ - 90^\circ)$. The average relative standard deviation was calculated to be $\Delta\Gamma/\Gamma \approx \pm 4 \text{ vol\%}$.

To visualize the dependence of the relaxation rate Γ from Q and ϕ^B selected linecuts along constant Q 's and ϕ^B 's are shown in fig. 7.8. The directions along constant Q 's and ϕ^B 's are indicated in the Q - ϕ^B -map and in fig. 7.8 by the lines of respective colours, which will be kept for all following plots of this kind. The plots of relaxations rate $\Gamma(\phi^B)$ along constant Q are shown in fig. 7.8 on top and of $\Gamma(Q)$ along constant ϕ^B at the bottom.

From the plot on top of fig. 7.8 it is evident that $\Gamma < 0.3 \text{ s}^{-1}$ and the dynamics perpendicular to the field is 5–10 times faster than parallel to it. Also the system speeds up by a factor 8 with increasing Q . For all Q 's it seems to show a similar behaviour - the relaxation rate reaches a plateau at respective $\phi^B \approx \pm 45^\circ$. The height of the plateau increases with increasing Q . The slope, which the curves show between the minimum and the plateau, differs depending on the selected Q . It increases with increasing Q . As a result, the $\Gamma(\phi^B)$ curves show a funnel shape along constant Q . The funnel is centred roughly at $\phi^B \approx 0^\circ$ and the shape of the cone narrows with increasing Q .

In the plot at the bottom of fig. 7.8 the relaxation rate Γ is plotted as a function of Q along constant ϕ^B values. It is evident that $\Gamma \propto Q$. This behaviour was modelled by a linear fit, which took into account the data from all Q 's. The highest slope perpendicular to the field is roughly 10 times higher than the smallest one parallel to it. The fitted curves cross $Q = 0 \text{ \AA}^{-1}$ close to the point of origin.

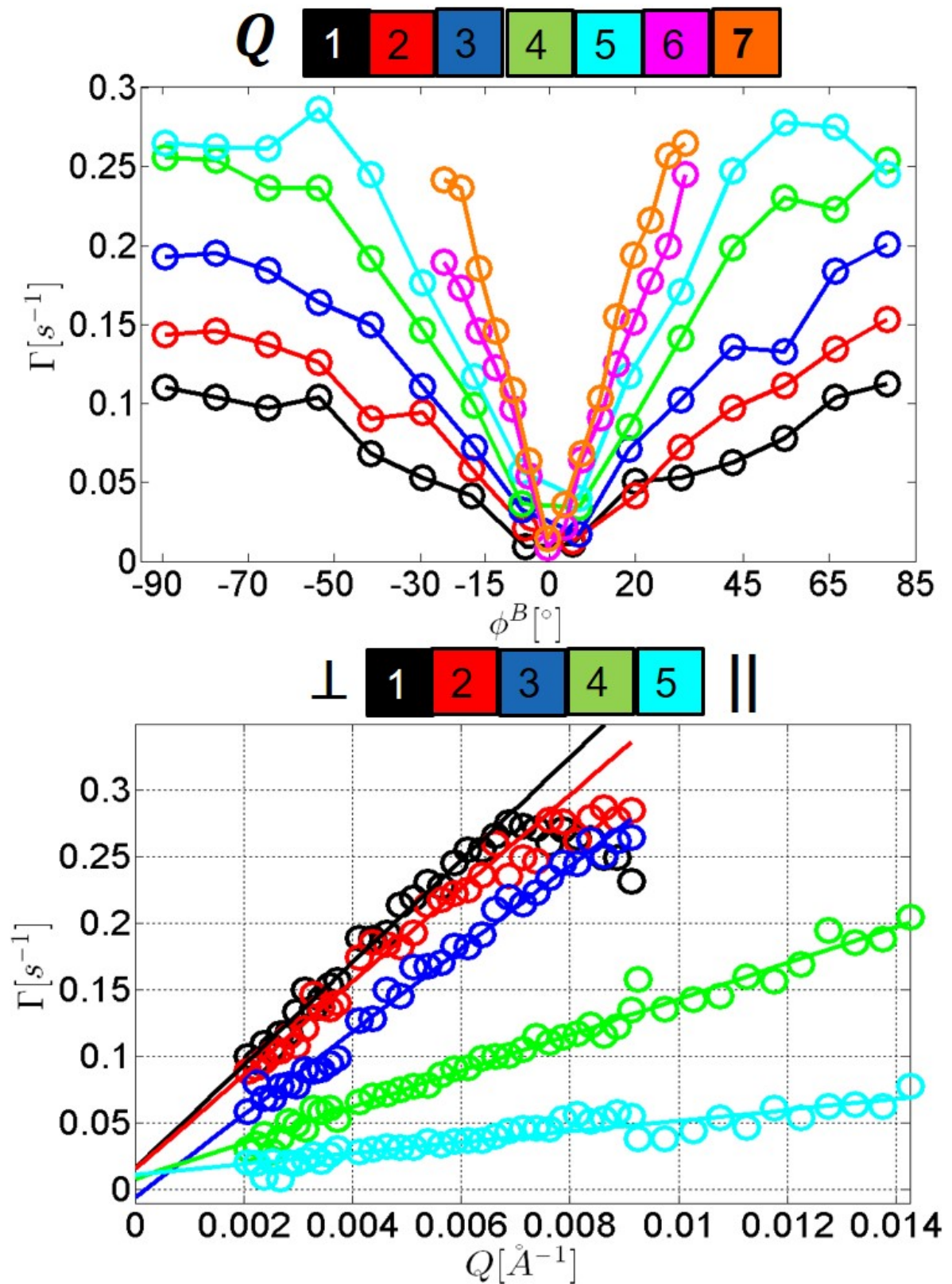


Figure 7.8.: Top: Relaxation rate Γ plotted as function of ϕ^B for different Q values. The solid lines are guides to the eye. Bottom: relaxation rate Γ plotted as function of Q for different ϕ^B values. The solid lines are linear fits to the data.

Short summary Combining the results from the Γ -map and γ -map we can conclude that in all directions the particles show a proportionality of the relaxation rate $\Gamma \propto Q$ and values of the relaxation exponent $\gamma \geq 1$. Both, the linear Q -dependence as well as a KWW exponent $\gamma \geq 1$ are reported for systems with ballistic motion [20, 22, 31, 55, 56, 62, 66].

The relaxation rate is $\Gamma < 0.3 \text{ s}^{-1}$. The slope of the linear fit of the $\Gamma \propto Q$ shows the characteristic velocity v of the ballistic motion. In the direction parallel to the applied magnetic field platelets are moving up to a factor 10 slower as on the corresponding length scale perpendicular to the field [62]. The most important information on the nematic phase at $c = 20 \text{ vol}\%$ are summarized in fig. 7.9.

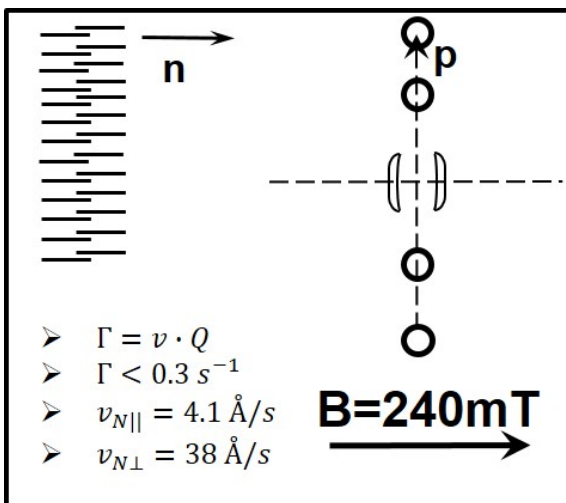


Figure 7.9.: Summary of the evaluation of the nematic phase at $c = 20 \text{ vol}\%$.

XPCS analysis of the anti-nematic phase (AN) at $B = 900$ mT

Preamble The platelets in AN phase align mostly with the long axis l perpendicular to the applied magnetic field ($\mathbf{n} \perp \mathbf{m}$). Therefore the scattering pattern turns with long axis \mathbf{p} parallel to the field ($\mathbf{p} \parallel \mathbf{m}$). The width of the scattering peaks is larger in ϕ^B than at $B = 240$ mT and the presmectic order (two peaks $\perp \mathbf{m}$ in nematic phase) is destroyed. In fig. 7.10 g_2 -functions are plotted versus delay time τ in the same order and with the same colour codes, as explained before.

Again, the relaxation time τ_c is larger parallel to the field than perpendicular to it. The contrast decreases and the dynamics are faster with increasing Q for both directions - parallel ($\phi^B = 0^\circ$) and perpendicular ($\phi^B = 90^\circ$) to the applied magnetic field. The solid lines display fits to the $g_2(Q, \phi^B)$ -curves using eq. 7.1.

The plots in fig. 7.10 right hand side show that for all Q the dynamics get slower with angle changing from $\phi^B \approx 90^\circ$ to $\phi^B \approx 0^\circ$. Again, the parameters obtained from the fit: baseline b , contrast β , relaxation rate Γ and relaxation exponent γ , are used to understand the underlying microscopic dynamics. Fig. 7.11 shows 2D-maps of the obtained values with Q on the vertical axis and ϕ^B on the horizontal axis, similar to the previous section.

Baseline b and contrast β All the values in the map of the baseline have magnitudes close to the expected value of $b = 1.002$ with an average standard deviation of $\overline{\Delta b} = \pm 0.002$ with several values only, which deviate from the expected values.

In contrast to the nematic phase (N), where the contour lines of small contrast values form the shape of an inverted pyramid, in the anti-nematic phase the isolines of the higher values of the contrast β form roughly the shape of a pyramid with centre at $\phi^B \approx 0^\circ$. The highest magnitude can be found at low Q values. With increasing Q the contrast decreases, but with different rates at different ϕ^B . The decrease is slowest for $\phi^B \approx 0^\circ$. The change of the contour lines during the phase transition from nematic to anti-nematic phase is caused by the change of the scattering pattern, which turned by $\Delta\phi^B \approx 90^\circ$ and broadened in the AN phase. The contrast values have a maximum of $\beta_{max} = 0.2$, but most of the values are $\overline{\beta} \approx 0.15$. The average standard deviation calculated for the contrast is $\overline{\Delta\beta} = \pm 0.003$. The decrease of contrast with increasing Q is discussed in Section 7.3.1 for all phases.

Stretching exponent γ and relaxation rate Γ The relaxation exponent is plotted as a Q - ϕ^B -map in fig. 7.11 on the bottom left. It shows values $\gamma \geq 1$, with a maximum of $\gamma = 2$. Most of the values are $\gamma \approx 1.7 \pm 0.2$, except for the values of the partitions near $\phi^B \approx 0^\circ$, where the decay exponent decreases to $\gamma \approx 1.1 \pm 0.3$. At small Q 's the values are even $\gamma < 1$. The average standard deviation was calculated to $\overline{\Delta\gamma} = \pm 0.06$.

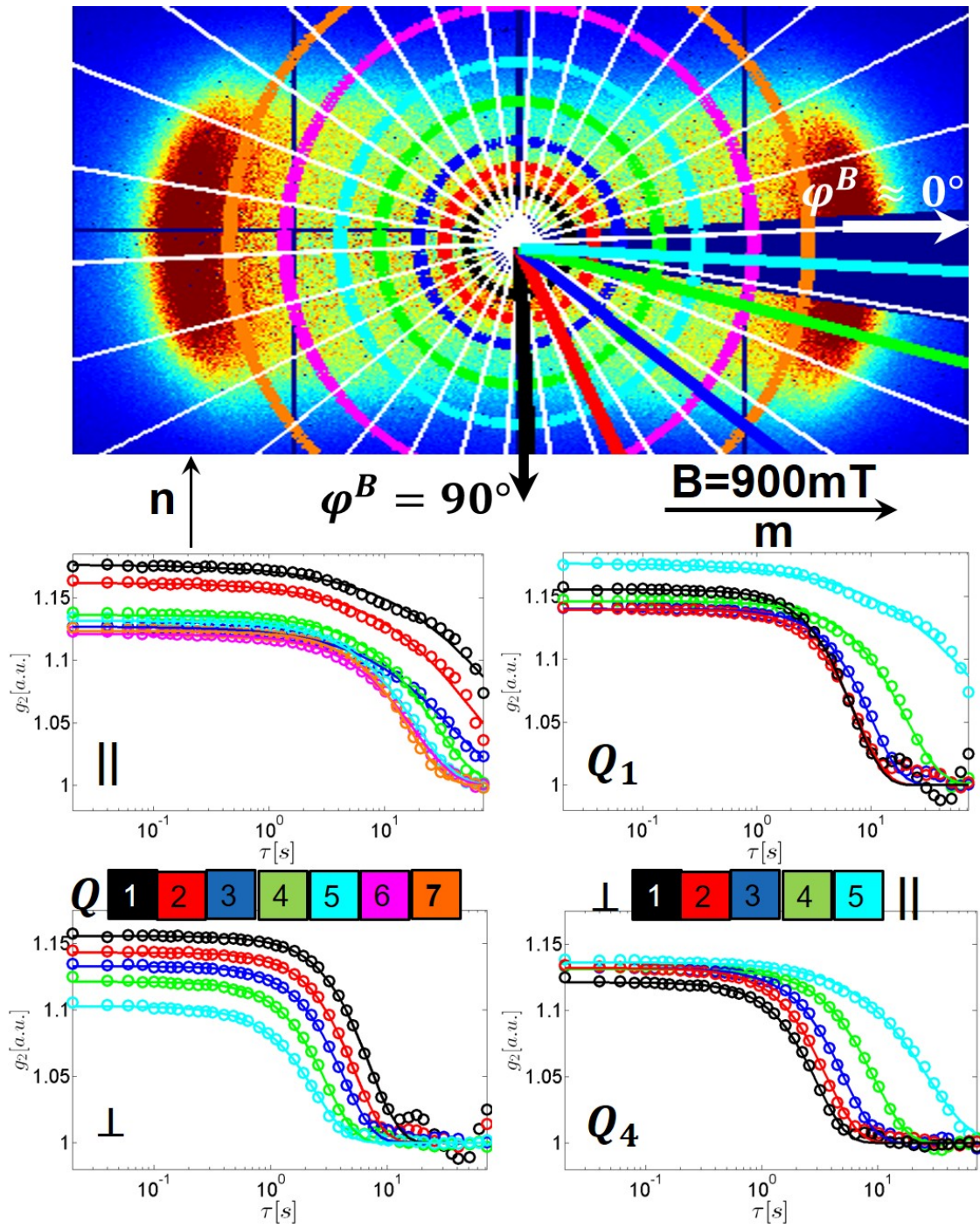


Figure 7.10.: Top: SAXS scattering pattern with Q rings and ϕ^B lines as explained in Section 7.1. Structural peaks are found near Q_1 ($\perp \mathbf{m}$ and Q_7 ($\parallel \mathbf{m}$), which are respectively shown as black and orange circles. Below: Examples of the calculated $g_2(Q, \phi^B)$ -functions. Left: for different Q values at $\phi^B \approx 0^\circ$ in the central row and at $\phi^B \approx 90^\circ$ at the bottom. Right: for different ϕ^B values at $Q_1 = 0.0024 \text{ \AA}^{-1}$ in the central row and $Q_4 = 0.0064 \text{ \AA}^{-1}$ at the bottom, which is shown as green ring. Solid lines are fits to the data using eq. 7.1.

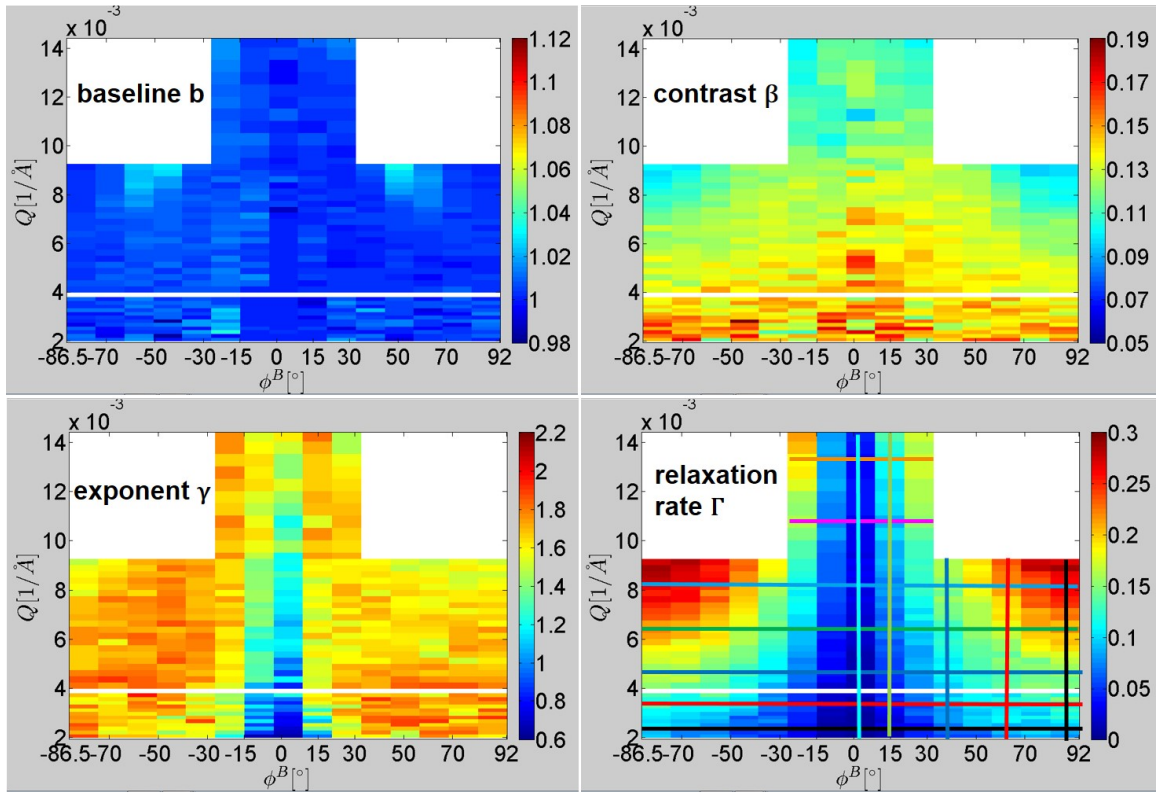


Figure 7.11.: Maps of the baseline values b on the top left, the contrast values β on the top right, the relaxation exponent values γ on bottom left and the relaxation rate values Γ on the bottom right for anti-nematic phase AN. The obtained values are plotted as 2D-maps with Q on the vertical axis and ϕ^B on the horizontal axis. The coloured lines in the Γ map indicate Q values $Q_1 - Q_7$ and ϕ^B values $\phi_{\parallel}^B = 0^\circ$ to $\phi_{\perp}^B = 90^\circ$, as described before. These values are also valid for other maps and correspond to the shown g_2 -functions evaluated on the same Q and ϕ^B values.

The relaxation rate Γ is shown on the bottom right in fig. 7.11. There is an area of low relaxation rate values at $\phi^B \approx 0^\circ$. The magnitude of Γ increases with increasing deviation from this direction. Maxima of the relaxation rate are found at $\phi^B \approx \pm 80^\circ$ for the highest accessible Q values. These maximal values are embedded into areas of high Γ -values, which decrease with decreasing Q . The map can be divided into two areas. An area of low relaxation rate, which is roughly parallel to the applied magnetic field, and an area, where the relaxation rate increases towards a maximum roughly perpendicular to the direction of the applied magnetic field. The average relative standard deviation of the relaxation rate is $\Delta\Gamma/\Gamma \approx \pm 2 \text{ vol\%}$.

From the plot on top of fig. 7.12, which shows Γ versus ϕ^B , it is evident that $\Gamma < 0.28 \text{ s}^{-1}$ and the dynamics perpendicular to the field are 5 – 10 times faster than parallel to it. At the smallest Q 's this difference is highest. The system speeds up with increasing Q . In general the $\Gamma(\phi^B)$ curves have a shape of a asymmetric funnel with a minimum roughly at $\phi^B \approx 0^\circ$. The slope of the funnel is steeper for higher Q . On the left side it is steeper than on the right for all Q . On both sides the slope changes at $\phi^B \approx \pm 50^\circ$, but the magnitude of the relaxation rate at the point of change is higher on

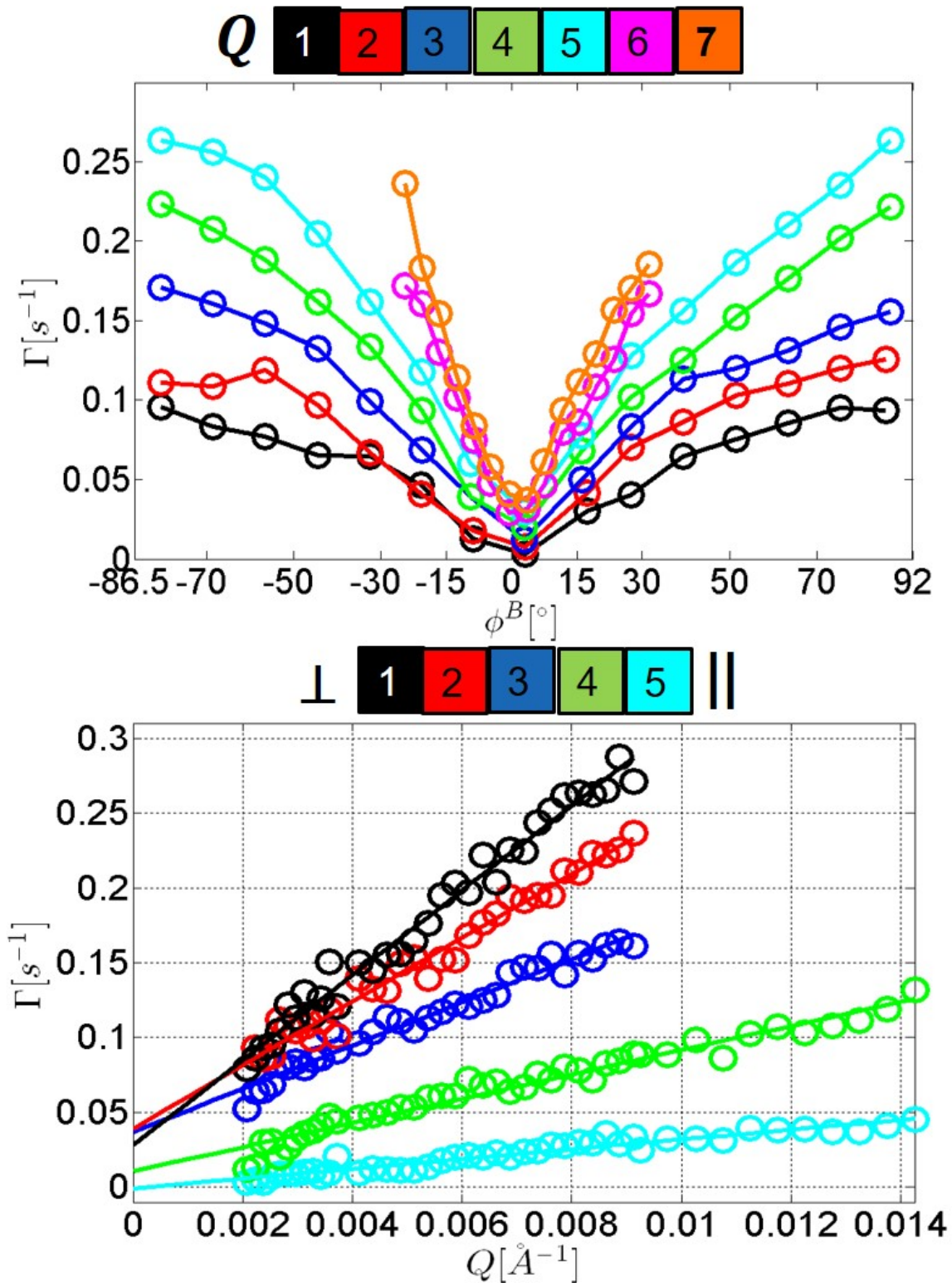


Figure 7.12.: Left: relaxation rate Γ plotted as function of ϕ^B for different constant Q 's. The solid lines are guides to the eye. Right: relaxation rate Γ plotted as function of Q along different constant ϕ^B 's. The solid lines show the linear fits to the data.

the left side. The point, at which the slope changes, grows with increasing Q for both sides.

The plot at the bottom of fig. 7.12 shows Γ as a function of Q . It is evident that $\Gamma \propto Q$, which was reinforced by the linear fit, which took into account data from all Q 's. The highest slope is perpendicular to the field and roughly 10 times higher than the smallest one, which is found parallel to the field. The fitted curves cross $Q = 0 \text{ \AA}^{-1}$ close to the point of origin.

Short summary The dynamics of the anti-nematic phase at $c = 20 \text{ vol\%}$ are similar to the dynamics in the nematic phase. The sample shows collective ballistic motion except for low Q 's along $\phi^B \approx 0^\circ$, where $\gamma < 1$ and therefore a heterogeneous motion was registered [31, 54]. The slopes of the curves $\Gamma(Q)$ represents the ballistic velocity of the motion. The values of the relaxation rate Γ are $\Gamma < 0.28 \text{ s}^{-1}$. The summary of the information obtained for anti-nematic phase at $c = 20 \text{ vol\%}$ is shown in fig. 7.13.

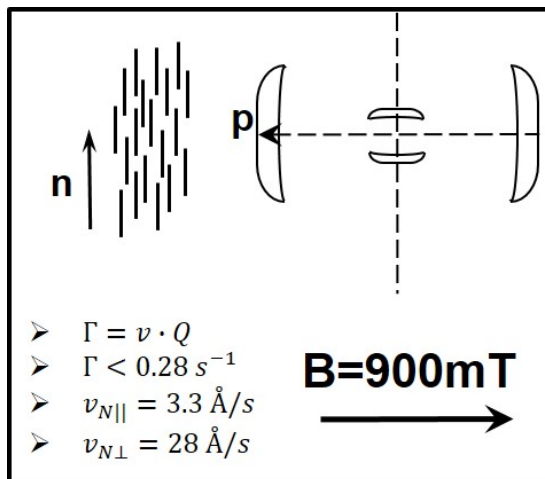


Figure 7.13.: Summary of the evaluation of the anti-nematic phase at $c = 20 \text{ vol\%}$.

Comparison of the microscopic dynamics for the nematic (N) and the anti-nematic (AN) phases at $c = 20 \text{ vol\%}$

A short summary of the data taken in a single phase - nematic (N) and anti-nematic (AN) - and a comparison of the parameters will be shown here. The difference after increasing the field and realignment of the particles is of major interest and will give clues for the detailed understanding of the dynamics in the mixed phases.

In fig. 7.6, 7.11, 7.8 and 7.12 the fit parameter maps and the plots of Γ as function of Q and ϕ^B are shown for the nematic and the anti-nematic phases. From the maps it is evident that the behaviour of both phases is quite similar. There is an area of slow dynamics with a minimum parallel to magnetic field. With increasing deviation from the direction parallel to the magnetic field the dynamics speed up and have a maximum roughly perpendicular to the magnetic field. The maxima of the relaxation rate are close

to each other for both phases. From the linecuts along constant Q values a change of the dynamics with ϕ^B is apparent. The curves for the nematic phase show a steeper slope and are symmetric, whereas for the anti-nematic phase the curves have a less steep slope and show an asymmetric behaviour in ϕ^B . The curves along constant ϕ^B show the same trend. Relaxation rates are linear with Q and the slope grows with increasing absolute values of ϕ^B . The slopes of the linear fits are slightly higher for all directions in the nematic phase (N) compared to the anti-nematic phase (AN).

In general, the relaxation exponents for both phases show the same trend. The exponent is lower at $\phi = 0^\circ$ with $1 \leq \gamma \leq 1.5$. For other angles the exponent is $\gamma \approx 1.7$ for both phases. The exponent γ in the nematic phase is in general slightly higher than γ in the anti-nematic phase.

For easier comparison, ratio maps were calculated, which are shown in fig. 7.14. They were calculated by dividing the Q - ϕ^B -maps of the relaxation rate and relaxation exponent of the anti-nematic phase by the corresponding maps of the nematic phase.

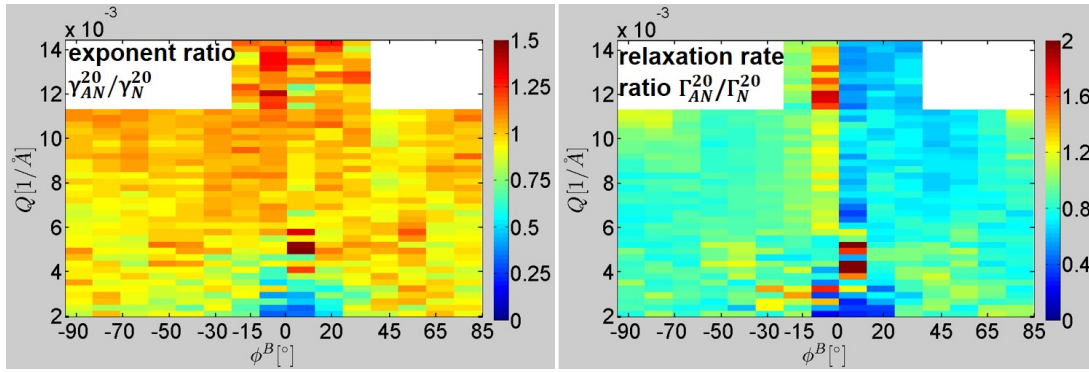


Figure 7.14.: Ratio maps for $c = 20$ vol% calculated by dividing the map of the relaxation exponent (left) and the relaxation rate (right) of anti-nematic phase (AN) by the map of the nematic phase (N).

The ratio map of the relaxation rate shows a value of ≈ 1 , except for $\phi^B \approx 0^\circ$, where it is < 1 and single values at low and high Q , which are higher - up to ≤ 2 . The comparison map of relaxation exponents shows a similar behaviour.

It is obvious that the dynamics of both phases are roughly the same, because the main value in the resulting ratio maps is ≈ 1 for almost all angles, except for $\phi^B = 0^\circ$, where the nematic phase (N) is roughly two times faster than the anti-nematic phase (AN). In contrast, at some small Q values, the anti-nematic phase (AN) is faster and at $\phi^B \approx -10^\circ$, the anti-nematic phase is up to two times faster, as well. This asymmetry is visible as well for positive angles. Because the slope for this direction and the according values for the anti-nematic phase are lower the ratio assumes values < 1 in this case.

It can be conducted that both phases - the nematic and the anti-nematic show a similar behaviour at $c = 20$ vol%. Both phases have $\Gamma < 0.3 \text{ s}^{-1}$ and show slow dynamics parallel to the applied magnetic field and fast dynamics perpendicular to it. With a relaxation exponent $\gamma \geq 1$ and a relaxation rate dependence $\Gamma \propto Q$ both phases show

ballistic dynamics in all directions. This is a remarkable behaviour. Goethite platelets in the nematic phase (N) are aligned with the long axis parallel to the field and therefore with a smaller surface perpendicular to the field. This should lead to a faster motion parallel to the field and slower dynamics perpendicular to it [47]. This is not the case. In fact, the motion parallel to the field was much slower in the nematic phase (N). In the anti-nematic phase (AN) goethite platelets turned to an orientation with the long axis perpendicular to the field, but the motion parallel to the field stayed the slowest. As a consequence of the comparison it is apparent that although the particles realigned partially, the relaxation exponent γ and the relaxation rate Γ changed only insignificantly with slightly faster dynamics in the nematic phase. The most significant values are shown as comparison in fig. 7.15.

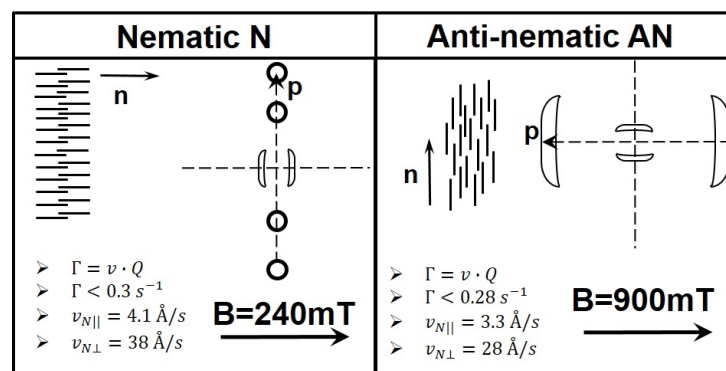


Figure 7.15.: Summary of the evaluation of the nematic and anti-nematic phases at $c = 20 \text{ vol\%}$ in comparison.

7.2.2. XPCS analysis of 16 vol%-suspensions

XPCS analysis of the nematic phase (N) at $B = 240$ mT

Preamble The platelets in the nematic phase are mostly aligned with the long axis l parallel to the applied magnetic field ($\mathbf{n} \parallel \mathbf{m}$) at $c = 16$ vol%, similar to the samples at $c = 20$ vol%. In the directions perpendicular to the applied magnetic field ($\perp \mathbf{m}$) a presmectic order can be observed as in the 20 vol%-suspension. In fig. 7.16 exemplary g_2 -functions are shown similar to fig. 7.5.

The relaxation time τ_c is higher parallel to the field than perpendicular to it. The plots on the right illustrate how the dynamics slows down, if the investigated direction changes from $\phi^B \approx -90^\circ$ to $\phi^B \approx 0^\circ$ for all Q . If Q at a chosen ϕ^B values increases, the contrast decreases and the dynamics speed up, as shown in the plots on the left. The shape of the curves can be described with a stretched or compressed single exponential decay. The solid lines in the plots show fits of the $g_2(Q, t)$ -curves using eq. 7.1.

To analyse the dynamics we look again at the parameters obtained from the fits of the g_2 -functions, which are plotted as maps in fig. 7.17 and will be discussed in the same manner as for the 20 vol%-suspension.

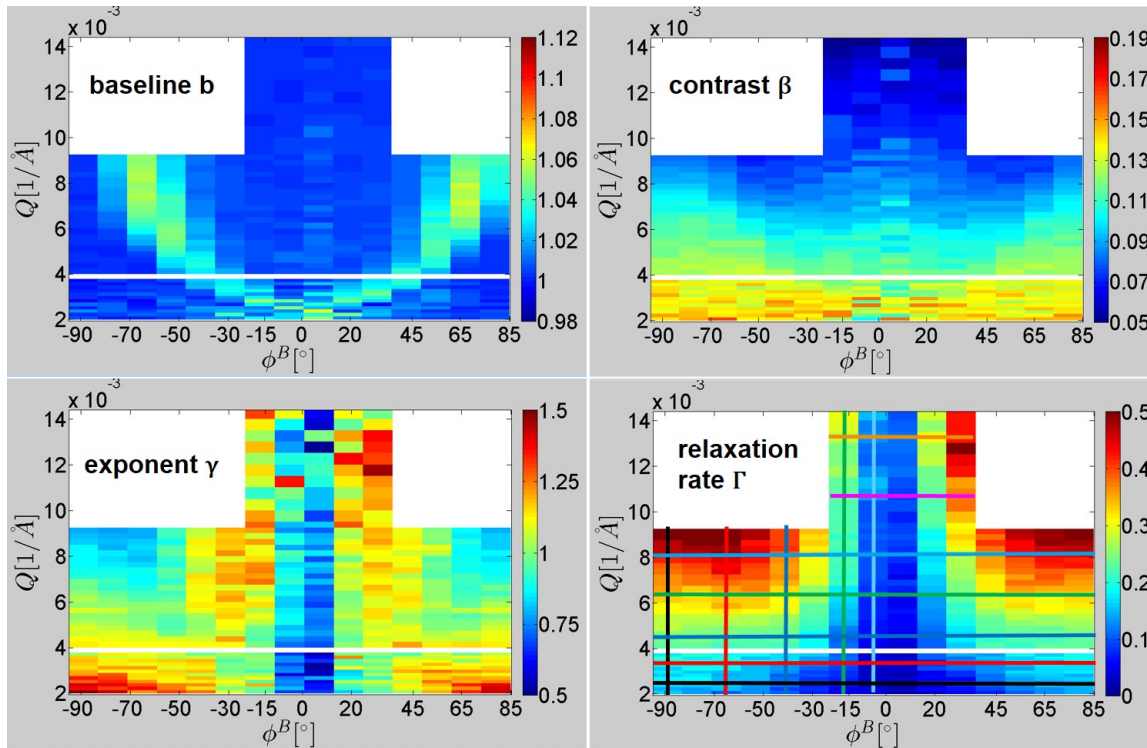


Figure 7.17.: Maps of the baseline values b (top left), the contrast values β (top right), the relaxation exponent values γ (bottom left) and the relaxation rate values Γ (bottom right) for the nematic phase N. The obtained values are plotted as 2D-maps with Q on the vertical axis and ϕ^B on the horizontal axis. The coloured lines in the Γ map indicate Q values $Q_1 - Q_7$ and ϕ^B values $\phi_{\parallel}^B = 0^\circ$ to $\phi_{\perp}^B = 90^\circ$, as described before. These values are also valid for other maps and correspond to the shown g_2 -functions evaluated on the same Q and ϕ^B values.

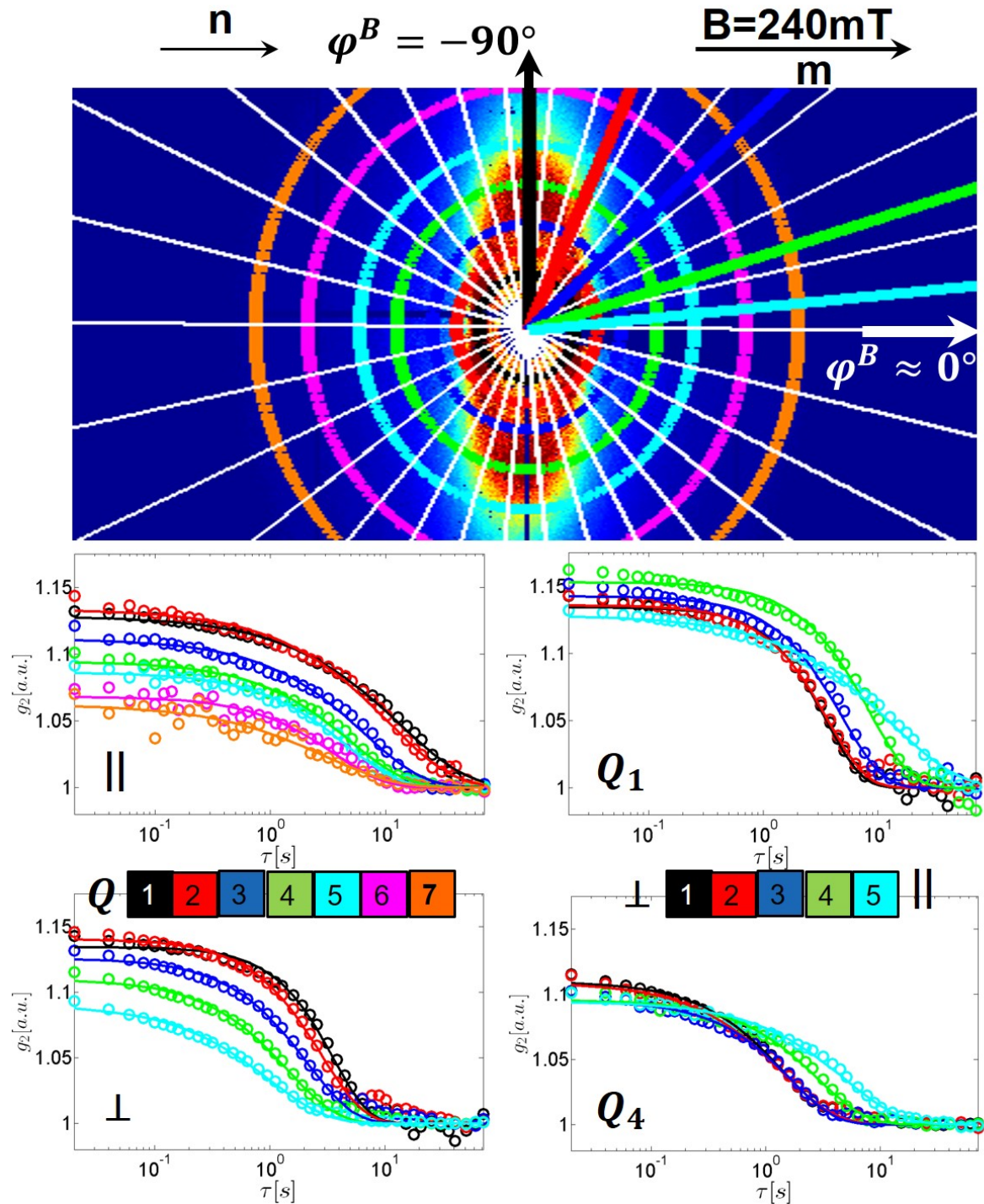


Figure 7.16.: Top: SAXS scattering pattern with Q rings and ϕ^B lines as explained in Section 7.1. The structural peaks are found near Q_1 ($\parallel m$) and Q_4 ($\perp m$), which are respectively shown as black and green circles. Below: Examples of calculated $g_2(Q, \phi^B)$ -functions. Left: $g_2(Q, \phi^B)$ for different Q 's at $\phi^B \approx 0^\circ$ (centre) and at $\phi^B \approx -90^\circ$ (bottom). Right: $g_2(Q, \phi^B)$ for different directions in ϕ^B at $Q_1 = 0.0024 \text{ \AA}^{-1}$ (centre) and $Q_4 = 0.0064 \text{ \AA}^{-1}$ (bottom). Solid lines represent fits of the data using eq. 7.1.

Baseline b and contrast β As for $c = 20\text{ vol}\%$, the baseline values are close to the expected values of $b = 1.002$. The average standard deviation was calculated to be $\overline{\Delta b} = \pm 0.002$. The highest values are found at $\phi^B \approx \pm 68^\circ$. There is an arc of elevated baseline values, which spreads from low Q and low ϕ^B values to high Q and high ϕ^B values. The shape of the scattering pattern of the nematic phase for the $16\text{ vol}\%$ -suspension is close to the shape of the SAXS pattern of the $20\text{ vol}\%$ -suspension. Therefore the increase of the baseline values can be similarly explained by the inhomogeneous distribution of the intensity inside partitions, which are located at the border of the scattering feature similar to the case illustrated in fig. 7.7.

The contrast values plotted on the top right in fig. 7.17 show high values at low Q and low values at high Q , where small contrast values form the shape of an inverse (upside-down) pyramid with a top at $\phi^B \approx 0^\circ$ and low Q , similar to the nematic phase at $c = 20\text{ vol}\%$. The difference is that the base of the pyramid is much wider and that there are small fluctuations with minima at $\phi^B \approx \pm 50^\circ$. The contrast decreases with increasing Q , which is discussed in Section 7.3.1 as mentioned before. The decrease is faster for the directions at $\phi^B \approx \pm 50^\circ$. The contrast map has a maximum of $\beta_{max} = 0.163$, which is close to the expected value of $\beta_{aerogel} = 0.175$. The average standard deviation calculated for the contrast is $\overline{\Delta\beta} = \pm 0.004$.

Stretching exponent γ and relaxation rate Γ The relaxation exponent is plotted as a Q - ϕ^B -map in fig. 7.17 on the bottom left. In the centre of the map at $\phi^B \approx 0^\circ$ an area of low values is visible. In addition, an arc of lower values spans from low Q and low ϕ^B -values to high Q and high ϕ^B -values. It corresponds to the border of a scattering feature, where partitions have uneven intensity distribution, as explained before for elevated baseline values. The map can be roughly divided into two areas: an area of low exponent values $\gamma \approx 0.7 \pm 0.1$ along $\phi^B \approx 0^\circ$ and all other directions, where γ is $\gamma \approx 1.1 \pm 0.2$. The average standard deviation of the exponent is $\overline{\Delta\gamma} = \pm 0.16$.

In the lower right part of fig. 7.17 the relaxation rate Γ is shown. The map shows low values for relaxation rate at low Q 's and high values at high Q 's, except for $\phi^B \approx 0^\circ$, where an area of low relaxation rate values is visible. The relaxation rate increases in general with increasing Q and with the increasing value of ϕ^B and reaches maximal values at $\phi^B \approx -80^\circ$ and $\phi^B \approx 90^\circ$. These maximal values are embedded into areas of high Γ -values and this map can be divided into two areas, too. The area of low relaxation rate, which is roughly parallel to the applied magnetic field, and the area, where relaxation rate grows with a maximum roughly perpendicular to the direction of the applied magnetic field. It is apparent that the relaxation rate increases with increasing Q up to factor 10. On the other hand it increases with ϕ^B , where the maximum factor is also ≈ 10 . The average relative standard deviation is $\Delta\Gamma/\Gamma = \pm 10\text{ vol}\%$.

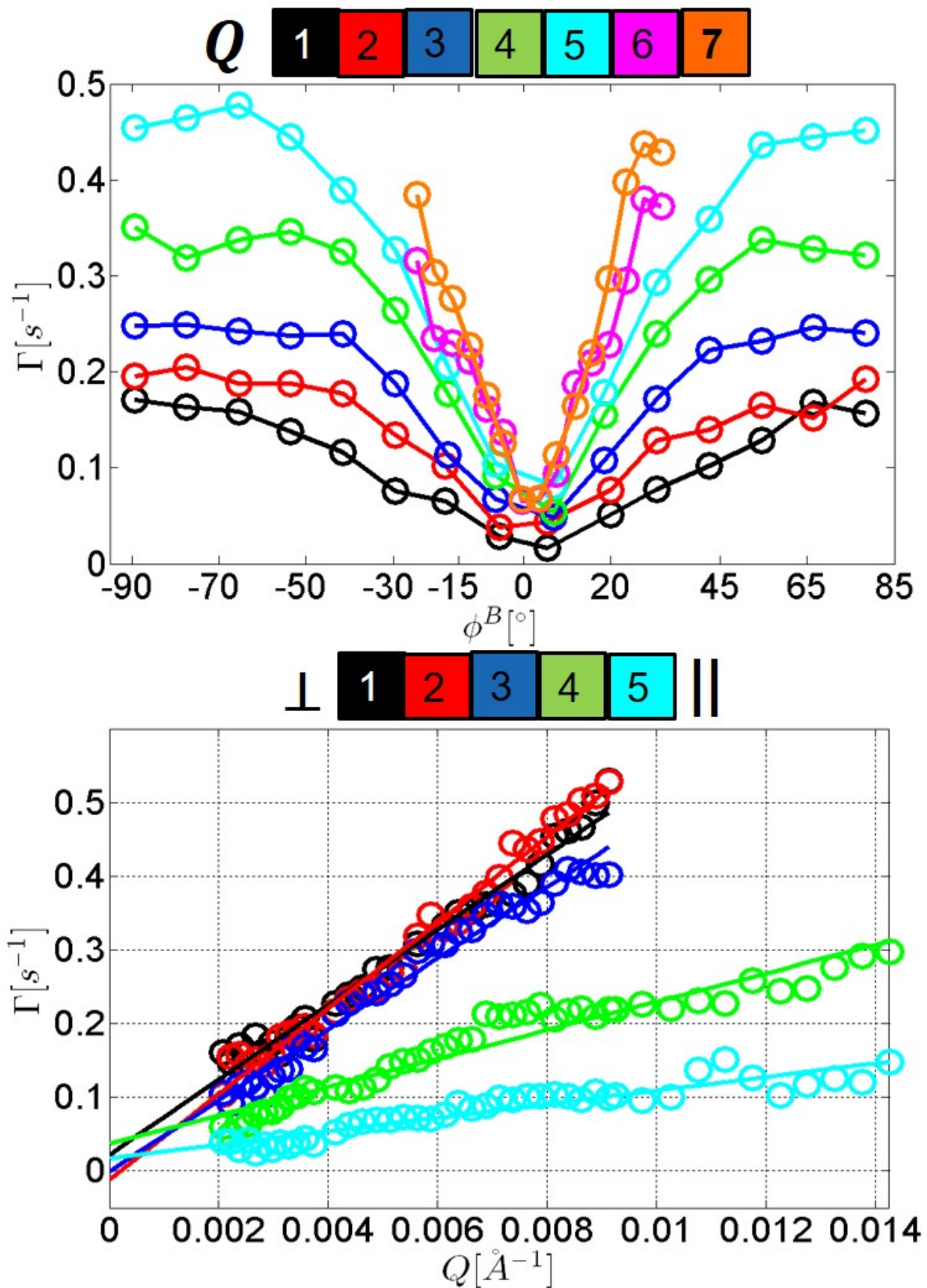


Figure 7.18.: Top: relaxation rate Γ plotted as a function of ϕ^B for different Q 's. Solid lines are guides to the eyes. Bottom: relaxation rate Γ plotted as a function of Q for different ϕ^B 's and according linear fits shown by solid lines.

From the plots of $\Gamma(Q)$ as a function of ϕ^B in the plot on the top of fig. 7.18 it is evident that $\Gamma < 0.5 \text{ s}^{-1}$ and the dynamics perpendicular to the field are 5–10 times faster than parallel to it, similar to the nematic and anti-nematic phases at $c = 20 \text{ vol}\%$. The system speeds up with increasing Q , with a stronger increase for increasing ϕ^B . Here the $\Gamma(\phi^B)$ curves have also the shape of a funnel centred roughly at $\phi^B \approx 0^\circ$, as already explained for the nematic phase N for the 20 vol%-suspension. The values reach a plateau at respective $\phi^B \approx \pm 50^\circ$. The slope of the cone increases with increasing Q as well as the value of the plateau.

In the plot at the bottom of fig. 7.18 the plots of Γ as a function of Q are shown. Again, it is evident that $\Gamma \propto Q$, which was subsequently verified by linear fits to the data from all Q 's. As in the nematic and the anti-nematic phases at $c = 20 \text{ vol}\%$ the fits cross $Q = 0 \text{ \AA}^{-1}$ close the point of origin. The highest slope is perpendicular to the field as well as the lowest one parallel to the field. In the nematic phase (N) at $c = 16 \text{ vol}\%$ the slope perpendicular to the field is only 5 times higher than the one parallel to it.

Short summary As mentioned before, $\Gamma \propto Q$ indicates ballistic motion [66], [62], [56], [22]. Collectivity was confirmed for the directions deviating from the direction of the magnetic field by $\gamma \geq 1$ [62], [66], [22], [55], [20], [31]. Parallel to the direction of the applied field $\gamma < 1$ was observed, which points to heterogeneous motions [55], [20], [31], [54]. It can be concluded that the nematic phase N of the 16 vol%-suspension shows a combination of motions - heterogeneous motion parallel to the magnetic field and ballistic motion in the directions $\parallel m$. The relaxation rate in the nematic phase at $c = 16 \text{ vol}\%$ showed values $\Gamma < 0.5 \text{ s}^{-1}$. The slopes of the curves $\Gamma(Q)$ represents the ballistic velocity of the motion. The most important features are summarized in fig. 7.19.

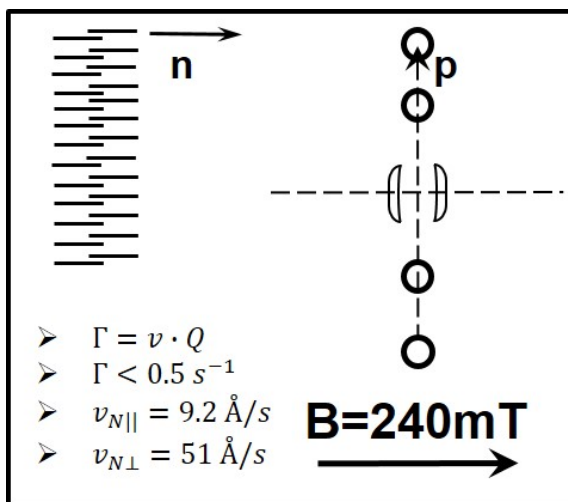


Figure 7.19.: Summary of the evaluation of the nematic phase at $c = 16 \text{ vol}\%$.

XPCS analysis of the anti-nematic phase (AN) at $B = 900$ mT

Preamble As at $c = 20$ vol%, the platelets in the anti-nematic phase align perpendicular to the applied magnetic field ($\mathbf{n} \perp \mathbf{m}$), the presmectic order is lost and the width of the scattering peaks is grown larger. In fig. 7.20 g_2 -functions are plotted in the same order as previously used.

Again, the relaxation time τ_c is higher parallel to the field than perpendicular to it. Also the contrast decreases and the dynamics get faster with increasing Q for both directions. The plots show that for all Q the dynamics get slower when the angle changes from $\phi^B \approx 90^\circ$ to $\phi^B \approx 0^\circ$. From the plots on the right it is apparent that at Q_1 the shape of the curves changes depending of the direction in ϕ^B (centre right). At Q_4 this effect is much less pronounced (bottom right). All curves seem to be stretched. In the direction perpendicular to the field the curves are less stretched than parallel to it. The curves are fitted by a stretched single exponential decay as in eq. 7.1, which are shown as solid lines in fig. 7.20.

As before four parameters can be extracted from the fits. 2D-maps of these parameters are shown in fig. 7.21 and discussed in the following.

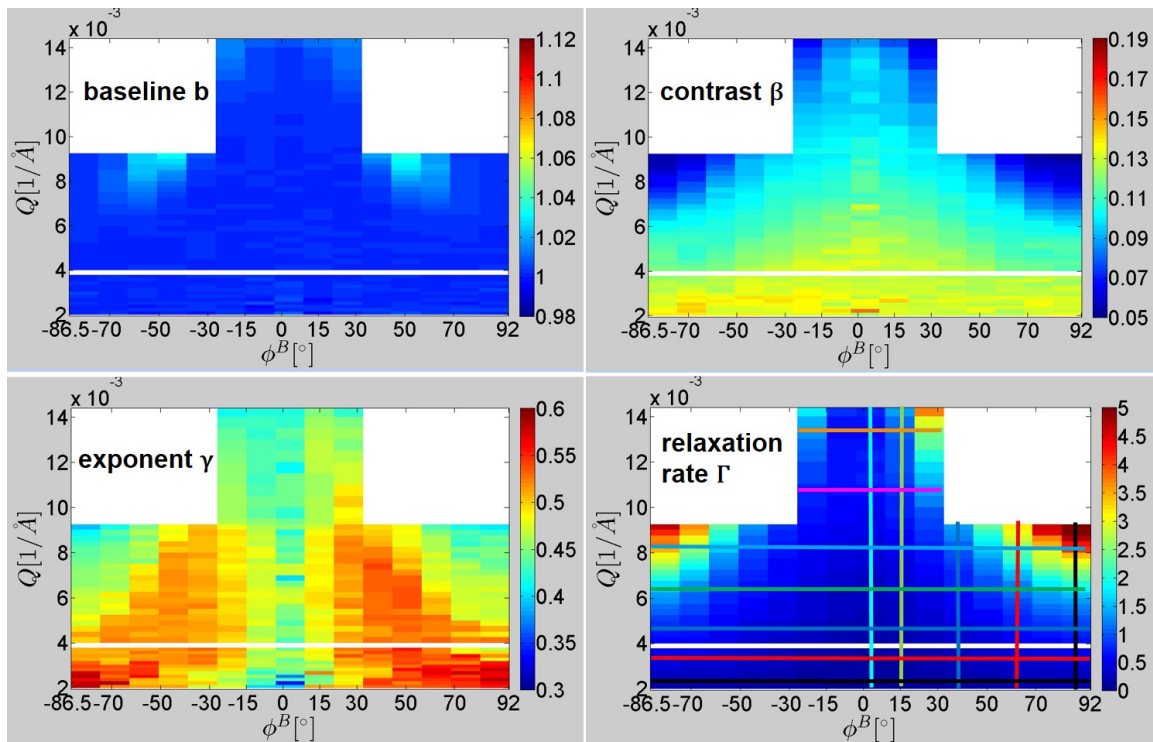


Figure 7.21.: Maps of the baseline values b on the top left, the contrast values β on the top right, the relaxation exponent values γ on the bottom left and the relaxation rate values Γ on the bottom right for the anti-nematic phase AN. The obtained values are plotted as 2D-maps with Q on the vertical axis and ϕ^B on the horizontal axis. The coloured lines in the Γ map indicate Q values $Q_1 - Q_7$ and ϕ^B values $\phi_{\parallel}^B = 0^\circ$ to $\phi_{\perp}^B = 90^\circ$, as described before. These values are also valid for other maps and correspond to the shown g_2 -functions evaluated on the same Q and ϕ^B values.

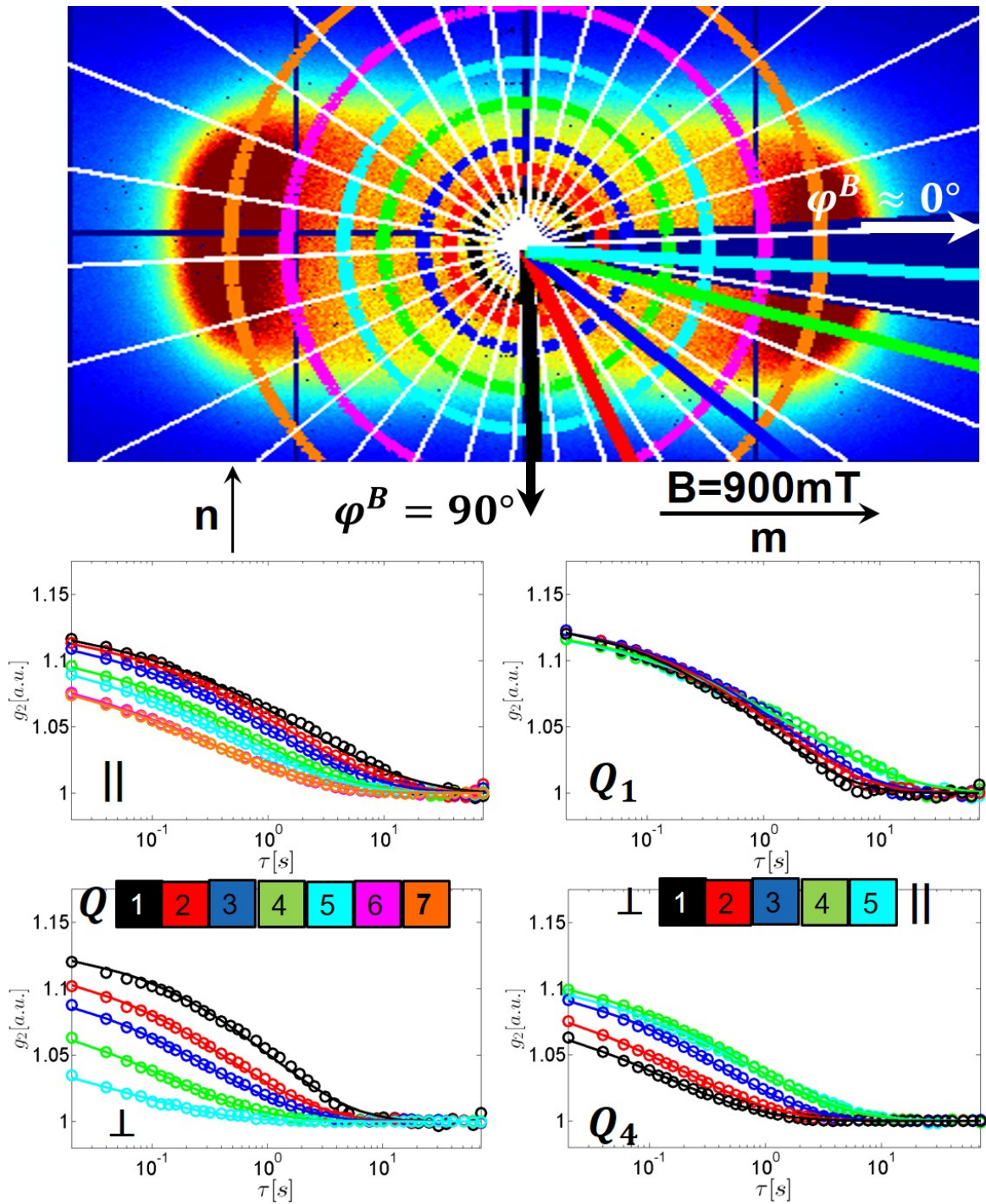


Figure 7.20.: Top: SAXS scattering pattern with Q rings and ϕ^B lines as explained in Section 7.1. The structural peaks are found near Q_1 ($\perp m$) and Q_7 ($\parallel m$), which are respectively shown as black and orange circles. Below: Examples of the calculated $g_2(Q, \phi^B)$ -functions for anti-nematic phase. Left: for different Q 's at $\phi^B \approx 3^\circ$ (centre) and at $\phi^B \approx 87^\circ$ (bottom). Right: for different directions in ϕ^B at $Q_1 = 0.0024 \text{ \AA}^{-1}$ (centre) and $Q_4 = 0.0064 \text{ \AA}^{-1}$ (bottom), which is shown as green ring. Solid lines represent fits of the data with eq. 7.1.

Baseline b and contrast β The baseline map shows almost no deviations from the expected values of $b = 1.002$. The average standard deviation of the fits is $\overline{\Delta b} = \pm 0.0004$.

Again, the map of the contrast values shows high contrast at low Q 's, which decreases with increasing Q . The high contrast values are forming a pyramid with tip at $\phi^B \approx 0^\circ$ as in the anti-nematic phase at $c = 20$ vol%. The difference is that the values are lower at $c = 16$ vol%, therefore the pyramid appears sharper. The contrast decrease is slower for the direction $\phi^B \approx 0^\circ$. The shape of the g_2 -curves (fig. 7.20) suggests that no plateau value was reached even at shortest delay times. This was taken into account - an imaginary point was introduced at $\tau = 0$ s, which was estimated by a first fit. Then a second fit was performed, using a curve including the imaginary point. A trend of decreasing contrast with increasing Q is observed, which will be discussed later in Section 7.3.1. The contrast values have a maximum of $\beta_{max} = 0.157$ and the average standard deviation calculated for the contrast is $\overline{\Delta \beta} = \pm 0.003$.

Stretching exponent γ and relaxation rate Γ The relaxation exponent is plotted as a Q - ϕ^B -map in fig. 7.21 on the bottom left. For all parts of the map it displays low values of $\gamma < 1$. More exact the values are $\gamma \approx 0.5 \pm 0.1$. Including the average standard deviation of $\overline{\Delta \gamma} = \pm 0.03$ the exponent has an average value of $\overline{\gamma} \approx 0.5$. This is a significant difference compared to the other cases investigated in this thesis before.

As expected at low Q 's the relaxation rate, which is shown in fig. 7.21 on the bottom right, shows low values, which increase with increasing Q . At $\phi^B \approx \pm 85^\circ$ the increase is higher compared to the directions around $\phi^B \approx 0^\circ$. Therefore this map can be divided into two areas. The area of low relaxation rate, which is roughly parallel to the applied magnetic field, and the area of higher relaxation rate with a maximum roughly perpendicular to the direction of the applied magnetic field, which was also valid for all previously investigated phases. The average relative standard deviation of the relaxation rate is $\Delta \Gamma / \Gamma = \pm 2$ vol%.

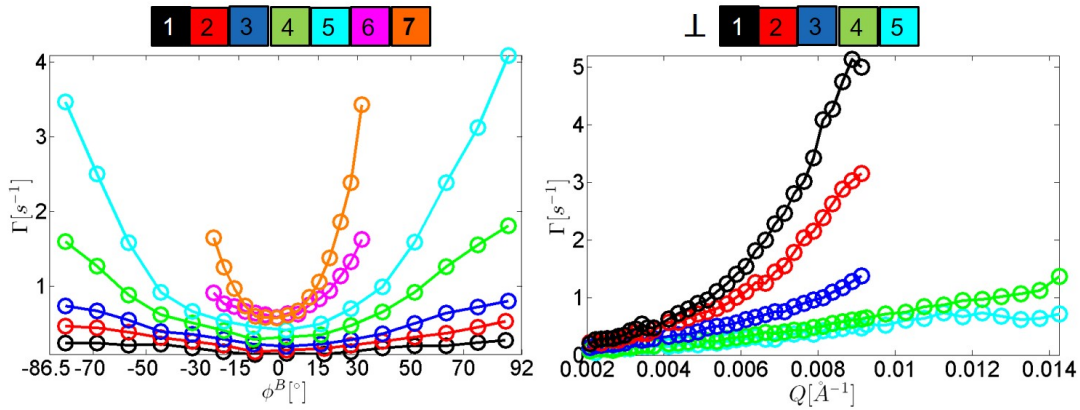


Figure 7.22.: Left: relaxation rate Γ plotted as a function of ϕ^B for different Q 's. Right: relaxation rate Γ plotted as a function of Q for different ϕ^B 's. The solid lines are guides to the eye.

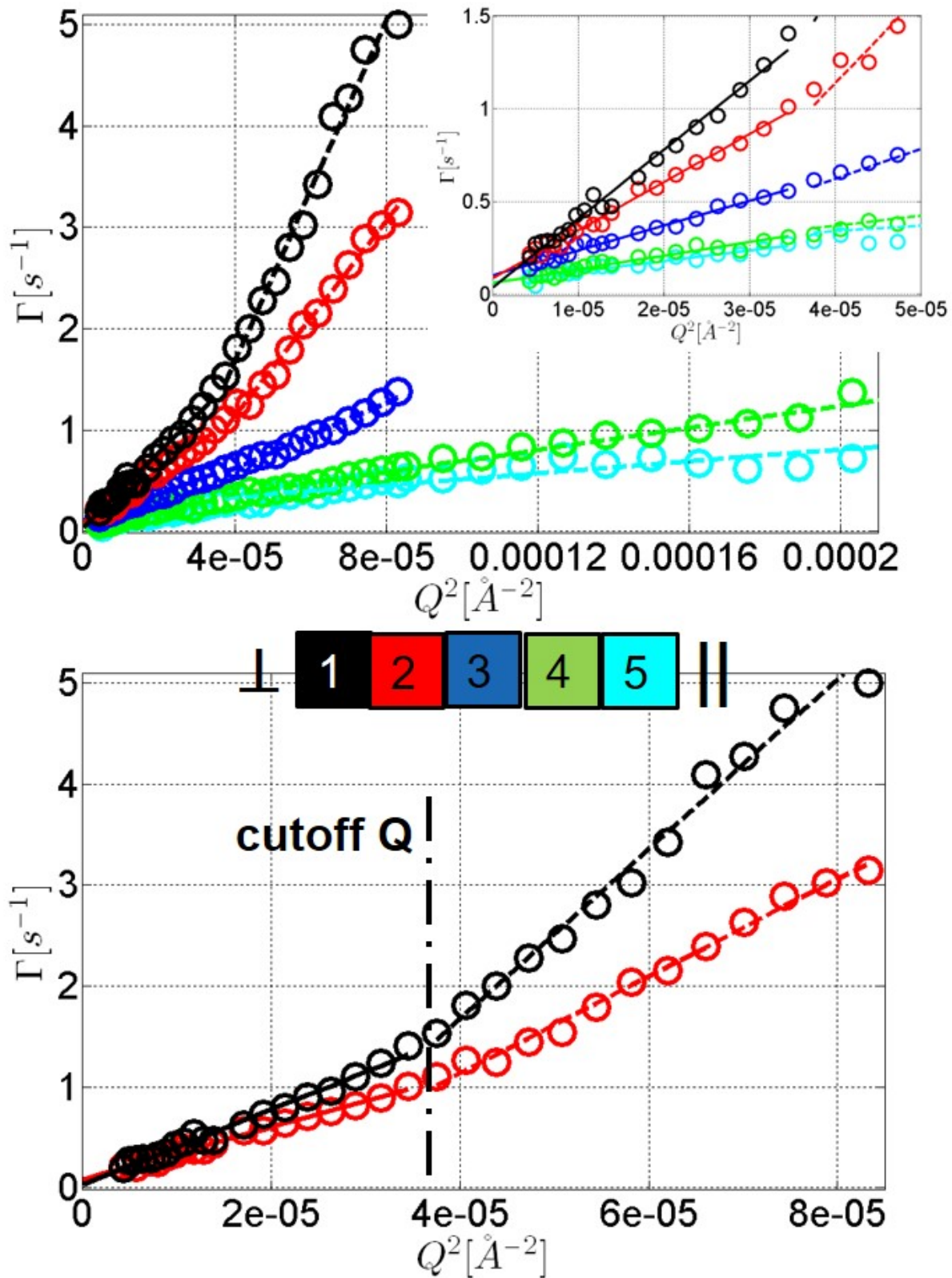


Figure 7.23.: The relaxation rate as a function of Q^2 : top - for 5 different angles with according fits as a function of Q^2 . The inset shows the area close to the point of the origin; bottom - for 2 different angles with according fits as a function of Q^2 , in order to show clearly the point of change of the Q^2 -dependence. The according fits of relaxation rate are shown with solid lines for $Q^2 < 3.6 \times 10^{-5}$ Å⁻² and dashed lines for $Q^2 > 3.6 \times 10^{-5}$ Å⁻².

Again a look on the linecuts along specific constant Q and ϕ^B values will give insight about the detailed behaviour of the relaxation rate. From the plot on the left of fig. 7.22 is evident that $\Gamma < 5\text{ s}^{-1}$ and the dynamics perpendicular to the field are 2–5 times faster than parallel to it. At small Q 's, $\Gamma^{90^\circ} \approx 2 \cdot \Gamma^{0^\circ}$, but with increasing Q it reaches $\Gamma^{90^\circ} \approx 4.5 \cdot \Gamma^{0^\circ}$. The $\Gamma(\phi^B)$ curves have a paraboloid shape with a centre at $\phi^B \approx 0^\circ$.

In fig. 7.22 on the right the relaxation rate is plotted as a function of Q . From this plot it is evident that the system dynamics increase up to a factor of 10, if the values at the smallest Q are compared to the values at the highest one. This increase is ϕ^B -independent. It is obvious that $\Gamma \propto Q$. In addition, it seems like the curve changes the slope around $Q = 0.006 \text{ \AA}^{-1}$. This Q corresponds to an interparticle distance of $d = 105 \text{ nm}$. Due to this the relaxation rate was fitted as a function of Q^2 for the regions $Q^2 < 3.6\text{e-}5 \text{ \AA}^{-2}$ (solid lines) and $Q^2 > 3.6\text{e-}5 \text{ \AA}^{-2}$ (dashed lines), as shown in fig. 7.23 at the top. The slopes of both parts are small parallel to the field and high perpendicular to it. The slopes perpendicular to the field are roughly 6.5 and 32 times higher than the respective slopes parallel to the field. In the direction $\phi^B \approx 0^\circ$ the slope at smaller Q is higher than the one at higher Q . In the direction $\phi^B \approx 90^\circ$ it is vice versa. In fig. 7.23 on the bottom the magnified view of two curves of relaxation rate versus Q^2 for $\phi^B \approx 60^\circ$ and $\phi^B \approx 90^\circ$ is shown. These curves illustrate best the cutoff point and the change of slope.

The fits show that the relaxation rate is in general proportional to Q^2 for the anti-nematic phase at $c = 16 \text{ vol\%}$. But there are two different areas - for displacement lengths $d < 105 \text{ nm}$ and $d > 105 \text{ nm}$. For all Q the dynamic parallel to the field are slower than perpendicular to it. For $\phi^B \approx 40^\circ$ the slope of the fit is almost the same for the whole Q -range. But for angles $\phi^B < 40^\circ$ the slope of the fits in the region $d > 105 \text{ nm}$ is higher than in the area with $d < 105 \text{ nm}$ and for $\phi^B > 40^\circ$ vice versa. The fitted curves at low Q values cross $Q = 0 \text{ \AA}^{-1}$ close to the point of origin.

Short summary The Q^2 proportionality of relaxation rate points towards diffusive motion in the anti-nematic phase at $c = 16 \text{ vol\%}$. The slopes of the curves $\Gamma(Q) \propto Q^2$ represent the diffusion constants, as described in Section 5.3. Here the slope at Q lower than cutoff Q is denoted with subscript 1 and the one at Q higher than cutoff Q with 2. This diffusion coefficients are higher perpendicular to the applied magnetic field than parallel to it, but in all directions it can be separated into two different regimes. Perpendicular to the field the slope is higher for the length scales $d < 105 \text{ nm}$ than for $d > 105 \text{ nm}$. Parallel to the field the slope for the distances $d > 105 \text{ nm}$ is higher than at shorter length scales. The relaxation rate in the anti-nematic phase at $c = 16 \text{ vol\%}$

is up to 10 times faster as relaxation rates seen before and shows values $\Gamma < 5 \text{ s}^{-1}$. The important parameters are again summarized in fig. 7.24.

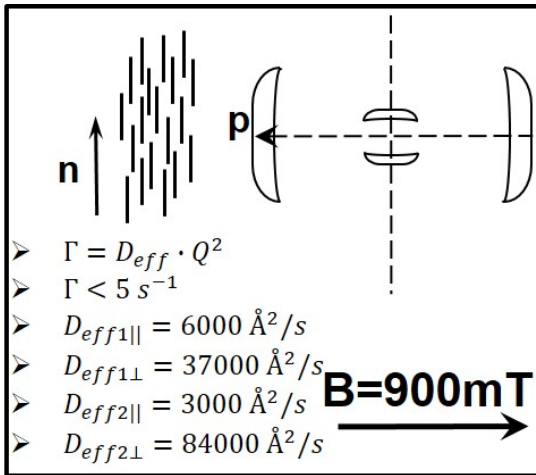


Figure 7.24.: Summary of the evaluation of the anti-nematic phase at $c = 16 \text{ vol}\%$.

Comparison of the microscopic dynamics in the nematic (N) and the anti-nematic (AN) phases for $c = 16 \text{ vol}\%$

In order to understand the dynamics of the mixed phases the dynamics of the non-mixed nematic and anti-nematic phases have to be compared. For this understanding the relaxation rate Γ and the relaxation exponent γ are compared, because the behaviour of these two values indicates the underlying microscopic dynamics of the phases. For comparison reasons we will use phase abbreviations N (nematic) and AN (anti-nematic) as subscripts. In figures 7.17, 7.21, 7.18 and 7.23 the maps of the relaxation rates and the relaxation exponents as well as the respective curves along selected Q - and ϕ^B -values for the relaxation rate are shown.

The nematic phase N shows two different areas for the relaxation exponent with $\gamma_N < 1$ for $\phi^B \approx 0^\circ$ and with $\gamma_N \geq 1$ for the directions not parallel to the applied magnetic field. For the anti-nematic phase AN the relaxation exponent is $\gamma_{AN} \approx 0.5$, which is true for the whole area of the Q - ϕ^B -map.

For both phases the minima of the relaxation rate maps are at low Q and along the direction parallel to the applied magnetic field. The maxima are roughly perpendicular to the field and at high Q values. Nevertheless these similarities, the maximal values are 10 times higher for the anti-nematic phase ($\Gamma_N < 0.5 \text{ s}^{-1}$ and $\Gamma_{AN} < 5 \text{ s}^{-1}$). The areas of maximal values are much narrower and the decrease is much faster for the anti-nematic phase as well. The difference is striking, when comparing fig. 7.18 and 7.23.

Looking at the relaxations rates as a function of ϕ^B it is apparent that the curves have different shapes - funnel-like for the nematic phase and parabolic for the anti-nematic phase. The shape of Γ_{AN} versus ϕ^B curves is much wider for the anti-nematic phase than for the nematic. For the nematic as also for the anti-nematic phase the

relaxation rate has low values along the direction parallel to the applied magnetic field and higher values if the direction is deviating. Nevertheless this similar trend, the anti-nematic phase shows much faster dynamics and different relaxation rate changes with dependence on ϕ^B . In fig. 7.25 ratio maps are shown, which were calculated by dividing the values of the relaxation rate (left) and relaxation exponent (right) for the anti-nematic phase by the corresponding values of the nematic phase.

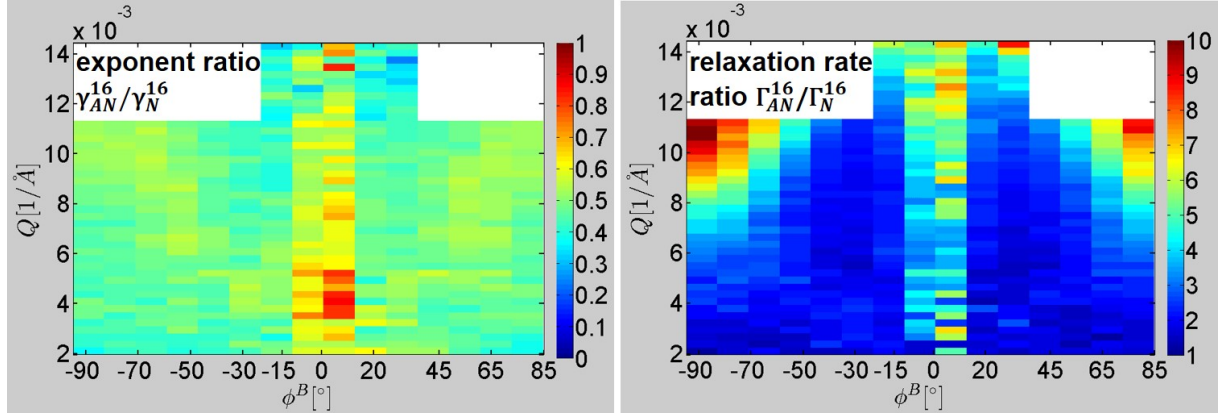


Figure 7.25.: Ratio maps calculated for $c = 16$ vol% by dividing the values of relaxation exponent (left) and the relaxation rate (right) of the anti-nematic phase by the respective values of the nematic phase.

The ratio map for the relaxation exponent shows that the exponent of the nematic phase is roughly two times higher than the exponent of the anti-nematic phase. The only exception is an area at $\phi^B \approx 0^\circ$, where the values in between 0.5 and 1 indicating that the difference parallel to the field is less pronounced. The ratio map of the relaxation rate shows that the anti-nematic phase is always faster than the nematic phase. At low Q and perpendicular to the applied field as well as along $\phi^B \approx \pm 40^\circ$ the anti-nematic phase is only 1.1 faster, but in the directions perpendicular to the magnetic field and at high Q values it reaches a factor of 10. Also parallel to the applied magnetic field the anti-nematic phase is much faster than the nematic phase - up to a factor 7.

The most crucial difference is visible in fig. 7.18 on top and in fig. 7.23. The Q -dependence is different for both phases. The nematic phase shows $\Gamma_N \propto Q$. For the anti-nematic phase the relaxation rate is $\Gamma_{AN} \propto Q^2$ and additionally it has two different Q^2 dependence regions, with a cutoff point at $Q \approx 0.006 \text{ \AA}^{-1}$.

The pivotal point of the comparison is that the initial proportionality of the relaxation rate $\Gamma_N \propto Q$ changed to $\Gamma_{AN} \propto Q^2$, accompanied by the decrease of the relaxation exponent. As a result of this change the particles in the suspension showed much faster dynamics. This is an essential fact, because the platelets in the suspension with $c = 16$ vol% realigned from a dominant orientation with the long axis parallel to the magnetic field in the nematic phase (N) ($\mathbf{n} \parallel \mathbf{m}$) to an orientation perpendicular to the field in the anti-nematic phase (AN) ($\mathbf{n} \perp \mathbf{m}$). This realignment is accompanied by

a major change of the dynamics. Not only did the particles in the suspension speed up, but also the nature of the motion changed from ballistic to diffusive. The diffusive motion in the anti-nematic phase shows differences depending on the length scale, too. The crucial observations in the nematic and anti-nematic phases are summarized in fig. 7.26.

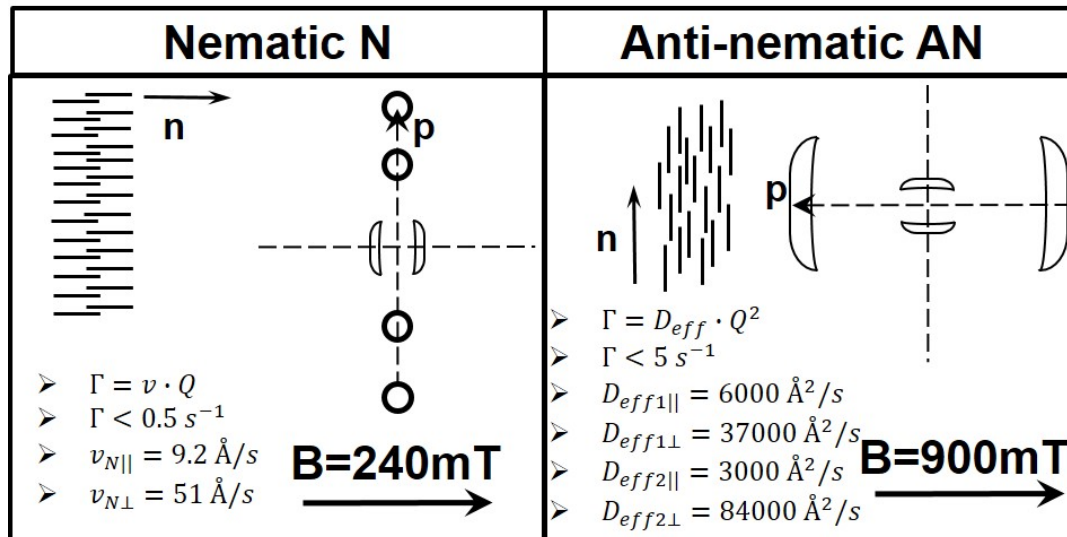


Figure 7.26.: Summary of the evaluation of the nematic and anti-nematic phases at $c = 16 \text{ vol\%}$.

7.2.3. Comparison of the dynamics in the nematic and anti-nematic phases of 20 vol%- and 16 vol%-suspensions

The nematic phase N showed for both concentrations ($c = 16\text{ vol}\%$ and $c = 20\text{ vol}\%$) a similar behaviour of the relaxation rate with $\Gamma \propto Q$. At both concentrations the relaxation rates increase linear with increasing Q . The peak values are higher for the 16 vol%-suspension, where the rate reaches $\Gamma_N^{16} = 0.5\text{ s}^{-1}$. The 20 vol%-suspension has a maximum value of the relaxation rate $\Gamma_N^{20} \approx 0.3\text{ s}^{-1}$. The relaxation rate is low parallel to the magnetic field and increases with increasing absolute values of ϕ^B . The maxima for a 20 vol%-suspension are $\phi^B \approx \pm 50^\circ$, at the lower concentration the maxima are at $\phi^B \approx \pm 65^\circ$.

For both concentrations the behaviour of the particles in the nematic phase is similar. The platelets partially aligned with the long axis parallel to the magnetic field exhibiting ballistic motion in all directions. The motion parallel to the field is much slower than the motion perpendicular to it. The slopes of the $\Gamma \propto Q$ -proportionality are higher for suspension with $c = 16\text{ vol}\%$ in all directions. In this case the slopes are a direct measure of the drift velocity of the particles.

The anti-nematic phase AN at $c = 20\text{ vol}\%$ shows a similar behaviour to the nematic phases of both concentrations. The maximum relaxation rate is also around $\Gamma_{AN}^{20} \approx 0.3\text{ s}^{-1}$, which is very close to the maximal values for the nematic phase at $c = 20\text{ vol}\%$ and close to the nematic phase at $c = 16\text{ vol}\%$.

The maxima of the relaxation rate of both concentrations in the nematic and anti-nematic phase are along the directions perpendicular to the applied field. The map of the relaxation rate at $c = 16\text{ vol}\%$ in the anti-nematic phase seems to show a similar behaviour, but the maximal values are much higher with $\Gamma_{AN}^{16} \approx 5\text{ s}^{-1}$. Also the areas of low values are much wider. From the curves of the relaxation rate plotted as a function of ϕ^B it is apparent that both nematic phases and the anti-nematic phase at $c = 20\text{ vol}\%$ have funnel shaped curves with minima at $\phi^B \approx 0^\circ$. The values increase with increasing absolute value of ϕ^B until they reach a plateau. In contrast to these three phases the anti-nematic phase at $c = 16\text{ vol}\%$ shows a parabolic shape.

The most significant difference is visible in the curves of the relaxation rate plotted as a function of Q . In these plots, both nematic phases and the anti-nematic phase at $c = 20\text{ vol}\%$ show a linear dependence of the relaxation rate in Q . For these phases the slope of the curves grows with increasing absolute value of ϕ^B . This is also valid for the slopes of the curves in the anti-nematic phase at $c = 16\text{ vol}\%$, but in this case the relaxation rate is proportional to Q^2 and there are two areas of proportionality with a cutoff point at $Q \approx 0.006\text{ \AA}^{-1}$.

In addition, differences in the relaxation exponents γ were noticed. At $c = 20\text{ vol}\%$ the relaxation exponent is $1 \leq \gamma^{20} \leq 1.5$ parallel to the magnetic field and $\gamma^{20} \approx 1.7$

for all other directions. Suspensions at $c = 16$ vol% show significant differences. In the nematic phase N the relaxation exponent is $\gamma_N^{16} < 1$ parallel to the magnetic field and $1 \leq \gamma_{AN}^{16} \leq 1.5$ for all other directions, whereas in the anti-nematic phase along all directions the relaxation exponent is $\gamma_{AN}^{16} \approx 0.5$. The most crucial observation for nematic and anti-nematic phases at $c = 20$ vol% and $c = 16$ vol% are shown in fig. 7.27 in comparison.

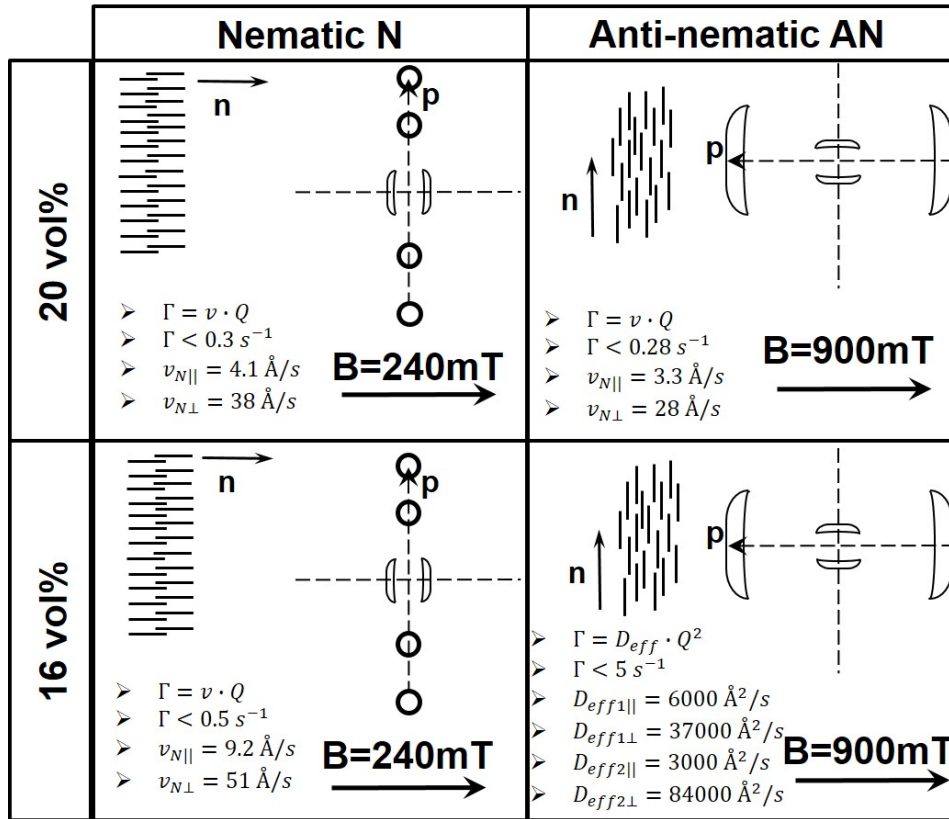


Figure 7.27.: Summary of the evaluation of the nematic and anti-nematic phases at $c = 20$ vol% and $c = 16$ vol% in comparison.

7.2.4. The microscopic dynamics of the mixed phases

The structural investigation revealed that the structural phases could be divided into three categories: patterns aligned with main axis \mathbf{p} perpendicular to the direction of the applied magnetic field \mathbf{m} , patterns aligned (mostly) parallel to the applied magnetic field ($\mathbf{p}||\mathbf{m}$ and pattern consisting of contributions of both. These patterns were assigned to the respective liquid crystal phases - the nematic (N), the anti-nematic (AN) and the mixed (M). The analysis of the data from mixed phases (M) will be described in following.

XPCS analysis of the mixed phase at $B = 370$ mT for $c = 20$ vol%

Preamble The scattering pattern in fig. 6.8 at the bottom left shows scattering features, which suggest, that at $c = 20$ vol% and $B = 370$ mT both phases, the nematic (N) and the anti-nematic (AN) are present. Here both phases are in equilibrium at angles, which are neither parallel nor perpendicular to the magnetic field. The nematic feature is at $\phi^B \approx -110^\circ$ and accordingly at $\phi^B = 70^\circ$. The anti-nematic feature is smeared, but the maximum intensity is at $\phi^B \approx 5^\circ$ and accordingly at $\phi^B \approx -175^\circ$. A presmectic order is present in the nematic phase, but in the direction perpendicular to the nematic orientation direction it is lost and the width of the scattering peaks is broader.

Fig. 7.28 shows the corresponding g_2 -functions. The order of the plots and colour code were kept identical to the previous sections. The solid lines in the images show fits of the $g_2(Q, t)$ data using eq. 7.1.

From a first glance at the data it is apparent that the relaxation time τ_c is larger parallel to the field than perpendicular to it. The contrast decreases and the dynamics gets faster with increasing Q for both directions. The curves show compressed shape. The plots show that independent of Q the dynamics get slower when the angle changes from $\phi^B \approx -110^\circ$ to $\phi^B \approx 0^\circ$. The curves for the first three angles show roughly similar relaxation times and shapes. The curve parallel to the field shows a much higher relaxation time and a different shape. The solid lines in the plots on the right display fits to the data using eq. 7.1.

Fig. 7.29 shows 2D-maps with Q on the vertical axis and ϕ^B on the horizontal axis of the baseline values b (top left), the contrast values β (top right), the decay exponent γ (bottom left) and the relaxation rate Γ (bottom right).

Baseline b and contrast β In the mixed phase the baseline values are close to the expected values of $b = 1.002$, as shown in fig. 7.29 top left. Like in the nematic phase there is an exception of an arc of elevated values. These values are not symmetric around $\phi^B \approx 0^\circ$. They start at low Q 's around $\phi^B \approx -20^\circ$ and end at high Q at $\phi^B \approx -86^\circ$ and $\phi^B \approx 40^\circ$. This arc corresponds to the partitions along the border of the scattering

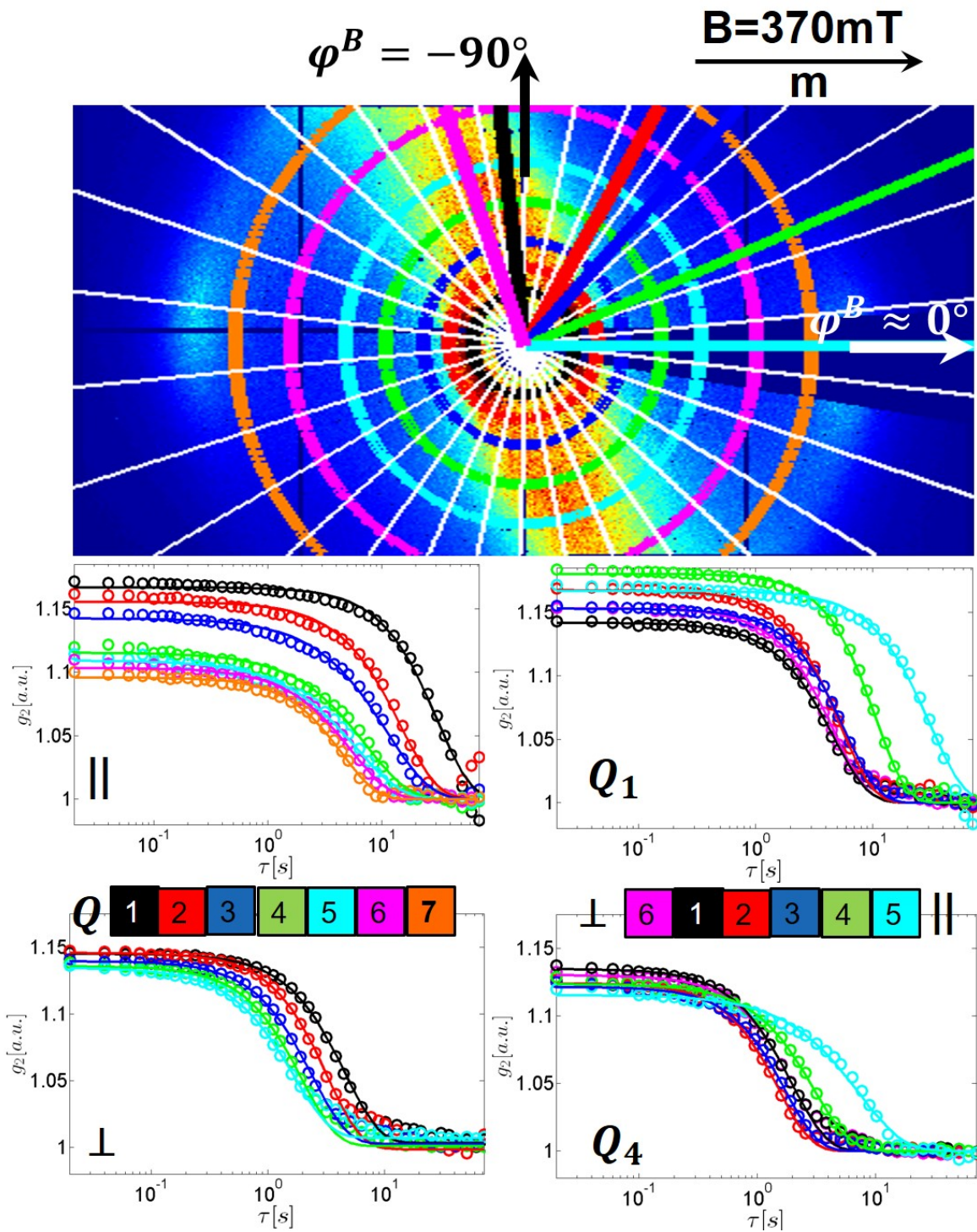


Figure 7.28.: Top: SAXS scattering pattern with Q rings and ϕ^B lines as explained in Section 7.1. The structural peaks are found near Q_1 and Q_7 ($\parallel \mathbf{m}$) and Q_4 ($\perp \mathbf{m}$), which are respectively shown as black, orange and green circles. Below: Examples of the calculated $g_2(Q, \phi^B)$ -functions for the mixed phase. Left: for different Q 's at $\phi^B \approx 0^\circ$ (centre) and at $\phi^B \approx -90^\circ$ (bottom). Right: for different directions in ϕ^B at $Q_1 = 0.0024 \text{ \AA}^{-1}$ (centre) and $Q_4 = 0.0064 \text{ \AA}^{-1}$ (bottom). Solid lines display fits to the data using eq. 7.1.

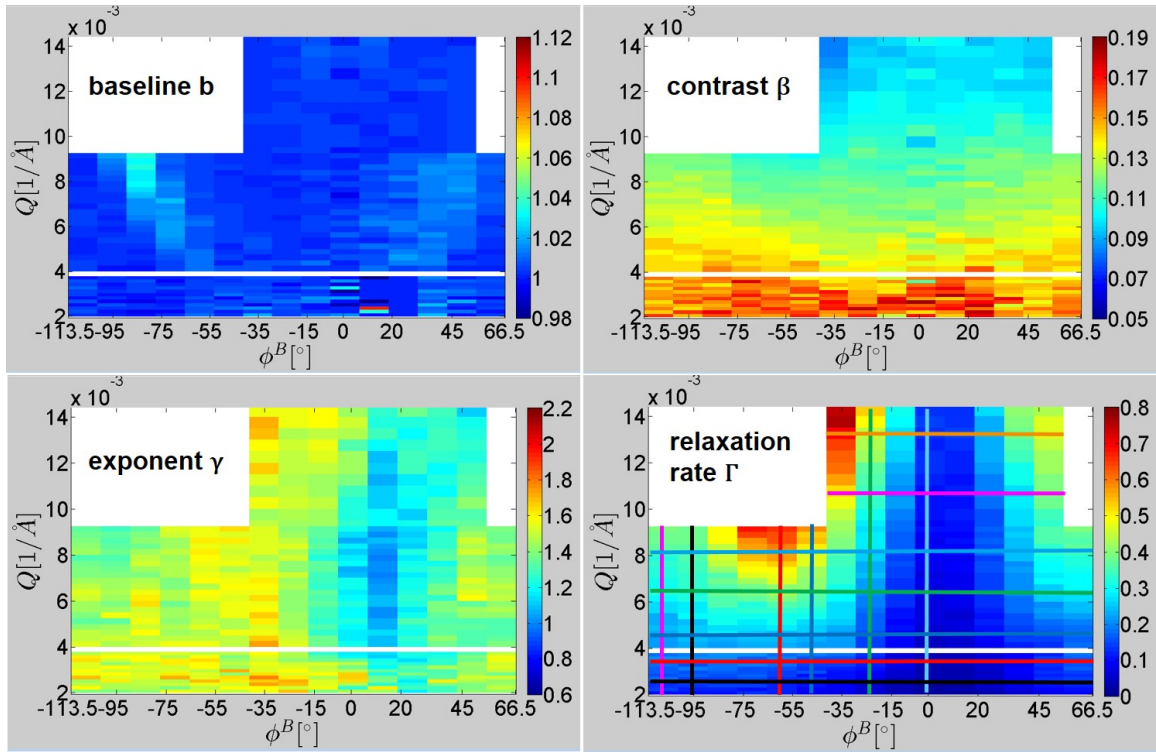


Figure 7.29.: Maps of the baseline values b on the top left, the contrast values β on the top right, the relaxation exponent values γ on the bottom left and the relaxation rate values Γ on the bottom right for mixed phase M. The obtained values are plotted as 2D-maps with Q on the vertical axis and ϕ^B on the horizontal axis. The coloured lines in the Γ map indicate Q values $Q_1 - Q_7$ and ϕ^B values $\phi_{\parallel}^B = 0^\circ$ to $\phi_{\perp}^B = 90^\circ$, as described before. These values are also valid for other maps and correspond to the shown g_2 -functions evaluated on the same Q and ϕ^B values.

feature for the nematic phase, which is also not symmetric with respect to $\phi^B = 0^\circ$ (fig. 6.8 bottom left). The calculated average standard deviation is $\overline{\Delta b} = \pm 0.003$.

The contrast map is shown in fig. 7.29 (top right). The contrast decreases with increasing Q and, as already mentioned before, it will be discussed together with other phases in Section 7.3.1. The low values form a parabolic shape. Therefore the decrease is slower for higher ϕ^B values. The strongest decrease is at $\phi^B \approx -20^\circ$. The contrast values show a maximum of $\beta_{max} = 0.184$, which is close to the expected value of $\beta_{aerogel} = 0.175$. The average standard deviation calculated for the contrast is $\overline{\Delta \beta} = \pm 0.005$.

Stretching exponent γ and relaxation rate Γ The relaxation exponent is plotted as a Q - ϕ^B -map in fig. 7.29 on the bottom left. There is no significant dependence of γ on Q , but roughly along $\phi^B \approx 10^\circ$ an area of lower γ -values is visible with $\gamma \approx 1.1 \pm 0.2$. In all other directions the relaxation exponent is $\gamma \approx 1.5 \pm 0.1$. The average standard deviation of the relaxation exponent is $\overline{\Delta \gamma} = \pm 0.07$.

The map of the relaxation rate Γ , which is shown in fig. 7.29 on the bottom right, shows similar features as for the nematic and anti-nematic phases at $c = 20$ vol%.

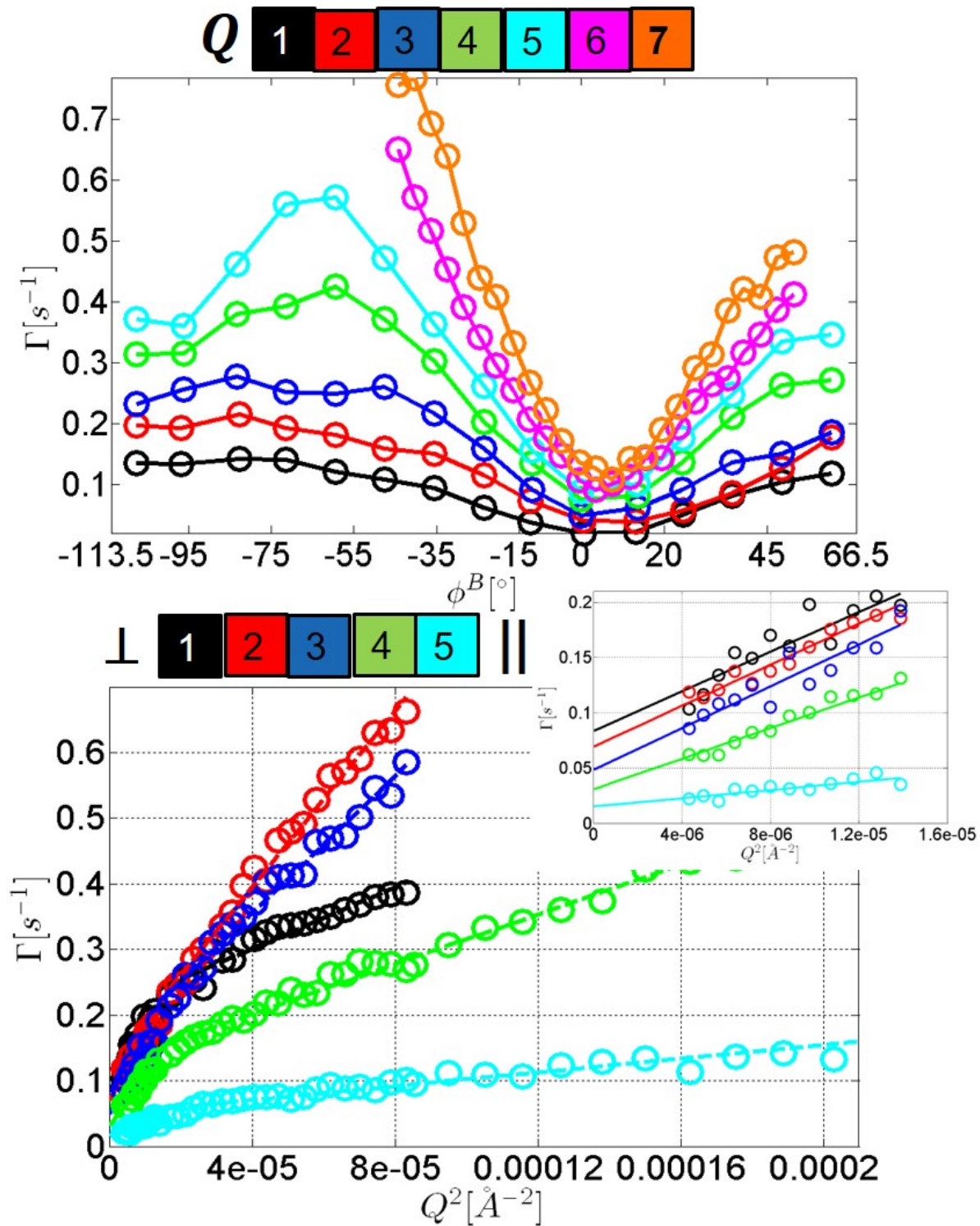


Figure 7.30.: Top: relaxation rate Γ plotted as a function of ϕ^B for different Q 's. The solid lines are guides to the eye. Bottom: relaxation rate Γ plotted as a function of Q for different ϕ^B 's and according fits as function of Q^2 shown by straight lines for $Q^2 < 0.000013 \text{ \AA}^{-2}$ and dashed lines for $Q^2 > 0.000013 \text{ \AA}^{-2}$. The inset shows the area close to the point of the origin for the first fit.

The position of the peaks of high Γ values is at $\phi^B \approx \pm 60^\circ$, suggesting a symmetry in respect to $\phi^B \approx 0^\circ$, as also displayed for other phases at this concentration. The distinguishing feature is that the centre of the area of low Γ values is to be found around $\phi^B \approx 10^\circ$. The average relative standard deviation of the relaxation rate was estimated as $\Delta\Gamma/\Gamma = \pm 4 \text{ vol\%}$.

On the left of fig. 7.30 the relaxation rate Γ is plotted as a function of ϕ^B . The minimum of all curves is around $\phi^B \approx 5^\circ$. There is an asymmetry of the slope to the left and to the right. The maximum value increases with increasing Q and is located at $\phi^B \approx -65^\circ$. For $Q_4 = 0.0064 \text{ \AA}^{-1}$ and $Q_5 = 0.081 \text{ \AA}^{-1}$ the curves decrease again for $\phi^B < -70^\circ$. It is evident that $\Gamma < 0.7 \text{ s}^{-1}$ and the dynamics perpendicular to the field are ≈ 5 times faster than parallel to it. The shape of the $\Gamma(\phi^B)$ curves is alike to the shape of the curves of the anti-nematic phase - the shape of an asymmetric funnel.

In the plot on top of fig. 7.30 the relaxation rate Γ is plotted as a function of Q . It is evident that $\Gamma \propto Q^2$. The slopes of the curves $\Gamma(Q) \propto Q^2$ represent the diffusion constants, as described in section 5.3. However, the dependence $\Gamma(Q) \propto Q^2$ is not constant. At $Q \approx 0.0036 \text{ \AA}^{-1}$ a change of the slope was observed. Both parts were fitted by quadratic functions. Again the slopes parallel to the field are smaller than the ones perpendicular to it. The ratio factors are roughly 7 and 5 respectively. In the mixed phase the slope at small Q is always higher than the slope at high Q . The fitted curves for low Q values cross $Q = 0 \text{ \AA}^{-1}$ close to the point of origin. The summary of the data extracted from the analysis of the mixed phase at $c = 20 \text{ vol\%}$ is shown in fig. 7.31.

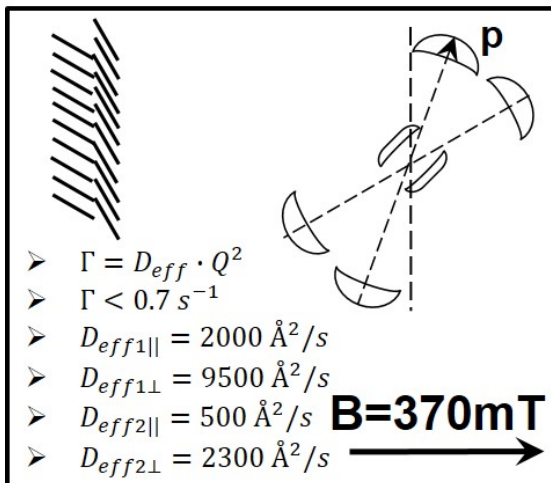


Figure 7.31.: Summary of the evaluation of the mixed phase at $c = 20 \text{ vol\%}$.

XPCS analysis of the mixed phase at $B = 370$ mT for $c = 16$ vol%

Preamble The presence of three phases was concluded from the observations based on the scattering features at $c = 16$ vol% and $B = 370$ mT, which is shown in fig. 6.7 on the bottom left. The main scattering feature at $\phi^B \approx 90^\circ$ corresponds to the nematic phase (N). Additionally, two features are observed roughly in the direction of the anti-nematic phase (AN). The scattering features are at $\phi^B \approx 20^\circ$ and $\phi^B \approx -160^\circ$, which correspond to positive anti-nematic phase (pAN) and negative anti-nematic phase (nAN), respectively. The presmectic order for pAN and nAN is lost, but is still present in the nematic phase (N).

The relaxation time τ_c is higher parallel to the field than perpendicular to it, which is apparent from fig. 7.32, where g_2 -functions are shown. Again, the contrast decreases and the dynamics get faster with increasing Q for both directions. The increase of the dynamics at $\phi^B \approx 0^\circ$ is less pronounced. The plots on the right show that at Q_1 the dynamics are nearly independent of ϕ^B . The contrast stays nearly constant at this Q . At Q_4 the dynamics get slower when the angle changes from $\phi^B \approx -90^\circ$ to $\phi^B \approx 0^\circ$ and the contrast increases likewise. The shape of the curves in all plots can be described by a stretched single exponential decays. The solid lines in the plots on the right show fits to the data using eq. 7.1.

Fig. 7.33 shows 2D-maps of the four parameters extracted from these fits: baseline b , contrast β , shaping exponent γ and relaxation rate Γ , which are plotted in the same way as before.

Baseline b and contrast β The baseline of the mixed phase at $c = 16$ vol% shows similarities to the mixed phase at $c = 20$ vol% and to both nematic phases. The values of the baseline are for most cases close to the expected values of $b = 1.002$, obtained from a low concentration sample. Compared to the expected value of b and taking the average standard deviation into account it is apparent that there are only a few values, which deviate from the expected values. These values form an arc, which begins at low Q and $\phi^B \approx 0^\circ$ and ends at the highest accessible Q 's around $\phi^B \approx \pm 80^\circ$. There are also some increased values at the highest Q around $\phi^B \approx 0^\circ$. These are locations in the Q - ϕ^B -map, which correspond to borders of a scattering feature. Therefore there are positions at which the intensity distribution in the Q - ϕ^B -partition are inhomogeneous, as already explained for the pure phases. This can lead to the diverging values of the baseline. The mean standard deviation arising from the data and the fit is $\overline{\Delta b} = \pm 0.001$.

The contrast values are plotted in fig. 7.33 on the top right. The contrast is high at low Q and decreases with increasing Q (see Section 7.3.1). The contrast values have a maximum of $\beta_{max} = 0.178$, which is close to the expected value of $\beta_{aerogel} = 0.175$. The average standard deviation calculated for the contrast is $\overline{\Delta \beta} = \pm 0.003$.

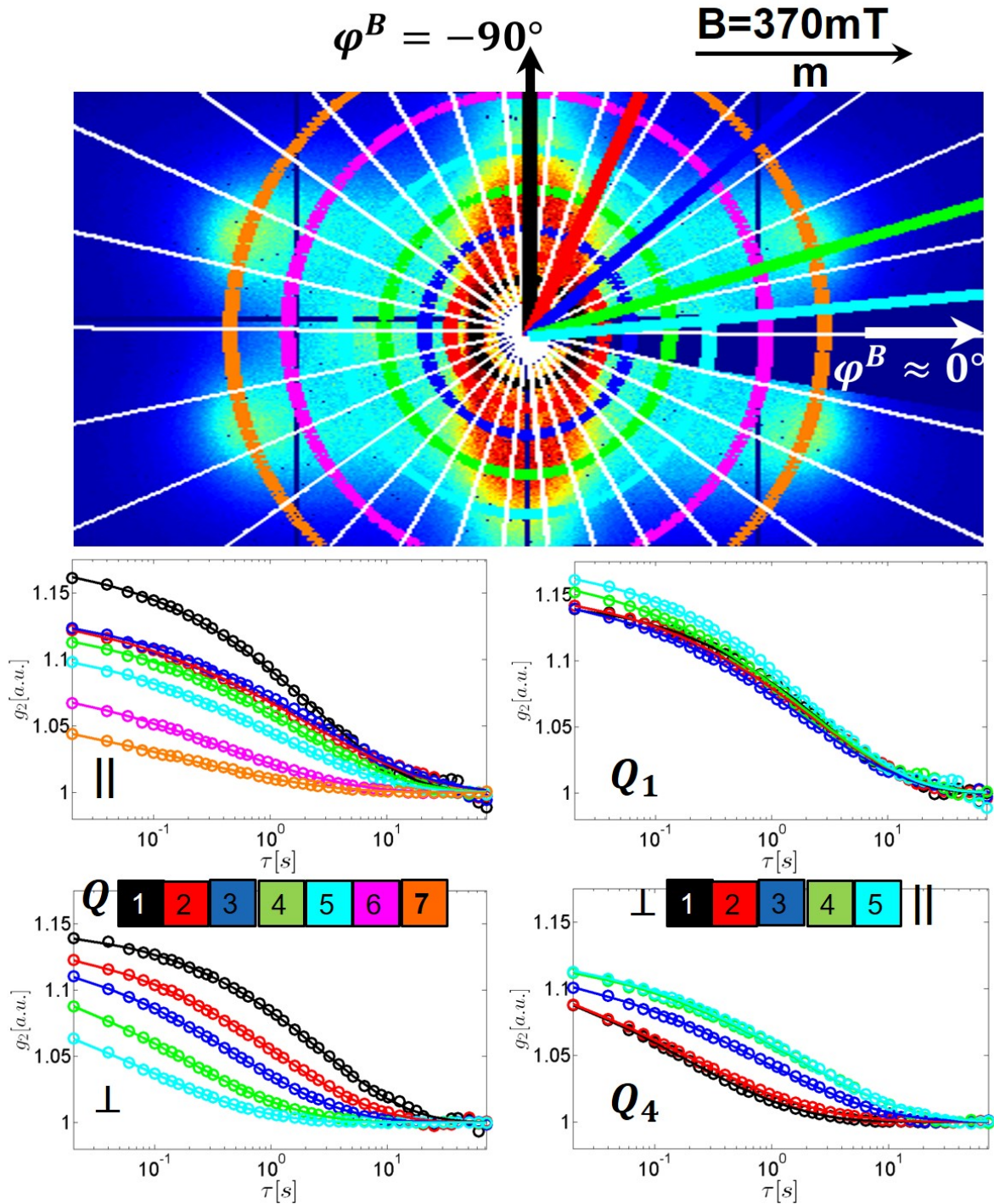


Figure 7.32.: Top: SAXS scattering pattern with Q rings and ϕ^B lines as explained in Section 7.1. The structural peaks are found near Q_1 and Q_7 ($\parallel m$) and Q_4 ($\perp m$), which are respectively shown as black, orange and green circles. Below: Examples of $g_2(Q, \phi^B)$ -functions for the anti-nematic phase. Left: at different Q 's at $\phi^B \approx 0^\circ$ (centre) and at $\phi^B \approx -90^\circ$ (bottom). Right: at different directions in ϕ^B at $Q_1 = 0.0024 \text{ \AA}^{-1}$ (centre) and $Q_4 = 0.0064 \text{ \AA}^{-1}$ (bottom). Solid lines are fits to the data using eq. 7.1.

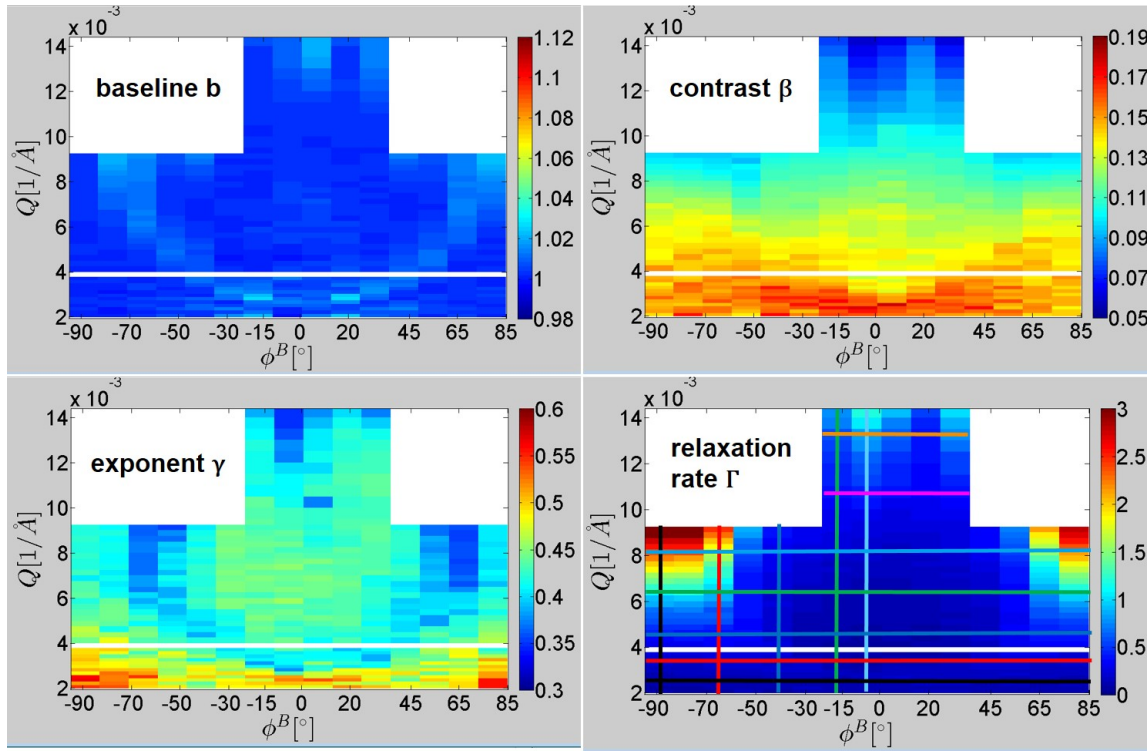


Figure 7.33.: Maps of the baseline values b on the top left, the contrast values β on the top right, the relaxation exponent values γ on the bottom left and the relaxation rate values Γ on the bottom right for mixed phase M. The obtained values are plotted as 2D-maps with Q on the vertical axis and ϕ^B on the horizontal axis. The coloured lines in the Γ map indicate Q values $Q_1 - Q_7$ and ϕ^B values $\phi_{\parallel}^B = 0^\circ$ to $\phi_{\perp}^B = 90^\circ$, as described before. These values are also valid for other maps and correspond to the shown g_2 -functions evaluated on the same Q and ϕ^B values.

Stretching exponent γ and relaxation rate Γ The relaxation exponent, which is plotted as a Q - ϕ^B -map in fig. 7.33 on the left bottom, shows values $\gamma \approx 0.5 \pm 0.1$. There is an area of increased values at low Q 's as well as an area of low values at the highest accessible Q 's. There is also an arc of lower values, which starts at low Q 's and $\phi^B \approx 0^\circ$ and ends at highest accessible Q 's and at $\phi^B \approx \pm 80^\circ$. These values correspond to the accordingly elevated values of the baseline b in the baseline map. If the baseline shifts up the respective g_2 -curve stretches and γ decreases. It can be concluded that the relaxation exponent is $\gamma \approx 0.5$ in all directions and at all Q 's. The average standard deviation is $\overline{\Delta\gamma} = \pm 0.03$.

The relaxation rate Γ is shown in fig. 7.33 on the bottom right. It is low for low Q and increases with increasing Q . The maximal values are at highest accessible Q perpendicular to the magnetic field. At $\phi^B \approx 0^\circ$ an area of low relaxation rate is visible. Here the rate increases first at low Q , decreases later and starts to increase constantly with increasing Q . The average relative standard deviation for relaxation rate is $\Delta\Gamma/\Gamma = \pm 2 \text{ vol\%}$.

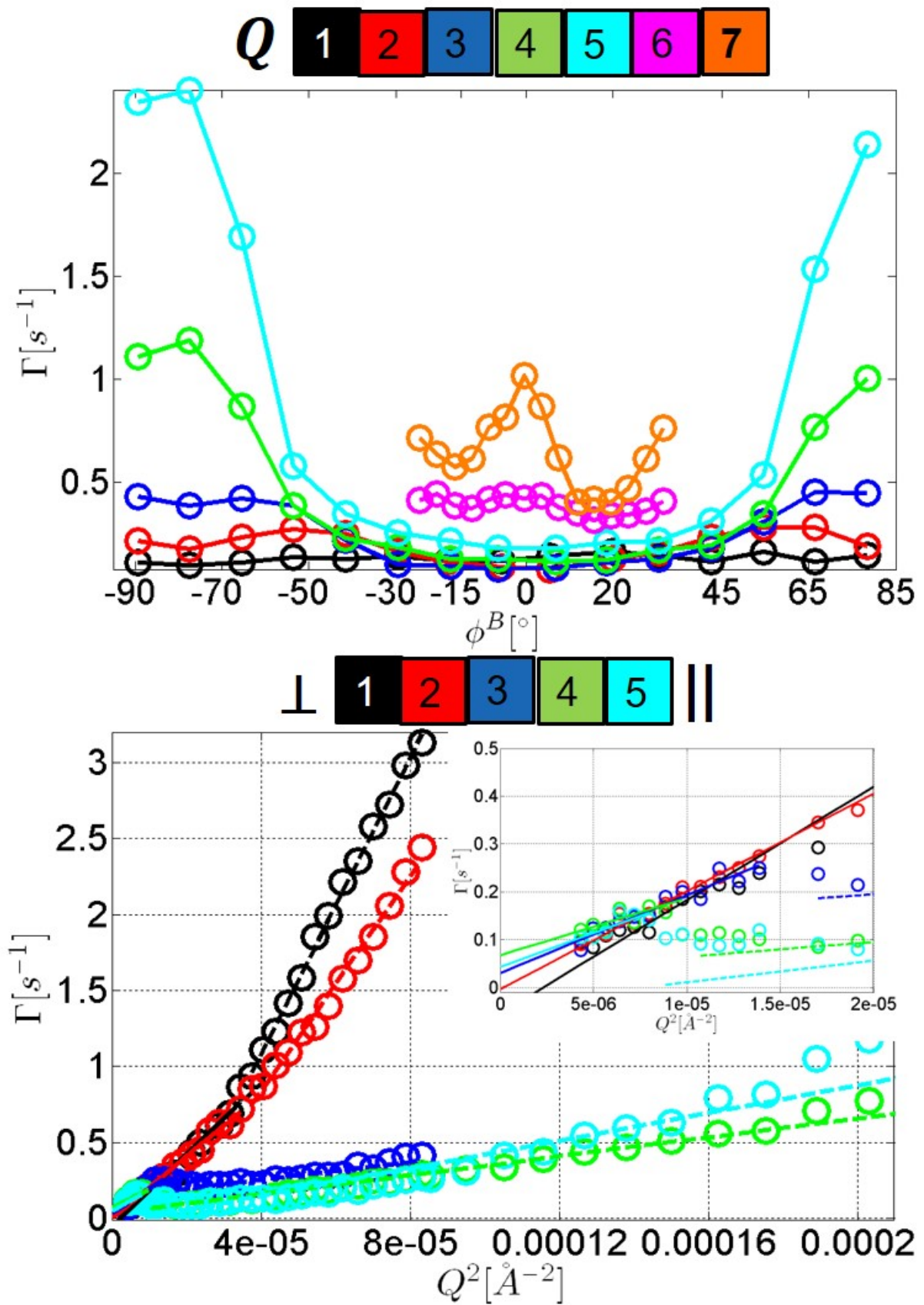


Figure 7.34.: Top: relaxation rate Γ plotted as a function of ϕ^B for different Q 's. The solid lines are guides to the eye. Bottom: relaxation rate Γ plotted as a function of Q for different ϕ^B 's. The fits as a function of Q^2 are shown by straight lines for Q smaller than cutoff Q and with dashed lines for Q higher than cutoff Q . The inset shows the area close to the point of the origin and for the fit at low Q values.

All plots of Γ as a function of ϕ^B (fig. 7.34, top) are centred at $\phi^B \approx 0^\circ$. All of them show a wide plateau of low values around the centre. Along the lowest Q values the relaxation rate stays constant. For all other Q values the $\Gamma(\phi^B)$ curves show a plateau at $-45^\circ < \phi^B < 45^\circ$, after which a steep rise is visible. With increasing Q the values of the minima increase as well as the values of the maxima and the slope in between them. At highest Q an oscillation is visible with a maximum around $\phi^B \approx 0^\circ$ and minima at $\phi^B \approx \pm 15^\circ$. It is evident that the dynamics perpendicular to the field are 5–10 times faster than parallel to it. In addition, the system speeds up with increasing Q , which is almost not observable for $\phi^B \approx 0^\circ$ and has a strong effect with increasing ϕ^B .

In the plot at the bottom of fig. 7.12 Γ is plotted as a function of Q^2 . It is evident that $\Gamma \propto Q^2$ and $\Gamma < 3.2 \text{ s}^{-1}$. The slopes of the curves $\Gamma(Q) \propto Q^2$ represent the diffusion constants, as described in section 5.3. Each curve displays multiple regions of proportionality, which was verified by the fits of quadratic functions to the different regions. At the highest angles ($\phi^B \approx -90^\circ$ and $\phi^B \approx -65^\circ$) the change of the slope is at $Q \approx 0.006 \text{ \AA}^{-1}$, for $\phi^B \approx -40^\circ$ it is at $Q \approx 0.0037 \text{ \AA}^{-1}$ and for the directions parallel to the magnetic field ($\phi^B \approx -20^\circ$ and $\phi^B \approx 0^\circ$) it is at $Q \approx 0.0028 \text{ \AA}^{-1}$. Again the slopes parallel to the field are lower than the ones perpendicular to it, which is a constant trend through all investigated phases and concentrations. This time the ratio factors are 1.5 and 10 respectively. In the mixed phase at $c = 16 \text{ vol\%}$ the slopes of the fits at low Q values is smaller than the slopes of the fits at high Q values perpendicular to the field and vice versa parallel to it. The fitted curves for low Q values cross $Q = 0 \text{ \AA}^{-1}$ close to the point of origin.

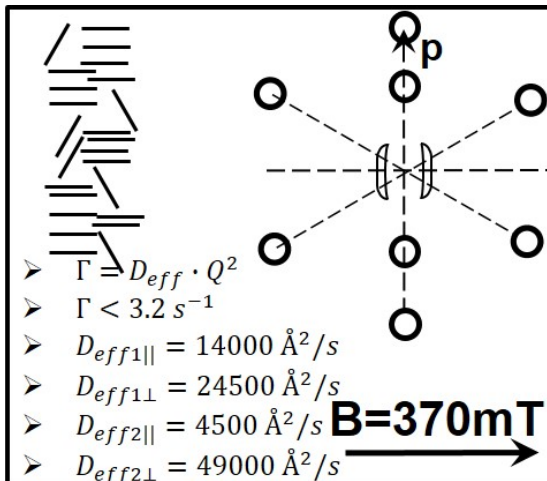


Figure 7.35.: Summary of the evaluation of the mixed phase at $c = 16 \text{ vol\%}$.

Comparison of the dynamics in the mixed phases for 20 vol%- and 16 vol%-suspensions

The mixed phases show significant differences depending on the concentration of the suspension. In fig. 7.36 the Q - ϕ^B -maps of the relaxation exponent γ and the relaxation rate Γ are shown respective on the left for $c = 20$ vol% and on the right for 16 vol% for better comparison.

In the mixed phases the relaxation exponents are different for different concentrations. For $c = 20$ vol% $\gamma_M^{20} \approx 1.5$ for all directions, except $\phi^B \approx 0^\circ$, where $\gamma_M^{20} \approx 1.1 \pm 0.1$. The direction of the minimal exponent is shifted towards positive angles, while it was centred around $\phi^B \approx 0^\circ$ for other phases and concentrations. Meanwhile for $c = 16$ vol% the relaxation exponent is $\gamma_M^{16} \approx 0.5$ for all directions.

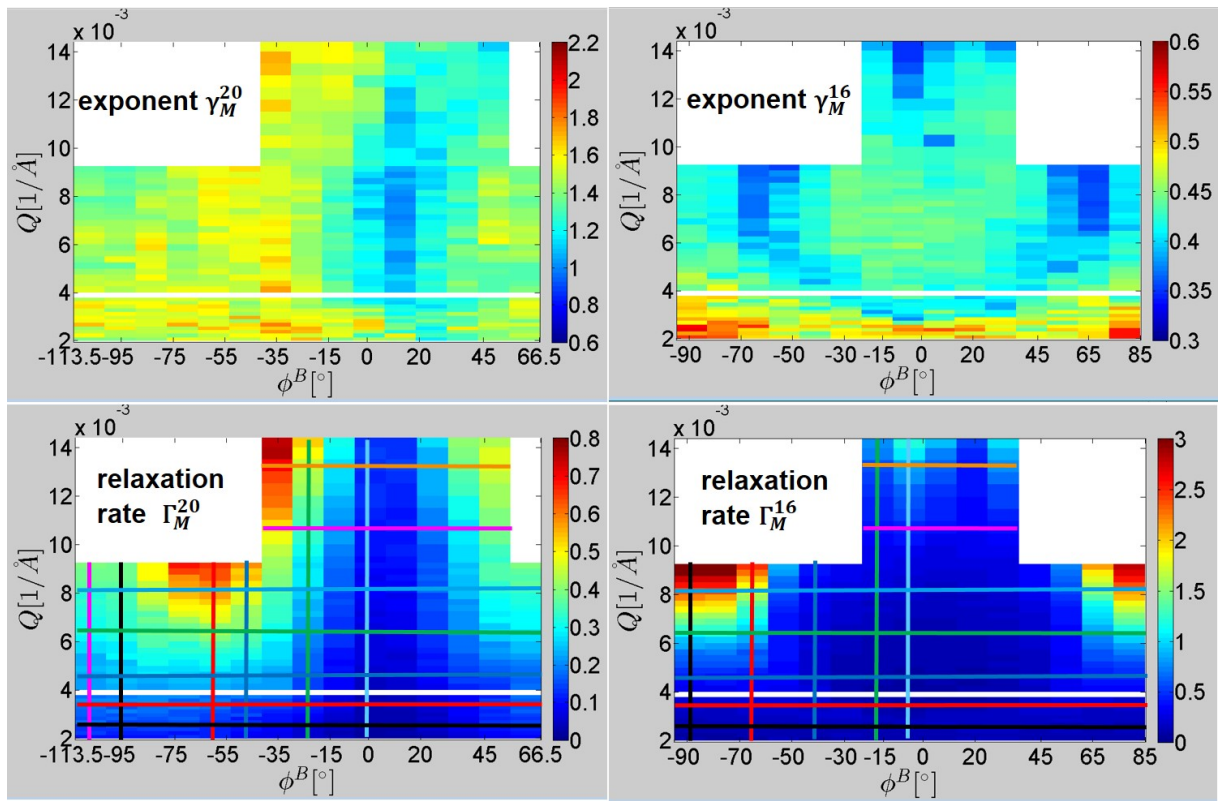


Figure 7.36.: Q - ϕ^B -maps of the exponent γ (top) and relaxation rate Γ (bottom) for mixed phases. Left: for 20 vol%-suspension. Right: for 16 vol%-suspension

The relaxation rates have in common that at low Q values the rates are low and increase with increasing Q . Otherwise the relaxation rate at $c = 16$ vol% shows a much higher maximal value with $\Gamma_M^{16} \approx 3.2 \text{ s}^{-1}$. For $c = 20$ vol% the relaxation rate reaches $\Gamma_M^{20} \approx 0.7 \text{ s}^{-1}$, only. The shape of $\Gamma(\phi^B)$ -curves is different. For $c = 20$ vol% it has narrow minima and reaches a plateau at $\phi^B \approx -60^\circ$, which decreases again for Q_4 and Q_5 at $\phi^B < -70^\circ$, while at $c = 16$ vol% it is constant for the lowest Q and shows a wide minimum with increasing Q 's until at highest Q -values a double minimum arises. At both concentrations $\Gamma(Q) \propto Q^2$. The 20 vol%-suspension shows two regions of

Q^2 -dependence with a common cutoff point at $Q = 0.0036 \text{ \AA}^{-1}$ for different ϕ^B , whereas the 16 vol%-suspension shows changing cutoff point along Q , which varies depending on the investigated direction along ϕ^B .

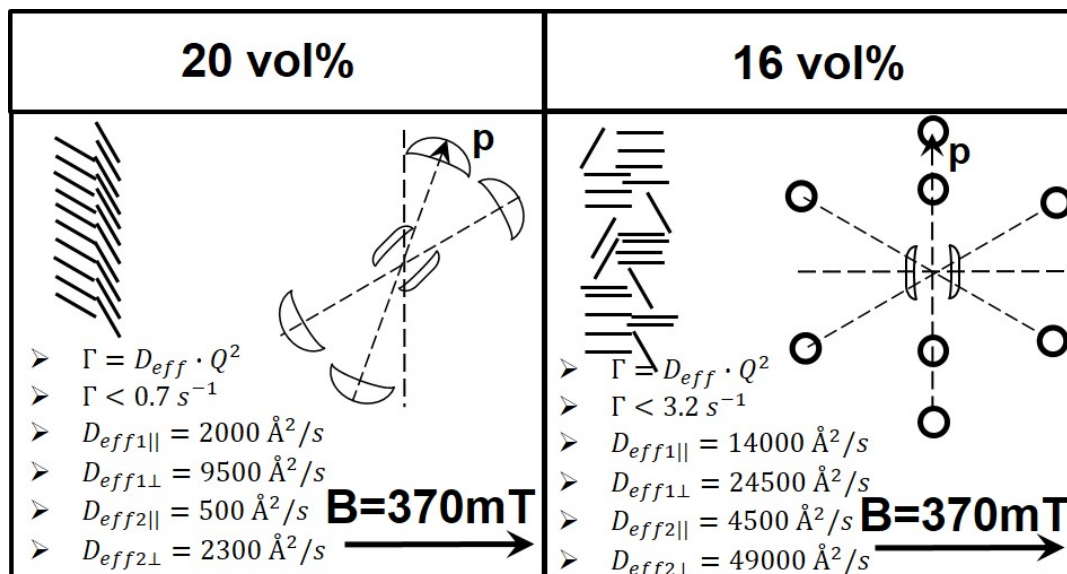


Figure 7.37.: Summary of the evaluation of the mixed phases at $c = 20 \text{ vol}\%$ and $c = 16 \text{ vol}\%$.

7.2.5. Comparison of the dynamics in the nematic and the anti-nematic phases with the dynamics in the mixed phases

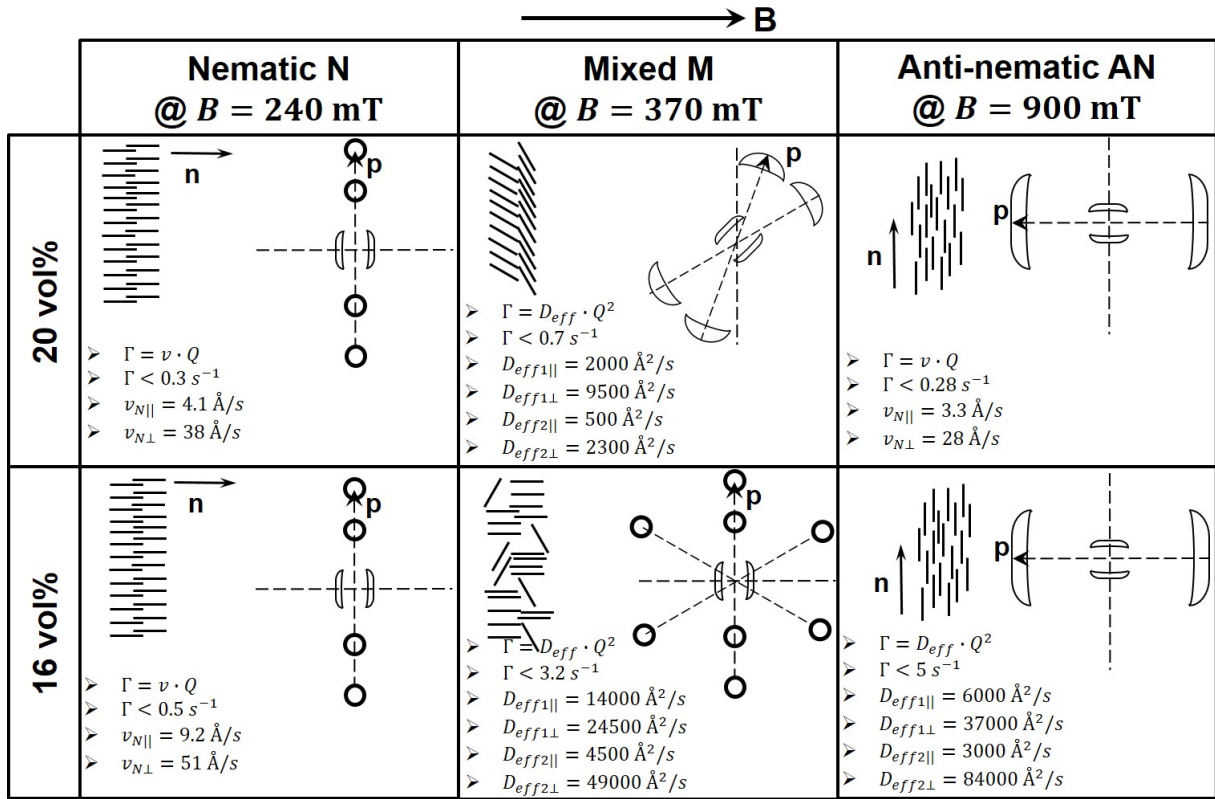


Figure 7.38.: Summary of the evaluation of all phases at $c = 20 \text{ vol}\%$ and $c = 16 \text{ vol}\%$ as comparison.

The relaxation exponents of the 20 vol%-suspension are quite constant independent of the phase. For all three phases along the direction $\phi^B \approx 0^\circ$ $1 \leq \gamma^{20} < 1.5$ and $\gamma^{20} \geq 1.5$ for all other directions. The relaxation rate in the nematic and the anti-nematic phases shows similar trends. The main difference in the mixed phase is the change of the proportionality from $\Gamma \propto Q$ in the nematic and anti-nematic phase to $\Gamma \propto Q^2$ in the mixed phase. In addition the mixed phase shows a higher maximal value of the relaxation rate.

At $c = 16 \text{ vol}\%$ the behaviour is more complex. The relaxation exponent in the nematic phase displays the highest values at this concentration, where $\gamma_N^{16} < 1$ parallel to the magnetic field and $\gamma_N^{16} > 1$ along all other directions. In the mixed and the anti-nematic phases the relaxation exponent drops to $\gamma^{16} \approx 0.5$ for all directions. The relaxation rate shows a large change with increasing B and thus changing phases, too. In the nematic phase the relaxation rate is low and shows similar trends as the nematic and anti-nematic phases at $c = 20 \text{ vol}\%$. Especially the proportionality $\Gamma(Q) \propto Q$ has to be mentioned. In the mixed and anti-nematic phase the proportionality changes to $\Gamma(Q) \propto Q^2$. In both phases two Q -regions with different proportionalities are apparent. In

the anti-nematic phase the change of the proportionality is at the same Q ($Q \approx 0.006 \text{ \AA}^{-1}$) for all directions. For the mixed phase the Q , at which the proportionality changes, depends on the direction in ϕ^B . The shape of the curves along constant Q is different in each phase: funnel-like with minimum at $\phi^B \approx 0^\circ$ in the nematic phase, broad minima at $\phi^B \approx 0^\circ$ with strong increase or double minima in the mixed phase and parabolic with minima at $\phi^B \approx 0^\circ$ for the anti-nematic phase. The results of the previous sections are summarized in fig. 7.38 and table 7.3.

Table 7.3.: Summary of the results obtained from XPCS evaluation

Parameters	20vol%			16vol%		
	N	M	AN	N	M	AN
cutoff Q	–	constant	–	–	varying	constant
$\gamma \parallel B$	$\approx 1.2 \pm 0.2$	$\approx 1.1 \pm 0.2$	$\approx 1.1 \pm 0.3$	$\approx 0.7 \pm 0.1$	$\approx 0.5 \pm 0.1$	$\approx 0.5 \pm 0.1$
γ others	$\approx 1.7 \pm 0.2$	$\approx 1.5 \pm 0.1$	$\approx 1.7 \pm 0.2$	$\approx 1.1 \pm 0.2$	$\approx 0.5 \pm 0.1$	$\approx 0.5 \pm 0.1$

7.3. Discussion and interpretation of the XPCS data

In this section, results obtained by the XPCS evaluation are discussed and interpreted. Based on this discussion a model of the behaviour of the goethite nanoplatelets in increasing magnetic fields is proposed. In following chapter three concepts: missing contrast, interparticle interactions and minimal interparticle distances, depending on the degree of freedom and orientation of the particles respective to each other, are discussed. These three subjects are necessary for a complete understanding of the XPCS data and for model development.

7.3.1. Preliminary discussion

Missing contrast analysis

As already mentioned in Section 7.2 the contrast $\beta(Q, \phi^B)$ decreases with increasing Q . A reason for missing contrast could be a fast non-ergodic process, which is in fact too fast for the detection time window. This assumption is based on Harmonically Bound Brownian Particles Model and semi-localized motions of the particles. In this case the decay of the contrast $\beta(Q, \phi^B)$ can be described by Debye-Waller-like form:

$$\beta(Q, \phi^B) = \beta_0 \cdot f_0^2 \cdot \exp(-2 \cdot Q^2 \cdot r_{loc}^2/6), \quad (7.2)$$

where r_{loc} is the localization length of the particles, which reflects the average rattle length-scale of a particle inside a cage of its neighbours [30, 61], $\beta_0 = 0.175$ is the initial contrast, measured using static aerogel sample, f_0 is the fraction of the colloids in the scattering volume, whose motion are localized to an average root-mean-squared displacement r_{loc} [13, 24, 29, 30], and $\beta(Q, \phi^B)$ is the measured contrast.

The contrast values, which are plotted as maps in Section 7.2, were fitted using eq. 7.2, as shown in fig. C.1 in Appendix C. From these fits the parameter $r_{loc}(\phi^B)$ and $f_0(\phi^B)$ were extracted. Localizations lengths r_{loc} are listed in table C.2 for $c = 20$ vol% and in table C.3 for $c = 16$ vol% in Appendix C. Both parameters were plotted as a function of ϕ^B in fig. 7.39 ($r_{loc}(\phi^B)$) and fig. 7.40 ($f_0(\phi^B)$). Here the colours black, red and blue represent the nematic (N), mixed (M) and anti-nematic phase (AN), respectively.

It is apparent from fig. 7.39 that the localization length r_{loc} does not depend on ϕ^B in the nematic and mixed phases for both concentrations. The average values of localization length are $\bar{r}_{loc}^{N20} \approx 11$ nm, $\bar{r}_{loc}^{M20} \approx 11$ nm, $\bar{r}_{loc}^{N16} \approx 16$ nm and $\bar{r}_{loc}^{M16} \approx 13$ nm. The displacement stays roughly the same for $c = 20$ vol% in both the nematic (N) and the mixed (M) phase. At $c = 16$ vol% the motion in the mixed phase has a shorter localization length, which is probably due to a distortion of the nearest neighbour cage because of the partial realignment of the particles in the suspension.

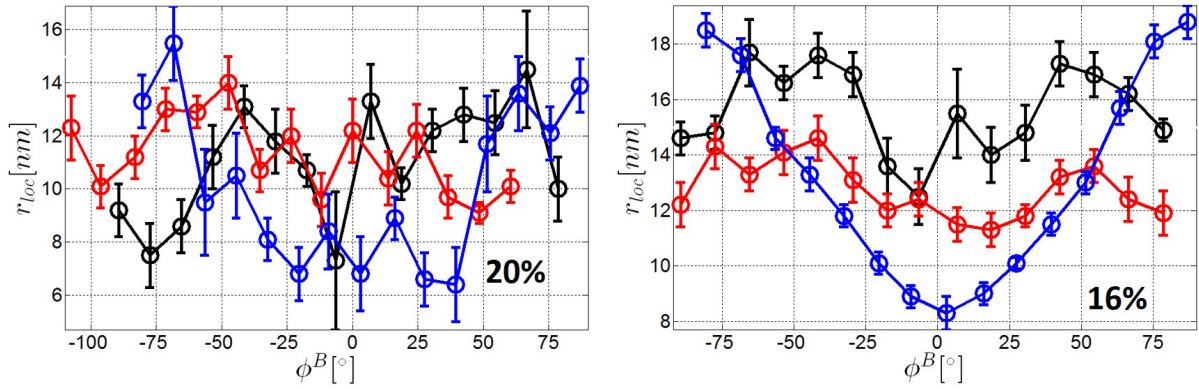


Figure 7.39.: Localization length r_{loc} plotted as function of ϕ^B for the nematic (black), mixed (red) and anti-nematic (blue) phase. Left: for the 20vol%-suspension; right: for the 16vol%-suspension

A notable difference is seen for the anti-nematic phase (AN). A strong dependence of the localization length on ϕ^B was observed there. At both concentrations the motion parallel to the field is significantly smaller ($r_{loc\parallel} \approx 8$ nm) than perpendicular to the field ($r_{loc\perp}^{AN20} = 15$ nm and $r_{loc\perp}^{AN16} = 18$ nm). In the anti-nematic phase the platelets mostly realign with the long axis perpendicular to the magnetic field. The process of this realignment, which distorts the cage of nearest neighbours at $c = 16$ vol% in the mixed phase, leads in the anti-nematic phase to the establishment of an asymmetry in the cage. It is notable that at $c = 20$ vol% there is a strong increase of r_{loc}^{AN20} at $\phi^B > \pm 50^\circ$ while at $c = 16$ vol% the localization length r_{loc}^{AN16} continuously increases from the direction parallel to the magnetic field to the direction perpendicular to it.

The values of the factor f_0 , which are plotted in fig. 7.40, allow to estimate the fraction of the particles in the according phase, whose motion are localized within an average root-mean-square displacement r_{loc} .

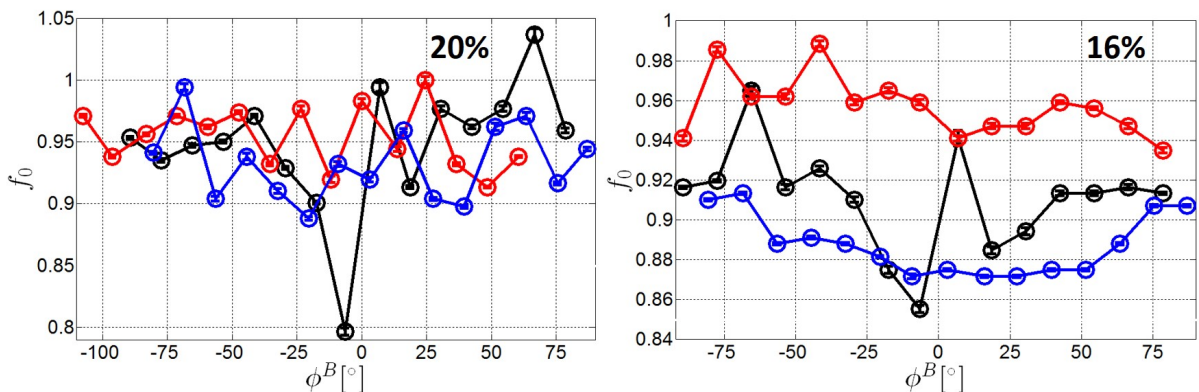


Figure 7.40.: Fraction of colloidal particles in the scattering volume f_0 , whose motion is localized with an average root-mean-squared displacement r_{loc} , plotted as a function of ϕ^B for nematic (black), mixed (red) and anti-nematic (blue) phases. Left: for the 20 vol%-suspension; right: for the 16 vol%-suspension

The f_0 values show that in between 90 vol% and 95 vol% of the particles are arrested. In the nematic phase the values are $\bar{f}_0^{N20} \approx 0.95$ and $f_0^{N16} \approx 0.91$. In the mixed phase the fraction of the arrested particles is ϕ^B -independent with $\bar{f}_0^{M20} \approx 0.95$ and $\bar{f}_0^{M16} \approx 0.96$ and therefore doesn't depend on the concentration of the suspension either. The ϕ^B -independence is also valid for the anti-nematic phase at $c = 20$ vol% with $\bar{f}_0^{AN20} \approx 0.93$. At $c = 16$ vol% a dependence on ϕ^B is visible. For $\phi^B > \pm 70^\circ$ $\bar{f}_0^{AN16} \approx 0.91$ and for all other directions it is $\bar{f}_0^{AN16} \approx 0.88$. Therefore in the anti-nematic phase more particles are arrested perpendicular to the field than parallel to it (direction of the long axis).

Nearest neighbour distance between particles depending on particle orientation and degree of freedom

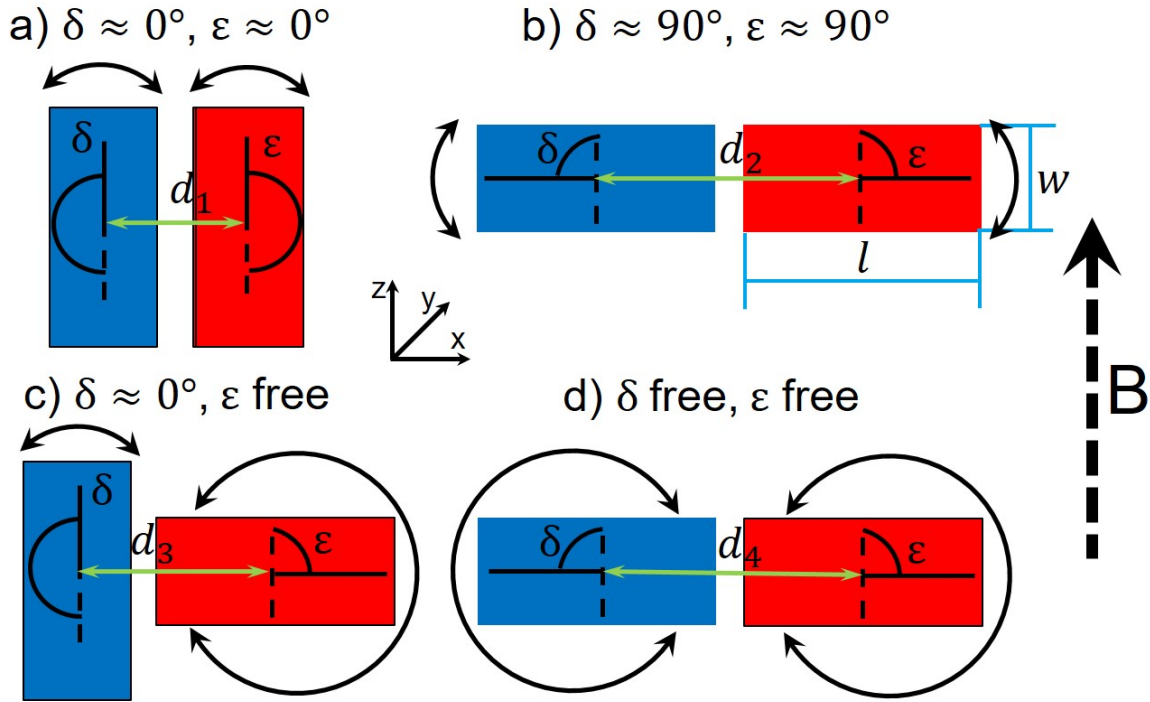


Figure 7.41.: Examples for the calculation of the next neighbour distances between particles a) Rotation is (almost) not allowed and the particles are stacked along their width w . b) Rotation is (almost) not allowed and the particles are stacked along their length l . c) Free rotation around y -axis is allowed, but only for one particle in the pair and the maximum angle is $\delta + \epsilon = 90^\circ$ and d) Free rotation around y -axis is allowed for both particles in a pair and the maximum angle could be $\delta + \epsilon = 180^\circ$.

In the discussion of the platelets dynamics the interparticle distances play an important role. Four nearest neighbour distances were calculated using equation

$$d = l/2 \cdot \sin \delta + w/2 \cdot |\cos \delta| + l/2 \cdot \sin \epsilon + w/2 \cdot |\cos \epsilon| \quad (7.3)$$

and are illustrated in fig. 7.41. The image on the top left (fig. 7.41 a)) shows a minimal interparticle distance of $d_1 \approx 2 \cdot \bar{w}/2 \approx 51$ nm. This distance is a result of a stacking of the particles along their width w , if the platelets are not allowed to rotate freely.

In fig. 7.41 b) on the top right rotation of the particles is still (almost) not allowed, but the particles are stacked along their long axis l . This results in a minimal interparticle distance $d_2 \approx 2 \cdot \bar{l}/2 \approx 216$ nm. In the image on the bottom left free rotation is allowed for one particle in a pair. After averaging over all possible orientations of the free particle the average nearest neighbour distance is $d_3 \approx 110$ nm. In the image on the bottom right free rotation for both particles in a pair is allowed. The averaging over all possible positions results in an average nearest neighbour distance of $d_4 \approx 175$ nm. All the distances are summarized in the table 7.4.

Table 7.4.: Nearest neighbour distances between particles dependent on the degree of freedom

Name	distance	δ	ϵ
d_1	51 nm	0°	0°
d_2	216 nm	90°	90°
d_3	110 nm	0°	free
d_4	175 nm	free	free

Interparticle interactions

The particles are stabilized via electrical charge, which can be described as hard-sphere repulsion at contact range, due to the strong screening of the particle charges. For distances larger than contact distances a magnetic dipole-dipole potential describes the interactions between the particles:

$$V_{ij}(\mathbf{r}_{ij}, \boldsymbol{\mu}_i, \boldsymbol{\mu}_j) = -\frac{\mu_0}{4\pi} \left(3 \frac{\boldsymbol{\mu}_i \cdot \mathbf{r}_{ij} \cdot \boldsymbol{\mu}_j \cdot \mathbf{r}_{ij}}{r_{ij}^5} - \frac{\boldsymbol{\mu}_i \cdot \boldsymbol{\mu}_j}{r_{ij}^3} \right), \quad (7.4)$$

where $\boldsymbol{\mu}_i$ and $\boldsymbol{\mu}_j$ are the magnetic moments and r_{ij} is the distance between dipoles (particles). In an applied magnetic field particles are aligned with their magnetic moments parallel to the field. In this case eq. 7.4 simplifies to:

$$V_{ij}(\mathbf{r}_{ij}, \boldsymbol{\mu}_i, \boldsymbol{\mu}_j) = -\frac{\mu_0 \mu_{rel}^2}{4\pi r_{ij}^3} \left(3 \cos^2 \phi^B - 1 \right), \quad (7.5)$$

where $\mu_{rel} = \Delta\chi H_{ext}$. Here $\Delta\chi$ is the magnetic susceptibility-anisotropy and H_{ext} is the external magnetic field strength.

For $\phi^B = 0^\circ$ the potential becomes $V_{ij}(r_{ij}) = -2 \frac{\mu_0 \mu_{rel}^2}{4\pi r_{ij}^3}$. Therefore parallel to the applied magnetic field magnetic attraction is dominant. For $\phi^B = 90^\circ$ the potential assumes the value $V_{ij}(r_{ij}) = \frac{\mu_0 \mu_{rel}^2}{4\pi r_{ij}^3}$. Hence magnetic repulsion is dominant perpendicular to the applied magnetic field [51].

7.3.2. Discussion and interpretation of the dynamics in the 20 vol%-suspensions

The behaviour of the goethite particles in the suspension at $c = 20$ vol% shows less variations and will therefore be discussed first. The dynamics of the nematic N and anti-nematic AN phases will give a basic understanding of the dynamics in the mixed phase.

Nematic and anti-nematic phases

In the nematic and anti-nematic phases the 20 vol%-suspension shows $\Gamma \propto Q$ and $\gamma \geq 1$. The linear proportionality of the relaxation rate Γ combined with values of the relaxation exponent γ higher than 1 indicate ballistic motion [66], [62], [56], [22]. Ballistic motion is a collective motion of the particles due to stress-field relaxation [24], [50]. The slope of the curve of Γ versus Q provides the drift velocity in the respective direction. Cipelletti et al. studied aqueous colloidal polystyrene gels, where $\gamma \approx 1.5$ and $\Gamma \propto Q$ were observed. In this case the values were explained by syneresis-induced network deformations, where every inhomogeneity acts as force dipole [10]. In our case the dipoles are given, because goethite particles are magnetic dipoles and react to the applied magnetic field.

In the nematic and anti-nematic phases the particles showed a low relaxation rate parallel to the applied magnetic field and high relaxation rate perpendicular to it. This can be explained by the dipole potential elaborated above. The motion is faster along the direction perpendicular to the field, since the particles attract each other along the direction of the field and repel each other perpendicular to it. The nematic phase N shows $v_{N\parallel} = 4.1 \pm 0.3 \text{ \AA} \cdot \text{s}^{-1}$ and $v_{N\perp} = 38 \pm 1 \text{ \AA} \cdot \text{s}^{-1}$. The nematic phase is therefore 10 times faster perpendicular to the field than parallel to it. In the anti-nematic phase the ballistic velocities are ≈ 25 vol% lower, but show a similar trend: $v_{AN\parallel} = 3.3 \pm 0.2 \text{ \AA} \cdot \text{s}^{-1}$ and $v_{AN\perp} = 28.4 \pm 0.7 \text{ \AA} \cdot \text{s}^{-1}$. Even though the particles turned with the long axis perpendicular to the field at $c = 20$ vol% the dynamics are basically the same.

The slopes, which represent the ballistic velocities in the nematic and the anti-nematic phases are plotted as function of ϕ^B in fig. 7.42. Both plots show similarities - the lowest values are at $\phi^B \approx 0^\circ$ and increase in inverse pyramidal shape to reach a plateau of high values, which are approximately 10 times higher than the minima. Nevertheless the shape of the curves is different. In the nematic phase the triangle is narrow and high values form a plateau at $\phi^B > \pm 50^\circ$. In the anti-nematic phase no plateau of high values is visible and the highest values are at $\phi^B \approx \pm 90^\circ$.

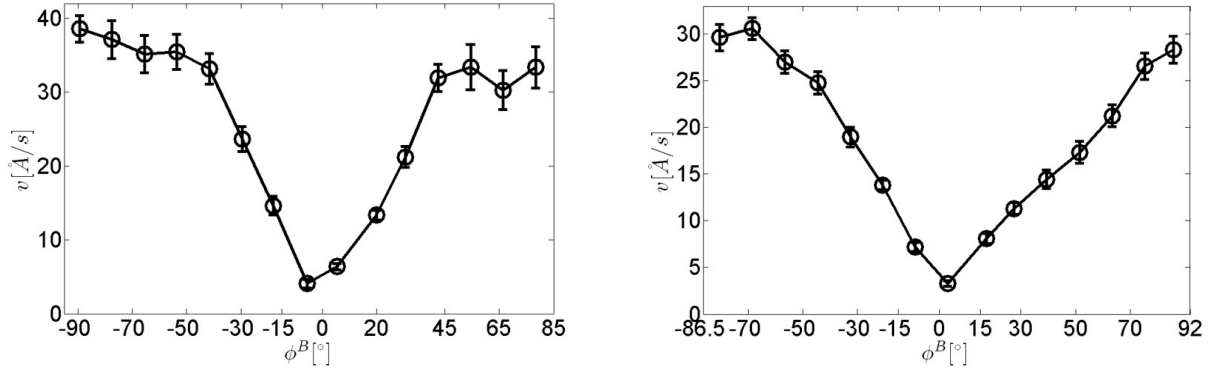


Figure 7.42.: Left: values of the ballistic velocity v in the nematic phase (N) plotted versus ϕ^B ; right: values of the ballistic velocity v in the anti-nematic phase (AN) plotted as function of ϕ^B . The solid lines are guides to the eye.

The relaxation exponent γ is lower parallel to the magnetic field. The decrease of the decay exponent is a sign for a distribution of relaxation times [31, 54, 55, 66]. In general stretched g_2 -functions can be expected, because the goethite platelets have a wide size distribution.

Mixed phase

The mixed phase of the 20 vol%-suspension shows strong deviation in behaviour compared to the nematic and anti-nematic phases. The mixed phase exhibits similar values of the relaxation exponent, but the proportionality of the relaxation rate is $\Gamma(Q) \propto Q^2$. This proportionality indicates diffusive motion. Combined with high values of the relaxation exponent the motion is actually hyperdiffusive and therefore faster than Brownian motion.

There is no simple dependence of $\Gamma \propto Q^2$, but there are cutoff Q -values, where the slope of the curves changes. The position of the cutoff is at $Q^2 \approx 1.3e-5 \text{ \AA}^{-2}$, which corresponds to $Q \approx 0.0036 \text{ \AA}^{-1}$ and an interparticle distance $d \approx 175 \text{ nm}$. The only structural feature at similar Q is a weak peak along $\phi^B \approx 45^\circ$ at $Q \approx 0.0032 \text{ \AA}^{-1}$. While this peak is visible only at $\phi^B \approx 45^\circ$, the cutoff Q is present along all directions in ϕ^B . Distance $d \approx 175 \text{ nm}$ corresponds to the average centre of mass distance d_4 of two platelets with dimensions $l = 216 \text{ nm}$ and $w = 52 \text{ nm}$, if they are both allowed to rotate freely along the y -axis, as shown in fig. 7.41 d). This takes probably place in a 20 vol%-suspension at $B = 370 \text{ mT}$. The platelets partially realign in the direction perpendicular to the applied magnetic field and therefore all the positions overlap to an average distance.

The slopes of the curves $\Gamma(Q)$ versus Q^2 correspond to the effective diffusion constants D_{eff} , which are shown in fig. 7.43. D_{eff2} for $Q \geq 0.0036 \text{ \AA}^{-1}$ is always lower than D_{eff1} for $Q \leq 0.0036 \text{ \AA}^{-1}$. D_{eff1} has a plateau of minimal values at $\phi^B \approx 20^\circ$. It reaches the plateau of high values at $\phi^B \approx -35^\circ$. D_{eff2} is symmetric around $\phi^B \approx 0^\circ$,

where it has its minimum. The maximum is reached at $\phi^B \approx -65^\circ$, which roughly corresponds the angle of the structural peak of the pAN phase at Q_7 (see Chapter 6). At $\phi^B < 75^\circ$ it decreases again.

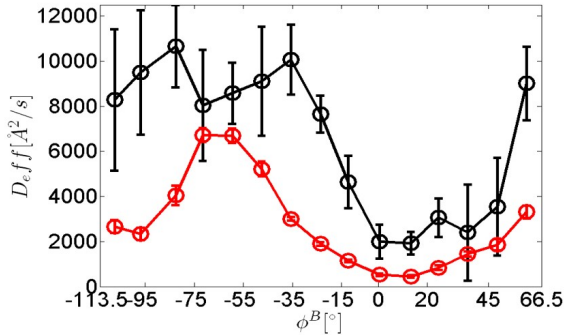


Figure 7.43.: The values of the effective diffusion coefficients D_{eff} in the mixed phase (M) at $c = 20$ vol% plotted as a function of ϕ^B . Black: D_{eff1} for $Q \leq 0.0036 \text{ \AA}^{-1}$; red: D_{eff2} for $Q \geq 0.0036 \text{ \AA}^{-1}$. The solid lines are guides to the eye.

The mixed phase shows the minimal diffusion rate parallel to the magnetic field for both regions - before and after cutoff, as well as fast diffusion rates along the direction perpendicular to the magnetic field, which was also observed in the nematic and anti-nematic phases. But also additional features were observed, which were not present in the nematic and anti-nematic phases.

7.3.3. Discussion and interpretation of the dynamics in the 16 vol%-suspensions

Nematic phase N

The behaviour of the nematic phase N at $c = 16$ vol% is similar to the behaviour of the nematic phase of the 20 vol%-suspension. The evaluation shows that the relaxation rate exhibits a proportionality $\Gamma(Q) \propto Q$. The decay exponent assumes values of $\gamma < 1$ in the direction parallel to the magnetic field and $\gamma \geq 1$ for all other directions. The combination of linear proportionality of $\Gamma(Q)$ and $\gamma \geq 1$ indicates ballistic motion as already discussed for $c = 20$ vol% [22, 56, 62, 66]. The values of $\gamma < 1$ combined with $\Gamma(Q) \propto Q$ indicate a heterogeneous motion [31], [54]. Therefore, we suspect that in the direction parallel to the magnetic field several relaxation times overlap, which causes the stretching of the g_2 -curves.

The motion parallel to the applied magnetic field, where the dipoles attract each other, is much slower ($v_{N\parallel} = 9.2 \pm 0.6 \text{ \AA} \cdot \text{s}^{-1}$) than perpendicular to it ($v_{N\perp} = 51 \pm 1.4 \text{ \AA} \cdot \text{s}^{-1}$), where the particles repel each other, but the fastest motion is found at $\phi^B \approx -65^\circ$ ($v_{N65deg} = 58 \pm 1.3 \text{ \AA} \cdot \text{s}^{-1}$). The velocities as function of ϕ^B are plotted in fig. 7.44.

The form of the curve is funnel-like similar to the nematic phase at $c = 20$ vol%. The minimum is roughly at $\phi^B \approx 0^\circ$, the plateaus of maximal values are reached at $\phi^B \approx \pm 50^\circ$. The highest velocity is roughly 5 times higher than the lowest one.

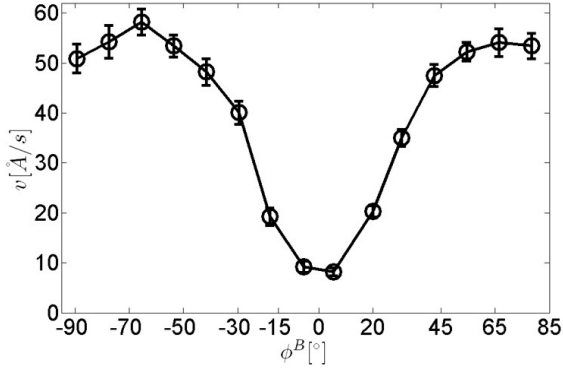


Figure 7.44.: Velocities v in the nematic phase (N) at $c = 16$ vol% plotted as function of ϕ^B . The solid lines are guides to the eye.

Anti-nematic phase AN

In the anti-nematic phase (AN) the behaviour of the particles differs significantly from the behaviour of the platelets in the nematic phase. The maximum value of the relaxation rate is increased up to $\Gamma \approx 5 \text{ s}^{-1}$ compared to $\Gamma \approx 0.5 \text{ s}^{-1}$ in the nematic phase. The highest diffusion rates are perpendicular to the applied magnetic field. Here the proportionality is $\Gamma(Q) \propto Q^2$, which points to diffusive motion. In addition, the relaxation exponent is $\gamma \approx 0.5$, which indicates a subdiffusive motion. The relaxation rate shows not a constant linear proportionality with Q^2 , but the slope changes around $Q \approx 0.006 \text{ \AA}^{-1}$ or accordingly at $Q^2 = 3.6 \text{e-}5 \text{ \AA}^{-2}$.

A structural peak at $Q \approx 0.006 \pm 0.0005 \text{ \AA}^{-1}$ is only present in the direction perpendicular to the applied magnetic field, but the cutoff Q in $\Gamma(Q, \phi^B)$ as a function of Q is present along all directions in ϕ^B . This Q corresponds to an interparticle distance of $d = 105 \text{ nm}$, which is roughly twice the width of a particle. On the other hand it is also the average distance d_3 between two particles, if only one particle is allowed to rotate freely, as shown in fig. 7.41 c).

The structural peak arises from the rest of the presmectic order in the nematic phase, which could explain the cutoff position in one direction. Since the cutoff is present in all directions, it probably arises from the average distance of the particles. The preferred direction of alignment of particles in the anti-nematic phase is with the long axis perpendicular to the applied magnetic field. As the azimuthal width of the structural peaks in ϕ^B is high, this means that only some particles could align perpendicular to the field. Because they are forced in this direction the angle between particles is maximally 90° and the cutoff Q is $Q \approx 0.006 \text{ \AA}^{-1}$.

From the slopes of the $\Gamma \propto Q^2$ curves, the effective diffusion constants D_{eff} can be derived. The diffusion constants, which correspond to Q below the cutoff Q are labelled D_{eff1} in the following. The diffusion constants, which correspond to Q above the cutoff Q , are called D_{eff2} . The highest diffusion constants of $D_{eff1} = 37000 \pm 1000 \text{ \AA}^2 \text{ s}^{-1}$ and $D_{eff2} = 84000 \pm 3000 \text{ \AA}^2 \text{ s}^{-1}$ are found perpendicular to the field, respective for $Q < 0.006 \text{ \AA}^{-1}$ and $Q > 0.006 \text{ \AA}^{-1}$. The lowest diffusion rates are observed parallel to the

magnetic field: $D_{eff1} = 5700 \pm 400 \text{ \AA}^2 \text{ s}^{-1}$ and $D_{eff2} = 2900 \pm 300 \text{ \AA}^2 \text{ s}^{-1}$. All the diffusion coefficients are plotted as function of ϕ^B in fig. 7.45.

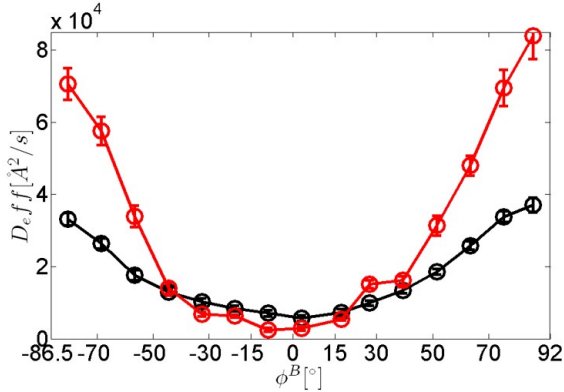


Figure 7.45.: Effective diffusion coefficients D_{eff} in the anti-nematic phase (AN) at $c = 16 \text{ vol\%}$ plotted as function of ϕ^B . Black D_{eff1} for $Q \leq 0.006 \text{ \AA}^{-1}$ and red D_{eff2} for $Q \geq 0.006 \text{ \AA}^{-1}$. The solid lines are guides to the eye.

The diffusion coefficient D_{eff1} is smaller than D_{eff2} at $40^\circ \leq \phi^B \leq 90^\circ$ and $-40^\circ \geq \phi^B \geq -90^\circ$, which can be considered to be basically perpendicular to the field, and higher than D_{eff2} for $-40^\circ \leq \phi^B \leq 40^\circ$, which can be considered to be basically parallel to the field. Both curves are symmetric around $\phi^B \approx 0^\circ$, but the slope is higher for D_{eff2} .

The motion along the attractive magnetic potential (parallel to the applied magnetic field) is also in the anti-nematic phase at $c = 16 \text{ vol\%}$ the slowest. In the anti-nematic phase the ratio between perpendicular and parallel motions is up to ≈ 15 . Remarkably perpendicular to the field the diffusion rate increases after the cutoff value of Q , but parallel to the field it decreases. At angle $\phi^B \approx 45^\circ$ both values are basically identical.

Mixed phase

In the mixed phase a relaxation exponent of $\gamma \approx 0.5$ was observed for all Q and ϕ^B values. Together with the proportionality $\Gamma(Q) \propto Q^2$ it indicates a subdiffusive motion. The $\Gamma(Q) \propto Q^2$ dependence is not simple. Every curve for every direction in ϕ^B shows two slopes. In the mixed phase at $c = 16 \text{ vol\%}$ the cutoff point is at different Q -values. For the curves at $\phi^B \approx -89^\circ$ and $\phi^B \approx -65^\circ$ the point of change is at $Q^2 = 3.6e-5 \text{ \AA}^{-2}$. For the dynamics at $\phi^B \approx 40^\circ$ the cutoff value is at $Q^2 = 1.4e-5 \text{ \AA}^{-2}$. Both curves, which are roughly parallel to the applied magnetic field at $\phi^B \approx -20^\circ$ and $\phi^B \approx 0^\circ$, have a cutoff point at $Q^2 = 0.7e-5 \text{ \AA}^{-2}$. For the curves with a cutoff at low Q it is complicated to verify the exact behaviour, because of the small number of points. Nevertheless there is a change in slope, which can be interpreted, based on the behaviour of the other directions.

At the cutoff values of Q structural peaks were determined by the structural analysis in Chapter 6 and are listed in tables in Appendix B. For the direction parallel to the magnetic field a structure factor peak at Q_1 was found. This position roughly

corresponds to $Q^2 = 0.7e-5 \text{ \AA}^{-2}$ and the cutoff value of Q for this direction. This cutoff value of Q corresponds to an interparticle distance $d \approx d_2 \approx 233 \text{ nm}$, as shown in fig. 7.41 b). This equals to the distance between two particles, which are aligned long axis at long axis. Therefore parallel to the direction of the magnetic field the diffusion rates are different for distances $d > d_2$ and $d < d_2$. The structural analysis of the mixed phase showed a rest of the nematic phase present with $\mathbf{p} \perp \mathbf{m}$. The particles in this partial phase would show the stacking long axis at long axis parallel to the magnetic field with an average distance $d \approx d_2 \approx 233 \text{ nm}$.

In the direction perpendicular to the magnetic field the cutoff value of Q is $Q = 0.006 \text{ \AA}^{-1}$, which corresponds to $Q^2 = 3.6e-5 \text{ \AA}^{-2}$ and an according interparticle distance of $d \approx d_3 \approx 105 \text{ nm}$. At this Q and along this direction a structure peak was recorded at Q_4 . The according length is the average distance between two particles, if one of the particles can rotate freely (see fig. 7.41 c)).

For the third direction roughly along $\phi^B = -41^\circ$ no structure peak was recorded at the cutoff value of $Q = 0.0037 \text{ \AA}^{-1}$, but in this direction there is only a peak at $Q = 0.0027 \text{ \AA}^{-1}$. The cutoff value of Q corresponds to $d \approx d_4 \approx 170 \text{ nm}$, which is the average distance between two platelets, if both can rotate freely, as illustrated in fig. 7.41 d).

In the nematic phase the particles are oriented parallel to the magnetic field and, as observable from the SAXS pattern in fig. 6.7 on the bottom left, some of the particles remain in this position, which might explain the difference in the diffusion below and above a distance $d \approx d_2 = 233 \text{ nm}$. The intermediate direction between parallel and perpendicular to the magnetic field shows a change in the dynamics between $d > d_4$ and $d < d_4$. The diffusive dynamics are different below and above the average distance between two particles. Along the direction perpendicular to the magnetic field the diffusion is different below and above $d \approx d_3$. This is the average particle distance, if one particle of a platelets pair can rotate freely (see fig. 7.41 c)).

From the inclination of the curve $\Gamma(Q)$ versus Q^2 the effective diffusion constant can be extracted, which is shown in fig. 7.46.

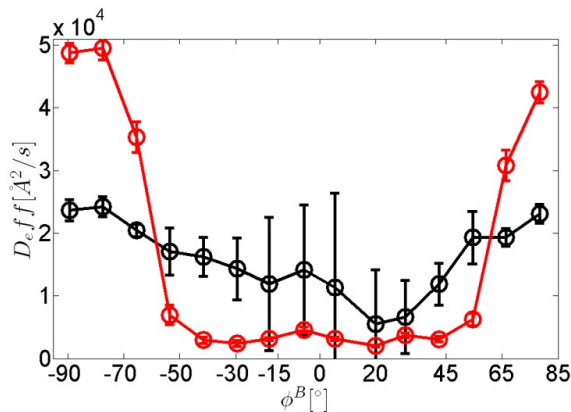


Figure 7.46.: Effective diffusion coefficients D_{eff} in the mixed phase (M) at $c = 16 \text{ vol\%}$ plotted as a function of ϕ^B . Black D_{eff1} for low Q and red D_{eff2} for high Q . The solid lines are guides to the eye.

Like in the anti-nematic phase also in the mixed phase (M) the diffusion coefficient D_{eff1} is higher than D_{eff2} perpendicular to the field ($50^\circ \leq \phi^B \leq 90^\circ$ and $-50^\circ \geq \phi^B \geq -90^\circ$) and lower than D_{eff2} parallel to the field ($-50^\circ \leq \phi^B \leq 50^\circ$). However, the shape of the curves is different. The coefficient D_{eff1} is roughly constant with a slight decrease of up to a factor 2 in the direction parallel to the field. The diffusion coefficient D_{eff2} for high Q is almost constant in the interval $-50^\circ \leq \phi^B \leq 50^\circ$ and increases up to factor 10 in the direction perpendicular to the field.

The diffusive motion at low Q values is slowest parallel to the field and highest perpendicular to it. D_{eff2} at high Q has the lowest value at $\phi^B \approx -30^\circ$, which is the direction of the structure peaks in ϕ^B and the highest value perpendicular to the applied magnetic field.

7.4. Model of the behaviour of the goethite nanoplatelets in suspensions under influence of a magnetic field

The findings of the XPCS analysis are combined into a qualitative model, which depicts the behaviour of the particles in different phases. The model for the nematic (N) and anti-nematic (AN) phases for 20 vol%-suspensions is presented in Section 7.4.1. In Section 7.4.2 the model for the nematic (N) and anti-nematic (AN) phases at $c = 16$ vol% is described. In Section 7.4.3 the data collected from the nematic (N) and anti-nematic (AN) phases is used to extend the schematic model to the mixed phases (M). The graphical model for different phases is summarized in Section 7.4.4.

7.4.1. Model for the behaviour of goethite particles in the nematic and anti-nematic phases in 20 vol%-suspension

For the nematic (N) and anti-nematic (AN) phase, schematic model of the platelets in suspension is shown in fig. 7.47. In general all prepared goethite suspensions in water are very slow. The dynamics of a low concentration suspensions in water could not be captured with the same setup, as used for the measurement of the high concentration suspensions. A comparison calculation using a formula proposed by Chandler showed that high concentration goethite suspensions are several orders slower than a dilute water suspension of hard spheres, which was additionally confirmed to the self-diffusion coefficients from publications [8, 27].

If $B < B_{crit}$ the magnetic moment M of a platelet is mostly induced along the long axis of the particles, which align then partially with the long axis parallel to the applied

magnetic field and induce the nematic phase (N). At some critical field B_{crit} a fraction of platelets start to realign with the long axis perpendicular to the field. The negative magnetic-susceptibility anisotropy $\Delta\chi = \chi_{\parallel} - \chi_{\perp}$ and therefore the magnetic energy E_m (see Section 5.4) are responsible for this partial realignment. The magnetic moments are then induced mainly along the shorter axis (width w) of the particles, which tends to align parallel to the applied magnetic field.

For entropic reasons the induced magnetic moments do not point into the same direction [41]. In addition, at B_{crit} the magnetic moment in the platelet is induced at some finite angle [41] and B_{crit} varies for different platelet size, as shown in Section 6.5. This causes a broad distribution of the directions of the induced magnetic moments at a given polydispersity and magnetic field strength. This is depicted schematically in fig. 7.47, 7.48 and 7.49, showing scenario of the behaviour for different observed phases.

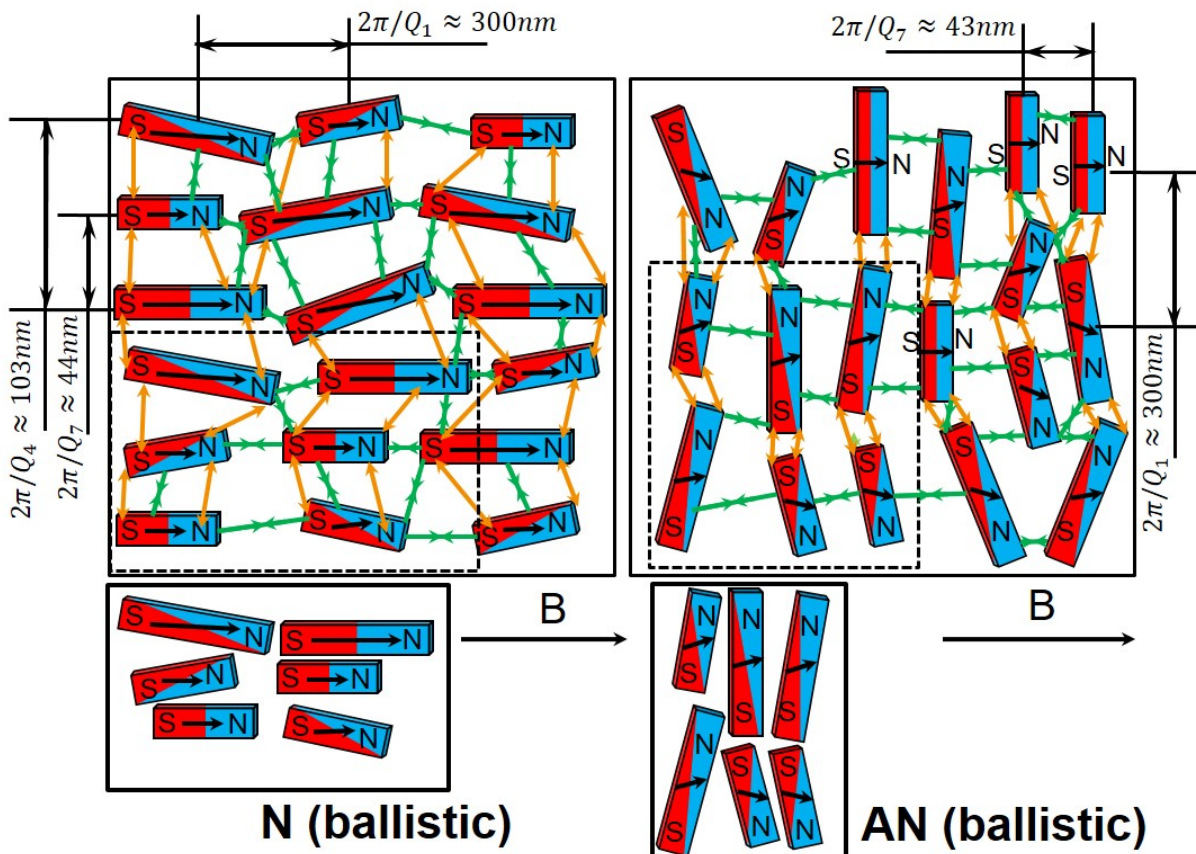


Figure 7.47.: Model of goethite platelets in a 20 vol%-suspension. Left: graphical model of the nematic phase (N); right: graphical model of the anti-nematic phase (AN). Both show ballistic motion. Black arrows inside the particles show the direction of the induced magnetic moment M . The letter S and red colour indicates south pole, the letter N and blue colour indicates the northern pole. The dark green arrows represent attractive interactions, orange arrows indicate repulsive interactions. The average distances between particles are shown as $2\pi/Q$. The insets shows true to scale distances illustrated on six particles.

The contribution of dipole-dipole interactions is small compared to the interaction between the particle dipole, the field and the induced magnetization, but it plays a role at short distances, which is the case for high concentration suspensions. An estimation of the magnetic dipole-dipole potential as defined in eq. 7.4 showed that at a distance of $d = 1$ nm the dipole-dipole interaction is up to two orders of magnitude higher than the magnetic energy of the suspension E_m , which is plotted in fig. 6.11 and 6.12 in Chapter 6. Because the dipole-dipole potential is inversely proportional to the third power of the distance d , already at $d = 10$ nm it is one order of magnitude weaker than the magnetic energy of the suspension E_m and at the distance $d = 50$ nm it is two to three orders of magnitude weaker. This leads to the formation of a structured attraction/repulsion interaction network in the nematic phase, which is illustrated in fig. 7.47, whereas in the anti-nematic phase this network is more disturbed and therefore less structured. The interparticle distances in the nematic and in the anti-nematic phases are very close to the average particle dimensions $d_1 > \bar{l} \approx 220$ nm and $d_3 \approx \bar{w} \approx 51$ nm.

In the nematic phase (N) the higher degree alignment was confirmed by the high respective values of the order parameters (OP): $S_1 = 0.85$, $S_2 = 0.67$ and $S_4 = 0.52$, and by the presence of two peaks in the direction perpendicular to the applied magnetic field at Q_4 and Q_7 , which indicate presmectic order. The particles start to stack up along the short axis as they are roughly aligned with the long axis parallel to the magnetic field. This higher degree of order in the nematic phase is also verified by the azimuthal width of the peaks, as listed in table 6.4. Nguyen et al. reported that with an increasing size of the particles the respective effective viscosity increases accordingly [47]. In the nematic phase the area of the smaller face $w \times t$, which faces in the direction parallel to the field, is smaller than the area of the bigger face $l \times t$, which faces in the direction perpendicular to the magnetic field. Therefore, considering the report by Nguyen et al., the dynamics in nematic phase should be faster parallel to the magnetic field (smaller face of the platelet) than perpendicular to it (bigger face of the platelet). Unanticipated this is not the case. In the nematic phase (N) the motion along the magnetic field and thus in the direction, where the smaller face of the platelets points roughly, was much slower than perpendicular to the magnetic field.

Surprisingly the behaviour reported by Nguyen et al. was observed in the anti-nematic phase (AN), where the platelets mostly realigned with the long axis perpendicular to the applied magnetic field. This realignment implies that the smaller face of platelets is turned in the direction perpendicular to the field. Therefore the faster dynamics should be observed in this direction, as it was the case in the analysed samples. Although the anti-nematic phase is less ordered, which is confirmed by absence of the presmectic peak at Q_4 , the larger azimuthal width of the peak at Q_7 and the lower values of order parameters: $S_1 = 0.19$, $S_2 = -0.45$ and $S_4 = 0.17$, it was observed that

the dynamics in the nematic and anti-nematic phases at $c = 20$ vol% are very similar. The cause of this behaviour are dipole-dipole interactions.

The dipoles attract each other along the applied field and repel each other perpendicular to it, as shown respectively with dark green and orange arrows in fig. 7.47. Therefore they can create soft linked chains along the field. Because of this bond parallel to the field the particles move slower along this direction and much faster perpendicular to the field along the mainly repelling particle axis. This is valid for the nematic as well as for the anti-nematic phases at $c = 20$ vol% and causes the ballistic motion in these phases, as it forces the platelets to move collectively. Additionally, along the third axis t no magnetic moment is induced. The repulsive motion perpendicular to the field is therefore less restricted, since the platelets can shift freely between layers in the third dimension (along t -axis of the platelet).

7.4.2. Model for the behaviour of goethite particles in the nematic and anti-nematic phases in a 16 vol%-suspension

The schematic model of the nematic phase (N) described for $c = 20$ vol% is also valid for the nematic phase at $c = 16$ vol%. It shows also the same structure and high degree of order with narrow presmectic peaks at Q_4 and Q_7 and high values of order parameter: $S_1 = 0.78$, $S_2 = 0.53$ and $S_4 = 0.33$. A significant difference was observed for the behaviour of the anti-nematic phase (AN) at $c = 16$ vol%. Again, the particles realigned with the long axis perpendicular to the field and a decrease of structural order was observed. Similar to $c = 20$ vol% the decrease of order is visible through the disappearance of the presmectic peak at Q_4 , increase of the width of the peak at Q_7 and decrease of the values of the order parameters: $S_1 = 0.16$, $S_2 = -0.47$ and $S_4 = 0.24$.

Despite these similarities to the 20 vol%-suspension the dynamics in the anti-nematic phase at $c = 16$ vol% changed from ballistic to diffusive. The interparticle distances in the anti-nematic phase in the 16 vol%-suspension are larger than in the 20 vol%-suspension. If in the 20 vol%-suspension the average distance parallel to the field is $d_3 \approx 44$ nm and perpendicular to the field $d_1 = 250$ nm, then at $c = 16$ vol% the respective distances are $d_3 \approx 50$ nm and $d_1 = 260$ nm, as listed in Appendix B. The position Q and width σ of the peak close to the beamstop in Q_{r1} -region is difficult to determine, therefore peaks in Q_{r3} -region were more important for the evaluation.

As already shown in the qualitative model for $c = 20$ vol% the weak dipole-dipole interactions form a disturbed network in the anti-nematic phase. If the interparticle distances increase, as in the 16 vol%-suspension, the dipole-dipole interactions decrease inversely proportional to the third power of the distance. Therefore an increase of interparticle distance of $\Delta d \approx 5-10$ nm leads to significant decrease in the strength of the

7.4. Model of the behaviour of the goethite nanoplatelets in suspensions under influence of a magnetic field

dipole-dipole interactions and weakens the network significantly, so that the diffusive motions replace the collective ballistic-type motion. Nevertheless at the discussed interparticle distances the dipole-dipole interactions still play a small role and the dynamics are slower in the direction of the attractive interactions (parallel to the field) and much faster in the direction of repulsion (perpendicular to the field), as illustrated in fig. 7.48.

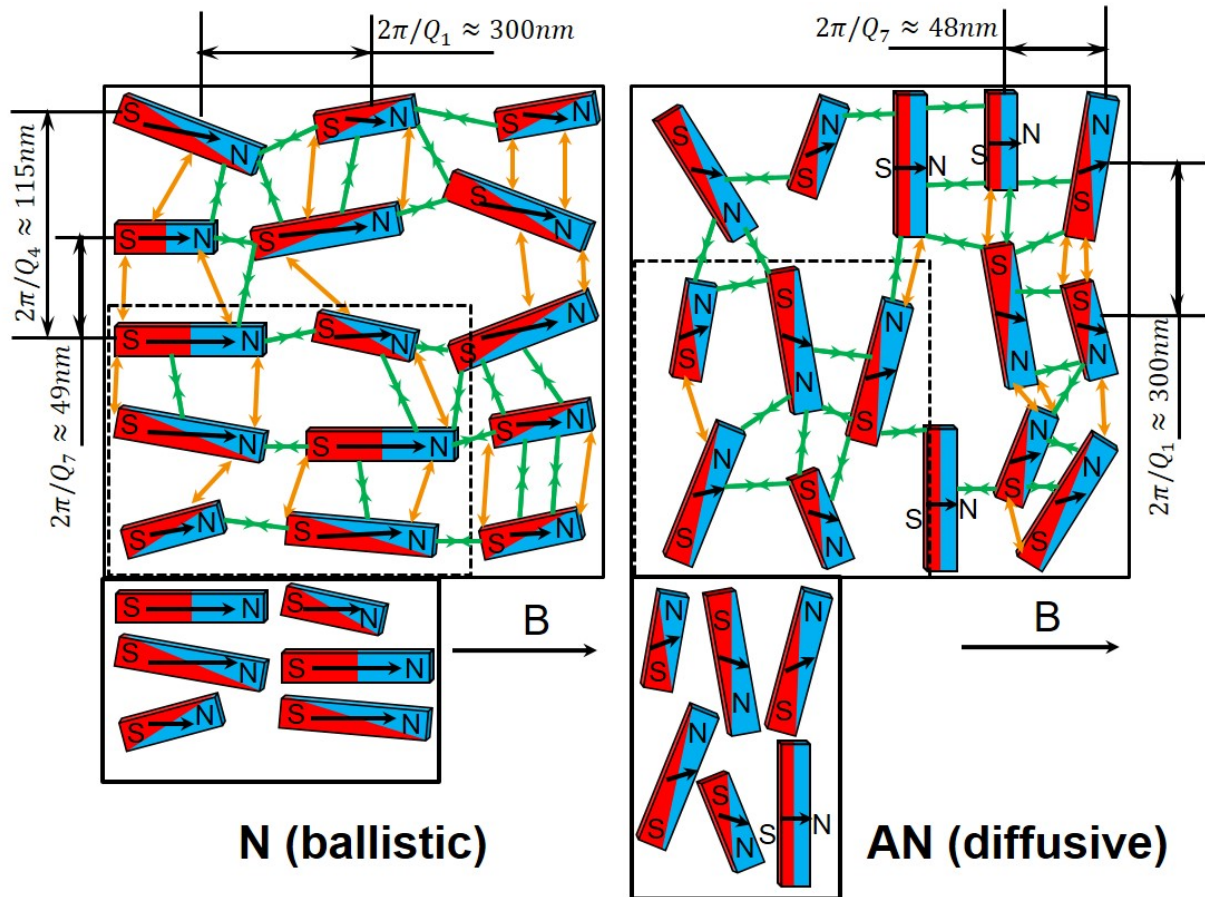


Figure 7.48.: Model of goethite platelets in a 16 vol%-suspension. Left: graphical model of the nematic phase (N), which shows ballistic motion; right: graphical model of the anti-nematic phase (AN), which shows diffusive dynamics. Black arrows inside the particles shows the direction of the induced magnetic moment M . The colour code is the same as in fig. 7.47. The average distances between particles are shown as $2\pi/Q$. The insets shows the true to scale distances illustrated on six particles.

The observed diffusive dynamics showed two dynamic regions for interparticle distances $d < 105\text{ nm}$ and $d > 105\text{ nm}$. The cutoff distance of $d_3 \approx d = 105\text{ nm}$ corresponds to the average interparticle distance, if one of the particles can rotate freely (see fig. 7.41 c)). At $c = 16\text{ vol}\%$ the repulsion, which is dominant at angles $\phi^B \geq 40^\circ$, leads to slower diffusive motion at large length scales $d > d_3$ than the diffusive motion at small length scales $d < d_3$. Attractive interactions, which are dominant roughly parallel to the applied magnetic field, cause this phenomena to invert. The diffusive motion

at large length scales $d > d_3$ is larger than the diffusive motion at small length scales $d < d_3$ in this direction.

7.4.3. Model for the dynamic behaviour of goethite particles in the mixed phases

In the mixed phases particles can be found at random angles. At $c = 20$ vol% only two dominant phases could be identified, whereas at $c = 16$ vol% even three phases were present. This strongly perturbs the attractive/repulsive dipole-dipole network and thus causes diffusive dynamics, as shown in fig. 7.49. Because the dipoles are mainly turned parallel to the field they still influence the direction dependent effective diffusion coefficients. Lower diffusion coefficients are observed for both concentrations parallel to the magnetic field.

Again a cutoff point for the effective diffusion coefficient is present as in the anti-nematic phase for $c = 16$ vol%. It was independent in ϕ^B at interparticle distances $d \approx 175$ nm at $c = 20$ vol%, but changes depending on the investigated direction for $c = 16$ vol%. In the 20 vol%-suspension the fastest diffusive motion for large length scales is observed in between $-50^\circ \leq \phi^B \leq -90^\circ$, whereas for smaller length scales it is along $-50^\circ \leq \phi^B \leq -60^\circ$. Surprisingly the diffusive motion for large length scales is significantly faster along all directions than the diffusive motion for small length scales along the same direction.

For the mixed phase at $c = 16$ vol% the trend is similar to the trend described for the anti-nematic phase at this concentration. The diffusive motion for directions in the range of $0^\circ \geq \phi^B \geq -40^\circ$ is faster for larger length scales than for smaller ones. The cutoff point varies depending on the investigated direction: parallel to the field it corresponds to $d = 232$ nm, perpendicular to it it corresponds to $d = 105$ nm and at $\phi^B \approx -40^\circ$ it corresponds to $d = 175$ nm. These distances respectively correspond to the average distances between two particles aligned long axis on long axis, the average distance between two particles if they both are allowed to rotate freely and the average distance between two particles, if one is allowed to rotate, as explained in fig. 7.41 b), d) and c) respectively. In the nematic phase the particles were mostly aligned with the long axis parallel to the field. A strong contribution from the original nematic phase is present in the mixed phases, therefore in the direction parallel to the field the cutoff point corresponds to the average length of an platelet l , as shown in fig. 7.41 b). The realignment needed for the mixed phase changes the average interparticle distances, as a fraction of the particles turns respective the original nematic orientation. Respective the particles oriented with the long axis along the direction $\phi^B \approx -40^\circ$ all the angles between the particles are allowed, because no preferred reorientation direction

7.4. Model of the behaviour of the goethite nanoplatelets in suspensions under influence of a magnetic field

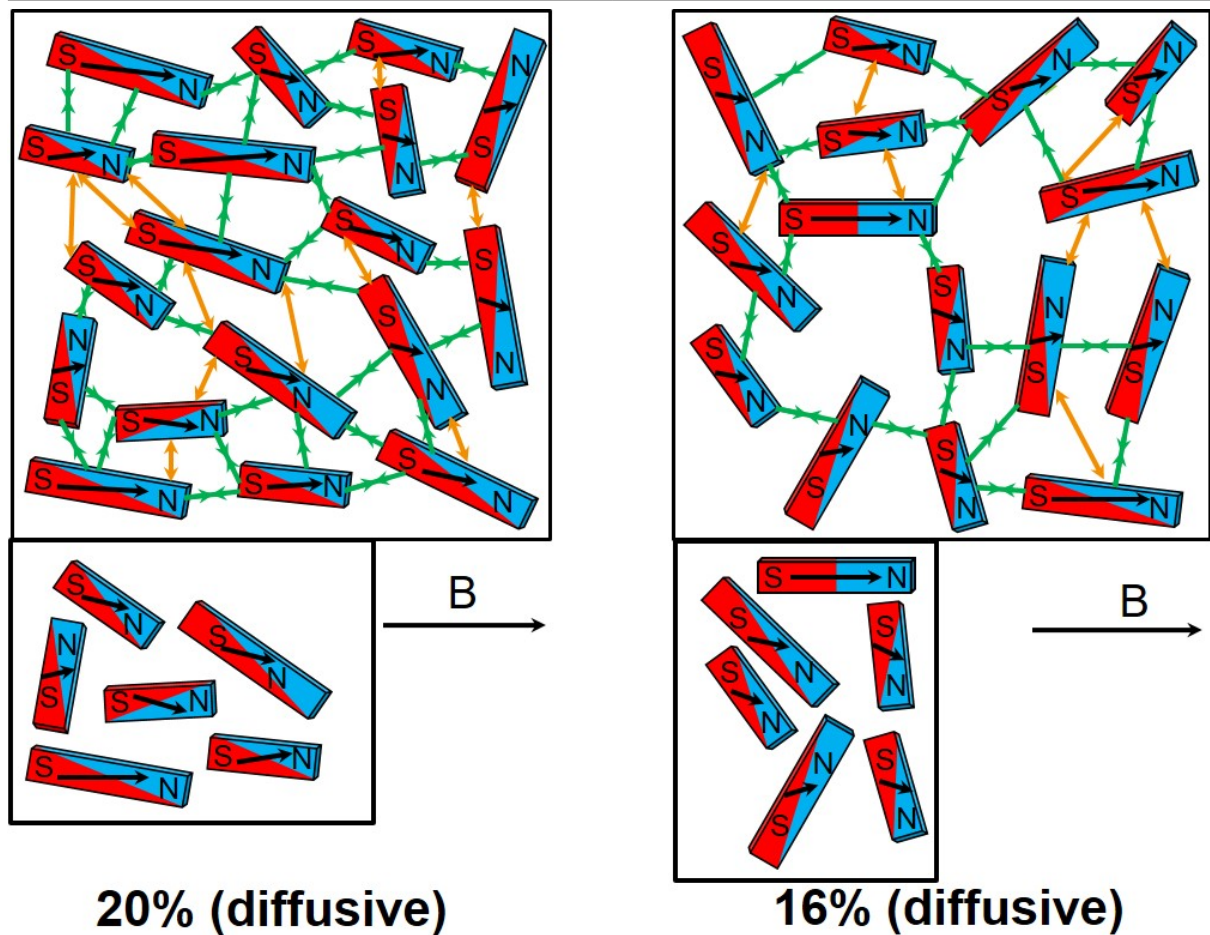


Figure 7.49.: Model of goethite platelets in the mixed phase (M). Left: graphical model for the mixed state of the 20vol%-suspension; right: graphical model for the mixed state of the 16vol%-suspension. Both show diffusive dynamics. Black arrows show the direction of the induced magnetic moment M . The letter S and red colour indicate south pole, the letter N and blue colour show the north pole. The dark green arrows represent attractive interactions, the orange lines indicate repulsive interactions. The insets shows the true to scale distances illustrated on six particles.

was observed. This is the reason, why the cutoff in this direction corresponds with interparticle distance $d \approx 170$ nm, as shown in fig. 7.41 d). Nevertheless all particles tend to reach the anti-nematic phase, where the difference in angle respective to the original nematic phase is $\Delta\phi^B \approx 90^\circ$, which explains the cutoff point in the direction perpendicular to the magnetic field corresponding with $d = 105$ nm, as shown in fig. 7.41 c) .

7.4.4. Summarized model behaviour of the goethite particles under influence of an increasing magnetic field

In summary, the generally very slow high concentration goethite suspensions in water show different behaviour with increasing magnetic field strength B . In the 20 vol%-suspension the dynamics undergoes changes from ballistic to diffusive and back to ballistic motion in the corresponding nematic, mixed and anti-nematic phases. Whereas for the 16 vol%-suspension the changes go from ballistic motion in the nematic phase to diffusive motion in the mixed phase, and it remains diffusive as the suspension makes the transition to the anti-nematic phase. The alignment of the platelets in the suspension is explained by the magnetic energy E_m , which is defined by a competition between the permanent magnetic moment of the nanoplatelets and the negative magnetic susceptibility anisotropy $\Delta\chi$ of the goethite platelets. The change in diffusivity along ϕ^B is explained by dipole-dipole interactions, which can be neglected in the general estimation of magnetic energy E_m , but play a significant role, if the interparticle distances are below $d \approx 50$ nm. The dipole-dipole interactions build an attractive/repulsive interaction network in the nematic phase, where attraction is parallel to the applied field and repulsion perpendicular to it. This network is only weakly coupled in the mixed phase. At $c = 20$ vol%, in spite the transition to the anti-nematic phase, where the platelets are realigned with the long axis perpendicular to the magnetic field, it is found that the network can be restored, because of the shorter interparticle distances. The interparticle distances at $c = 16$ vol% are larger and it is likely that the dipole-dipole interaction network can not be restored in the anti-nematic phase. The dominant type of the dynamics stays diffusive, even after transition.

8. Summary

In this thesis investigations of structural and dynamical properties of goethite α -FeOOH suspensions were performed under the influence of a magnetic field of increasing strength. Experiments were conducted on suspensions of five different concentrations and for six different magnetic field strengths.

The structural investigation using small angle X-ray scattering yielded data, which made it possible to extend the phase diagram of goethite suspensions, as shown in fig. 6.13. This data also showed for the first time, a coexistence of the oriented isotropic (OI) and the anti-nematic (AN) phases at $c = 10$ vol% and at $c = 7.8$ vol%, which is induced through the magnetic field. Additionally, it demonstrated that at intermediate field strength of several hundred millitesla ($370 \text{ mT} \leq B \leq 410 \text{ mT}$) the low concentration suspensions do not form an isotropic state, but a coexistence regime of oriented isotropic (OI) and anti-oriented isotropic (AOI) phases. With increasing concentration of the suspension these partial phases are more pronounced. It was confirmed that upon increase of the magnetic field strength a realignment of the platelets from an orientation with the long axis parallel to the field in the nematic phase (N) to the orientation with the long axis perpendicular to the field in the anti-nematic phase (AN) occurs. This phenomenon is explained by the magnetic energy E_m , which is defined through the competition between the permanent magnetic moment of the nanoplatelets and the negative magnetic susceptibility anisotropy $\Delta\chi$ of the goethite platelets, as introduced by the work of Lemaire et al. [38, 39, 40, 41, 42].

The dynamics of the suspensions of goethite platelets at $c \leq 10$ vol% could not be captured by the same experimental setup as used for investigation of the dynamics at high concentration $c \geq 16$ vol%, since they were too fast and exceeded the time window. However, the investigation of the underlying dynamic properties in concentrated suspensions of magnetic interacting goethite platelets by X-ray photon correlation spectroscopy showed anomalous dynamics. The dynamics of the studied systems are extremely slow. It is several orders of magnitude slower than the self-diffusion of a dilute hard sphere system with radius $R = 110$ nm.

The exact nature of the dynamics depends on the concentration of the investigated suspension. For the 20 vol%-concentration the dynamics changes from ballistic to diffusive and back to ballistic as it peruses the nematic, mixed and anti-nematic phases.

In all three phases the motion parallel to the field is much slower than perpendicular to it, which is counterintuitive in the nematic phase and surprising after a realignment of the particles in the anti-nematic phase.

The change of the dynamics can be explained by magnetic dipole-dipole interactions at short interparticle distances, where the dipoles are induced by the magnetic field. In the nematic phase particles aligned mostly with the long axis parallel to the magnetic field and a dipole-dipole interactions network is induced, due to interaction of the permanent magnetic moments along the long particle axis with the magnetic field. This network has an attractive contribution parallel to the magnetic field and a repelling one perpendicular to it, which explains the different dynamics in these directions.

The dipole-dipole network is strongly disturbed by the realignment of the particles as the nematic phase changes to the mixed one. The SAXS analysis revealed that during this change the interparticle distances increase as the direction of the induced dipole in the platelets changes. This disturbance allows a diffusive motion in the mixed phase. After an (almost) complete realignment of the particles with long axis perpendicular to the magnetic field in the anti-nematic phase, the dipole-dipole interaction network can only partly restore. This is confirmed by the SAXS analysis, which showed lower structural order of the anti-nematic phase compared to the nematic one. Nevertheless, the attractive contribution of the dipole-dipole interactions at small interparticle distances parallel to the magnetic field and the repelling one perpendicular to it leads to a ballistic motion with parameters very similar to the parameters in the nematic phase.

The 16 vol%-suspension is initially in the nematic state, too. It shows similar parameter values as the nematic phase at $c = 20$ vol%. Therefore one can assume that a dipole-dipole interaction network is present again. The underlying motion is ballistic. With increasing magnetic field the platelets start to realign, which destroys the interaction network in the mixed phase and leads to diffusive motion with diffusion rates much higher than at $c = 20$ vol%. After the (almost) complete realignment of the goethite particles into the anti-nematic phase, the degree of order in the suspension increases, but exhibits a lower value compared to the nematic phase.

The interparticle distances at this lower concentration are larger, which leads to the fact that the dipole-dipole interaction network can not completely restore. Therefore the dynamics stays diffusive in the anti-nematic phase at $c = 16$ vol%. The diffusion coefficients are lower than the ones of the mixed phase parallel to the magnetic field and higher than the ones of the mixed phase perpendicular to the magnetic field. This change of the diffusion coefficients can be explained through a partial restoration of the dipole-dipole interaction network, which would lead to a ballistic motion at higher concentration and therefore closer interparticle distances, as seen at $c = 20$ vol%.

These descriptions could be confirmed by the observation of cutoff points for diffusive dynamics. The cutoff points mark the change of the $\Gamma(Q) \propto Q^2$ proportionality and point to different diffusion behaviour below and above certain length scales. These length scales were found to be determined by the average nearest neighbour distances in the suspension and differ depending on the concentration and applied magnetic field strength, but appear only in phases with diffusive motions. The cutoff point is direction independent in ϕ^B for the anti-nematic phase at $c = 16$ vol% and the mixed phase at $c = 20$ vol% with corresponding cutoff length scales of $d_3 = 105$ nm and $d_4 = 175$ nm. In these two subphases the dipole-dipole interaction network is disturbed, but they are more structured than the least structured mixed phase at $c = 16$ vol%, where the cutoff points and corresponding length scales vary depending on the investigated direction in ϕ^B .

By establishing qualitative model, which explain the anomalous dynamics via a magnetic dipole-dipole interaction network in liquid crystalline phases this thesis could connect the unusual structural behaviour of the liquid crystalline phases of high concentration goethite suspensions to the anomalous diffusion of magnetic interacting goethite nanoparticles and thus contribute to the understanding of unusual properties of these "smart nanoparticles" suspensions.

9. Outlook

This thesis clarified the appearance of several liquid crystal phases in goethite platelet suspensions under the influence of an increasing magnetic field, which led to a realignment of the platelets. It allowed to extend the phase diagram of goethite suspensions. Most importantly, evidence for the underlying anomalous anisotropic dynamics in high concentration suspensions of goethite nanoplatelets, interacting via magnetic potential and realigning in increasing magnetic field, was collected and analysed, as described in Chapter 7.

A goal of this thesis was to find a material, which allows a controlled change of liquid crystal phases by applying an external stimulus, i.e. a magnetic field of varying strength. Goethite suspensions are such a system, which offers not only a rich phase diagram, but also go beyond the "typical" model system towards a "realistic" one. Single phases can be induced through changes in concentration or magnetic field strength. The investigation of the underlying dynamics in the suspension should connect structural properties of the liquid crystal phases to their microscopic dynamics and ultimately deliver the ability to control a certain behaviour or at least gain an understanding how to implement one. The experiments described here, could clarify several very important aspects of the phase transitions in goethite nanoparticles suspensions and come closer to the specified goal. Nevertheless, the complexity of the investigated suspensions and the high polydispersity of the platelets hinder the implementation of a controlling mechanism.

To continue the work started in this thesis, the phase transition borders and coexistence regions have to be narrowed down. This can be achieved by including more concentration and magnetic field points in the measurements, additionally to the five concentrations and six magnetic field strengths already discussed. A very important point would be a clarification of the undisturbed state. The suspension has to be carefully evaluated at $B = 0$ mT, where two measurements have to be compared - the original state after filling the capillaries and the state at true zero, where the suspension even at high concentrations are forced into the true equilibrium state.

To clarify the dynamic response of the suspension to the magnetic field, experiments with switching magnetic field should be carried out. The evaluation of these data sets could deliver hints about the stability of the liquid crystal phases. Already recorded

data showed signs of the time dependence of the liquid crystal phases. Depending on the strength of the applied magnetic field and the duration of the application, the suspension could return into its original state, which was present before the field was applied, or continue to change until a new stable phase is reached, after a "point of no return" was passed. In order to verify this "point of no return" and to understand the underlying dynamics, these experiments should be supported by dynamics measurements with evaluation of the two-time correlation function, which would give access to the dynamics even in the out-of-the equilibrium states.

This thesis uses a single exponential decay to fit the g_2 functions. In some of the sets, especially parallel to the applied magnetic field, indications of a double exponential decay were observed. Additionally, a contrast loss in most of the sets appeared, which indicates the presence of a fast non-ergodic relaxation process, which was too fast for the detection window in the presented experiments. The presence of these processes has to be precisely evaluated, in order to help to refine the presented model.

Using the example of goethite this thesis showed that a real system is difficult to handle. One of the major reasons for these complications is the high polydispersity, which is also a reason for the highly complex phase diagram of goethite suspensions. An equilibrium between the controlling ability of the phase transition and therefore the polydispersity and the richness of the phase diagram has to be found. Therefore future investigations have to show if α -FeOOH platelets can be used for the precisely controlled creation of liquid crystal phases or another system with less complex phase diagram, but better possibility for control has to be found.

A. Appendix A: order parameter

Table A.1.: Order parameter S_1 for different sample concentrations at different magnetic fields

B/c	4vol%	7.8vol%	10vol%	16vol%	20vol%
180mT	0.56	0.63	0.73	0.75	0.86
240mT	0.56	0.62	0.73	0.78	0.85
310mT	0.54	0.6	0.7	0.78	0.78
370mT	0.52	0.54	0.51	0.42	0.46
410mT	0.5	0.50	0.47	0.37	0.48
900mT	0.26	0.24	0.25	0.16	0.19

Table A.2.: Order parameter S_2 for different sample concentrations at different magnetic fields

B/c	4vol%	7.8vol%	10vol%	16vol%	20vol%
180mT	0.1	0.22	0.41	0.47	0.68
240mT	0.09	0.21	0.39	0.53	0.67
310mT	0.07	0.17	0.34	0.52	0.58
370mT	0.03	0.08	0.05	-0.09	0
410mT	0	0.01	-0.01	-0.18	0.02
900mT	-0.34	-0.37	-0.37	-0.47	-0.45

Table A.3.: Order parameter S_4 for different sample concentrations at different magnetic fields

B/c	4vol%	7.8vol%	10vol%	16vol%	20vol%
180mT	0.01	0.04	0.13	0.28	0.49
240mT	0.01	0.04	0.12	0.33	0.52
310mT	0.02	0.04	0.1	0.28	0.58
370mT	0.02	0.03	0.1	0.22	0.26
410mT	0.02	0.03	0.11	0.24	0.22
900mT	0.1	0.12	0.11	0.24	0.17

B. Appendix B: structure peaks

B.1. Low concentration samples

Table B.1.: Peak positions, corresponding length scales and peak widths along Q for 4vol%-suspension at different magnetic field strengths.

B			\perp	
	Parameter	Value	Parameter	Value
180 mT 240 mT	$Q_{r1}[\text{\AA}^{-1}]$	0.0017	$Q_{r1}[\text{\AA}^{-1}]$	0.002
310 mT 370 mT	$\sigma_1[\text{\AA}^{-1}]$	0.0005	$\sigma_1[\text{\AA}^{-1}]$	0.0008
410 mT	$\approx 2 \cdot d_2[\text{nm}]$	370 ± 55	$\approx 2 \cdot d_2[\text{nm}]$	315 ± 60
900 mT	$Q_{r1}[\text{\AA}^{-1}]$	0.0025	$Q_{r1}[\text{\AA}^{-1}]$	0.0017
	$\sigma_1[\text{\AA}^{-1}]$	0.0002	$\sigma_1[\text{\AA}^{-1}]$	0.0005
	$\approx d_2[\text{nm}]$	250 ± 10	$\approx 2 \cdot d_2[\text{nm}]$	370 ± 55

Table B.2.: Peak positions, corresponding length scales and peak widths along Q for 7.8vol%-suspension at different magnetic field strengths.

B			\perp	
	Parameter	Value	Parameter	Value
180 mT 240 mT	$Q_{r1}[\text{\AA}^{-1}]$	0.002	$Q_{r1}[\text{\AA}^{-1}]$	0.0027
310 mT 370 mT	$\sigma_1[\text{\AA}^{-1}]$	0.0004	$\sigma_1[\text{\AA}^{-1}]$	0.0004
410 mT	$\approx 2 \cdot d_2[\text{nm}]$	320 ± 30	$\approx d_2[\text{nm}]$	235 ± 20
900 mT	–	–	$Q_{r1}[\text{\AA}^{-1}]$	0.0021
	–	–	$\sigma_1[\text{\AA}^{-1}]$	0.0004
	–	–	$\approx d_2[\text{nm}]$	300 ± 30
	$Q_{r2}[\text{\AA}^{-1}]$	0.007	–	–
	$\sigma_2[\text{\AA}^{-1}]$	0.0014	–	–
	$\approx 2 \cdot d_1[\text{nm}]$	90 ± 9	–	–

Table B.3.: Peak positions, corresponding length scales and peak widths along Q for 10 vol%-suspension at different magnetic field strengths.

B			⊥	
	Parameter	Value	Parameter	Value
180 mT 240 mT	$Q_{r1}[\text{\AA}^{-1}]$	0.0019	$Q_{r1}[\text{\AA}^{-1}]$	0.003
310 mT 370 mT	$\sigma_1[\text{\AA}^{-1}]$	0.0004	$\sigma_1[\text{\AA}^{-1}]$	0.0003
410 mT	$\approx 1.5 \cdot d_2[\text{nm}]$	330 ± 35	$\approx d_2[\text{nm}]$	210 ± 20
370 mT	$Q_{r2}[\text{\AA}^{-1}]$	0.0105	–	–
	$\sigma_2[\text{\AA}^{-1}]$	0.00004	–	–
	$\approx d_1[\text{nm}]$	60 ± 2	–	–
410 mT	$Q_{r2}[\text{\AA}^{-1}]$	0.009	–	–
	$\sigma_2[\text{\AA}^{-1}]$	0.001	–	–
	$\approx d_1[\text{nm}]$	70 ± 4	–	–
900 mT	–	–	$Q_{r1}[\text{\AA}^{-1}]$	0.0024
	–	–	$\sigma_1[\text{\AA}^{-1}]$	0.0003
	–	–	$\approx d_2[\text{nm}]$	260 ± 15
	$Q_{r2}[\text{\AA}^{-1}]$	0.0095	–	–
	$\sigma_2[\text{\AA}^{-1}]$	0.0011	–	–
	$\approx d_1[\text{nm}]$	66 ± 4	–	–

B.2. High concentration samples

Table B.4.: Peak positions, corresponding length scales and peak widths along Q for 16 vol%-suspension at different magnetic field strengths.

B			⊥	
	Parameter	Value	Parameter	Value
180 mT	$Q_{r1}[\text{\AA}^{-1}]$	0.0021	–	–
	$\sigma_1[\text{\AA}^{-1}]$	0.0002	–	–
	$\approx d_2[\text{nm}]$	300 ± 15	–	–
240 mT	–	–	$Q_{r2}[\text{\AA}^{-1}]$	0.0056
	–	–	$\sigma_2[\text{\AA}^{-1}]$	0.0005
	–	–	$\approx 2 \cdot d_1[\text{nm}]$	115 ± 5
310 mT	–	–	$Q_{r3}[\text{\AA}^{-1}]$	0.0128
	–	–	$\sigma_3[\text{\AA}^{-1}]$	0.0007
	–	–	$\approx d_1[\text{nm}]$	49 ± 2
370 mT	$Q_{r1}[\text{\AA}^{-1}]$	0.0021	$Q_{r1}[\text{\AA}^{-1}]$	0.0034
	$\sigma_1[\text{\AA}^{-1}]$	0.0002	$\sigma_1[\text{\AA}^{-1}]$	0.00004
	$\approx d_2[\text{nm}]$	300 ± 15	$\approx d_4[\text{nm}]$	185 ± 2
	$Q_{r2}[\text{\AA}^{-1}]$	0.0061	$Q_{r2}[\text{\AA}^{-1}]$	0.0058
	$\sigma_2[\text{\AA}^{-1}]$	0.0005	$\sigma_2[\text{\AA}^{-1}]$	0.0005
	$\approx d_3[\text{nm}]$	105 ± 10	$\approx d_3[\text{nm}]$	108 ± 5
	$Q_{r3}[\text{\AA}^{-1}]$	0.0125	$Q_{r3}[\text{\AA}^{-1}]$	0.0128
	$\sigma_3[\text{\AA}^{-1}]$	0.0006	$\sigma_3[\text{\AA}^{-1}]$	0.0007
410 mT	$Q_{r1}[\text{\AA}^{-1}]$	0.0021	$Q_{r1}[\text{\AA}^{-1}]$	0.0025
	$\sigma_1[\text{\AA}^{-1}]$	0.0001	$\sigma_1[\text{\AA}^{-1}]$	0.0002
	$\approx d_2[\text{nm}]$	300 ± 8	$\approx d_2[\text{nm}]$	250 ± 10
	$Q_{r2}[\text{\AA}^{-1}]$	0.0062	$Q_{r2}[\text{\AA}^{-1}]$	0.0057
	$\sigma_2[\text{\AA}^{-1}]$	0.0005	$\sigma_2[\text{\AA}^{-1}]$	0.0004
	$\approx d_3[\text{nm}]$	100 ± 10	$\approx d_3[\text{nm}]$	110 ± 4
	$Q_{r3}[\text{\AA}^{-1}]$	0.0122	$Q_{r3}[\text{\AA}^{-1}]$	0.0128
	$\sigma_3[\text{\AA}^{-1}]$	0.0007	$\sigma_3[\text{\AA}^{-1}]$	0.0007
900 mT	$Q_{r1}[\text{\AA}^{-1}]$	0.0021	$Q_{r1}[\text{\AA}^{-1}]$	0.0024
	$\sigma_1[\text{\AA}^{-1}]$	0.0001	$\sigma_1[\text{\AA}^{-1}]$	0.0002
	$\approx d_2[\text{nm}]$	300 ± 8	$\approx d_2[\text{nm}]$	260 ± 10
	–	–	$Q_{r2}[\text{\AA}^{-1}]$	0.006
	–	–	$\sigma_2[\text{\AA}^{-1}]$	0.0042
	–	–	$\approx d_3[\text{nm}]$	105 ± 40
	$Q_{r3}[\text{\AA}^{-1}]$	0.013	$Q_{r3}[\text{\AA}^{-1}]$	0.0129
	$\sigma_3[\text{\AA}^{-1}]$	0.0009	$\sigma_3[\text{\AA}^{-1}]$	0.0005
	$\approx d_1[\text{nm}]$	48 ± 4	$\approx d_1[\text{nm}]$	49 ± 1

Table B.5.: Peak positions, corresponding length scales and peak widths along Q for 20 vol%-suspension at different magnetic field strengths.

B			⊥	
	Parameter	Value	Parameter	Value
180mT	$Q_{r1}[\text{\AA}^{-1}]$	0.0021	–	–
240mT	$\sigma_1[\text{\AA}^{-1}]$	0.0002	–	–
310mT	$\approx d_2[\text{nm}]$	300 ± 14	–	–
180mT	$Q_{r2}[\text{\AA}^{-1}]$	–	$Q_{r2}[\text{\AA}^{-1}]$	0.0061
240mT		–	–	–
370mT	$\sigma_2[\text{\AA}^{-1}]$	–	$\sigma_2[\text{\AA}^{-1}]$	0.0005
410mT		–	–	–
900mT	–	–	$\approx 2 \cdot d_1[\text{nm}]$	103 ± 5
180mT	–	–	$Q_{r3}[\text{\AA}^{-1}]$	0.0143
240mT	–	–	$\sigma_3[\text{\AA}^{-1}]$	0.0006
	–	–	$\approx d_1[\text{nm}]$	44 ± 1
310mT	–	–	$Q_{r2}[\text{\AA}^{-1}]$	0.0078
	–	–	$\sigma_2[\text{\AA}^{-1}]$	0.0007
	–	–	$\approx d_3[\text{nm}]$	81 ± 4
	$Q_{r3}[\text{\AA}^{-1}]$	0.0146	$Q_{r3}[\text{\AA}^{-1}]$	0.014
	$\sigma_3[\text{\AA}^{-1}]$	0.0006	$\sigma_3[\text{\AA}^{-1}]$	0.001
	$\approx d_1[\text{nm}]$	43 ± 1	$\approx d_1[\text{nm}]$	45 ± 2
370mT	$Q_{r1}[\text{\AA}^{-1}]$	0.0023	$Q_{r1}[\text{\AA}^{-1}]$	0.0026
	$\sigma_1[\text{\AA}^{-1}]$	0.0002	$\sigma_1[\text{\AA}^{-1}]$	0.00005
	$\approx d_2[\text{nm}]$	300 ± 30	$\approx d_2[\text{nm}]$	242 ± 3
	$Q_{r3}[\text{\AA}^{-1}]$	0.0146	$Q_{r3}[\text{\AA}^{-1}]$	0.0128
	$\sigma_3[\text{\AA}^{-1}]$	0.0006	$\sigma_3[\text{\AA}^{-1}]$	0.0008
	$\approx d_1[\text{nm}]$	43 ± 1	$\approx d_1[\text{nm}]$	49 ± 2
410mT	$Q_{r1}[\text{\AA}^{-1}]$	0.0022	$Q_{r1}[\text{\AA}^{-1}]$	0.0025
	$\sigma_1[\text{\AA}^{-1}]$	0.0001	$\sigma_1[\text{\AA}^{-1}]$	0.0002
	$\approx d_2[\text{nm}]$	286 ± 7	$\approx d_2[\text{nm}]$	250 ± 10
	$Q_{r3}[\text{\AA}^{-1}]$	0.0146	$Q_{r3}[\text{\AA}^{-1}]$	0.014
	$\sigma_3[\text{\AA}^{-1}]$	0.0006	$\sigma_3[\text{\AA}^{-1}]$	0.0007
	$\approx d_1[\text{nm}]$	43 ± 1	$\approx d_1[\text{nm}]$	45 ± 2
900mT	$Q_{r1}[\text{\AA}^{-1}]$	0.0021	$Q_{r1}[\text{\AA}^{-1}]$	0.0025
	$\sigma_1[\text{\AA}^{-1}]$	0.0002	$\sigma_1[\text{\AA}^{-1}]$	0.0002
	$\approx d_2[\text{nm}]$	300 ± 14	$\approx d_2[\text{nm}]$	250 ± 10
	$Q_{r3}[\text{\AA}^{-1}]$	0.0146	$Q_{r3}[\text{\AA}^{-1}]$	0.0144
	$\sigma_3[\text{\AA}^{-1}]$	0.0008	$\sigma_3[\text{\AA}^{-1}]$	0.0005
	$\approx d_1[\text{nm}]$	43 ± 2	$\approx d_1[\text{nm}]$	44 ± 1

C. Appendix C: missing contrast evaluation

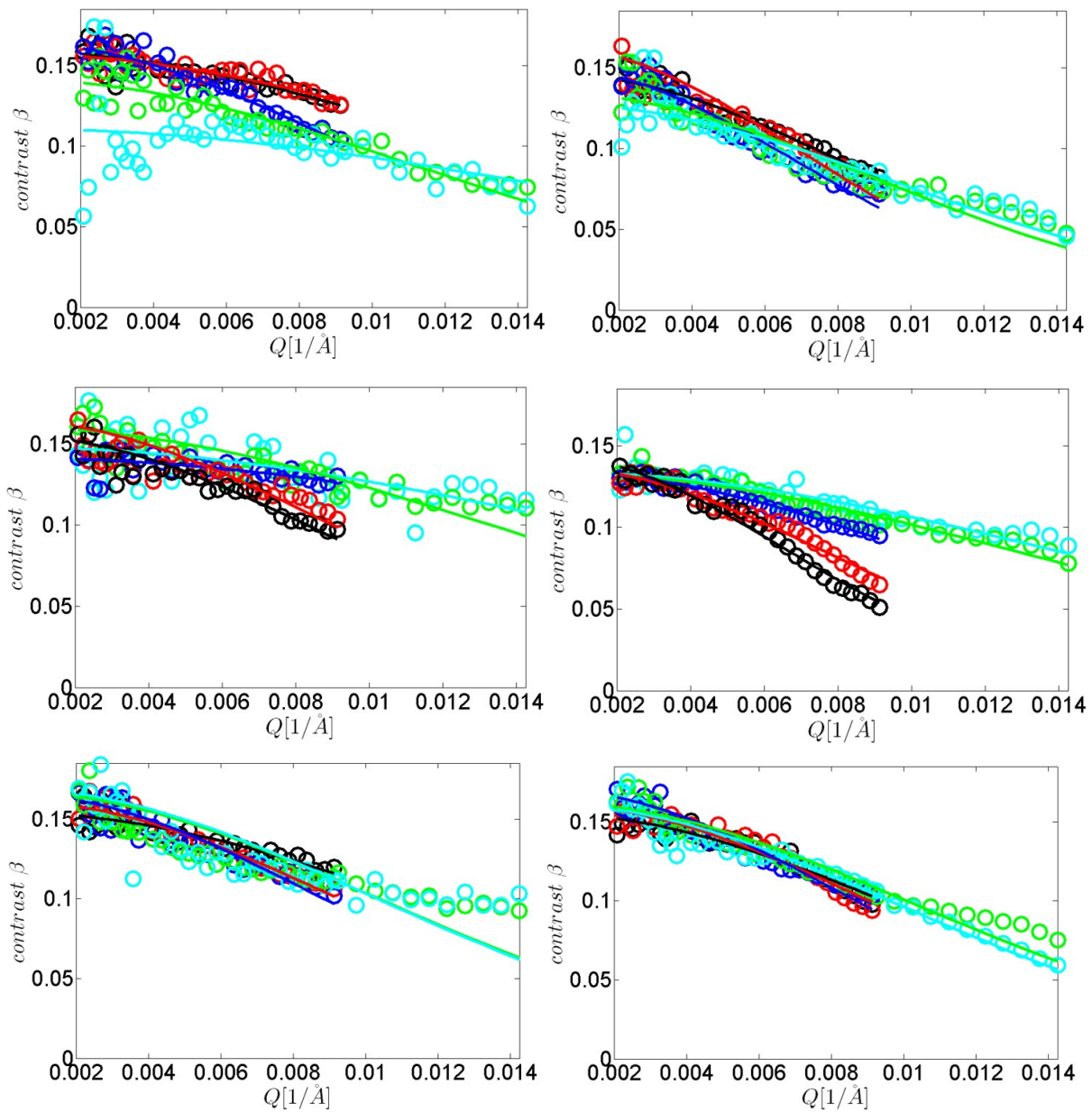


Figure C.1.: Contrast plotted as a function of Q and fitted using the Debye-Waller expression. Left: for $c = 20 \text{ vol\%}$; right: for $c = 16 \text{ vol\%}$. Upper row: nematic phase (N); middle row: anti-nematic phase (AN); bottom row: mixed phase (M). The colours indicate the angles as shown in table C.1.

Table C.1.: Colours of the different lines for the angles chosen from the Q - ϕ^B -partitions as shown in fig. C.1. In the plots the colour indicates the according angle, which stays constant through the whole thesis.

Colour	direction	angle in N and M at 16 vol%	angle in AN	angle in M at 20 vol%
black	\perp to B	$\phi_1^B = -89^\circ$	$\phi_1^B = 86^\circ$	$\phi_1^B = -96^\circ$
red	64° to B	$\phi_2^B = -65.5^\circ$	$\phi_2^B = 63.5^\circ$	$\phi_2^B = -60^\circ$
blue	40° to B	$\phi_3^B = -41.5^\circ$	$\phi_3^B = 39.5^\circ$	$\phi_3^B = -48^\circ$
green	16° to B	$\phi_4^B = -17.5^\circ$	$\phi_4^B = 16^\circ$	$\phi_4^B = -24^\circ$
cyan	\parallel to B	$\phi_5^B = -6.5^\circ$	$\phi_5^B = 3^\circ$	$\phi_5^B = 0^\circ$

Table C.2.: Angle ϕ^B and according localization lengths r_{loc} for 20 vol%-suspensions

N		AN		M	
Angle ϕ^B	$r_{loc}[nm]$	Angle ϕ^B	$r_{loc}[nm]$	Angle ϕ^B	$r_{loc}[nm]$
-89.4°	9 ± 0.5	-80.5°	13 ± 0.5	-89.4°	12 ± 0.6
-77.5°	8 ± 0.6	-68.5°	16 ± 0.7	-77.5°	10 ± 0.4
-65.5°	9 ± 0.5	-56.5°	10 ± 1	-65.5°	11 ± 0.4
-53.5°	11 ± 0.6	-44.5°	11 ± 0.8	-53.5°	13 ± 0.4
-41.5°	13 ± 0.4	-32.5°	8 ± 0.4	-41.5°	13 ± 0.3
-29.5°	12 ± 0.6	-20.5°	7 ± 0.5	-29.5°	14 ± 0.5
-17.5°	11 ± 0.3	-9.3°	8 ± 0.7	-17.5°	11 ± 0.4
-6.5°	7 ± 1.3	3°	7 ± 0.7	-6.5°	12 ± 0.5
6.9°	13 ± 0.7	16.1°	9 ± 0.4	6.9°	10 ± 0.5
18.6°	10 ± 0.3	27.5°	7 ± 0.5	18.6°	12 ± 0.6
30.5°	12 ± 0.4	39.5°	6 ± 0.7	30.5°	10 ± 0.5
42.5°	13 ± 0.5	51.5°	12 ± 0.9	42.5°	12 ± 0.5
54.5°	13 ± 0.6	63.5°	14 ± 0.7	54.5°	10 ± 0.4
66.5°	15 ± 1.1	75.5°	12 ± 0.5	66.5°	9 ± 0.2
78.5°	10 ± 0.6	83°	14 ± 0.5	78.5°	10 ± 0.3

Table C.3.: Angle ϕ^B and according localization lengths r_{loc} for 16 vol%-suspension

N		AN		M	
Angle ϕ^B	$r_{loc}[nm]$	Angle ϕ^B	$r_{loc}[nm]$	Angle ϕ^B	$r_{loc}[nm]$
-89.4°	15 ± 0.3	-80.5°	19 ± 0.3	-107.5°	12 ± 0.4
-77.5°	15 ± 0.3	-68.5°	18 ± 0.3	-96.3°	14 ± 0.4
-65.5°	18 ± 0.6	-56.5°	15 ± 0.2	-83.2°	13 ± 0.3
-53.5°	17 ± 0.3	-44.5°	13 ± 0.3	-71.5°	14 ± 0.4
-41.5°	18 ± 0.4	-32.5°	12 ± 0.2	-59.5°	15 ± 0.4
-29.5°	17 ± 0.4	-20.5°	10 ± 0.2	-47.5°	13 ± 0.4
-17.5°	14 ± 0.5	-9.3°	9 ± 0.2	-35.5°	12 ± 0.3
-6.5°	13 ± 0.5	3°	8 ± 0.3	-23.5°	12 ± 0.3
6.9°	16 ± 0.8	16.1°	9 ± 0.2	-11.9°	12 ± 0.3
18.6°	14 ± 0.5	27.5°	10 ± 0.1	0°	11 ± 0.3
30.5°	15 ± 0.5	39.5°	12 ± 0.2	13.7°	12 ± 0.2
42.5°	17 ± 0.4	51.5°	13 ± 0.2	24.5°	13 ± 0.3
54.5°	17 ± 0.4	63.5°	16 ± 0.3	36.5°	14 ± 0.3
66.5°	16 ± 0.3	75.5°	18 ± 0.3	48.5°	12 ± 0.4
78.5°	15 ± 0.2	87°	19 ± 0.3	60.5°	12 ± 0.4

List of Figures

2.1.	Comparison chart for brilliance of several X-ray sources [14]	4
2.2.	Aerial view of the PETRA III ring on the left and schematic position of the beamlines in the PETRA III hall on the right [15].	5
2.3.	Layout drawing of P10 beamline [74].	6
2.4.	Image of the sample chamber at EH2. The sample chamber is mounted on the diffractometer stage. Some additional elements have been marked. The operative coordinate system at the beamline is indicated [74].	7
2.5.	The vacuum chamber of the 4-circle setup. Left - side view of DN100 cube and right - top view of DN100 cube	8
2.6.	Images of the standard sample insert. Top left: the drawing of the standard sample insert; top right: photo of the standard sample insert before operation and at the bottom: drawing of the standard sample insert with mounted holder for permanent magnets.	9
3.1.	Schematic view of the solenoid wound around a core with attached yoke pieces. The dimensions (in mm) of the components are displayed.	14
3.2.	Magnetic sample system for variable magnetic field at P10. Top: complete sample environment with part numbers on the left and description on the right side. Central row: the two key elements of the setup: left - the flange with attached yokes; right - the sample insert (AB - aluminum block, IH - impedance heater, SC - sensor cable connector, VC - vacuum isolated couplings for cooling liquid). Bottom: left - photograph of the flange with yokes; right - photograph of the sample insert.	15

3.3.	Scans of the magnetic field. s. - for short yoke, l. - for long yoke. The axes are defined in fig. 3.2. Left: Scans at the edge of the yoke: black squares and blue triangles pointing up - along y-direction for respective short and long yoke; red circles and magenta triangles pointing down - along z- and x-directions respective for short and long yoke. Right: Scans in center of the gap. Black squares - short yoke along y-direction; green diamonds - short yoke along x-direction; red circles - long yoke along x-direction; blue triangles - long yoke along z-direction. The scans of long yoke along y and x give the same values as respective scans of short yoke along y and z. The area between dashed lines represents a size of a standard capillary.	17
3.4.	On the left: hysteresis of the magnetic sample system; on the right: same data in the linear area with linear fits	18
4.1.	Results of the XRD analysis of the end products of the synthesis protocols proposed by Gilbert et al. [23] Left: In black the XRD data obtained from the batch produced on 02.07.2013 at $\vartheta = 45^\circ\text{C}$ and in green the magnetite reference from ICSD. Right: in black and violet the XRD data obtained from batches produced on 02.03.2013 and 03.07.2013 at $\vartheta = 25^\circ\text{C}$ respectively and in blue the goethite reference from ICSD.	23
4.2.	XRD data of the synthesis product of method #3 by Krehula et al. [32] . .	23
4.3.	Results of XRD analysis of the end products of the approaches proposed by Thies-Weesie et al. [65] Left: in black the XRD data obtained from the batch produced at high temperature of $\vartheta = 100^\circ\text{C}$ and in red the hematite reference from ICSD. Right: in violet, black and brown the XRD data obtained from batches produced in the first attempt, second attempt and third attempt at room temperature respectively and in blue the goethite reference from ICSD.	24
4.4.	TEM images of goethite particles from two different batches. Left: TEM image of the particles synthesized in batch 10102013rT on 10.10.2013 at room temperature. Right: TEM image of the particles synthesized in batch 22052015rT on 22.05.2015 at room temperature.	25
4.5.	Left: A model of an average goethite nanoplatelet based on the size distributions shown on the right. Right: Size distributions of the particles received by simple counting and measuring of the particles on the TEM images. The distributions are the mean from all analysed batches, because otherwise the counting statistics would be too low for reliable results. From top to bottom the distributions of length, width and thickness of the goethite particles are shown.	26

4.6.	Models of different phases of goethite suspensions and simulations of the respective scattering pattern: 1) Top row: models of the orientation of the particles in the respective phases - from left to right: isotropic (I), nematic (N) and smectic A (SmA), the images were taken from reference [37]; 2) Bottom row: simulated scattering pattern for these respective orientations are shown, the images were taken from reference [3].	27
4.7.	Two possible orientations of the particles in columnar phases are shown: Left - the two possible stacking directions of the platelets in the columnar phase are shown (taken from reference [37]); centre - possible orientation with stacking parallel to the beam and resulting scattering pattern (taken from the reference [34]); right - a possible orientation with stacking perpendicular to the direction of the beam and resulting scattering pattern (taken from the reference [34]).	28
5.1.	A schematic sketch of a typical experimental SAXS setup.	30
5.2.	Figure for definition of the angles β and θ for the ODF analysis, drawn after figure 1 Leadbetter et al. [35]. On the left: top - sketch of partially aligned particles in the nematic phase with the direction of the director $\mathbf{m} B$ and of the average nematic orientation direction \mathbf{n} . Bottom: schematic drawing of the resulting scattering pattern with insert showing a position of one particle from the sketch above with according angles β and θ . On the right: sketches of the particles in four different smectic phases and respective schematic scattering pattern. Additionally the directions of the magnetic field B and the director $\mathbf{m} B$ are shown.	34
5.3.	Three ideal particle orientations in a suspension. Top row: for ideally isotropic distribution of the particles; centre: for particles ideally aligned with long axis parallel to the field ($\mathbf{n} \mathbf{m}$); bottom: for particles ideally aligned with long axis perpendicular to the field ($\mathbf{n}\perp\mathbf{m}$). Left is a schematic view of the particles in suspension, in the centre the resulting scattering pattern and on the right in blue the resulting intensity distribution $I(\theta)$ from the scan at the peak Q	37
5.4.	On top - Left: Simulated intensity distributions $I(\theta)$ with equal areas versus θ with different width of the arc. Right: according orientation distribution functions $f(\beta)$ (ODF) versus β resulting from original $I(\theta)$ distributions on the left, with widths indicated by colours: $w = 5^\circ, 10^\circ, 20^\circ, 40^\circ$ with black, red, blue and green. The red, blue and green curves are multiplied by 5 for better visibility. At the bottom: the according order parameter S_n with S_1 in black, S_2 in red and S_4 in blue.	38

-
- 5.5. The dependence of the OP on the width (FWHM) and position of the ODF: Left - dependence of S_1 (top), S_2 (center) and S_4 (bottom) on the position of the ODF; right - dependence of S_1 (top), S_2 (center) and S_4 (bottom) on the width of the ODF 39
- 5.6. Left: an example for an X-ray speckle pattern; right: frequency-scattering vector space covered by XPCS and complementary techniques such as photon correlation spectroscopy (PCS), Nuclear Forward Scattering (NFS), Spin-Echo Spectroscopy, Inelastic X-ray Scattering (IXS), Inelastic Neutron Scattering (INS), Raman- and Brillouin-Scattering [26]. 40
- 5.7. A schema of the crystal and magnetic structure of goethite, drawn after figure 1 in [11]. The big black and white, checked circles represent iron Fe^{3+} -ions, the big circles coloured with gradient of grey stand for oxygen O^{2-} -ions and small red gradient circles depict hydrogen H^+ -ions. The dimensions of particles are noted with letters and directions of the spins of iron ions are shown by the black arrows. According antiferromagnetic sublattices are inclined by $\pm 13^\circ$ to spin directions of the iron ions. 44
- 6.1. Examples of the scattering patterns from different phases observed during the measurements. Top left: exemplary SAXS pattern from combination of oriented isotropic phase and anti-oriented isotropic phase observed from a 4 vol%-suspension at $B = 370$ mT. The colour circles in the image on top left visualize the Q -range: blue - $Q_3 = 0.005 \text{ \AA}^{-1}$, magenta - $Q_6 = 0.011 \text{ \AA}^{-1}$, yellow - $Q_9 = 0.015 \text{ \AA}^{-1}$ and brown - $Q_{15} = 0.025 \text{ \AA}^{-1}$. In addition, the Q -axes are inserted, to visualize the Q -values once, as they stay constant through whole thesis. Top right: pattern from oriented isotropic phase from a 10 vol%-suspension at $B = 240$ mT. Centre left: pattern from anti-oriented isotropic phase from a 4 vol%-suspension at $B = 900$ mT. Centre right: exemplary SAXS pattern from nematic phase from a 20 vol%-suspension at $B = 240$ mT. Bottom left: pattern from mixed phase, which is a combination of positive nematic and positive anti-nematic phases observed from a 20 vol%-suspension at $B = 370$ mT. Bottom right: pattern from anti-nematic phase from a 20 vol%-suspension at $B = 900$ mT. 54
- 6.2. The SAXS patterns from the 4 vol%-suspension are shown for different magnetic field strengths. The direction of the field \mathbf{m} is shown by white arrows. An elongated pattern along vertical direction ($\mathbf{p} \perp \mathbf{m}$) indicates a preferred horizontal alignment direction of the particles ($\mathbf{n} \parallel \mathbf{m}$) and vice versa. 56
- 6.3. The SAXS patterns from 7.8 vol%-suspension at different magnetic field strengths, as already explained in 6.2. 57

6.4.	The SAXS patterns from 10 vol%-suspension at different magnetic field strengths, as already explained in 6.2 and 6.3.	58
6.5.	S_2 order parameter versus magnetic field strength B at low concentrations: $c \leq 10$ vol%. Black: $c = 4$ vol%; red: $c = 7.8$ vol% and blue: $c = 10$ vol% . . .	59
6.6.	Ellipticity for low concentrations: top row: left - an example of the SAXS pattern indicating the directions of the linecuts; right - the resulting linecuts for $c = 10$ vol% and $B_6 = 900$ mT. The structural peaks have a different position in Q depending on direction of the linecut - the peaks are falling either in Q_{r1} or in Q_{r2} region, as defined in Section 6.2. The black lines indicate Q 's chosen for calculation of the ellipticity, calculated with equations 6.1 and 6.2. Center row: left - $E_{perp}^{Q_{12}}$ versus B ; right - $E_{dia}^{Q_{12}}$ versus B . Bottom row: left - $E_{perp}^{Q_{17}}$ versus B ; right - $E_{dia}^{Q_{17}}$ versus B	61
6.7.	The scattering patterns from 16 vol%-suspension at different magnetic field strength	66
6.8.	The scattering patterns from 20 vol%-suspension at different magnetic field strength	67
6.9.	Nematic order parameter S_2 versus magnetic field strength B . Black: for $c = 16$ vol%; red: for $c = 20$ vol%. Lines are guidelines for eyes	68
6.10.	Plots of $I \cdot Q^2$ versus Q at varying B . Top row: for $c = 16$ vol%; left - parallel to the field, right - perpendicular to the field. Bottom row: for $c = 20$ vol%; left - parallel to the field, right - perpendicular to the field.	70
6.11.	Magnetic energy E_m of long particles with $l_1 = 219$ nm versus ϕ^B . Left: for $c = 16$ vol%; right: for $c = 20$ vol%. The magnetic energy for $B_6 = 900$ mT is divided by 5 to ensure better comparability of the curves. The colours represent the magnetic fields as previously explained.	72
6.12.	Magnetic energy E_m of short particles with $l_2 = 146$ nm versus ϕ^B . Left: for $c = 16$ vol%; right: for $c = 20$ vol%. The magnetic energy for $B_6 = 900$ mT is divided by 5 to ensure better comparability of the curves. The colours represent the magnetic fields as previously explained.	73
6.13.	Phase diagram of the liquid crystalline phases of goethite suspensions plotted versus magnetic field B on the bottom and concentration of the suspension c on the left. Dark colours indicate measured phases, lighter shadows of the same colour denote the estimation of the outreach of the phase. Green stands for isotropic subphases and blue for nematic ones. Black crosses show the measured points. The red diagonal lines indicate the subphases, which were reported for the first time.	79

- 7.1. The Q - ϕ -partitioning is shown with white grid for $Q \geq 0.007 \text{ \AA}^{-1}$ on top, $Q = 0.004 - 0.009 \text{ \AA}^{-1}$ on the bottom left and $Q = 0.002 - 0.004 \text{ \AA}^{-1}$ on the bottom right. The coloured rings mark respective Q -values: blue - $Q_3 = 0.005 \text{ \AA}^{-1}$, magenta - $Q_6 = 0.011 \text{ \AA}^{-1}$ and yellow - $Q_9 = 0.015 \text{ \AA}^{-1}$ 82
- 7.2. Q - ϕ -partitioning illustrating, which examples of g_2 -functions will be shown later. On top for a nematic and on the bottom for an anti-nematic scattering pattern. The circles of different colours in fig. 7.2 represent chosen Q 's. In the images the colours in the bar assigns the colour to a Q value as listed in table 7.1. The straight lines of different colour indicate different angles ϕ^B , which are explained in table 7.2. 83
- 7.3. Evaluation of the total integrated intensity, as a function of the elapsed experimental time in seconds. 84
- 7.4. Example of two-time correlation functions at different Q - ϕ^B 's for a sample at $c = 16 \text{ vol\%}$ and $B = 240 \text{ mT}$ 85
- 7.5. Top: SAXS scattering pattern with Q rings and ϕ^B lines as explained in Section 7.1. Structural peaks are found near Q_1 ($\parallel \mathbf{m}$) and near Q_4 ($\perp \mathbf{m}$), which are respectively shown as black and green circles. Below: Examples of the calculated $g_2(Q, \phi^B)$ -functions. Left: for different Q 's at $\phi^B \approx 0^\circ$ in the central row and at $\phi^B \approx -90^\circ$ at the bottom. Right: for different directions in ϕ^B at $Q_1 = 0.0024 \text{ \AA}^{-1}$ in the central row and $Q_4 = 0.0064 \text{ \AA}^{-1}$ at the bottom. Solid lines represent fits of the data with eq. 7.1. 87
- 7.6. Maps of the baseline values b on the top left, the contrast values β on the top right, the relaxation exponent values γ on the bottom left and the relaxation rate values Γ on the bottom right for nematic phase N. The obtained values are plotted as 2D-maps with Q on the vertical axis and ϕ^B on the horizontal axis. The coloured lines in the Γ map indicate Q values $Q_1 - Q_7$ and ϕ^B values $\phi_{\parallel}^B = 0^\circ$ to $\phi_{\perp}^B = 90^\circ$, as described before. These values are also valid for other maps and correspond to the shown g_2 -functions evaluated on the same Q and ϕ^B values. The white spaces show areas not accessible at high Q , due to the shape of the Lambda detector. 89
- 7.7. Illustration of the inhomogeneous partitions at the border of the scattering feature at $B = 240 \text{ mT}$, which leads to elevated baseline values b 89
- 7.8. Top: Relaxation rate Γ plotted as function of ϕ^B for different Q values. The solid lines are guides to the eye. Bottom: relaxation rate Γ plotted as function of Q for different ϕ^B values. The solid lines are linear fits to the data. 91
- 7.9. Summary of the evaluation of the nematic phase at $c = 20 \text{ vol\%}$ 92

- 7.10. Top: SAXS scattering pattern with Q rings and ϕ^B lines as explained in Section 7.1. Structural peaks are found near Q_1 ($\perp \mathbf{m}$) and Q_7 ($\parallel \mathbf{m}$), which are respectively shown as black and orange circles. Below: Examples of the calculated $g_2(Q, \phi^B)$ -functions. Left: for different Q values at $\phi^B \approx 0^\circ$ in the central row and at $\phi^B \approx 90^\circ$ at the bottom. Right: for different ϕ^B values at $Q_1 = 0.0024 \text{ \AA}^{-1}$ in the central row and $Q_4 = 0.0064 \text{ \AA}^{-1}$ at the bottom, which is shown as green ring. Solid lines are fits to the data using eq. 7.1. 94
- 7.11. Maps of the baseline values b on the top left, the contrast values β on the top right, the relaxation exponent values γ on bottom left and the relaxation rate values Γ on the bottom right for anti-nematic phase AN. The obtained values are plotted as 2D-maps with Q on the vertical axis and ϕ^B on the horizontal axis. The coloured lines in the Γ map indicate Q values $Q_1 - Q_7$ and ϕ^B values $\phi_{\parallel}^B = 0^\circ$ to $\phi_{\perp}^B = 90^\circ$, as described before. These values are also valid for other maps and correspond to the shown g_2 -functions evaluated on the same Q and ϕ^B values. 95
- 7.12. Left: relaxation rate Γ plotted as function of ϕ^B for different constant Q 's. The solid lines are guides to the eye. Right: relaxation rate Γ plotted as function of Q along different constant ϕ^B 's. The solid lines show the linear fits to the data. 96
- 7.13. Summary of the evaluation of the anti-nematic phase at $c = 20 \text{ vol\%}$ 97
- 7.14. Ratio maps for $c = 20 \text{ vol\%}$ calculated by dividing the map of the relaxation exponent (left) and the relaxation rate (right) of anti-nematic phase (AN) by the map of the nematic phase (N). 98
- 7.15. Summary of the evaluation of the nematic and anti-nematic phases at $c = 20 \text{ vol\%}$ in comparison. 99
- 7.17. Maps of the baseline values b (top left), the contrast values β (top right), the relaxation exponent values γ (bottom left) and the relaxation rate values Γ (bottom right) for the nematic phase N. The obtained values are plotted as 2D-maps with Q on the vertical axis and ϕ^B on the horizontal axis. The coloured lines in the Γ map indicate Q values $Q_1 - Q_7$ and ϕ^B values $\phi_{\parallel}^B = 0^\circ$ to $\phi_{\perp}^B = 90^\circ$, as described before. These values are also valid for other maps and correspond to the shown g_2 -functions evaluated on the same Q and ϕ^B values. 100

- 7.16. Top: SAXS scattering pattern with Q rings and ϕ^B lines as explained in Section 7.1. The structural peaks are found near Q_1 ($\parallel \mathbf{m}$) and Q_4 ($\perp \mathbf{m}$), which are respectively shown as black and green circles. Below: Examples of calculated $g_2(Q, \phi^B)$ -functions. Left: $g_2(Q, \phi^B)$ for different Q 's at $\phi^B \approx 0^\circ$ (centre) and at $\phi^B \approx -90^\circ$ (bottom). Right: $g_2(Q, \phi^B)$ for different directions in ϕ^B at $Q_1 = 0.0024 \text{ \AA}^{-1}$ (centre) and $Q_4 = 0.0064 \text{ \AA}^{-1}$ (bottom). Solid lines represent fits of the data using eq. 7.1. 101
- 7.18. Top: relaxation rate Γ plotted as a function of ϕ^B for different Q 's. Solid lines are guides to the eyes. Bottom: relaxation rate Γ plotted as a function of Q for different ϕ^B 's and according linear fits shown by solid lines. . . . 103
- 7.19. Summary of the evaluation of the nematic phase at $c = 16 \text{ vol\%}$ 104
- 7.21. Maps of the baseline values b on the top left, the contrast values β on the top right, the relaxation exponent values γ on the bottom left and the relaxation rate values Γ on the bottom right for the anti-nematic phase AN. The obtained values are plotted as 2D-maps with Q on the vertical axis and ϕ^B on the horizontal axis. The coloured lines in the Γ map indicate Q values $Q_1 - Q_7$ and ϕ^B values $\phi_{\parallel}^B = 0^\circ$ to $\phi_{\perp}^B = 90^\circ$, as described before. These values are also valid for other maps and correspond to the shown g_2 -functions evaluated on the same Q and ϕ^B values. 105
- 7.20. Top: SAXS scattering pattern with Q rings and ϕ^B lines as explained in Section 7.1. The structural peaks are found near Q_1 ($\perp \mathbf{m}$) and Q_7 ($\parallel \mathbf{m}$), which are respectively shown as black and orange circles. Below: Examples of the calculated $g_2(Q, \phi^B)$ -functions for anti-nematic phase. Left: for different Q 's at $\phi^B \approx 3^\circ$ (centre) and at $\phi^B \approx 87^\circ$ (bottom). Right: for different directions in ϕ^B at $Q_1 = 0.0024 \text{ \AA}^{-1}$ (centre) and $Q_4 = 0.0064 \text{ \AA}^{-1}$ (bottom), which is shown as green ring. Solid lines represent fits of the data with eq. 7.1. . . . 106
- 7.22. Left: relaxation rate Γ plotted as a function of ϕ^B for different Q 's. Right: relaxation rate Γ plotted as a function of Q for different ϕ^B 's. The solid lines are guides to the eye. 107
- 7.23. The relaxation rate as a function of Q^2 : top - for 5 different angles with according fits as a function of Q^2 . The inset shows the area close to the point of the origin; bottom - for 2 different angles with according fits as a function of Q^2 , in order to show clearly the point of change of the Q^2 -dependence. The according fits of relaxation rate are shown with solid lines for $Q^2 < 3.6e-5 \text{ \AA}^{-2}$ and dashed lines for $Q^2 > 3.6e-5 \text{ \AA}^{-2}$ 108
- 7.24. Summary of the evaluation of the anti-nematic phase at $c = 16 \text{ vol\%}$ 110

7.25. Ratio maps calculated for $c = 16$ vol% by dividing the values of relaxation exponent (left) and the relaxation rate (right) of the anti-nematic phase by the respective values of the nematic phase.	111
7.26. Summary of the evaluation of the nematic and anti-nematic phases at $c = 16$ vol%.	112
7.27. Summary of the evaluation of the nematic and anti-nematic phases at $c = 20$ vol% and $c = 16$ vol% in comparison.	114
7.28. Top: SAXS scattering pattern with Q rings and ϕ^B lines as explained in Section 7.1. The structural peaks are found near Q_1 and Q_7 ($\parallel \mathbf{m}$) and Q_4 ($\perp \mathbf{m}$), which are respectively shown as black, orange and green circles. Below: Examples of the calculated $g_2(Q, \phi^B)$ -functions for the mixed phase. Left: for different Q 's at $\phi^B \approx 0^\circ$ (centre) and at $\phi^B \approx -90^\circ$ (bottom). Right: for different directions in ϕ^B at $Q_1 = 0.0024 \text{ \AA}^{-1}$ (centre) and $Q_4 = 0.0064 \text{ \AA}^{-1}$ (bottom). Solid lines display fits to the data using eq. 7.1.	116
7.29. Maps of the baseline values b on the top left, the contrast values β on the top right, the relaxation exponent values γ on the bottom left and the relaxation rate values Γ on the bottom right for mixed phase M. The obtained values are plotted as 2D-maps with Q on the vertical axis and ϕ^B on the horizontal axis. The coloured lines in the Γ map indicate Q values $Q_1 - Q_7$ and ϕ^B values $\phi_{\parallel}^B = 0^\circ$ to $\phi_{\perp}^B = 90^\circ$, as described before. These values are also valid for other maps and correspond to the shown g_2 -functions evaluated on the same Q and ϕ^B values.	117
7.30. Top: relaxation rate Γ plotted as a function of ϕ^B for different Q 's. The solid lines are guides to the eye. Bottom: relaxation rate Γ plotted as a function of Q for different ϕ^B 's and according fits as function of Q^2 shown by straight lines for $Q^2 < 0.000013 \text{ \AA}^{-2}$ and dashed lines for $Q^2 > 0.000013 \text{ \AA}^{-2}$. The inset shows the area close to the point of the origin for the first fit.	118
7.31. Summary of the evaluation of the mixed phase at $c = 20$ vol%.	119
7.32. Top: SAXS scattering pattern with Q rings and ϕ^B lines as explained in Section 7.1. The structural peaks are found near Q_1 and Q_7 ($\parallel \mathbf{m}$) and Q_4 ($\perp \mathbf{m}$), which are respectively shown as black, orange and green circles. Below: Examples of $g_2(Q, \phi^B)$ -functions for the anti-nematic phase. Left: at different Q 's at $\phi^B \approx 0^\circ$ (centre) and at $\phi^B \approx -90^\circ$ (bottom). Right: at different directions in ϕ^B at $Q_1 = 0.0024 \text{ \AA}^{-1}$ (centre) and $Q_4 = 0.0064 \text{ \AA}^{-1}$ (bottom). Solid lines are fits to the data using eq. 7.1.	121

7.33. Maps of the baseline values b on the top left, the contrast values β on the top right, the relaxation exponent values γ on the bottom left and the relaxation rate values Γ on the bottom right for mixed phase M. The obtained values are plotted as 2D-maps with Q on the vertical axis and ϕ^B on the horizontal axis. The coloured lines in the Γ map indicate Q values $Q_1 - Q_7$ and ϕ^B values $\phi_{\parallel}^B = 0^\circ$ to $\phi_{\perp}^B = 90^\circ$, as described before. These values are also valid for other maps and correspond to the shown g_2 -functions evaluated on the same Q and ϕ^B values.	122
7.34. Top: relaxation rate Γ plotted as a function of ϕ^B for different Q 's. The solid lines are guides to the eye. Bottom: relaxation rate Γ plotted as a function of Q for different ϕ^B 's. The fits as a function of Q^2 are shown by straight lines for Q smaller than cutoff Q and with dashed lines for Q higher than cutoff Q . The inset shows the area close to the point of the origin and for the fit at low Q values.	123
7.35. Summary of the evaluation of the mixed phase at $c = 16$ vol%.	124
7.36. Q - ϕ^B -maps of the exponent γ (top) and relaxation rate Γ (bottom) for mixed phases. Left: for 20 vol%-suspension. Right: for 16 vol%-suspension	125
7.37. Summary of the evaluation of the mixed phases at $c = 20$ vol% and $c = 16$ vol%.	126
7.38. Summary of the evaluation of all phases at $c = 20$ vol% and $c = 16$ vol% as comparison.	127
7.39. Localization length r_{loc} plotted as function of ϕ^B for the nematic (black), mixed (red) and anti-nematic (blue) phase. Left: for the 20 vol%-suspension; right: for the 16 vol%-suspension	130
7.40. Fraction of colloidal particles in the scattering volume f_0 , whose motion is localized with an average root-mean-squared displacement r_{loc} , plotted as a function of ϕ^B for nematic (black), mixed (red) and anti-nematic (blue) phases. Left: for the 20 vol%-suspension; right: for the 16 vol%-suspension	130
7.41. Examples for the calculation of the next neighbour distances between particles a) Rotation is (almost) not allowed and the particles are stacked along their width w . b) Rotation is (almost) not allowed and the particles are stacked along their length l . c) Free rotation around y -axis is allowed, but only for one particle in the pair and the maximum angle is $\delta + \epsilon = 90^\circ$ and d) Free rotation around y -axis is allowed for both particles in a pair and the maximum angle could be $\delta + \epsilon = 180^\circ$	131
7.42. Left: values of the ballistic velocity v in the nematic phase (N) plotted versus ϕ^B ; right: values of the ballistic velocity v in the anti-nematic phase (AN) plotted as function of ϕ^B . The solid lines are guides to the eye.	134

- 7.43. The values of the effective diffusion coefficients D_{eff} in the mixed phase (M) at $c = 20$ vol% plotted as a function of ϕ^B . Black: D_{eff1} for $Q \leq 0.0036 \text{ \AA}^{-1}$; red: D_{eff2} for $Q \geq 0.0036 \text{ \AA}^{-1}$. The solid lines are guides to the eye. 135
- 7.44. Velocities v in the nematic phase (N) at $c = 16$ vol% plotted as function of ϕ^B . The solid lines are guides to the eye. 136
- 7.45. Effective diffusion coefficients D_{eff} in the anti-nematic phase (AN) at $c = 16$ vol% plotted as function of ϕ^B . Black D_{eff1} for $Q \leq 0.006 \text{ \AA}^{-1}$ and red D_{eff2} for $Q \geq 0.006 \text{ \AA}^{-1}$. The solid lines are guides to the eye. 137
- 7.46. Effective diffusion coefficients D_{eff} in the mixed phase (M) at $c = 16$ vol% plotted as a function of ϕ^B . Black D_{eff1} for low Q and red D_{eff2} for high Q . The solid lines are guides to the eye. 138
- 7.47. Model of goethite platelets in a 20 vol%-suspension. Left: graphical model of the nematic phase (N); right: graphical model of the anti-nematic phase (AN). Both show ballistic motion. Black arrows inside the particles show the direction of the induced magnetic moment M . The letter S and red colour indicates south pole, the letter N and blue colour indicates the northern pole. The dark green arrows represent attractive interactions, orange arrows indicate repulsive interactions. The average distances between particles are shown as $2\pi/Q$. The insets shows true to scale distances illustrated on six particles. 140
- 7.48. Model of goethite platelets in a 16 vol%-suspension. Left: graphical model of the nematic phase (N), which shows ballistic motion; right: graphical model of the anti-nematic phase (AN), which shows diffusive dynamics. Black arrows inside the particles shows the direction of the induced magnetic moment M . The colour code is the same as in fig. 7.47. The average distances between particles are shown as $2\pi/Q$. The insets shows the true to scale distances illustrated on six particles. 143
- 7.49. Model of goethite platelets in the mixed phase (M). Left: graphical model for the mixed state of the 20 vol%-suspension; right: graphical model for the mixed state of the 16 vol%-suspension. Both show diffusive dynamics. Black arrows show the direction of the induced magnetic moment M . The letter S and red colour indicate south pole, the letter N and blue colour show the north pole. The dark green arrows represent attractive interactions, the orange lines indicate repulsive interactions. The insets shows the true to scale distances illustrated on six particles. 145

C.1. Contrast plotted as a function of Q and fitted using the Debye-Waller expression. Left: for $c = 20$ vol%; right: for $c = 16$ vol%. Upper row: nematic phase (N); middle row: anti-nematic phase (AN); bottom row: mixed phase (M). The colours indicate the angles as shown in table C.1. 160

List of Tables

2.1. Photon flux at P10 at $E = 8 \text{ keV}$ and according longitudinal coherence length [74].	6
4.1. Reaction conditions for the synthesis of goethite as proposed by Krehula et al.	21
6.1. The colour of the different lines for the Q values chosen from Q - ϕ^B -partitions as shown in fig. 7.2 for illustration of the g_2 -examples. In the images the colour bar shows the according Q values, which stay constant through whole thesis.	53
6.2. Basic phases identified from the SAXS scattering patterns	55
6.3. The line and symbol colours used for different magnetic field strengths. In the images the colourbar shows the according B values, which will be always the same in the whole thesis.	69
6.4. Angle and azimuthal FWHM of the scattering structural peaks in ϕ^B depending on the strength of the applied magnetic field for high concentration suspensions	74
7.1. The colour code for the Q values chosen from Q - ϕ^B -partitions as shown in fig. 7.2 for illustration of examples of time autocorrelation function. In the images the colours in the bar show the according Q values, which stay constant through the whole thesis.	83
7.2. The colour code for the angles ϕ^B chosen from Q - ϕ^B -partitions as shown in fig. 7.2 for illustration of examples of time autocorrelation function. In the images the colours in the bar show the according number of the angle, which stays constant through whole thesis.	84
7.3. Summary of the results obtained from XPCS evaluation	128
7.4. Nearest neighbour distances between particles dependent on the degree of freedom	132
A.1. Order parameter S_1 for different sample concentrations at different magnetic fields	153
A.2. Order parameter S_2 for different sample concentrations at different magnetic fields	153

A.3. Order parameter S_4 for different sample concentrations at different magnetic fields	153
B.1. Peak positions, corresponding length scales and peak widths along Q for 4 vol%-suspension at different magnetic field strengths.	155
B.2. Peak positions, corresponding length scales and peak widths along Q for 7.8 vol%-suspension at different magnetic field strengths.	155
B.3. Peak positions, corresponding length scales and peak widths along Q for 10 vol%-suspension at different magnetic field strengths.	156
B.4. Peak positions, corresponding length scales and peak widths along Q for 16 vol%-suspension at different magnetic field strengths.	157
B.5. Peak positions, corresponding length scales and peak widths along Q for 20 vol%-suspension at different magnetic field strengths.	158
C.1. Colours of the different lines for the angles chosen from the Q - ϕ^B -partitions as shown in fig. C.1. In the plots the colour indicates the according angle, which stays constant through the whole thesis.	161
C.2. Angle ϕ^B and according localization lengths r_{loc} for 20 vol%-suspensions .	161
C.3. Angle ϕ^B and according localization lengths r_{loc} for 16 vol%-suspension . .	162

Bibliography

- [1] D.L. Abernathy, G. Gruebel, S. Brauer, I. McNulty, G.B. Stephenson, S.G.J. Mochrie, A.R. Sandy, N. Mulders, and M. Sutton. Small-angle x-ray scattering using coherent undulator radiation at the esrf. *Journal of Synchrotron Radiation*, 5:37–47, 1998.
- [2] J. Als-Nielsen and D. McMorrow. *Elements of Modern X-ray Physics*. John Wiley & Sons, Inc., 2011.
- [3] M. A. Bates and G. R. Luckhurst. X-ray scattering patterns of model liquid crystals from computer simulation: Calculation and analysis. *The Journal of Chemical Physics*, 118, 2003.
- [4] L. Bergmann and C. Schaefer. *Lehrbuch der Experimentalphysik: Elektromagnetismus*, volume 2. de Gruyter, 9th edition, 2006. Wilhelm Raith.
- [5] B.J. Berne and R. Pecora. *Dynamic Light Scattering With Applications to Chemistry, Biology, and Physics*. John Wiley & Sons, Inc., 19.
- [6] S. Bocquet, R. J. Pollard, and J. D. Cashion. Dynamic magnetic phenomenon in fine-particle goethite. *Physical Review B*, 46(18), 1992.
- [7] R. Borsalli and R. Pecora, editors. *Soft-Matter Characterization*. Springer, 2008. Redouane Borsali and Robert Pecora.
- [8] D. Chandler. Rough hard sphere theory of the self-diffusion constant for molecular liquids. *Journal of Chemical Physics*, 62(4):1358–1363, 1975.
- [9] S. Chandrasekhar. *Liquid Crystals*. Cambridge University Press, 2. edition, 1992.
- [10] L. Cipelletti, S. Manley, R. C. Ball, and D.A. Weitz. Universal aging features in the restructuring of fractal colloidal gels. *Physical Review Letters*, 84(10), 2000.
- [11] J. M. D. Coey, A. Barry, J. M. Brotto, H. Rakoto, S. Brennan, W. N. Mussel, A. Col-lomb, and D. Fruchart. Spin flop in goethite. *Journal of Physics*, 7:759 – 768, 1995.

- [12] J. J. Crassous, M. Siebenbürger, M. Ballauff, M. Drechsler, O. Henrich, and M. Fuchs. Thermosensitive core-shell particles as model systems for studying the flow behavior of concentrated colloidal dispersions. *Journal of Chemical Physics*, 2006.
- [13] O. Czakkel and A. Madsen. Evolution of dynamics and structure during formation of a cross-linked polymer gel. *A Letters Journal Exploring the Frontiers of Physics*, 95, 2011.
- [14] DESY. Petra iii: A low emittance synchrotron radiation source. technical design report. Technical report, DESY, February 2004.
- [15] DESY. Hasylab homepage, 2011.
- [16] M. Deutsch. Orientational order determination in liquid crystals by x-ray diffraction. *Physical Review A*, 44(12):8264–8270, December 1991.
- [17] A. M. Donald, A. H. Windle, and S. Hanna. *Liquid Crystalline Polymers*. Cam, 2nd edition, 2006.
- [18] A. Duri, T. Sutenrieth, L.-M. Stadler, O. Leupold, Y. Chushkin, G. Gruebel, and C. Gutt. Two-dimensional heterogeneous dynamics at the surface of a colloidal suspension. *Physical Review Letters*, 102:145701, 2009.
- [19] M.D. Ediger, C.A. Angell, and S.R. Nagel. Supercooled liquids and glasses. *Journal of Physical Chemistry*, 100:13200–13212, 1996.
- [20] Z. Evenson, B. Ruta, S. Hechler, M. Stolpe, E. Pineda, I. Gallino, and R. Busch. X-ray photon correlation spectroscopy reveals intermittent aging dynamics in a metallic glass. *Physical Review Letters*, 115, 2015.
- [21] A. Fluerasu. *Coherent X-ray Studies of Non-Equilibrium Processes*. PhD thesis, McGill University, 2003.
- [22] A. Fluerasu, A. Moussaïd, A. Madsen, and A. Schofield. Slow dynamics and aging in colloidal gels studied by x-ray photon correlation spectroscopy. *PHYSICAL REVIEW E*, 76, 2007.
- [23] F. Gilbert, P. Refait, F. Leveque, C. Remazeilles, and E. Conforto. synthesis of goethite from $Fe(OH)_2$ precipitates: Influence of $Fe(II)$ concentration and stirring speed. *Journal of Physics and Chemistry of Solids*, 69(8):2124, 2009.
- [24] V. M. Giordano and B. Ruta. Unveiling the structural arrangements responsible for the atomic dynamics in metallic glasses during physical aging. *Nature Communications*, 2016.

-
- [25] O. Glatter and O. Kratky. *Small Angle X-Ray Scattering*. Academic Press Inc., 1982.
- [26] G. Gruebel, A. Madsen, and A. Robert. *Soft-Matter Characterization*, chapter X-ray Photon Correlation Spectroscopy (XPCS), pages 953–997. Springer, 2008.
- [27] G. Gruebel and F. Zontone. Correlation spectroscopy with coherent x-rays. *Journal of Alloys and Compounds*, 362, 2004.
- [28] A. Guinier. *Small Angle Scattering of X-rays*. Books on Demand, 1996.
- [29] H. Guo, S. Ramakrishnan, J. L. Harden, and R. L. Leheny. Connecting nanoscale motion and rheology of gel-forming colloidal suspensions. *PHYSICAL REVIEW E*, 81:050401, 2010.
- [30] H. Guo, S. Ramakrishnan, J. L. Harden, and R. L. Leheny. Gel formation and aging in weakly attractive nanocolloid suspensions at intermediate concentrations. *The Journal of Chemical Physics*, 2011.
- [31] E. M. Herzig, A. Robert, D. D. van t Zand, L. Cipelletti, P. N. Pusey, and P. S. Clegg. Dynamics of a colloid-stabilized cream. *PHYSICAL REVIEW E* 79, 2009.
- [32] S. Krehula, S. Popovic, and S. Music. Synthesis of acicular alpha-FeOOH particles at very high pH. *Materials Letters*, 54:108–113, 2002.
- [33] A. Kuijk, D. V. Byelov, A. V. Petukhov, A. van Blaaderen, and Arnout Imhofa. Phase behavior of colloidal silica rods. *Faraday Discussions*, 159:181–199, 2012.
- [34] S. Kumar. *Chemistry of Discotic Liquid Crystals: From Monomers to Polymers*. CRC Press, 2010.
- [35] A. J. Leadbetter and E. K. Norris. Distribution functions in three liquid crystals from x-ray diffraction measurements. *Molecular Physics*, 38(3):669–686, 1979.
- [36] S.-D. Lee. A numerical investigation of nematic ordering based on a simple hard-rod model. *Journal of Chemical Physics*, 87, 1987.
- [37] H. N. W. Lekkerkerker and G. J. Vroege. Liquid crystal phase transitions in suspensions of mineral colloids: new life from old roots. *Philosophical transactions of the royal society A*, 2013.
- [38] B. J. Lemaire, P. Davidson, J. Ferre, J. P. Jamet, P. Panine, I. Dozov, and J. P. Jolivet. Outstanding magnetic properties of nematic suspensions of goethite (alpha - FeOOH) nanorods. *Physical Review Letters*, 88(12), 2002.

- [39] B. J. Lemaire, P. Davidson, J. Ferre, J. P. Jamet, D. Petermann, P. Panine, I. Dozov, D. Stoenescu, and J. P. Jolivet. The complex phase behaviour of suspensions of goethite (alpha-feooh) nanorods in a magnetic field. *Faraday Discussions*, 128:271–283, 2005.
- [40] B. J. Lemaire, P. Davidson, P. Panine, and J. P. Jolivet. Magnetic-field-induced nematic-columnar phase transition in aqueous suspensions of goethite (alpha-feooh) nanorods. *Physical Review L*, 93, 2004.
- [41] B.J. Lemaire, P. Davidson, J. Ferre, J.P. Jamet, D. Petermann, P. Panine, I. Dozov, and J.P. Jolivet. Physical properties of aqueous suspensions of goethite (alpha - feooh) nanorods. part i: In the isotropic phase. *The European Physical Journal E*, 13:291–308, April 2004.
- [42] B.J. Lemaire, P. Davidson, D. Petermann, P. Panine, I. Dozov, D. Stoenescu, and J. P. Jolivet. Physical properties of aqueous suspensions of goethite (alpha-feooh) nanorods, part ii: In the nematic phase. *The European Physical Journal E*, 13:309–319, 2004.
- [43] L. Li, D. Chen, Y. Zhang, Z. Deng, X. Ren, X. Meng, F. Tang, J. Ren, and L. Zhang. Magnetic and flueorescent multifunctional chitosan nanoparticles as a smart drug delivery system. *Nanotechnology*, 2007.
- [44] A. Madsen, R.L. Leheny, H. Guo, M. Sprung, and O. Czakkel. Beyond simple exponential correlation functions and equilibrium dynamics in x-ray photon correlation spectroscopy. *New Journal of Physics*, 12:055001, 2010.
- [45] J. Miao. Extending the methodology of x-ray crystallography to allow imaging of micrometre-sized non-crystalline specimens. *Letters to nature*, 400:342–344, 1999.
- [46] Ch. Märkert. Präparation und untersuchungen zur struktur unf dynamik von sususpension formanisotroper kolloide. Master’s thesis, Universitz of Rostock, 2012.
- [47] C.T. Nguyen, F. Desgranges, G. Roy, N. Galanis, T. Mare, S. Boucher, and H. Angue Mintsa. Temperature and particle-size dependent viscosity data for water-based nanofluids - hysteresis phenomenon. *International Journal of Heat and Fluid Flow*, 28:1492 – 1506, 2007.
- [48] A. A. Olowe and J. M. R. Genin. The mechanism of oxidation of ferrous hydroxide in sulphated aqueous media: influence of the initial ratio of the reactants. *Corrosion Science*, 32(9):965–984, 1991.

-
- [49] L. Onsager. The effects of shape on the interaction of colloidal particles. *Annals New York Academy of science*, 1949.
- [50] O.D. Parashchuk, T.V. Laptinskaya, M.A. Ananieva, and D.Y. Parashchuk. Hyperdiffusive dynamics in conjugated polymer blends and fullerene absorbing solutions. *Soft Matter*, 7:5585, 2011.
- [51] Ch. Passow, B. Fischer, M. Sprung, M. Köckerling, and J. Wagner. Direction-dependent freezing of diamagnetic colloidal tracers suspended in paramagnetic ionic liquids. *Langmuir*, 2014.
- [52] J. S. Pedersen. Analysis of small-angle scattering data from colloids and polymer solutions: model and least-squares fitting. *Advances in Colloid and Interface Science*, 70:171–210, 1997.
- [53] W. C. K. Poon. The physics of a model colloid-polymer mixture. *Journal of Physics: Condensed Matter*, 2002.
- [54] Ranko Richert. Heterogeneous dynamics in liquids: fluctuations in space and time. *JOURNAL OF PHYSICS: CONDENSED MATTER*, 14, 2002.
- [55] B. Ruta, Y. Chushkin, G. Monaco, L. Cipelletti, E. Pineda, P. Bruna, V. M. Giordano, and M. Gonzalez-Silveira. Atomic-scale relaxation dynamics and aging in a metallic glass probed by x-ray photon correlation spectroscopy. *PHYSICAL REVIEW LETTERS*, 109, 2012.
- [56] B. Ruta, O. Czakkel, Y. Chushkin, F. Pignon, R. Nervo, F. Zontone, and M. Rinaudo. Silica nanoparticles as tracers of the gelation dynamics of a natural biopolymer physical gel. *Soft Matter*, 10, 2014.
- [57] C. Schroer. Lectures: Interaction of x-rays with matter. 2010.
- [58] F. Schüth, A. Lu, and E. L. Salabas. Magnetische nanopartikel: Synthese, stabilisierung, funktionalisierung und anwendung. *Angewandte Chemie*, 2007.
- [59] U. Schwertmann and R. M. Cornell. *Iron Oxides in Laboratory: Preparation and Characterization (Chemistry)*. WILEY-WCH, 2000.
- [60] Banu Yavuztürk Seyda Bucak and Ali Demir Sezer. *Recent Advances in Novel Drug Delivery*, chapter Magnetic Nanoparticles: Synthesis, Surface modifications and Application in Drug Delivery, pages 165–200. INTECH, 2012.
- [61] D. S. Simmons, M. T. Cicerone, Q. Zhong, M. Tyagi, and J. F. Douglas. Generalized localization model of relaxation in glass-forming liquids. *Soft Matter*, 8(45):11455–11461, 2012.

- [62] Melissa Spannuth, S. G. J. Mochrie, S. S. L. Peppin, and J. S. Wettlaufer. Dynamics of colloidal particles in ice. *Soft Condensed Matter*, 2010.
- [63] M. Sprung. Xpcsgui.
- [64] M. Sutton. Observation of speckle by diffraction with coherent x-rays. *Letters to nature*, 352:608–610, August 1991.
- [65] D. M. E. Thies-Weesie, J. P. de Hoog, M. H. Hernandez Mendiola, A. V. Petukhov, and G. J. Vroege. Synthesis of goethite as a model colloid for mineral liquid crystals. *Chemistry of M*, 19:5538 – 5546, 2007.
- [66] V. Trappe, E. Pitard, L. Ramos, A. Robert, H. Bissig, and L. Cipelletti. Investigation of q-dependent dynamical heterogeneity in a colloidal gel by x-ray photon correlation spectroscopy. *Physical Review E*, 76, 2007.
- [67] O.K.C. Tsui and S.G.J. Mochrie. Dynamics of concentrated colloidal suspensions probed by x-ray correlation spectroscopy. *Physical Review E*, 57(2):2030–2034, 1998.
- [68] O.K.C. Tsui, S.G.J. Mochrie, and L.E. Berman. Statistical analysis of x-ray speckle at the nsls. *Journal of Synchrotron Radiation*, 5:30–36, 1998.
- [69] E. van den Pol, A. Lupascu, M. A. Diaconeasa, A. V. Petukhov, D. V. Byelov, and G J Vroege. Onsager revisited: Magnetic field induced nematic-nematic phase separation in dispersions of goethite nanorods. *The Journal of Physical Chemistry Letters*, 1:2174–2178, 2010.
- [70] E. van den Pol, A. V. Petukhov, D. M. E. Thies-Weesie, D. V. Byelov, and G J Vroege. Experimental realization of biaxial liquid crystal phase in colloidal dispersions of boardlike particles. *Physical Review Letters*, 103:258301, 2009.
- [71] G. J. Vroege and H. N. W. Lekkerkerker. Phase transitions in lyotropic colloidal and polymer liquid crystals. *Reports on Progress in Physics*, 55(8):1241, 1992.
- [72] H. H. Wensink and G. J. Vroege. Nematic order of model goethite nanorods in a magnetic field. *Physical Review E*, (72), 2005.
- [73] A. Yethiraj and A. van Blaaderen. A colloidal model system with an interaction tunable from hard sphere to soft and dipolar. *Letters to Nature*, 2002.
- [74] A. Zozulya, S. Bondarenko, and M. Sprung. P10 coherence beamline user guide. Technical report, Deutsches Elektronen-Synchrotron, 2011.

Publications

1. M. A. Schroer, F. Westermeier, F. Lehmkuhler, H. Conrad, **A. Schavkan**, A. V. Zozulya, B. Fischer, W. Roseker, M. Sprung, Ch. Gutt and G. Grübel. Colloidal crystallite suspensions studied by high pressure small angle X-ray scattering. *The Journal of Chemical Physics* 144(8):084903 (2016)
2. A. Ricci, N. Poccia, B. Joseph, D. Innocenti, G. Campi, A. V. Zozulya, F. Westermeier, **A. Schavkan**, F. Coneri, A. Bianconi and H. Takeya. Direct observation of nanoscale interface phase in the superconducting chalcogenide $K_xFe_{2-y}Se_2$ with intrinsic phase separation. *Physical Review B* 91(2):020503 (2015)
3. T. Sobisch, F. Westermeier, B. Fischer, A. V. Zozulya, M. Sprung, A. Ricci, **A. Schavkan**, G. Grübel, D. Kaviani-poor and D. Lerche. Phase Transition and Ordering. *Kolloidgesellschaft* (2013)
4. F. Westermeier, A. V. Zozulya, S. Bondarenko, A. Parenti, M. Lohmann, **A. Schavkan**, G. Grübel and M. Sprung. X-ray photon correlation spectroscopy using the Mythen 1D detector. *Journal of Physics Conference Series* 425(20):202005 (2013)
5. V. Zozulya, S. Bondarenko, **A. Schavkan**, F. Westermeier, G. Grübel and M. Sprung. Microfocusing transfocator for 1D and 2D compound refractive lenses. *Optics Express* 20(17):18967-76 (2012)
6. **A. Schavkan**, F. Westermeier, A. V. Zozulya, S. Bondarenko, G. Grübel, Ch. Schroer, and M. Sprung. Using the MAXIPIX detector for coherent X-ray scattering applications. *Journal of Physics Conference Series* 425(20):202004 (2012)
7. **A. Schavkan** and M. Kordon. The Translational and Rotational Dynamics of CigarShaped Colloid Particles, *DESY* (2009)

Acknowledgements

It was a great opportunity to work at Deutsches Elektronen-Synchrotron (DESY). A possibility to do science at a large scale facility, especially that famous and brilliant one, was a tremendous event in my life - a life of a student in the middle of the study then. Therefore I want to acknowledge all the people, who made it possible.

First of all I want to thank Prof. Dr. Gerhard Grübel and Prof. Dr. Wilfried Wurth for making it possible for me to write my thesis at DESY. Especially I want to thank Dr. Michael Sprung, who welcomed me to the Coherence Beamline P10 and supervised me during the whole period of work. Of course I also want to thank all the members of the beamline: Dr. Alexej Zozulya, Dr. Alessandro Ricci, Sergej Bondarenko, Daniel Weschke and Eiryn Müller. Also I want to thank Prof. Dr. Christian Gutt, who supported me since I joined DESY as a summer student and helped me to find the current topic.

Especial thanks are going to Dr. Fabian Westermeier, who shared his expertise with me in lot of discussions and joined me during many experiments, Dr. Birgit Fischer, who helped me during my first attempts in the chemistry lab and guided me in this aspect through whole thesis, as well as Avni Jain, PhD for fruitful discussions.

I would like to thank my supervisor Dr. Michael Sprung, the P10 staff members Dr. Alessandro Ricci and Dr. Alexej Zozulya, as well as Dr. Fabian Westermeier, Dr. Birgit Fischer, Dr. Martin Schroer, Dina Sheyfer, Matthias Kampmann and Michael Walther for help during my beamtimes.

Additional thanks are going to Andreas Kornowski and Almuth Barck as members of the Institute of Physical Chemistry at University of Hamburg for support in performing TEM and XRD measurements.

The colleagues, which I shared the office with, were a great source of motivation and immediate help, if needed, therefore I thank Dr. Alexander Schoekel and Dr. Eric Stellamanns. The proofreading of a thesis is a part, which can go on without end. Therefore I thank all the people, who took a burden upon themselves to proofread my thesis: Dr. Michael Sprung, Dr. Fabian Westermeier, Dr. Andre Phillipi-Kobs, Dr. Wojciech Roseker, Dr. Birgit Fischer, Dr. Alessandro Ricci and Dr. Eric Stellamanns. Dr. Toni Koegler I want additionally to thank for his motivation and general support during my rare visits in Dresden.

A PhD-thesis consists of sweat, blood, tears and coffee - unimaginable amounts of coffee. I thank Matthias Kampmann and Dina Sheyfer for the coffee supply, discussions and work, done during this coffee resupply breaks. I also want to thank my family for supporting me during my studies for the last eleven years and my girlfriend Iuliia Bykova and friends, who didn't let me work all time and gave me chances to recreate and take a break.

Eidesstattliche Erklärung

Hiermit erkläre ich an Eides statt, dass die vorliegende Dissertation von mir eigenhändig verfasst worden ist, abgesehen von den angegebenen Hilfsmitteln und der Beratung durch wissenschaftliche Betreuer. Diese Arbeit wurde an keiner anderen Stelle im Rahmen eines Prüfungsverfahrens eingereicht, weder teilweise noch ganz.

Hamburg, den 24.02.2017

(Alexander Schavkan)